
Precious metal based bulk glass-forming liquids: Development, thermodynamics, kinetics and structure



Dissertation

zur Erlangung des Grades des

Doktors der Ingenieurwissenschaften (Dr.-Ing.)

der

Naturwissenschaftlich-Technischen Fakultät

der

UNIVERSITÄT DES SAARLANDES

vorgelegt von

Oliver Gross

SAARBRÜCKEN
2018

Tag des Kolloquiums:	02.05.2019
Dekan:	Prof. Dr. rer. nat. Guido Kickelbick
Berichterstatter:	Prof. Dr. rer. nat. Ralf Busch Prof. Dr. rer. nat. Gerhard Wilde Prof. Dr. rer. nat. Wulff Possart
Vorsitz:	Prof. Dr.-Ing. Dirk Bähre
Akad. Mitarbeiter:	Dr.-Ing. Florian Schäfer

Abstract

Bulk glass-forming alloy compositions are found in various noble-metal based systems. Their superior properties and their high noble metal content predestinate these alloy classes for the application as jewelry alloys. This work is separated into two parts and focuses on the gold- and platinum-based bulk glass-forming liquids. In the case of the 18 karat white gold bulk glass-forming alloy composition $\text{Au}_{49}\text{Ag}_{5.5}\text{Pd}_{2.3}\text{Cu}_{26.9}\text{Si}_{16.3}$, a fast color change is observed which is attributed to a corrosion process when worn on human skin. A strategy to modify the alloy composition was developed and evaluated that on the one hand allows the improvement of the corrosion resistance and on the other hand maintains the ability of the liquid to form a bulk metallic glass. The second part of this work comprises the evaluation of the thermophysical properties of platinum-phosphorous-based glass-forming liquids. The thermophysical properties are used in combination with high- and low-temperature crystallization experiments to determine the origin of the high glass-forming ability. Moreover, the observed differences within the platinum-phosphorous class as well as those to the compositionally related palladium-phosphorous alloys are investigated in in-situ synchrotron X-ray scattering experiments. The results suggest that the temperature dependence of the atomic dynamics in platinum-phosphorous-based liquids is reflected by structural ordering processes on certain length scales. The differences in the representative structural units and their connection scheme between platinum-phosphorous- and palladium-phosphorous-based liquids might be responsible for the different sensitivity to annealing induced embrittlement which was already reported in literature.

Zusammenfassung

Massivglasbildende Legierungszusammensetzungen existieren in verschiedenen edelmetallbasierten Systemen. Ihre überlegenen Eigenschaften und ihr hoher Edelmetallgehalt prädestinieren diese Legierungsklassen für die Anwendung als Schmucklegierungen. Der Schwerpunkt der zweiteiligen Arbeit liegt auf Gold- und Platin-basierten massivglasbildenden Legierungen. Im Fall der massivglasbildenden 18 Karat Weißgoldlegierungen $\text{Au}_{49}\text{Ag}_{5.5}\text{Pd}_{2.3}\text{Cu}_{26.9}\text{Si}_{16.3}$ wurde eine rasche Farbänderung beobachtet, die auf einen Korrosionsprozess durch das Tragen auf der Haut zurückzuführen ist. Es wurde ein Anpassungskonzept entwickelt und umgesetzt, das einerseits die Verbesserung der Korrosionsresistenz bewirkt und andererseits die Fähigkeit der Schmelze ein metallisches Massivglas zu bilden erhält. Der zweite Teil der Arbeit beschäftigt sich mit der Bestimmung der thermophysikalischen Eigenschaften von Platin-Phosphor-basierten glasbildenden Schmelzen. Die thermophysikalischen Eigenschaften werden in Kombination mit Hoch- und Tieftemperaturkristallisationsexperimenten verwendet um den Ursprung der hohen Glasbildungsfähigkeit der Legierungen zu ergründen. Darüber hinaus wurden die beobachteten Unterschiede innerhalb der Platin-Phosphor Klasse sowie die zu den kompositionell verwandten Palladium-Phosphor-basierten Legierungen in strukturaufklärenden Synchrotron-Röntgenstreuexperimenten untersucht. Die Ergebnisse weisen darauf hin, dass sich die Temperaturabhängigkeit der atomaren Dynamik in Platin-Phosphor-basierten Schmelzen in strukturellen Ordnungsprozessen auf gewissen Längenskalen widerspiegeln. Die strukturellen Unterschiede zwischen Platin- und Palladium-Phosphor-basierten Legierungen im Bereich der repräsentativen Struktureinheiten und deren Verbindungsart könnten die in der Literatur berichtete unterschiedliche Sensitivität für anlassinduzierte Versprödung sein.

Danksagung

Besonderen Dank möchte ich Prof. Dr. Ralf Busch für die Betreuung dieser Arbeit aussprechen. Seine Unterstützung und konstruktiven Anregungen haben wesentlich zum Gelingen beigetragen. Weiterer Dank gilt Dr. Isabella Gallino, die mich schon während meiner Diplomarbeit in den Bereich der Kalorimetrie eingeführt hat und mir immer mit Rat und Tat zur Seite stand. Vielen Dank auch an meine Kollegen und Freunde Alexander Kuball, Benedikt Bochtler, Simon Hechler, Nico Neuber und Maximilian Frey für die bereichernden Diskussionen und die großartige Zusammenarbeit. Besonders in Erinnerung wird mir der „Alles ist möglich Freitag“ bleiben, an dem wir gemeinsam kreative Elementkombination oder Herstellungsprozesse getestet haben, was durchaus von Erfolg gekrönt war. Meinen aufrichtigen Dank möchte ich Moritz Stolpe und Dr. Shuai Wei entgegenbringen, die mir die Streuexperimente am DESY nähergebracht haben und durch deren Feedback ich beim Schreiben von Veröffentlichungen viel gelernt habe. Des Weiteren möchte ich mich bei Dr. William Hembree, Dr. Jochen Heinrich, Dr. Zach Evenson und Dr. Sanja Stanojevic bedanken, von deren Wissen ich als „Jung-Doktorand“ sehr profitiert habe. Genauso danken möchte ich Dr. Frank Aubertin für die zahlreichen Erläuterungen zu intermetallischen Phasen und zu vielen anderen Themen. Bei Dr. Miriam Eisenbart und Dr. Ulrich Klotz vom Forschungsinstitut für Edelmetalle und Metallchemie in Schwäbisch Gmünd bedanke ich mich für die langjährige und gelungene Zusammenarbeit. Für die pfeilschnelle Behebung von technischen Problemen und ihr Engagement bei der kontinuierlichen Weiterentwicklung der Laboranlagen gebührt mein Dank Jörg Eiden und Hermann Altmeyer. Herzlichen Dank auch an Lisa Schmitt, Lamia Ciftci, Sascha Riegler und an die anderen HIWIs für die Unterstützung bei den zahlreichen Experimenten und der Probenherstellung sowie an Martina Stemmler für die XRD Messungen. Auch möchte ich mich bei der guten Seele des Lehrstuhls Sigrid Neusius bedanken, die wesentlich zum tollen Arbeitsklima beiträgt. Großer Dank gebührt meinen Eltern Olaf und Susanne und meiner Schwester Lisa, deren Zuspruch und Liebe mir eine wichtige Stütze sind. Ganz besonders möchte ich mich bei meiner Frau Caroline für ihre bedingungslose Unterstützung, Geduld und Liebe bedanken.

Contributions and publications

The work in Chapter 4 was carried out in a project funded by the German Federation of Industrial Research Associations (AiF/IGF) through Project No. 17716N in cooperation with the *Forschungsinstitut für Edelmetalle und Metallchemie (fem)* in Schwäbisch Gmünd. Dr. M. Eisenbart (*fem*) and Dr. U. E. Klotz (*fem*) conducted the corrosion experiments, analyzed the corrosion data and performed the ThermoCalc calculations. The author supervised the Bachelor Thesis of Lamia Ciftci and the Master Thesis of Nico Neuber which partially contribute to Chapter 4. The work in Chapter 4/5 was partially funded by the Deutsche Forschungsgemeinschaft through Grant No. GA 1721/2-2. The crystallization experiments in Chapter 5 on Pt_{42.5}Cu₂₇Ni_{9.5}P₂₁ were measured in the framework of the Bachelor Thesis of Sascha S. Riegler who the author supervised. The synchrotron X-ray scattering experiments shown in Chapter 5 were collected during the beamtimes applied by Prof. Dr. J. J. Kruzic, Moritz Stolpe and the author. The scattering experiments were carried out by M. Stolpe, Dr. S. Wei, Dr. W. Hembree, Dr. Z. Evenson, Dr. I. Gallino, B. Bochtler, S. Hechler, A. Kuball, N. Neuber, M. Frey and the author.

The work of this thesis is published in the following peer-reviewed articles:

- [O. Gross](#), M. Eisenbart, L.-Y. Schmitt, N. Neuber, L. Ciftci, U.E. Klotz, R. Busch, I. Gallino, Development of novel 18-karat, premium-white gold bulk metallic glasses with improved tarnishing resistance, *Mater. Des.* 140 (2018) 495–504. doi:10.1016/j.matdes.2017.12.007.
- [O. Gross](#), S. S. Riegler, M. Stolpe, B. Bochtler, A. Kuball, S. Hechler, R. Busch, I. Gallino, On the high glass-forming ability of Pt-Cu-Ni/Co-P-based liquids, *Acta Mater.* 141 (2017) 109–119. doi:10.1016/j.actamat.2017.09.013.
- [O. Gross](#), B. Bochtler, M. Stolpe, S. Hechler, W. Hembree, R. Busch, I. Gallino, The kinetic fragility of Pt-P- and Ni-P-based bulk glass-forming liquids and its thermodynamic and structural signature, *Acta Mater.* 132 (2017) 118–127. doi:10.1016/j.actamat.2017.04.030.

Additionally, the author contributed to the following peer-reviewed publications:

- S. Hechler, B. Ruta, M. Stolpe, E. Pineda, Z. Evenson, [O. Gross](#), A. Bernasconi, R. Busch, I. Gallino, Microscopic evidence of the connection between liquid-liquid transition and dynamical crossover in an ultra-viscous metallic glass former, *Phys. Rev. Lett.* 085603 (2018) 1–6. doi:10.1103/PhysRevMaterials.2.-085603.
- A. Kuball, B. Bochtler, [O. Gross](#), V. Pacheco, M. Stolpe, S. Hechler, R. Busch, On the Bulk Glass Formation in the Ternary Pd-Ni-S System, *Acta Mater.* 158 (2018) 13–22. doi:10.1016/J.ACTAMAT.2018.07.039.
- A. Kuball, [O. Gross](#), B. Bochtler, R. Busch, Sulfur-bearing metallic glasses: A new family of bulk glass-forming alloys, *Scripta Mater.* 146 (2018) 73–76. doi:10.1016/j.scriptamat.2017.11.011.
- S. Wei, M. Stolpe, [O. Gross](#), W. Hembree, S. Hechler, J. Bednarcik, R. Busch, P. Lucas, Structural evolution on medium-range-order during the fragile-strong transition in Ge₁₅Te₈₅, *Acta Mater.* 129 (2017) 259–267. doi:10.1016/j.actamat.-2017.02.055.

- B. Bochtler, O. Gross, R. Busch, Indications for a fragile-to-strong transition in the high- and low-temperature viscosity of the $\text{Fe}_{43}\text{Cr}_{16}\text{Mo}_{16}\text{C}_{15}\text{B}_{10}$ bulk metallic glass forming alloy, *Appl. Phys. Lett.* 111 (2017) 261902. doi:10.1063/1.5013108.
- B. Bochtler, O. Gross, I. Gallino, R. Busch, Thermo-physical characterization of the $\text{Fe}_{67}\text{Mo}_6\text{Ni}_{3.5}\text{Cr}_{3.5}\text{P}_{12}\text{C}_{5.5}\text{B}_{2.5}$ bulk metallic glass forming alloy, *Acta Mater.* 118 (2016) 129–139. doi:10.1016/j.actamat.2016.07.031.
- S. Wei, M. Stolpe, O. Gross, Z. Evenson, I. Gallino, W. Hembree, J. Bednarcik, J.J. Kruzic, R. Busch, Linking structure to fragility in bulk metallic glass-forming liquids, *Appl. Phys. Lett.* 106 (2015). doi:10.1063/1.4919590.
- Z. Evenson, T. Koschine, S. Wei, O. Gross, J. Bednarcik, I. Gallino, J.J. Kruzic, K. Rätzke, F. Faupel, R. Busch, The effect of low-temperature structural relaxation on free volume and chemical short-range ordering in a $\text{Au}_{49}\text{Cu}_{26.9}\text{Si}_{16.3}\text{Ag}_{5.5}\text{Pd}_{2.3}$ bulk metallic glass, *Scripta Mater.* 103 (2015) 14–17. doi:10.1016/j.scriptamat.2015.02.026.
- Z. Evenson, S.E. Naleway, S. Wei, O. Gross, J. J. Kruzic, I. Gallino, W. Possart, M. Stommel, R. Busch, β -relaxation and low-temperature aging in a Au-based bulk metallic glass: From elastic properties to atomic-scale structure, *Phys. Rev. B.* 89 (2014) 174204. doi:10.1103/PhysRevB.89.174204.
- I. Gallino, O. Gross, G. Dalla Fontana, Z. Evenson, R. Busch, On the kinetic and thermodynamic fragility of the $\text{Pt}_{60}\text{Cu}_{16}\text{Co}_2\text{P}_{22}$ and $\text{Pt}_{57.3}\text{Cu}_{14.6}\text{Ni}_{5.3}\text{P}_{22.8}$ bulk metallic glasses, *J. Alloys Compd.* 615 (2014) S35–S39. doi:10.1016/j.jallcom.-2013.12.006.

Articles without peer-review process:

- S. Hechler, B. Ruta, M. Stolpe, E. Pineda, Z. Evenson, O. Gross, W. Hembree, A. Bernasconi, R. Busch, I. Gallino, Liquid-liquid transition revealed by quasi-static cooling of an ultra-viscous metallic liquid, *ArXiv*. 1704.06703 (2017). <http://arxiv.org/abs/1704.06703>.

The result of this thesis have been presented as contributions to various conferences:

- **2018.** *DPG (Deutsche Physikalische Gesellschaft) Frühjahrstagung* Berlin, GERMANY. Oral presentation: On the high glass-forming ability of Pt-Cu-Ni/Co-P-based liquids.
- **2017.** *The 16th International Conference on Rapidly Quenched and Metastable Materials (RQ16)* Leoben, AUSTRIA. Oral presentation: The kinetic fragility of Pt-P based glass-forming liquids and its thermodynamic and structural signature.
- **2017.** *DPG (Deutsche Physikalische Gesellschaft) Frühjahrstagung* Dresden, GERMANY. Oral presentation: Thermodynamic and dynamic studies of phosphorus containing bulk metallic glass forming liquids.

- **2016.** *16th International Conference on Liquid and Amorphous Metals (LAM-16)* Bonn Bad Godesberg, GERMANY. Oral presentation: Thermodynamic and dynamic studies of phosphorus containing bulk metallic glass forming liquids.
- **2015.** *22nd International Symposium on Metastable, Amorphous and Nanostructured Materials* Paris, FRANCE. Poster contribution: Thermodynamic and kinetic studies of Pt-P- and Ni-P-based bulk metallic glass forming alloys.
- **2013.** *2013 MRS Fall Meeting (Materials Research Society)* Boston, MA. USA. Oral presentation: Thermodynamic and kinetic studies of Pt-based bulk glass forming alloys.

Patent application:

- **DE102016008074A1.** Inventor: O. Gross, I. Gallino, R. Busch, M. Eisenbart, U.E. Klotz. "*Massivglasbildende Weißgoldlegierung*"
- **EP17001437.7-1373.** Inventor: A. Kuball, O. Gross, B. Bochtler, R. Busch. "*Schweifelhaltige Metallische Gläser*"
- **2018062914194200DE.** Inventor: A. Kuball, O. Gross, B. Bochtler, S. Hechler, R. Busch. "*Vorrichtung und Verfahren zur Herstellung eines aus einem amorphen oder teilamorphen Metall gebildeten Gussteils sowie Gussteil*"

Proposals and Education

Proposals accepted:

- **IGF 17716N**. "Legierungsentwicklung und thermoplastisches Formen von amorphen 18kt Weißgoldlegierungen". Authors: O. Gross and M. Eisenbart, 2015.
- **IGF 19979N**. "Entwicklung, Herstellung und thermoplastisches Formen nickelfreier platinbasierter, biokompatibler metallischer Massivgläser". Authors: O. Gross and M. Eisenbart, 2018.
- **I-20170938**, Scheduled beamtime at **DESY** (Deutsche Elektronen Synchrotron), 48 h in 2018, O. Gross, B. Bochtler, A. Kuball, R. Busch, "Investigation of the compositional dependence of structural changes of Pt/Pd-Cu-Ni-P bulk glass forming liquids and their connection to kinetic fragility", 2017.
- **I-20150545**, Scheduled beamtime at **DESY** (Deutsche Elektronen Synchrotron), 48 h in 2016, M. Stolpe, O. Gross, S. Hechler, R. Busch, *Investigation of the high temperature structural changes in non-Zr based bulk metallic glass-forming liquids*, 2015.
- **I-20140115** Scheduled beamtime at **DESY** (Deutsche Elektronen Synchrotron), 48 h in 2015, S. Wei, M. Stolpe, O. Gross, R. Busch, C. A. Angell *Investigation of structural connection to kinetic fragility of bulk metallic glass-formers*, 2014.
- **TEMPUS** (Tiegelfreies Elektromagnetisches Prozessieren Unter Schwerelosigkeit), 5 Parabolos, A. Kuball, B. Bochtler, O. Gross, R. Busch, "Viskosität und Oberflächenspannung der Schmelze der neuartigen, massivglasbildenden Titanlegierung $Ti_{65}Zr_{10}Cu_{15}Ni_2S_8$ ", 2018
- **TEMPUS** (Tiegelfreies Elektromagnetisches Prozessieren Unter Schwerelosigkeit), 5 Parabolos, O. Gross, B. Bochtler, R. Busch, "Melt viscosity and volume evolution in the undercooled liquid of the $Pt_{42.5}Cu_{27}Ni_{9.5}P_{21}$ bulk glass forming liquid", 2017.
- **TEMPUS** (Tiegelfreies Elektromagnetisches Prozessieren Unter Schwerelosigkeit), 5 Parabolos, B. Bochtler, O. Gross, R. Busch, "Melt viscosity of the $Fe_{43}Cr_{16}Mo_{16}C_{15}B_{10}$ bulk metallic glass-forming liquid", 2016.
- **TEMPUS** (Tiegelfreies Elektromagnetisches Prozessieren Unter Schwerelosigkeit), 5 Parabolos, O. Gross, W. Hembree, B. Bochtler, R. Busch, "Melt viscosity of a the newly discovered $Fe_{67}Mo_6Ni_{3.5}Cr_{3.5}P_{12}C_{5.5}B_{2.5}$ bulk metallic glass-forming liquid", 2015.
- **TEMPUS** (Tiegelfreies Elektromagnetisches Prozessieren Unter Schwerelosigkeit), 5 Parabolos, O. Gross, W. Hembree, M. Stolpe, Z. Evenson, I. Gallino, R. Busch, "Melt viscosity of a the newly discovered $Ni_{69}Cr_{8.5}Nb_3P_{16.5}B_3$ bulk metallic glass-forming liquid", 2014.

The author has supervised or supervised parts (p) of the following theses. Some contribute in part to Chapter 4 and 5.

- **Master Thesis:** S. S. Riegler, *"Investigations on the annealing induced structural changes in Zr-Cu-Al-Ag bulk metallic glasses and their effects on the kinetic and mechanical properties"*, Saarland University, 2019.
- **Master Thesis:** N. Neuber, *"Alloy Development and Thermophysical Characterization of Amorphous 18kt White Gold Bulk Metallic Glasses with Improved Tarnishing Resistance"*, Saarland University, 2017.
- **Master Thesis (p):** L.-Y. Schmitt, *"Relaxation studies with a 18 carat Au-based glass-forming alloy"*, Master Thesis, Saarland University, 2017.
- **Master Thesis (p):** V. Pacheco, *"Optimization and characterization of a novel Pd - Ni based bulk metallic glass forming alloy"*, Saarland University, 2016.
- **Master Thesis:** B. Bochtler, *"Characterization of a novel iron-phosphorus based bulk metallic glass forming alloy"*, Saarland University, 2015.
- **Master Thesis (p):** S. Gärtner, *"Untersuchung verschiedener kinetischer Eigenschaften der metallischen massivglasbildenden Legierungen $Zr_{60}Cu_{25}Al_{15}$ und $Zr_{65}Cu_{17,5}Ni_{10}Al_{7,5}$ "*, Saarland University, 2015.
- **Bachelor Thesis:** L. Ruschel, *"Entwicklung metalloidgehaltiger metallischer Gläser auf Titanbasis"*, Saarland University, 2018
- **Bachelor Thesis:** J. Rosar, *"Erstellen von Kühlkurven während eines konventionellen Gießprozesses von massivglasbildenden Zr / Cu- Legierungen"*, Saarland University, 2018
- **Bachelor Thesis:** S. S. Riegler, *"Bestimmung des isothermen und des kontinuierlichen ZTU-Diagramms des metallischen Massivglases $Pt_{42,5}Cu_{27}Ni_{9,5}P_{21}$ "*, Saarland University, 2016
- **Bachelor Thesis:** L. Ciftci, *Legierungsentwicklung einer 18-karätigen massivglasbildenden Weißgoldlegierung & Recyclbarkeit der $Au_{51,59}Ag_{5,79}Pd_{2,42}Cu_{20,175}Si_{13,3}Ga_{6,725}$* , Saarland University, 2016

Contents

1	Introduction	1
2	Glass formation in metallic systems	5
2.1	Metallic Glasses: Frozen-in liquids	5
2.2	The driving force for nucleation and the glass-forming region	7
2.3	The fragility classification	12
2.3.1	Thermodynamic and kinetic signature of fragility	12
2.3.2	Structural signature of fragility	16
2.4	Nucleation, growth and the glass-forming ability	20
2.5	Properties of the frozen-in and supercooled liquid	31
2.5.1	The entropy catastrophe	31
2.5.2	From the glass to the supercooled liquid: phenomena of structural relaxation	33
2.5.3	Crystallization of the supercooled liquid	37
2.6	Structure of Metallic Liquids	39
3	Materials and Methods	43
3.1	Sample preparation and analysis	43
3.2	Corrosion tests and color measurements	45
3.3	Measurements of the thermophysical properties	46
3.3.1	Calorimetric measurements	46
3.3.2	Viscosity measurements	50
3.4	In-situ synchrotron X-ray scattering measurements	52
4	Development of a gold based bulk metallic glass with improved tarnishing resistance	57
4.1	Alloy development	59
4.2	Corrosion in artificial saliva	62
4.3	Discussion	63
4.4	Summary and Outlook	72
5	Pt-P-based bulk metallic glasses	75
5.1	Thermodynamics and kinetics of the liquid	76
5.1.1	Thermodynamic properties	76
5.1.2	The kinetic fragility	79
5.2	Crystallization of the supercooled liquid	85
5.3	Compositional dependent and temperature-induced structural evolution in Pt-P-based liquids	90
5.4	Discussion	92
5.4.1	Origin of the high glass-forming ability	92
5.4.2	Differences between Pt- and Pd-P-based alloys and the role of short- and medium-range order	98
5.5	Summary and Outlook	112

A Copyright Permissions	115
Bibliography	117

List of Figures

1.1	Schematic time-temperature-transformation diagram	2
1.2	Critical casting thickness and critical cooling rate of different bulk glass-forming alloy families	3
2.1	Volume and viscosity/structural relaxation time of a glass-forming liquid as a function of temperature	6
2.2	Gibbs free energy of the liquid and the crystal as a function of temperature	8
2.3	Driving force for nucleation and crystallization in an eutectic system and metastable regions of the solid solution	11
2.4	Angell plot of different glass-forming liquids	13
2.5	Thermodynamic fragility plot	15
2.6	Kinetic and thermodynamic signature of fragility in (bulk metallic) glass-forming liquids	17
2.7	Simulated specific heat capacity and viscosity of the $\text{Cu}_{64}\text{Zr}_{36}$ and the $\text{Pd}_{82}\text{Si}_{18}$ liquids	18
2.8	Evolution of the characteristic short-range order and cluster sharing typ in $\text{Cu}_{64}\text{Zr}_{36}$ and $\text{Mg}_{65}\text{Cu}_{25}\text{Y}_{10}$	19
2.9	Structural fragility parameter vs. kinetic fragility index of different bulk glass-forming liquids	20
2.10	Change in the Gibbs free energy of a liquid through the formation of a spherical, crystalline particle	22
2.11	Nucleation rate and growth rate as a function of temperature	24
2.12	Effect of the Gibbs free energy difference between the liquid and the crystal on the nucleation rate, growth rate and the TTT diagram	26
2.13	Effect of the kinetic fragility of the liquid) on the nucleation rate, growth rate and the TTT diagram	27
2.14	Effect of the interfacial energy on the nucleation rate and the TTT diagram	28
2.15	Effect of thermodynamic and kinetic parameter on crystallization nose	29
2.16	Effect of heterogeneous nucleation on the TTT diagram	30
2.17	Decoupling of translational diffusion and structural relaxation and TTT diagram of Vit1	32
2.18	Change in the thermophysical properties of metallic glass upon heating	34
2.19	Isothermal viscosity relaxation	36
2.20	Isothermal TTT diagram upon heating and cooling of $\text{Au}_{49}\text{Ag}_{5.5}\text{Pd}_{2.3}\text{-Cu}_{26.9}\text{Si}_{16.3}$	38
2.21	Short- and medium-range order in metallic glass-forming liquids	40
3.1	Tilt-cast samples of $\text{Au}_{49}\text{Ag}_{5.5}\text{Pd}_{2.3}\text{Cu}_{26.9}\text{Si}_{16.3}$ with varying diameter	43
3.2	Alloying procedure of P-containing alloys in a fused silica tube	44
3.3	Determination of the crystallization enthalpy from a thermogram	48
3.4	T_g -shift measurement of an amorphous sample	49

3.5	Measurement of a continuous-cooling/heating-transformation and time-temperature-transformation diagram	51
3.6	Atomic form factor and weighting factor	54
4.1	Color change of an amorphous white gold ring	57
4.2	Tarnishing mechanism at the surface of a Au-based bulk metallic glass	58
4.3	Ternary Au-Cu-Si phase diagram	59
4.4	XRD measurements of $\text{Au}_{49}\text{Ag}_{5.5}\text{Pd}_{2.3}\text{Cu}_{23.5}\text{Ga}_{3.4}\text{Si}_{16.3}$ and $\text{Au}_{49}\text{Ag}_{5.5}\text{Pd}_{2.3}\text{Cu}_{20.2}\text{Ga}_{6.7}\text{Si}_{16.3}$ and SEM images of $\text{Au}_{49}\text{Ag}_{5.5}\text{Pd}_{2.3}\text{Cu}_{20.2}\text{Ga}_{6.7}\text{Si}_{16.3}$	60
4.5	Melting interval of different Au-based alloys	61
4.6	XRD and DSC measurements of $\text{Au}_{51.6}\text{Ag}_{5.8}\text{Pd}_{2.4}\text{Cu}_{20.2}\text{Ga}_{6.7}\text{Si}_{13.3}$	62
4.7	XRD measurements of Sn-, In- and Sb-containing Au-based alloys	63
4.8	Melting interval of different Sn-containing alloys and XRD measurements of $\text{Au}_{51.6}\text{Ag}_{5.8}\text{Pd}_{2.4}\text{Cu}_{20.2}\text{Sn}_{6.7}\text{Si}_{13.3}$	64
4.9	Ion release in artificial saliva of different Au-based alloys	65
4.10	FIB cuts into the surface of different Au-based alloys	65
4.11	Evolution of the Yellowness Index during a wearing test	66
4.12	Integrated melting event of different Au-based alloy and entropy of fusion vs. reduced glass transition temperature	67
4.13	Effect of the primary precipitating phase on the nucleation temperature and its indication on the GFA	68
4.14	Calculated liquidus projections of the Au-Ga-Si and Au-Sn-Si system	70
4.15	Effect of the substitution of Cu by Ga on the Cu release and d_c	71
4.16	Effect of the Ga implantation on the tarnishing behavior of a Au-BMG	72
4.17	Photography of tarnished and freshly ground samples	73
5.1	Amorphous wedding band made of $\text{Pt}_{57.3}\text{Cu}_{14.6}\text{Ni}_{5.3}\text{P}_{22.8}$	75
5.2	Specific heat capacity of $\text{Pt}_{42.5}\text{Cu}_{27}\text{Ni}_{9.5}\text{P}_{21}$ and $\text{Pt}_{60}\text{Cu}_{16}\text{Co}_2\text{P}_{22}$	76
5.3	Enthalpy pathway of $\text{Pt}_{42.5}\text{Cu}_{27}\text{Ni}_{9.5}\text{P}_{21}$	79
5.4	Enthalpy of the undercooled liquid of $\text{Pt}_{42.5}\text{Cu}_{27}\text{Ni}_{9.5}\text{P}_{21}$ and $\text{Pt}_{60}\text{Cu}_{16}\text{Co}_2\text{P}_{22}$ with respect to the crystal as a function of temperature	80
5.5	Isothermal viscosity measurements below the calorimetric glass transition of $\text{Pt}_{60}\text{Cu}_{16}\text{Co}_2\text{P}_{22}$ and $\text{Pd}_{43}\text{Cu}_{27}\text{Ni}_{10}\text{P}_{20}$	81
5.6	T_g -shift measurements of $\text{Pt}_{42.5}\text{Cu}_{27}\text{Ni}_{9.5}\text{P}_{21}$	82
5.7	Isothermally and continuously measured viscosity of $\text{Pt}_{42.5}\text{Cu}_{27}\text{Ni}_{9.5}\text{P}_{21}$ and $\text{Pt}_{60}\text{Cu}_{16}\text{Co}_2\text{P}_{22}$ as a function of temperature	83
5.8	Angell Plot of the equilibrium viscosity of different BMG forming liquids	84
5.9	Crystallization experiments on $\text{Pt}_{42.5}\text{Cu}_{27}\text{Ni}_{9.5}\text{P}_{21}$	85
5.10	Crystallization of the primary phase in $\text{Pt}_{60}\text{Cu}_{16}\text{Co}_2\text{P}_{22}$	86
5.11	Continuous cooling experiments of $\text{Pt}_{60}\text{Cu}_{16}\text{Co}_2\text{P}_{22}$	87
5.12	Continuous heating and cooling transformation diagram of (a) $\text{Pt}_{42.5}\text{Cu}_{27}\text{Ni}_{9.5}\text{P}_{21}$ and (b) $\text{Pt}_{60}\text{Cu}_{16}\text{Co}_2\text{P}_{22}$	88
5.13	Time-temperature-transformation diagram of $\text{Pt}_{42.5}\text{Cu}_{27}\text{Ni}_{9.5}\text{P}_{21}$ and $\text{Pt}_{60}\text{Cu}_{16}\text{Co}_2\text{P}_{22}$	89
5.14	Temperature-induced evolution of the total-scattering structure function of $\text{Pt}_{42.5}\text{Cu}_{27}\text{Ni}_{9.5}\text{P}_{21}$	90
5.15	Total-scattering structure function of different Pt/Pd-P-based alloys	91
5.16	Compositional dependence of the total-scattering structure function	92
5.17	Total-scattering structure function of $\text{Pt}_{42.5}\text{Cu}_{27}\text{Ni}_{9.5}\text{P}_{21}$ and $\text{Pd}_{43}\text{Cu}_{27}\text{Ni}_{10}\text{P}_{20}$ as function of temperature	93

5.18	Gibbs free energy difference between the supercooled liquid and the crystal of Pt- and Pd-P-based alloys	94
5.19	Time-temperature-transformation diagram of $\text{Pd}_{43}\text{Cu}_{27}\text{Ni}_{10}\text{P}_{20}$	95
5.20	Comparison of the kinetic fragility, the driving force for crystallization and the interfacial energy of different liquids	97
5.21	Origin of the glass-forming ability of different BMG forming alloy systems	99
5.22	Comparison of the nucleation rate, growth rate and crystallization time of $\text{Pt}_{42.5}\text{Cu}_{27}\text{Ni}_{9.5}\text{P}_{21}$ and $\text{Pd}_{43}\text{Cu}_{27}\text{Ni}_{10}\text{P}_{20}$	100
5.23	Normalized specific heat capacity of Pt-P- and Pd-P-based liquids	101
5.24	Reduced pair distribution function of $\text{Pt}_{42.5}\text{Cu}_{27}\text{Ni}_{9.5}\text{P}_{21}$ and $\text{Pd}_{43}\text{Cu}_{27}\text{Ni}_{10}\text{P}_{20}$ as a function of temperature	103
5.25	Second nearest neighbor and connections schemes	104
5.26	Compositional dependence of the reduced pair distribution function of Pt/Pd-P-based glasses	105
5.27	Influence of Q_{max} on $G(r)$	106
5.28	Temperature-induced structural evolution on the MRO length scale in Pt-P-based alloys	107
5.29	Temperature-induced structural evolution on the MRO length scale of $\text{Pt}_{42.5}\text{Cu}_{27}\text{Ni}_{9.5}\text{P}_{21}$ at high and low temperatures	108
5.30	Temperature-induced structural evolution on the MRO length scale of $\text{Pd}_{43}\text{Cu}_{27}\text{Ni}_{10}\text{P}_{20}$ at high and low temperatures	109
5.31	Peak position of the FSDP of $\text{Pt}_{42.5}\text{Cu}_{27}\text{Ni}_{9.5}\text{P}_{21}$ and $\text{Pd}_{43}\text{Cu}_{27}\text{Ni}_{10}\text{P}_{20}$ as function of temperature	110
5.32	TTT diagrams with critical fictive temperature for $\text{Pd}_{43}\text{Cu}_{27}\text{Ni}_{10}\text{P}_{20}$ and $\text{Pt}_{42.5}\text{Cu}_{27}\text{Ni}_{9.5}\text{P}_{21}$	111

List of Tables

4.1	Thermophysical properties of Au-based BMGs	67
5.1	Fitting parameter of the specific heat capacity	77
5.2	Characteristic temperature, enthalpy and entropy of fusion of different Pt-P-based alloys	78
5.3	Kinetic parameters of Pt-P-based liquids	84
5.4	Values of the interfacial energy and the pre-factor obtained from the fitting of the isothermal crystallization data	96
5.5	Structural fragility parameter of Pt/Pd-P-based alloys	107

List of Abbreviations

3PBB	three-point beam bending
AG	Adam-Gibbs
BMG	Bulk Metallic Glass
BSAP	bicapped square antiprism
BSE	backscattered electron
CCT	continuous-cooling transformation
CHT	continuous-heating transformation
CSRO	chemical short-range order
DSC	differential scanning calorimetry
DTA	differential thermal analysis
ECP	efficient cluster packing
FDSC	fast differential scanning calorimetry
FIB	focused ion beam
FSDP	first sharp diffraction peak
GFA	glass-forming ability
GFR	glass-forming region
GUN	geometrically unfavored motif
ICO-OES	inductively coupled plasma optical emission spectroscopy
ISRO	icosahedral short-range order
JMAK	Johnson-Mehl-Avrami-Kolmogorov
KWW	Kohlrausch-Williams-Watts
MG	metallic glass
MRO	medium-range order
NBED	nanobeam electron diffraction
SEM	scanning electron microscopy
SRO	short-range order
TPF	thermoplastic forming
TSRO	topological short-range order
TTP	tricapped trigonal prism
TTT	time-temperature-transformation
VFT	Vogel-Fulcher-Tammann
XRD	X-ray diffraction
YI	Yellowness Index

Für Caroline.

Chapter 1

Introduction

Crystalline metals or alloys are known for thousands of years and are nowadays essential to our everyday life. The knowledge of their periodic atomic structure and how it reacts on external stimuli or how it can be modified to fit certain requirements is the basis of the success of this material class. The pioneering works of Turnbull brought insights into the mechanisms enabling the atoms to form a periodic crystal structure from the disordered melt [1, 2]. The crystalline microstructure that is formed from the melt is strongly affected by the processing conditions and can alter the mechanical properties significantly. The attempts of Duwez and co-workers in 1959 to form a supersaturated solid solution in vicinity of the Au-Si eutectic by rapid quenching gave rise to a completely new material class. For the first time they succeeded to suppress the crystallization process, which is governed by thermodynamic and kinetic constraints, and produced the first metallic glass (MG) with a thickness of 10 μm [3]. The recipe to successfully avoid crystallization of the $\text{Au}_{75}\text{Si}_{25}$ ¹ alloy composition and to preserve the amorphous structure of the liquid phase was an extremely high cooling rate. As visualized in the *time-temperature-transformation* (TTT) diagram in Fig. 1.1, crystallization is a time depended process occurring in the supercooled liquid region below the melting point of the alloy. In the experiment performed by Duwez and co-workers, the liquid alloy was subject to a cooling rate that was higher or equal to the *critical cooling rate* (R_c) i.e. the minimum cooling rate needed to bypass the crystallization event and to conserve the macroscopically disordered structure of the liquid (amorphous structure). The first metallic glasses was difficult to characterize in terms of the mechanical and thermo-physical properties as it readily crystallizes at ambient conditions due to its thermodynamically unstable nature. Further developments aimed at increasing the *glass-forming ability* (GFA) of the metallic alloys. The GFA depends on the time that the crystalline phase needs to form within the undercooled liquid which is represented by the crystallization nose in the TTT diagram. For alloys whose crystallization process is shifted to longer times, a much lower R_c is need to maintain the amorphous structure of the liquid at low temperatures. R_c is connected to the maximum diameter or *critical diameter* d_c up to which a fully amorphous structures is obtained. As d_c is easier accessible than R_c , d_c is mostly used as a measure of the GFA. However, both values are connected through [4]

$$R_c = \frac{10}{d_c^2} K \text{cm}^2 \text{s}^{-1}. \quad (1.1)$$

In the following decades, it was observed that glass formation is a common phenomenon in metallic systems and a variety of metallic glass-forming compositions were discovered [5–9]. Among these systems, some exceed a d_c of 1 mm and were

¹All concentrations are given in atomic percent (at%).

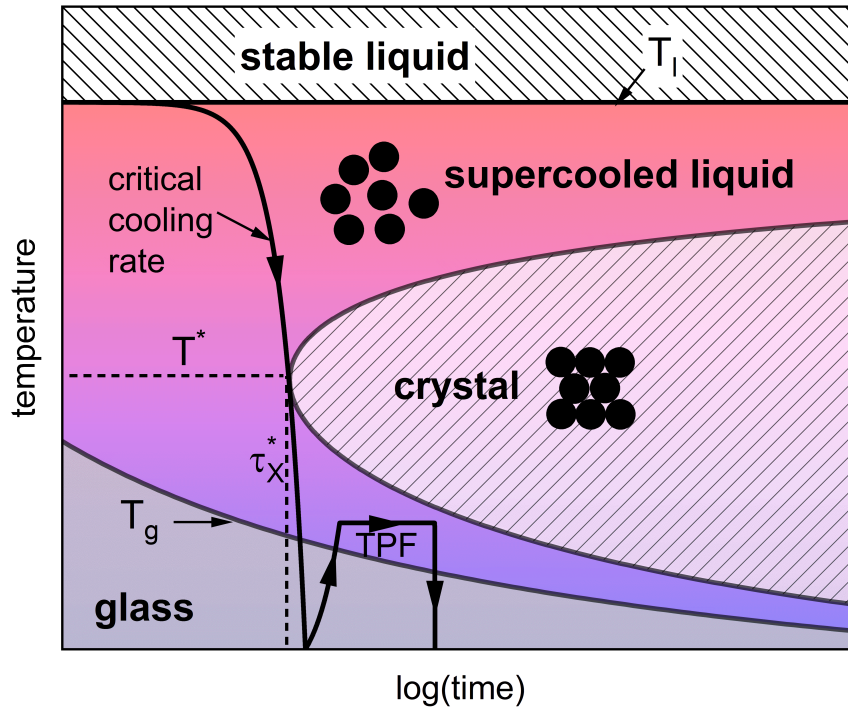


FIGURE 1.1: Schematic time-temperature-transformation (TTT) diagram of a glass-forming metallic liquid. The critical cooling rate (R_c) is the minimum cooling rate that is needed to bypass the crystallization event in the supercooled liquid region below the liquidus temperature T_l and to conserve the macroscopically disordered structure of the liquid at the glass transition temperature T_g . The minimum time for crystal formation τ_X^* is found at the temperature T^* . During the thermoplastic forming (TPF) process, the glassy sample is heated into the supercooled liquid region, shaped and cooled again below T_g before the crystallization onset is reached.

henceforth termed *bulk metallic glasses* (BMGs). Figure 1.2 shows the current record holders in terms of d_c in the known alloy families.

BMGs combine a high strength, which is close to the theoretical strength, with a large elasticity of approximately two percent [10, 11]. Moreover, some alloys feature an extraordinary thermal stability upon reheating and do not directly crystallize above the glass transition. These alloys can be shaped applying a temperature protocol as shown in Fig. 1.1. In the supercooled liquid region, pattern on the nanometer scale can be replicated [12] or amorphous powder can be consolidate in order to circumvent the limitation of the critical casting thickness [13]. If the liquid is cooled below the *glass transition temperature* T_g before the onset of crystallization is reached, the amorphous structure is preserved. This process is called *thermoplastic forming* (TPF) and is well known for polymers and oxide glasses, however it is a novelty for metals.

The discovery of a variety of BMG forming compositions gave rise to empirical rules that were derived from the similarities observed in the different glass-forming alloying systems [26–28]. The rules are found to increase the probability to find a bulk glass-forming alloy:

- Multicomponent system: The alloy should contain at least three components.

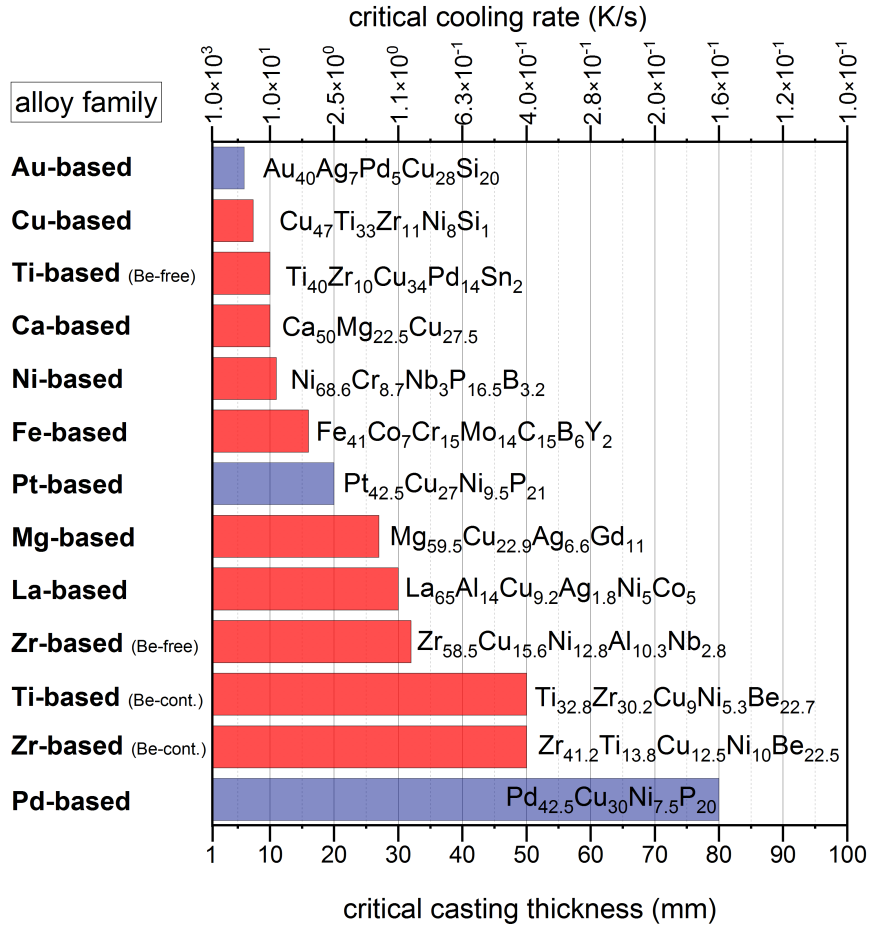


FIGURE 1.2: Critical casting thickness d_c and critical cooling rate R_c shown on a non-linear scale (calculated according to Eq. 1.1) of different bulk glass alloy families. An example of each family is listed. Data taken from Refs. [14–25].

- Significant atomic size difference: The atomic size difference of the main constituents should be above 12%.
- Negative heat of mixing among the main constituents.
- Proximity to a deep eutectic.

The involvement of different elements is thought to impede the selection of a competing crystalline phase and this confusion increases the probability to form a glass [29]. A certain atomic size distribution increases the packing density in the liquid and decreases the average atomic mobility. The requirement of a negative heat of mixing among the main constituents guarantees the formation of a homogeneous glassy phase. The importance of a low melting (T_m) or liquidus temperature (T_l), which is usually found at or in vicinity of a eutectic reaction, was already noticed by Turnbull [28]. He introduced the reduced glass transition temperature T_{rg} which is the ratio of T_g and T_l^2 . On the one hand, metallic liquids in vicinity of a eutectic reaction are already stabilized to low temperatures and exhibit a more sluggish atomic mobility. On the other hand, T_g is found to be less sensitive to compositional variations [28]

²Originally the melting temperature T_m was used instead of the liquidus temperature T_l . In vicinity of the eutectic reaction, T_m is invariant and does not account for variations in the GFA. T_g/T_l shows a better correlation with the GFA as T_g/T_m [30].

with the result that alloys with a low T_l need to pass a smaller temperature interval ($T_l - T_g$) in which crystallization can occur [31].

The aforementioned rules are useful tools to find BMG forming compositions. However, the recent development of sulfur bearing BMGs [32] underlines that these rules should not be considered as a limitation for exploring new systems because, among the potentially existing 10^6 BMG forming alloy compositions [33], many will be located at off-eutectic compositions.

In the following, a strategy, based on the empirical rules, is developed to modify the alloy composition of a Au-based BMG. This alloy development aims at the reduction of the abnormally fast surface tarnishing [34] and simultaneously maintaining the ability of the alloy to form a bulk glass. The origin of changes in the GFA is assessed by thermodynamic considerations and T_{rg} . The effect on the tarnishing resistance is evaluate by corrosion tests in artificial saliva.

Moreover, the thermophysical properties of different Pt-P-based BMGs are determined and compared to the compositionally related Pd-P-based BMGs. By combining calorimetric crystallization experiments with the thermophysical properties, an isothermal TTT diagram is constructed and the origin of the high GFA of Pt-P-based BMGs is identified. The results indicate that, despite the compositional similarities between Pt-P- and Pd-P-based BMGs, structural difference exist. The compositional and temperature induced structural evolution of Pt- and Pd-P-based liquids is investigated in synchrotron X-ray diffraction experiments, suggesting significant structural differences in the two alloy families.

Chapter 2

Glass formation in metallic systems

2.1 Metallic Glasses: Frozen-in liquids

The transition from the crystalline solid to the liquid state of a one-component system (e.g. a pure metal) occurs at T_m , at which both states are in thermodynamic equilibrium. In multicomponent alloys, several crystalline phases with different thermal stability may be present in the solid state. Consequently, melting often takes place in a temperature interval and is completed at T_l . The process of melting involves the dissolution of the characteristic long-range order of the crystal, represented by the periodic arrangement of atoms. The liquid state is in general labeled as disordered or amorphous, although atomic order may not be entirely lost. Liquids possess a rather localized order, termed short- and medium-range order (SRO, MRO), whose extent is temperature depended [35].

Upon cooling from the stable equilibrium liquid, the passing of T_l opens two different solidification pathways to the liquid. Figure 2.1(a) schematically shows the volume as a function of temperature which decreases continuously with decreasing temperature in the liquid state. The supercooled liquid region below T_l is a metastable state with a finite lifetime¹. Nucleation and growth of crystals can occur at an undercooling $\Delta T (= T_l - T > 0)$, accompanied by a discontinuous change in volume and the release of the latent heat (path 1 in Fig. 2.1(a)). If the crystallization process is avoided during undercooling, the metastable supercooled liquid follows path 2 in Fig. 2.1(a) and experiences a continuous change in its thermal expansion coefficient at approximately 0.5 to $0.66 \times T_l$ [36]. This change marks the transition to the vitreous state at T_g , a kinetic phenomenon observed among various liquids with a wide range of chemical diversity. T_g defined upon cooling is often referred to as *fictive temperature* $T_{fictive}$ which is the only unambiguous definition of the glass transition as it is independent of the thermal history of the glass [37]. In the temperature region where both solid states can exist, they exhibit an almost identical thermal expansion. However, the volume of the glass is in general larger than that of the crystalline mixture.

Although the decrease in volume with decreasing temperature of the liquid suggests a reduction of the atomic mobility, the dramatic change in the dynamics of the liquid, that accompanies the undercooling, can not be deduced from Fig. 2.1(a). Figure 2.1(b) shows the viscosity of the liquid on the same temperature scale as used for the volume plot. The viscosity $\eta(T)$ is connected to the *structural α -relaxation time* $\tau_\alpha(T)$

¹At very small degrees of undercooling the large nucleation barrier allows the liquid to reside in metastable state virtually infinitely long.

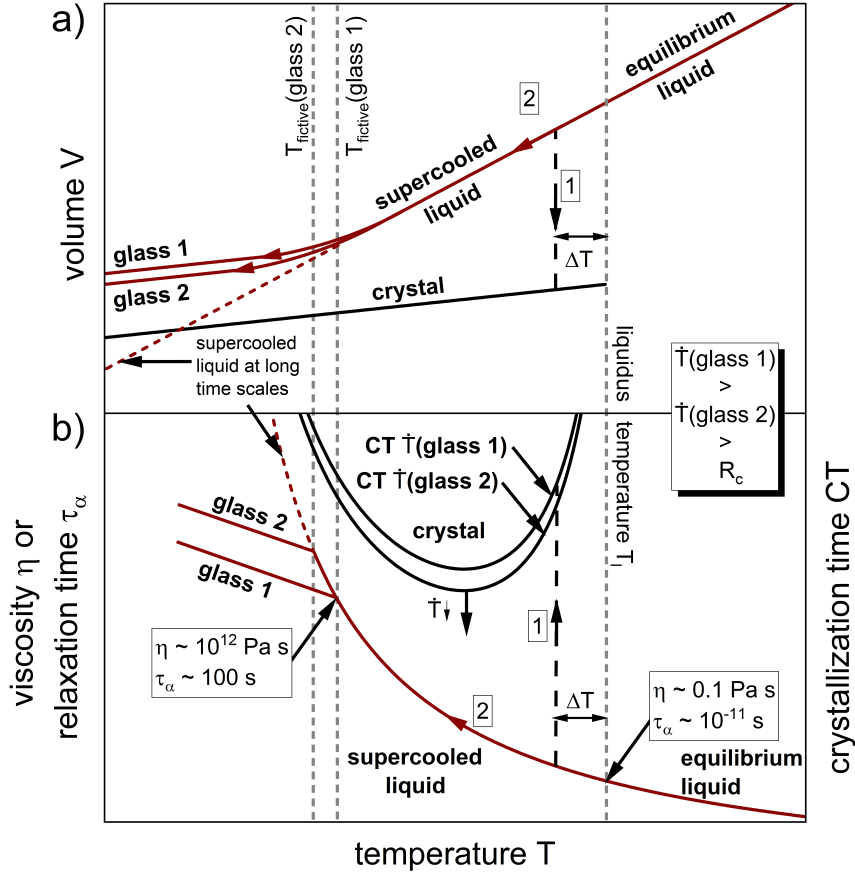


FIGURE 2.1: Schematic plot of the (a) volume and (b) the viscosity or structural α -relaxation time of a glass-forming liquid as a function of temperature. Below T_l , the liquid either crystallizes (1) or undercools (2) until vitrification occurs. The fictive temperature $T_{fictive}$ at which the supercooled liquid freezes to a glass depends on the cooling rate. The minimum cooling rate up to which crystallization is avoided is the critical cooling rate (R_c). At cooling rates below R_c , the crystallization time (CT) cuts the metastable equilibrium ($\tau_\alpha(T)$) line of the supercooled liquid.

of the liquid, representing the rearrangement time of the atoms in the (metastable) equilibrium state [38], via the Maxwell relation

$$\eta = G_\infty \tau, \quad (2.1)$$

where G_∞ is the *high-frequency shear modulus*. Upon undercooling, the viscosity or relaxation time of the liquid increases by several orders of magnitude. At T_l , the equilibrium viscosity of bulk glass-forming liquids is in the range of 0.1 Pa s [39–41] and rises to around 10^{12} Pa s at T_g . As observed for the $V(T)$ curve, vitrification forces the system to deviate from the metastable equilibrium line. The reason is the crossing of the inherent time scale of the liquid, $\tau_\alpha(T)$, and the time scale of the experiment, which is given by the applied cooling rate [42]. In other words, the liquid leaves the metastable equilibrium line if the applied cooling rate does not provide sufficient time for the liquid to fully equilibrate [43]. For this reason, the transition from the metastable undercooled liquid to the unstable glassy state is termed as "falling out of equilibrium" or "freezing-in" [37, 43, 44]. The connection between structural relaxation time and the applied cooling rate rules out the existence of a

single, universal glassy structure and rather implies that a spectrum of structural states can be frozen-in. As shown in Fig. 2.1(a) and (b), a slower cooling rate allows the liquid to follow the metastable equilibrium line to lower temperatures. Consequently, vitrification occurs at a higher viscosity value and the frozen-in structure is more densely packed. The amount of excess volume ($V_{ex} = V_{glass} - V_{crystal}$) that is maintained in the glassy state substantially affects the mechanical properties of the solid and is limited downwards during a casting process by R_c , representing the slowest cooling rate needed to suppress crystallization. At cooling rates below R_c , the crystallization nose would cut the metastable equilibrium line of the supercooled liquid in Fig. 2.1(b), resulting in the partial or overall crystallization of the liquid.

2.2 The driving force for nucleation and the glass-forming region

On falling below T_l , the pathway of crystallization opens up to the liquid. The urge to crystallize arises from the different temperature dependencies of the *Gibbs free energy* of the liquid $G_l(T)$ and crystalline state $G_x(T)$ (Fig. 2.2). The system strives towards the state with the lowest Gibbs free energy, which is the crystalline state below T_l ². Upon undercooling, the difference between the Gibbs free energy of the liquid and the crystal increases continuously, and the probability that the liquid crystallizes on a finite time scale increases. $G_l(T)$ and $G_x(T)$ can be expressed by

$$G_l(T) = H_l(T) - TS_l(T) \quad (2.2)$$

and

$$G_x(T) = H_x(T) - TS_x(T), \quad (2.3)$$

where $H(T)$ and $S(T)$ denotes the enthalpy and entropy as a function of temperature of the corresponding state. The Gibbs free energy difference between the supercooled liquid and the crystal³ is given by

$$\begin{aligned} \Delta G_{l-x}(T) &= G_l(T) - G_x(T) \\ &= H_l(T) - TS_l(T) - H_x(T) + TS_x(T) \\ &= \Delta H_{l-x}(T) - T\Delta S_{l-x}(T). \end{aligned} \quad (2.4)$$

The enthalpy and entropy difference between liquid and the crystal (*excess enthalpy and entropy*) $\Delta H_{l-x}(T)$ and $\Delta S_{l-x}(T)$ can be defined as

$$\Delta H_{l-x}(T) = \Delta H_f - \int_T^{T_l} \Delta C_p^{l-x}(T') dT' \quad (2.5)$$

and

$$\Delta S_{l-x}(T) = \Delta S_f - \int_T^{T_l} \frac{\Delta C_p^{l-x}(T')}{T'} dT', \quad (2.6)$$

where ΔH_f and ΔS_f are the *enthalpy and entropy of fusion*, respectively. $\Delta C_p^{l-x}(T')$ is the difference between the specific heat capacity of the liquid $C_p^l(T')$ and the crystal $C_p^x(T')$ as a function of temperature derived from fitting of experimental data with

²In multiphase systems, T_l is regarded as the stability threshold of the most stable crystalline phase. A driving force for the formation of the crystalline mixture is generated if the temperature falls below the stability threshold of each individual crystalline phase.

³Here, "the crystal" always refers to the crystalline mixture.

the following two empirical equations [45]

$$C_p^l(T') = 3R + aT' + bT'^{-2} \quad (2.7)$$

and

$$C_p^x(T') = 3R + cT' + dT'^2, \quad (2.8)$$

where R is the universal gas constant and a, b, c and d are fitting parameters. The low temperature C_p values of the glass and the crystal can be described by [46, 47]

$$C_p^{g,x}(T') = 3R/M(1 - \exp(-1.5T'/T_D)), \quad (2.9)$$

where M and T_D are fitting constants. Using Eq. 2.5, 2.6, 2.7 and 2.8, $\Delta G_{l-x}(T)$ (Eq.

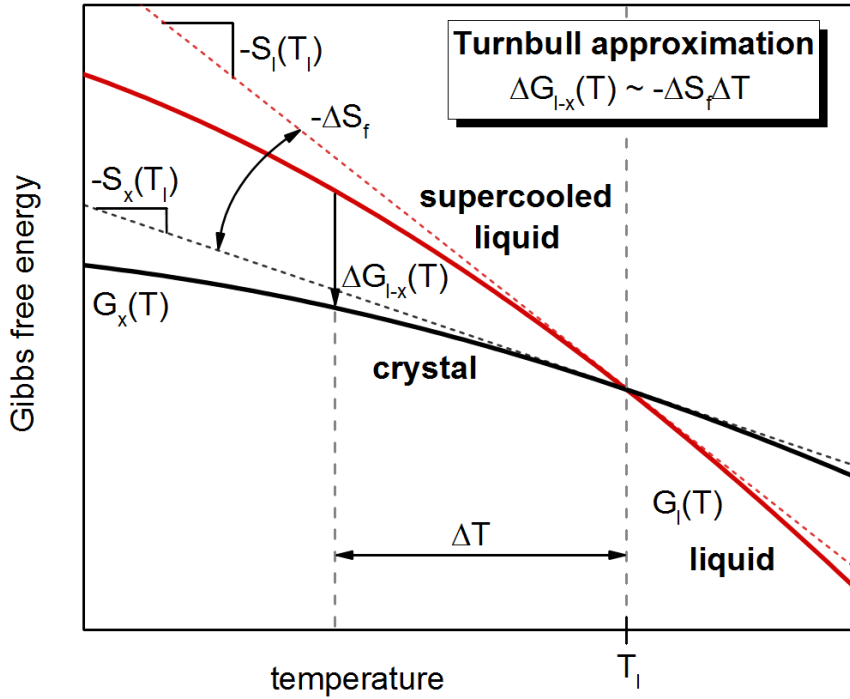


FIGURE 2.2: Schematic Gibbs free energy curves of the liquid $G_l(T)$ and the crystal $G_x(T)$ as a function of temperature. The difference between $G_l(T)$ and $G_x(T)$, $\Delta G_{l-x}(T)$, vanishes at the liquids temperature T_l . At an undercooling ΔT , $\Delta G_{l-x}(T)$ can be used as an approximation for the driving force for crystallization. The dashed lines are estimations of $G_l(T)$ and $G_x(T)$, neglecting the temperature dependencies of the enthalpy and entropy. The difference between the slopes ($S_l(T_l)$, $S_x(T_l)$) of the estimated curves is the entropy of fusion ΔS_f , which can be used to estimate the driving force for crystallization for small undercoolings (Turnbull approximation).

2.4) can be rewritten as follows:

$$\begin{aligned} \Delta G_{l-x}(T) = & \Delta H_f - T\Delta S_f \\ & - \left[\frac{1}{2}(a-c)T'^2 - bT'^{-1} - \frac{1}{3}dT'^3 \right. \\ & \left. - (a-c)T' + \frac{1}{2}bT'^{-2} + \frac{1}{2}dT'^2 \right]_T^{T_l}. \end{aligned} \quad (2.10)$$

The expression above is used for the calculation of the crystal nucleation and the growth rate in Chapter 2.4. At T_l , the Gibbs free energy difference between the liquid and the crystals vanishes, which yields the expression

$$\Delta S_f = \frac{\Delta H_f}{T_l}. \quad (2.11)$$

This allows the determination of ΔS_f from calorimetric measurements of ΔH_f . For small undercoolings ΔT , the difference in the specific heat capacity between the liquid and the crystal (the *excess heat capacity*) $\Delta C_p^{l-x}(T')$ can be neglected [1], which simplifies Eq. 2.4 to

$$\begin{aligned} \Delta G_{l-x}(T) &\approx \Delta H_f - T \frac{\Delta H_f}{T_l} = \Delta H_f \left(1 - \frac{T}{T_l}\right) \\ &= -\frac{\Delta H_f}{T_l} (T - T_l) = -\Delta S_f \Delta T. \end{aligned} \quad (2.12)$$

This approximation (Turnbull approximation) is valid for undercoolings of about 100 K [48]. As the modeling of the time-dependent nucleation and growth process in Pt-based liquids in Chapter 5 covers approximately the temperature range from T_l to T_g , the exact description of $\Delta G_{l-x}(T)$ (Eq. 2.10) is more appropriate.

Irrespective of the discussion on the usage of different expressions for $\Delta G_{l-x}(T)$, it should be kept in mind that in a multiphase system $\Delta G_{l-x}(T)$ always refers to the Gibbs free energy difference between the liquid and a phase mixture. ΔH_f and ΔS_f are derived from the melting process of the crystalline mixture and $C_p^x(T)$ is the specific heat capacity of the crystalline mixture. Therefore, the Gibbs free energy difference between the liquid and the crystal does not necessarily match the driving force for nucleation (also termed driving force for crystallization) [49]. The driving force for nucleation refers to the energy profit, given by the difference in the chemical potential $\Delta\mu$, which the system attains if nuclei of a certain crystalline phase are formed. The chemical potential of a component i , describing how the total Gibbs free energy G' of a system changes by adding a small quantity of i , dn_i mol, at constant pressure, temperature and amount of substances n_j , is given by [50]

$$\mu_i = \left(\frac{\partial G'}{\partial n_i} \right)_{T,p,n_j}. \quad (2.13)$$

The change in the molar Gibbs free energy with varying molar fractions X_A and X_B ($X_A = 1 - X_B$) is expressed by the Gibbs-Duhem equation as [50]

$$G = \mu_A X_A + \mu_B X_B. \quad (2.14)$$

To illustrate the difference between $\Delta G_{l-x}(T)$ and the driving force for the formation of a nucleus of the α -phase (driving force for nucleation), $\Delta\mu^{L-\alpha}$, an eutectic system is chosen as a model system (Fig. 2.3(a)). Composition X_q is quenched from the equilibrium liquid to the glassy state. During this process "snapshots" of the molar Gibbs free energy curves of the competing phases, which are given by Eq. 2.14, are depicted in Fig. 2.3(b) at the temperature T_1 and in Fig. 2.3(c) at the temperature T_2 . Upon passing T_l , the liquid enters the two phase region, where the liquid and the α -phase are in thermodynamic equilibrium. At T_1 , the blue, dashed tangent in Fig. 2.3(b), connecting G^α (or G^β) and G^L determines the compositional region, where $\mu_A^\alpha = \mu_A^L$ (or $\mu_B^\alpha = \mu_B^L$) and therefore both phases coexist. The distance between the

G^L and the blue tangent at X_q is the Gibbs free energy difference, $\Delta G_{l-x}(T)$. Due to the limited undercooling at T_1 , the $\Delta G_{l-x}(T)$ is hardly recognizable. At T_2 (Fig. 2.3(c)), which corresponds to a much larger undercooling, the α -phase and β -phase are in thermodynamic equilibrium and ΔG_{l-x} at X_q has grown significantly (see Fig. 2.2 for $\Delta G_{l-x}(\Delta T)$). The driving force for the formation of a nucleus of the α -phase, is given by the parallel tangent construction (dashed-dotted lines in Fig. 2.3(b) and (c)) and is mathematically expressed as [49]

$$\left(\frac{\partial G^L}{\partial X_B}\right)_{X_q} = \left(\frac{\partial G^\alpha}{\partial X_B}\right)_{X_n(T)}. \quad (2.15)$$

The vertical distance between the two tangents $\Delta\mu_A^{L-\alpha}$ ($= \mu_A^{L,x_q} - \mu_A^{\alpha,x_q} = \Delta\mu_B^{L-\alpha}$) represent the driving force for the nucleation of an α -nucleus of the composition $X_n(T)$ within the liquid with the composition X_q . The composition of the nucleus $X_n(T)$ is different from that of the equilibrium composition of the α -phase, which is given by the vertical dashed line in Fig. 2.3(b) and (c). It is evident, that ΔG_{l-x} in general underestimates the driving force for the formation of a crystalline nucleus. However, the determination of the molar Gibbs free energy of the different phases that compete with the liquid phase in a multicomponent system is rather difficult, making ΔG_{l-x} the best possible approximation.

In this context it should be mentioned that access to the real molar Gibbs free energy curves⁴ would allow the determination of the compositional extent of the *glass-forming region* (GFR) [52]. Assuming that kinetic constraints prohibit long range diffusion during a quenching process, the equilibrium microstructure and composition is not accessible. This limitation requires that crystallization occurs from a homogeneous liquid without any compositional changes (*polymorphic transition*). Such a transition can only occur at a composition, where G^L is higher than G^α or G^β and a Gibbs free energy difference ΔG_p exists (Fig. 2.3(c)). The compositional limit for a polymorphic transition at a certain temperature yields the intersection point between G^α or G^β and G^L curves. In Fig. 2.3(b) and 2.3(c) these points are marked as $c_0^{\alpha,\beta}(T)$. The intersection points are transferred into Fig. 2.3(a) from which the $T_0^\alpha(X_B)$ and $T_0^\beta(X_B)$ curves are constructed. Both curves represent the compositional limit for the polymorphic transition from the liquid to the supersaturated solid solution α or β and vice versa. In between the T_0 -lines, an eutectic solidification is not possible for rapid quenching as it requires long-range diffusion [44] and the liquid vitrifies when the glass transition temperature is passed. The construction of the T_0 -lines illustrates why bulk glass-forming liquids are usually found in the proximity to a deep eutectic. The non-polymorphic transition requires the segregation of the components A and B to the α and β phase [44], which is responsible for a substantially longer nucleation time [52].

⁴A correct determination of the T_0 -lines requires the consideration of the ascending specific heat capacity of the liquid upon undercooling as it strongly effects the G^L curve [51].

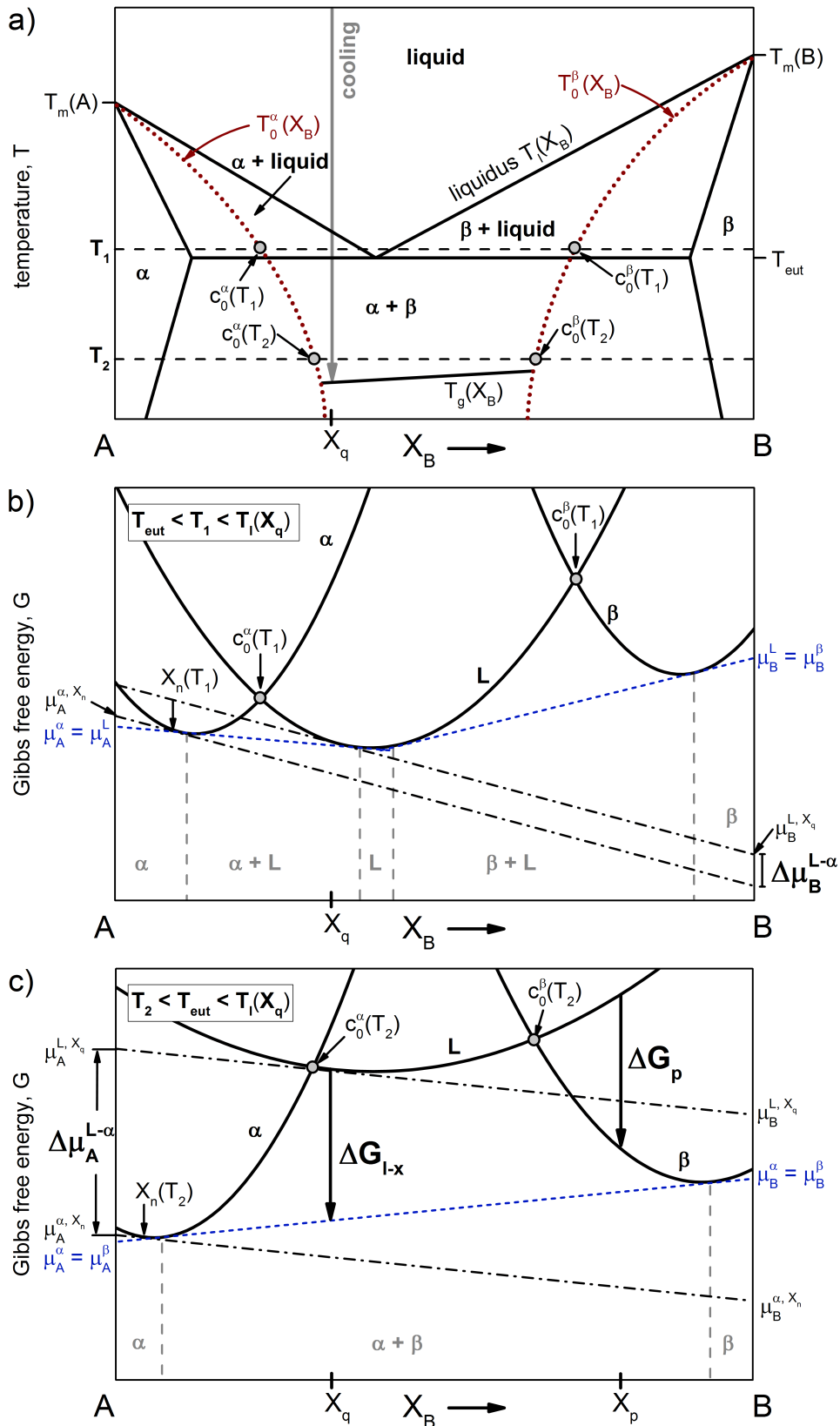


FIGURE 2.3: (a) Phase diagram of a binary eutectic system at constant pressure. The red, dotted lines $T_0^{\alpha,\beta}(X_B)$ correspond to the intersection points of the Gibbs free energy curves G^α or G^β and G^L as a function of temperature ($c_0^{\alpha,\beta}(T)$). Excluding long-range diffusion,

the liquid transforms polymorphically to the supersaturated solid solution at $T_0^{\alpha,\beta}(X_B)$. (b) Gibbs free energy curves of the competing phases at the temperature $T_1 < T_l$. The blue, short-dashed tangents determine the compositional region of the equilibrium phases. The difference between the dashed-dotted, parallel tangents $\Delta\mu_B^{L-\alpha}$ ($=\Delta\mu_B^{L-\alpha}$) represents the driving force for the nucleation of a nucleus with the composition X_n of the α -phase for a liquid with the composition X_q . (c) Gibbs free energy curves of the competing phases at the temperature $T_2 < T_1 < T_l$. $\Delta G_{l-x}(T)$ is the Gibbs free energy difference between the liquid and the crystalline mixture ($\alpha+\beta$). ΔG_p is the Gibbs free energy difference of a polymorphic transition from the liquid phase to the supersaturated β -phase at X_p .

2.3 The fragility classification

2.3.1 Thermodynamic and kinetic signature of fragility

The relaxation time τ_α and viscosity η of a liquid, which are connected through Eq. 2.1, change as function of temperature. For some liquids, the temperature dependence of both quantities can be described by an Arrhenius equation of the form [53]

$$\ln(k(T)) = \ln(A) + \frac{E_A}{RT}, \quad (2.16)$$

where $k(T)$ is the viscosity or relaxation time, A the pre-exponential factor and E_A an average activation energy. E_A is obtained from the slope E_A/R for $\ln(k)$ plotted as a function of the inverse temperature. The activation energy represents the energy barrier, created by the surrounding atoms [54], that needs to be overcome for translational atomic movements to accomplish viscous flow. The higher E_A , the more temperature dependent the atomic rearranging process. It is rather an exception than the rule that liquids possess a constant E_A over a large temperature region. In these cases, the activation energy can be defined at each temperature T' by [53]

$$E_A = -RT^2 \left(\frac{d\ln(k(T))}{dT} \right)_{T=T'}. \quad (2.17)$$

A mathematical description of the non-Arrhenius behavior of viscosity was provided by Fulcher [55], Vogel [56] and Tammann and Hesse [57], who discovered the equation independently [58]. The most common form of the Vogel-Fulcher-Tammann (VFT) equation is [59]

$$k(T) = k_0 \exp\left(\frac{D^* T_0}{T - T_0}\right), \quad (2.18)$$

where D^* is termed *fragility parameter* and T_0 is the *VFT temperature* at which the quantity k diverges. The pre-exponential factor k_0 represents the infinite temperature limit of η or τ_α . η_0 can be calculated as [60]

$$\eta_0 = \frac{hN_A}{v_m}, \quad (2.19)$$

where h is Planck's constant, N_A is Avogadro's number and v_m is the atomic volume. τ_0 can be calculated using Eq. 2.1 and is usually in the order of 10^{-14} s [61, 62].

The measurement of the temperature dependence of the equilibrium viscosity or structural relaxation time permits a classification of a liquid in terms of its *kinetic fragility*. In Angell's fragility concept "*fragile*" liquids show a rapid increase in viscosity and the associated relaxation time upon cooling, which is connected to a rapidly ascending activation energy E_A and a low D^* -value. "*Strong*" liquids feature a more slowly increasing viscosity or relaxation time upon approaching T_g , implying that these liquids possess a structure that is less sensitive to temperature changes. A typical example for a strong liquid is SiO_2 ($D^* \sim 100$ [63]), featuring a network structure with strong directional bonds which are rather insensitive to temperature changes reflected by a near-Arrhenius behavior and a well-defined E_A . The variety of the different temperature dependencies of η or τ_α of various liquid is best visualized in the so-called Angell plot shown in Fig. 2.4. The plot depicts the logarithmic viscosity as

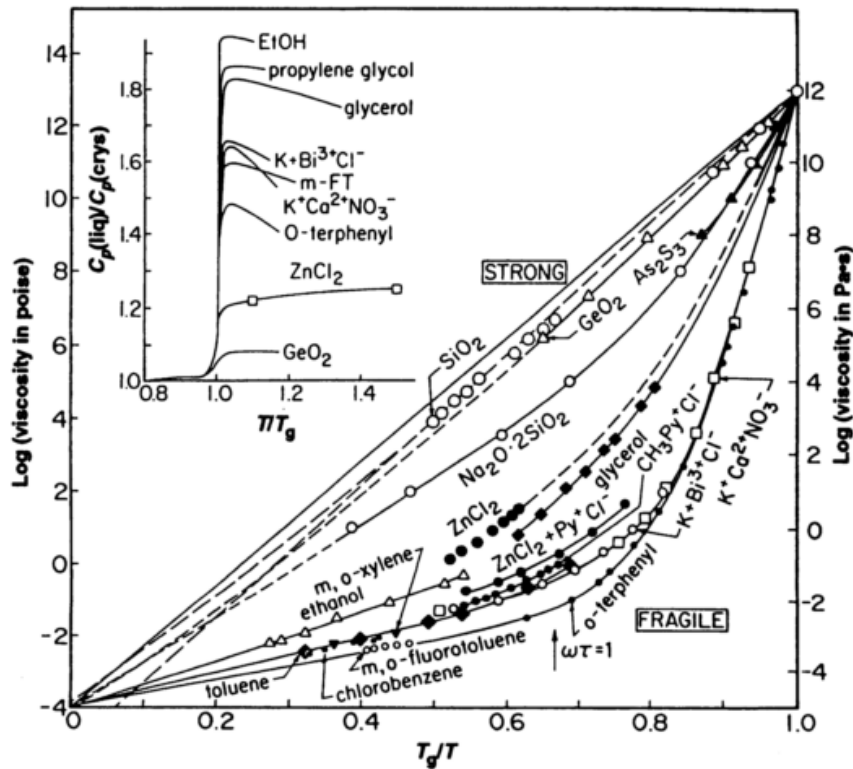


FIGURE 2.4: Angell plot, showing the variety of temperature dependencies of the equilibrium viscosities in glass-forming systems. The abscissa is normalized to the temperature at which the liquids reach a viscosity value of 10^{12} Pa s, T_g^* . The inset shows the jump in C_p at T_g , which is generally larger for fragile than for strong liquids. Figure taken from Ref. [59].

a function of the inverse temperature normalized to the glass transition temperature T_g^* , defined as the temperature at which the supercooled liquid reaches a viscosity value of 10^{12} Pa s. In comparison to oxide glasses, the atoms in metallic liquids have weaker orientational constraints and therefore possess kinetic fragilities ranging from intermediate values of $D^* \sim 20-36$ [64, 65] to values way below a D^* of 20 [18, 66, 67]. In the notation of the activation energy, the kinetic fragility of a liquid is often described by the *fragility index* m representing the slope of the curves in the

Angell plot at T_g^* . m is mathematically expressed as

$$m = \left. \frac{d \log_{10}(\eta)}{d(T_g^*/T)} \right|_{T=T_g^*}. \quad (2.20)$$

D^* -values can be converted into m -values via

$$m = \frac{D^* T_0 T_g^*}{\ln(10)(T_g^* - T_0)^2}. \quad (2.21)$$

Another expression that describes the non-Arrhenius behavior of η or τ_α is the Adam-Gibbs (AG) equation [68]

$$k(T) = k_0 \exp\left(\frac{C}{T S_c(T)}\right), \quad (2.22)$$

where the C parameter contains a free energy barrier for cooperative rearrangements and $S_c(T)$ is the configurational part of the entropy of the liquid as function of temperature. The theory of Adam and Gibbs is based on the idea that the supercooled liquid consist of groups of atoms that, independently of their environment, form cooperatively rearranging regions that adopt different configurations [69]. Upon undercooling, the cooperatively rearranging regions grow in size and the relaxation process requires a higher cooperativity, leading to a growing paucity of available configurations [69]. This circumstance is reflected in Eq. 2.22 by the configurational entropy $S_c(T)$, whose loss with decreasing temperature explains the dramatically increasing η or τ_α upon approaching T_g . The excess entropy $\Delta S_{l-x}(T)$ is often used to approximate $S_c(T)$, assuming that the $\Delta S_{l-x}(T)$ is purely configurational, i.e. the vibrational contribution is neglected⁵. As a result, the dynamic slowdown upon cooling can be approximated by

$$k(T) \approx k_0 \exp\left(\frac{C}{T \Delta S_{l-x}(T)}\right) \quad (2.23)$$

Assuming that $\Delta C_p^{l-x}(T)$ can be represented by a hyperbolic function ($\Delta C_p^{l-x}(T') = K/T'$), Eq. 2.23 is rewritten to

$$\begin{aligned} k(T) &\approx k_0 \exp\left(\frac{C}{T \int_{T_K}^T K/T'^2 dT'}\right) \\ &= k_0 \exp\left(\frac{C}{TK\left(-\frac{1}{T} + \frac{1}{T_K}\right)}\right) \\ &= k_0 \exp\left(\frac{CT_K}{K(T - T_K)}\right). \end{aligned} \quad (2.24)$$

⁵The validity of assuming $S_c(T) = \Delta S_{l-x}(T)$ is controversial. As inferred by Goldstein, the excess heat capacity is only partly configurational in nature [70]. The success of the AG equation, despite the use of $\Delta S_{l-x}(T)$, was attributed to a proportional change of $S_c(T)$ and $\Delta S_{l-x}(T)$ [71]. Furthermore it was conjectured that the configurational contribution is smaller for fragile liquid [71]. This was shown to be the case in organic liquids, where the contribution of the configurational part of the excess heat capacity decrease to about 50% with increasing fragility index [72]. Recent measurements on metallic liquids (ZrCu(Al)) showed that the contribution of the vibrational entropy to the excess entropy is minor (5%) and is unaffected by the fragility of the liquid [73]. However, the assumption that $S_c(T)$ can be approximated by $\Delta S_{l-x}(T)$ was shown to not apply in BMG forming systems [65].

T_K represents the *Kauzmann temperature*, the temperature at which the excess entropy vanishes (see Chapter 2.5). In the case of T_K and T_0 being identical (both representing the limit for viscous flow), the VFT equation (Eq. 2.18) is obtained with $D^* = C/K$. The connection between the empirical VFT and the AG equation shows that the fragility parameter D^* is related to the kinetic quantity C (\propto activation energy for cooperative rearrangements) and the thermodynamic quantity K [59, 74]. In principle, K is connected to the height of the jump of the specific heat capacity that occurs at T_g . Strong liquids tend to show a small and fragile liquids a large jump in $\Delta C_p^{l-g}(T_g)$ [59], as shown in the inset in Fig. 2.4. However, exceptions to this rule exist (see ethanol in Fig. 2.4). The jump is often approximated by $\Delta C_p^{l-x}(T_g)$ due to a negligible difference between specific heat capacity of the glass $C_p^g(T)$ and the crystal $C_p^x(T)$ [75]. In the case of fragile liquids, the pronounced jump in $\Delta C_p^{l-x}(T_g)$ points towards a larger degeneracy of the potential energy hypersurface, which means that a higher density of configurational states is available to the fragile liquid [74]. This is in turn connected to a more rapidly changing $S_c(T)$ with temperature for fragile liquids [74]. Within this framework, Martinez and Angell showed that the rate of change in $\Delta S_{l-x}(T)$ ($=S_{ex}(T)$) is high for fragile liquids, which suggests that $S_c(T)$ and $\Delta S_{l-x}(T)$ change proportionally [71]. If the excess entropy is plotted as $1/\Delta S_{l-x}(T)$ normalized to its value at T_g as a function of T_g/T (thermodynamic fragility plot), Fig. 2.5 appears similar to Fig. 2.4 and the liquids are arranged in the sequence expected from their kinetic fragilities [71]. However,

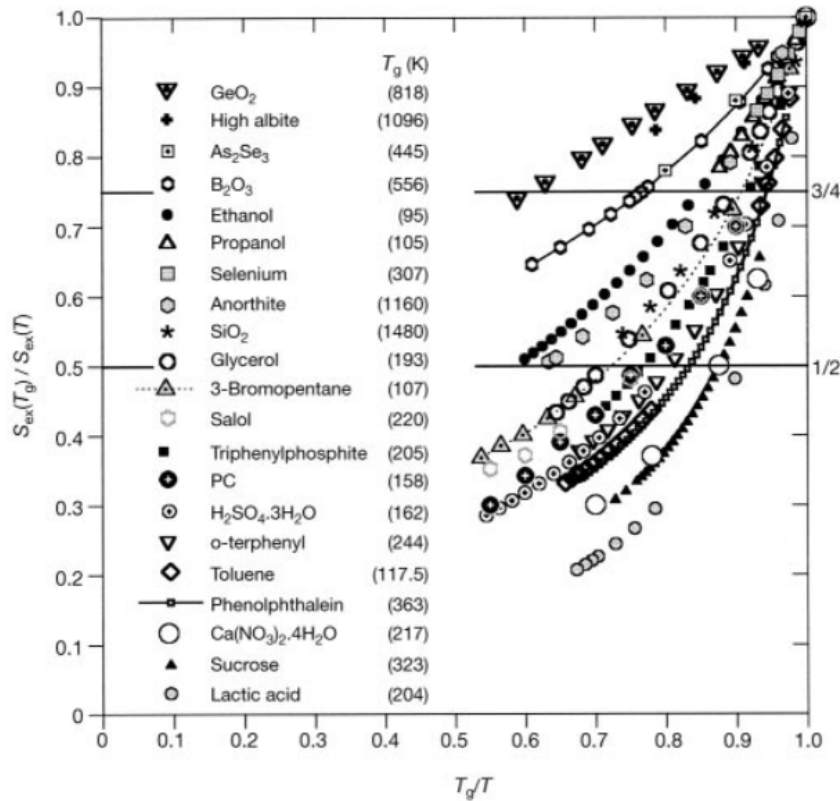


FIGURE 2.5: Thermodynamic fragility plot. The scaled, inverse excess entropies of different liquids as function of the T_g -scaled inverse temperature. The liquids are arranged in the sequence expected from their kinetic fragilities. For fragile liquids, the rate of change in the excess entropy is high. Figure taken from Ref. [71].

it is noted by Martinez and Angell that the scaling factor, the excess entropy at T_g ($\Delta S_{l-x}(T_g)$ or $S_{ex}(T_g)$), plays a decisive role⁶ [71]. It is calculated from Eq. 2.6, which relies on the entropy of fusion ΔS_f . As mentioned in the previous section, the determination of the ΔS_f requires the definition of a unique temperature, where ΔG_{l-x} vanishes. In multicomponent systems that do not show a pure eutectic melting, the complex melting process prohibits the determination of ΔS_f -values that allow a sensible comparison of bulk metallic glass-forming liquids as shown in Fig. 2.5.

Despite their limitations, the connection between thermodynamic and kinetic aspects of glass-forming liquids can be schematically generalized as shown in Fig. 2.6. In contrast to strong glass-forming liquids, fragile liquids possess a more rapidly increasing viscosity as the glass transition is approached. This is related to a distinctly ascending specific heat capacity upon undercooling, responsible for a rapid loss in excess entropy. The loss in excess entropy, being proportional to the loss in configurational entropy, reflects the growing paucity of available configurations, causing the viscous slowdown. However, exceptions to this pattern exist, e.g. Pd-based bulk glass-forming liquids (see Chapter 5).

2.3.2 Structural signature of fragility

The proposed connection between the configurational entropy and the viscous slowdown upon cooling supports the idea that temperature-induced structural changes are the origin of the kinetic fragility of a glass-forming liquid. Computer simulations on $\text{Cu}_{64}\text{Zr}_{36}$ show that the rapidly ascending specific heat capacity of the supercooled liquid upon cooling is connected to a pronounced enthalpy reduction associated with icosahedral ordering [76]. In contrast, the dominant polyhedra (locally preferred structure or characteristic SRO [77]) in the $\text{Pd}_{82}\text{Si}_{18}$ liquid follow a rather linear temperature dependence [76]. Although a densification through the increase of the coordination number from eight to nine is observed, the accelerated enlargement of a certain polyhedra is not detected [76]. As a consequence, the increase in the specific heat capacity upon cooling is less pronounced for $\text{Pd}_{82}\text{Si}_{18}$ (see Fig. 2.7(a)) and the calculated viscosities reveal a kinetically stronger behavior (Fig. 2.7(b)) [76].

Similar results are obtained for the $\text{Mg}_{65}\text{Cu}_{25}\text{Y}_{10}$ bulk glass-forming alloy composition [78], which can be considered as a prototype system for a kinetically and thermodynamically strong metallic glass former [63, 65]. Cu-centered bicapped square antiprisms (BSAP) and tricapped trigonal prisms (TTP) are found to be the locally preferred structures [78]. The amount of locally preferred structures grow linearly as a function of the inverse temperature whereas the fraction of full icosahedra in $\text{Cu}_{64}\text{Zr}_{36}$ increases sharply upon approaching the glass transition (Fig. 2.8(a)) [77, 79]. Experimental evidence of icosahedral SRO and its increase with the degree of undercooling is found in the elastic neutron scattering experiments on levitated droplets by Holland-Moritz et al. and Schenk et al. [80, 81].

⁶It is due to the scaling factor that the thermodynamic and kinetic fragility of SiO_2 do not coincide.

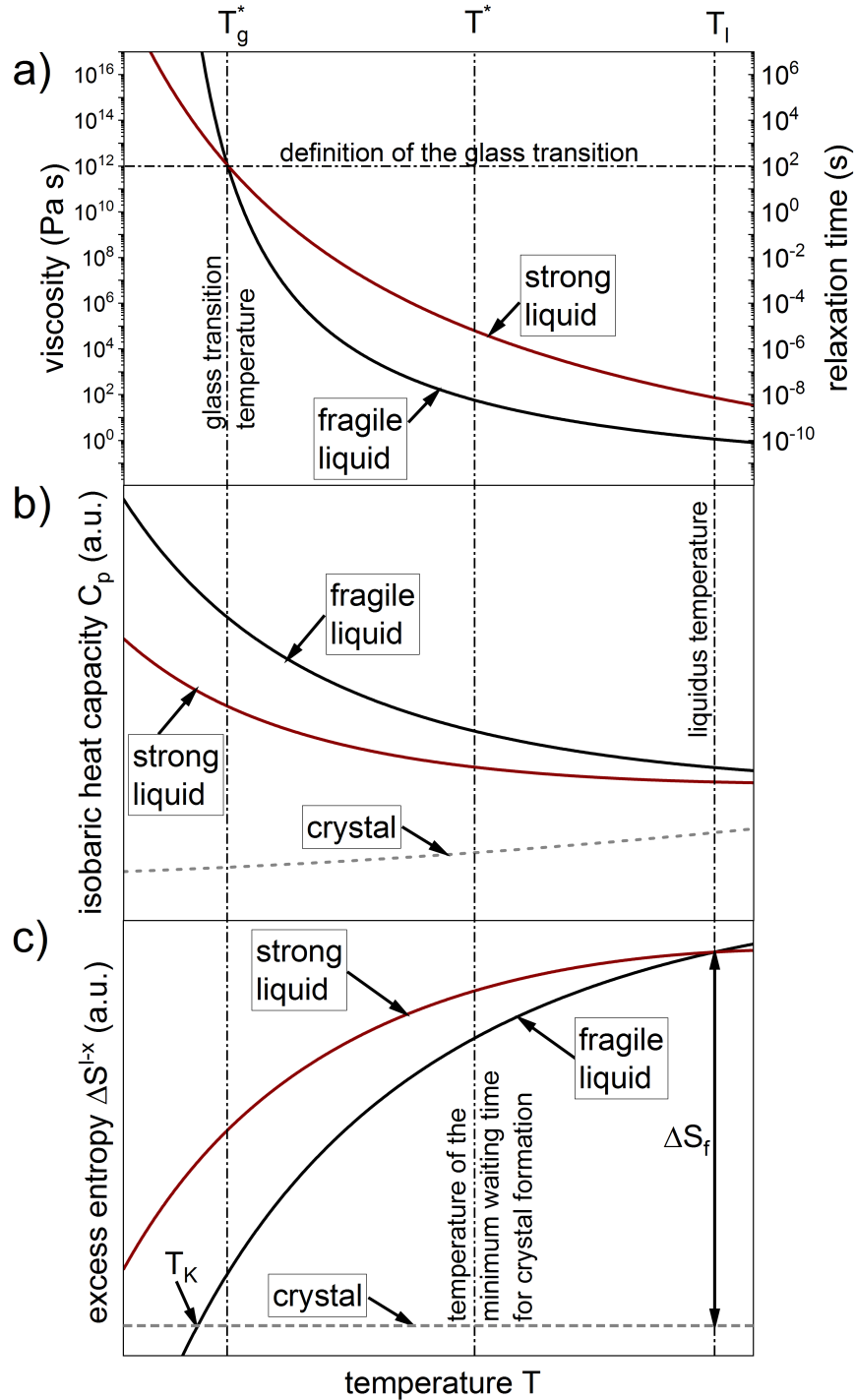


FIGURE 2.6: Schematic illustration of the kinetic and thermodynamic signature of fragility for (bulk metallic) glass-forming liquids. T_g^* represents the glass transition temperature, T^* the temperature of the minimum waiting time for crystal formation in an isothermal TTT diagram and T_l the liquidus temperature. (a) Temperature dependence of the equilibrium viscosity/relaxation time of a strong and a fragile glass-forming liquid. The glass transition is defined as the temperature at which the viscosity of the liquid reaches a value of 10^{12} Pa s. (b) Isobaric heat capacity of the crystal, the fragile, and the strong liquid as a function of temperature. (c) Loss in excess entropy upon

undercooling for a strong and a fragile liquid. To highlight the different rates at which the excess entropy decreases, it is assumed that both liquids possess the same entropy of fusion ΔS_f . The temperature at which the difference between the entropy of the liquid and the crystal vanishes, is the Kauzmann temperature T_K (see chapter 2.5).

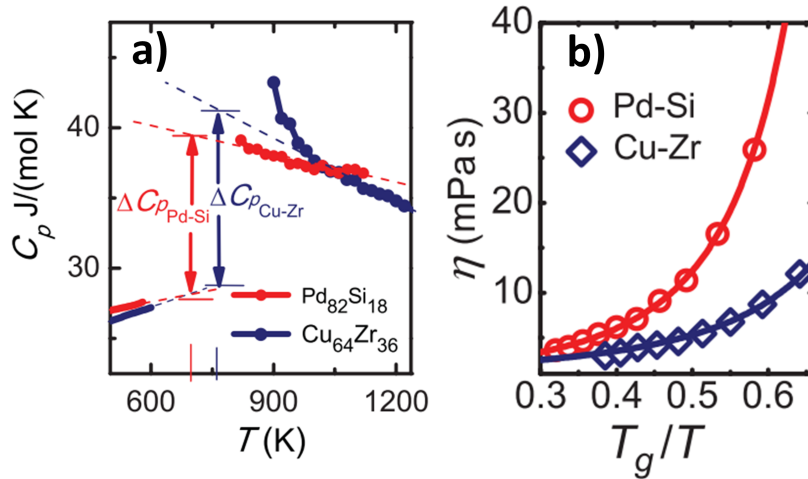


FIGURE 2.7: (a) Calculated specific heat capacity as function of temperature of the $\text{Cu}_{64}\text{Zr}_{36}$ and the $\text{Pd}_{82}\text{Si}_{18}$ liquids. The icosahedral ordering causes the rapidly ascending specific heat capacity in $\text{Cu}_{64}\text{Zr}_{36}$ upon cooling. ΔC_p marks the jump of the specific heat capacity at T_g . (b) Calculated high temperature viscosity of the $\text{Cu}_{64}\text{Zr}_{36}$ and $\text{Pd}_{82}\text{Si}_{18}$ alloy compositions as a function of the inverse, T_g -scaled temperature. Note that the ordinate is in a linear scale and that only the high temperature segment is shown. In this temperature regime, the viscosity of the stronger liquid ($\text{Pd}_{82}\text{Si}_{18}$) rises faster than that of the fragile one $\text{Cu}_{64}\text{Zr}_{36}$. This can also be seen on a log-scale in Fig. 2.6(a). Figures taken from Ref. [76].

Beyond the extend of local order with decreasing temperature, it is found in simulations that the representative structural units interconnect, preferably via face sharing (3-atoms) and at the expense of edge sharing (2-atoms) [77, 78, 82]. As can be seen in Fig. 2.8(b), this type of medium-range structural evolution [78] is more pronounced for the fragile liquid $\text{Cu}_{64}\text{Zr}_{36}$ [77] and gets more significant for slower cooling rates [82]. Other simulations show that the interpenetrating icosahedra exhibit a strong spatial correlation through the formation of a stable string-like network [83, 84], permeating the liquid upon cooling [83]. These observations suggest, that, beside the local SRO, MRO affects the kinetic fragility.

Experimental evidence of the relevance of MRO for the kinetic fragility is found in in-situ synchrotron X-ray scattering experiments, performed in the supercooled liquid region of various bulk metallic glass-forming liquids and above T_l for the *Vit106a* ($\text{Zr}_{58.5}\text{Cu}_{15.6}\text{Ni}_{12.8}\text{Al}_{10.3}\text{Nb}_{2.8}$) alloy composition [85, 86]. It is reported that the temperature-induced structural evolution on the length scale of $\sim 3 - 4$ atomic diameters, corresponding to inter-cluster correlations, shows a strong correlation with the fragility index m [85, 86]. The temperature-induced changes in the third and fourth peak position of the reduced pair distribution function $G(r)$, r_3 and r_4 ,

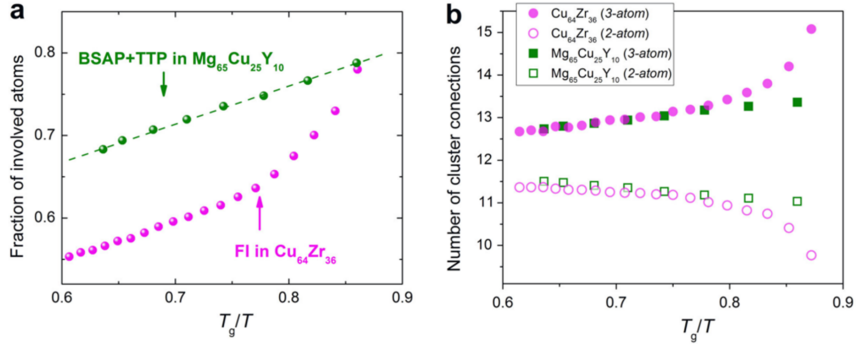


FIGURE 2.8: (a) Evolution of characteristic SRO represented by the fraction of atoms involved. The fraction of full icosahedra (FI) increases sharply for the fragile liquid $Cu_{64}Zr_{36}$ as the glass transition is approached, whereas the fraction of the bicapped square antiprisms (BSAP) and tricapped trigonal prisms (TTP) in the strong liquid $Mg_{65}Cu_{25}Y_{10}$ increases linearly as a function of the inverse temperature. (b) Temperature dependent evolution of the average cluster connection per atom in $Cu_{64}Zr_{36}$ and $Mg_{65}Cu_{25}Y_{10}$. The terms 3-atom and 2-atom (number of atoms shared) refer to face and edge sharing of the locally preferred clusters. Figures taken from Ref. [77].

are assumed to be representative for the temperature-induced change in the average radius of the third and fourth coordination shell. With this in mind, the volume dilatation in between the third and fourth coordination shell can be written as

$$\begin{aligned} \epsilon_{4-3} &= -\frac{\Delta V_{4-3}(T)}{V_{4-3}(T'_g)} \\ &= -\frac{V_{4-3}(T) - V_{4-3}(T'_g)}{V_{4-3}(T'_g)} \end{aligned} \quad (2.25)$$

where $V_{4-3}(T) = 4/3\pi(r_4^3(T) - r_3^3(T))$ and T'_g is the onset of the supercooled liquid region upon heating [85]. The rate of volume dilatation defined in the style of Eq. 2.20 as

$$m_{str}^{V4-3} = \left. \frac{d\epsilon_{4-3}}{d(T'_g/T)} \right|_{T=T'_g} \quad (2.26)$$

yields the *structural fragility parameter* m_{str}^{V4-3} . The correlation between the m_{str}^{V4-3} and the kinetic fragility index m is shown in Fig. 2.9 and suggests that kinetically fragile liquids experience pronounced structural changes on the MRO length scale. In Refs. [85] and [86], these structural changes are interpreted in terms of a volume contraction on a length scale of about 1 nm upon cooling and might point towards a rapid expansion of MRO, resembling what is observed in computer simulations [87].

In a study by Mauro et al., the peak height of the first sharp diffraction peak of the total-scattering structure function $S(Q)$ is used as structural metric that is correlated with the kinetic fragility [88]. The mismatch between the value for $S(Q_1)$ of the high temperature liquid at T_g , obtained from a linearly extrapolation of the high temperature data, and $S(Q_1)$ at T_g is larger for fragile liquids. The accelerated change in $S(Q_1)$ that fragile liquids need to undergo upon approaching T_g is attributed to the

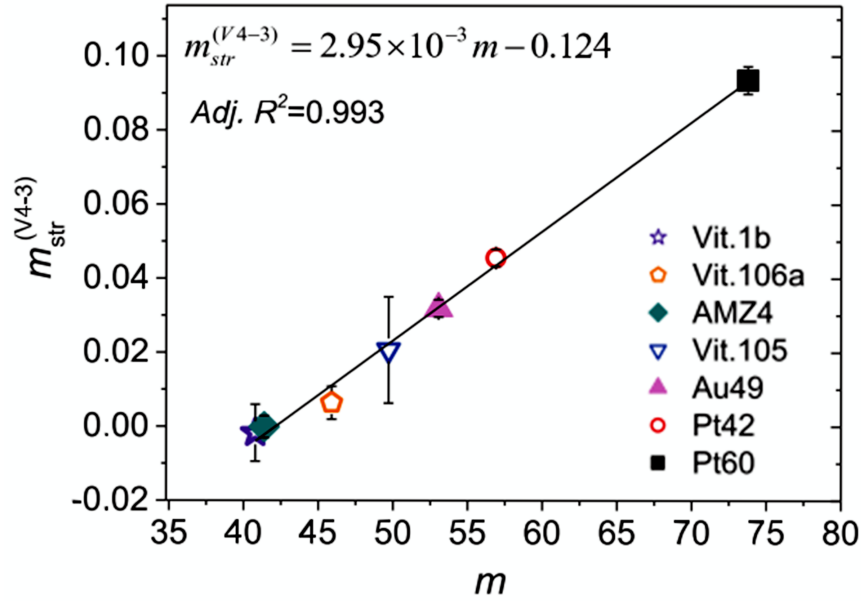


FIGURE 2.9: Correlation between the structural fragility parameter m_{str}^{V4-3} and the kinetic fragility index m of different bulk glass-forming liquids. The compositions of the alloys can be found in Ref. [85].
Figure taken from Ref. [85].

rate of ordering in the liquid [88]. However, the study does not consider the occurrence of a fragile to strong transition in the liquid upon cooling. The alloy composition Vit106⁷ ($Zr_{57}Cu_{15.4}Ni_{12.6}Al_{10.0}Nb_5$), which is chosen to represent a kinetically strong liquid, shows a distinctly stronger behavior at low than at high temperatures [39]. In the related alloy composition, Vit106a, the difference between high and low temperature fragility is a result of a transition from a fragile to a strong liquid occurring in the supercooled liquid [86]. The occurrence of such a transition is even suggested for a binary Cu-Zr alloy [84].

2.4 Nucleation, growth and the glass-forming ability

Although a driving force for the formation of a crystalline nucleus is generated as soon as the temperature of the liquid falls below T_l (see Chapter 2.2), crystallization does not necessarily occur on a finite time scale. The reason is that the formation of small particle of a solid phase first rises the Gibbs free energy of the system. The Gibbs free energy of a system, containing a volume V_S of a solid phase is given by

$$G_{LS} = G_L + \Delta G, \quad (2.27)$$

where G_L is the Gibbs free energy of the pure liquid. The change in the Gibbs free energy due to the formation of solid cluster is expressed as

$$\Delta G = -V_S \Delta G_{l-x}(T) + A_{SL} \gamma_{l-x}, \quad (2.28)$$

⁷The alloy composition in Ref. [88] is indicated as Vit106a. However, the stated alloy composition is commonly termed as Vit106 [64].

where $\Delta G_{l-x}(T)$ is the volumetric Gibbs free energy difference given by Eq. 2.4⁸, A_{SL} is the interfacial area between the solid and the liquid and γ_{l-x} is the solid/liquid *interfacial energy*. As the structure of the liquid changes upon undercooling (decreasing configurational entropy, evolution of short-/medium range order), γ_{l-x} is strictly speaking a function of temperature. However, in further considerations it is assumed to be constant. From Eq. 2.28 it can be seen that the formation of a solid cluster with a volume V_S yields a negative contribution to ΔG as $\Delta G_{l-x}(T)$ is always positive below T_l (see Fig. 2.2). The formation of a new interface between the liquid and the crystalline cluster contributes positively to the change in the Gibbs free energy, thus acting against a spontaneous crystal formation. Assuming the formation of a spherical particle with a radius r , Eq. 2.28 becomes

$$\Delta G = -\frac{4}{3}\pi r^3 \Delta G_{l-x}(T) + 4\pi r^2 \gamma_{l-x}. \quad (2.29)$$

The visualization of Eq. 2.29 in Fig. 2.10 explains why the system can remain in the metastable supercooled liquid state almost indefinitely for a small undercooling. The competition between surface and volume contribution at a given ΔT leads to the situation that Eq. 2.29 passes through a maximum at a value r^* , the *critical nucleus size*. At cluster sizes below r^* the surface contribution dominates, and the system can lower its Gibbs free energy by the dissolution of the crystalline assembly of atoms (embryo). If statistical fluctuations lead to the formation of a cluster with a radius r^* , a reduction of the Gibbs free energy can either be obtained by the dissolution or the growth of the cluster. Clusters who exceed r^* are called supercritical nuclei and contribute to the crystallization of the entire liquid. r^* is deduced from $\frac{d\Delta G}{dr} = 0$ and is given by

$$r^* = \frac{2\gamma_{l-x}}{\Delta G_{l-x}(T)}. \quad (2.30)$$

Inserting Eq. 2.30 into Eq. 2.29 yields the *nucleation barrier* ΔG^* that needs to be overcome to form a supercritical nucleus

$$\Delta G^* = \frac{16\pi\gamma_{l-x}^3}{3\Delta G_{l-x}(T)^2}. \quad (2.31)$$

By applying the Turnbull approximation for the driving force for crystallization (Eq. 2.12), r^* and ΔG^* can be written as a function of ΔT :

$$r^* = \frac{2\gamma_{l-x}T_l}{\Delta H_f\Delta T}, \quad (2.32)$$

$$\Delta G^* = \frac{16\pi\gamma_{l-x}^3T_l^2}{3\Delta H_f^2\Delta T^2}. \quad (2.33)$$

The dependence of r^* and ΔG^* on the level of undercooling indicates that the probability that a supercritical nucleus forms increases with increasing undercooling (Fig. 2.10). The average number of spherical clusters with a radius r per volume is given by [50]

$$n_r = n_0 \exp\left(\frac{\Delta G}{k_B T}\right), \quad (2.34)$$

⁸In Eq. 2.4, $\Delta G_{l-x}(T)$ is given in J/g-atom, in Eq. 2.28 in J/m³.

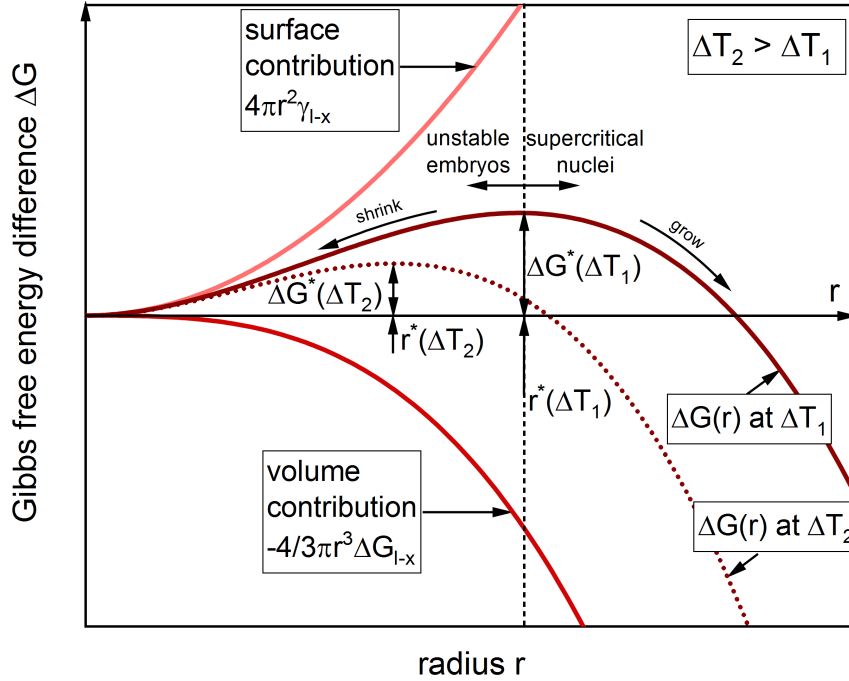


FIGURE 2.10: Change in the Gibbs free energy of a liquid through the formation of a spherical, crystalline particle with radius r . ΔG comprises a surface and a volume contribution. r^* and ΔG^* denote the critical nucleus size and the nucleation barrier. Particles smaller than r^* will on average shrink whereas those larger than r^* will on average grow. Upon undercooling (ΔT), r^* and ΔG^* decrease and the probability for the formation of supercritical nuclei increases.

where k_B is the Boltzmann's constant, n_0 is total number of atoms in the system and ΔG is the Gibbs free energy change caused by the formation of embryos with a radius r according to Eq. 2.29. This relation only applies for $r \leq r^*$ since clusters exceeding r^* already belong to the solid phase. The nucleation rate is given by the number of clusters that become supercritical. Clusters that may become supercritical need to grow to the critical nucleus size r^* . Their amount per volume can be obtained from Eq. 2.34 as [50]

$$n_r^* = n_0 \exp\left(\frac{\Delta G^*}{k_B T}\right), \quad (2.35)$$

by substituting ΔG with the nucleation barrier ΔG^* (Eq. 2.31). As shown in Fig. 2.10, critical nuclei (those with a radius r^*) can either dissolve or grow, since both paths lower the Gibbs free energy of the system. The occurrence of supercritical nuclei depend on the number of atoms that jump from the adjacent liquid to the critical nuclei and the process is therefore governed by atomic diffusion [44]. The *average atomic diffusion coefficient* D is connected to the characteristic *atomic jump frequency* ν via

$$D(T) = a_0^2 \nu(T) = a_0^2 \nu_0 \exp\left(\frac{-E_A}{k_B T}\right), \quad (2.36)$$

containing an average activation energy for atomic diffusion E_A , the average atomic diameter a_0 and the vibration frequency of the atoms ν_0 [44]. The time independent nucleation rate $I_v(T)$, the *steady state nucleation rate*, is obtained by multiplication of the amount of critical nuclei and the atomic jump frequency, reflecting jumps toward

the critical nuclei,

$$I_v(T) = Av(T) \exp\left(\frac{\Delta G^*}{k_B T}\right), \quad (2.37)$$

where A is a constant. Turnbull argued that the average atomic jump time $1/\nu$ should scale with the shear viscosity [28]. The diffusion coefficient, being proportional to the jump frequency, is connected to the viscosity via the Stokes-Einstein relation:

$$D(T) = \frac{k_B T}{6\pi\eta(T)a_0}. \quad (2.38)$$

Assuming that the Stokes-Einstein relation is valid in the temperature range between T_l and T_g , the jump frequency in Eq. 2.37 can be replaced by the temperature depended viscosity which is given by Eq. 2.18. Inserting Eq. 2.31 in Eq. 2.37 yields the following expression for the nucleation rate [44]:

$$I_v(T) = \frac{A_v}{\eta(T)} \exp\left(\frac{-16\pi\gamma_{l-x}^3}{k_B T \Delta G_{l-x}(T)^2}\right), \quad (2.39)$$

where A_v is a constant and $\Delta G_{l-x}(T)$ is given by Eq. 2.10. The temperature depended velocity at which the solid/liquid interface of a supercritical nucleus proceeds, the *growth rate* u , can be calculated as [89]

$$u(T) = \frac{fk_B T}{3\pi a_0^2 \eta(T)} \left[1 - \exp\left(\frac{n\Delta G_{l-x}(T)}{k_B T}\right) \right], \quad (2.40)$$

where n is the average atomic volume and the pre-factor f reflects the roughness of the interface between liquid and crystal on an atomic scale [90] and is assumed to be unity if $\Delta H_f/T_l < 2R$ (rough interface) and $0.2(T - T_l)/T_l$ if $\Delta H_f/T_l > 4R$ (smooth interface) [89, 90].

The general shape of $I_v(T)$ and $u(T)$ are shown in Fig. 2.11. Due to the high atomic mobility and the low Gibbs free energy difference between the liquid and the crystal, the nucleation rate is vanishingly small, and growth dominates. The high driving force and low atomic mobility at low temperatures changes the balance of power between nucleation and growth. The different temperature regions, in which nucleation or growth dominate, lead to the commonly observed dependence of the crystalline microstructure on the level of undercooling. At slow cooling rates, crystallization occurs at a low level of undercooling and the crystalline solid is composed of a small amount of large grains, grown from the few supercritical nuclei. Higher cooling rates give rise to a more fine-grained microstructure.

Assuming that $I_v(T)$ and $u(T)$ are independent of time, that $u(T)$ is isotropic (transforming regions stay spherical), and that the transformation is polymorphic [91], the crystallized volume fraction x in a liquid at a time $t > t'$ can be expressed as [92]

$$\begin{aligned} X(T) &= \frac{4\pi}{3} I_v(T) u(T)^3 \int_{t'=0}^t (t-t')^3 dt' \\ &= \frac{\pi}{3} I_v(T) u(T)^3 t^4, \end{aligned} \quad (2.41)$$

where t' is the time up to which $X(T)$ is zero. Equation 2.41 is only valid in the initial stage of the crystallization process [92]. As the nuclei grow in size with time, they impinge on each other and develop a common interface. If impingements are taken

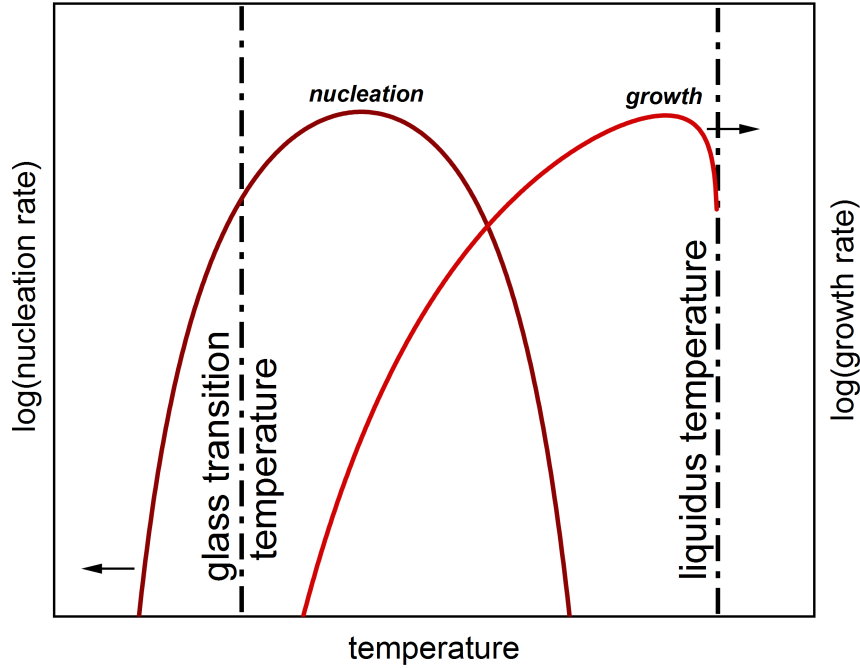


FIGURE 2.11: Nucleation rate and growth rate as a function of temperature. At the liquidus temperature the Gibbs free energy difference between the liquid and the crystal vanishes.

into account, $X(T)$ can be written as

$$\begin{aligned}
 -\ln(1 - X(T)) &= \frac{4\pi}{3} I_v(T) u(T)^3 \int_{t'=0}^t (t - t')^3 dt' \\
 X(T) &= 1 - \exp\left(\frac{\pi}{3} I_v(T) u(T)^3 t^4\right),
 \end{aligned} \tag{2.42}$$

which is known as the *Johnson-Mehl-Avrami-Kolmogorov* (JMAK) equation [91, 92]. For a fixed volume fraction of crystals X , Eq. 2.42 can be transformed into the form

$$t(T) = \left(\frac{-3\ln(1 - x)}{\pi I_v(T) u(T)^3} \right)^{1/4}, \tag{2.43}$$

describing the typically nose shaped temperature dependence of the crystallization process in a TTT diagram as shown in Fig. 1.1. The T_g -line in the TTT diagrams is derived from the VFT equation (Eq. 2.18) and is mathematically expressed as

$$T_g(\tau_\alpha) = T_0 + \left(\frac{D^* T_0}{\ln(\tau_\alpha / \tau_0)} \right). \tag{2.44}$$

$I_v(T)$ and $u(T)$ in Eq. 2.43 determine the shape and the position of the crystallization nose. Both quantities depend on the Gibbs free energy between the liquid and the crystal, the atomic mobility represented by the viscosity of the liquid and the interfacial energy between the liquid and the competing crystal. Therefore, these parameters are the crucial factors determining the glass-forming ability of bulk glass-forming liquids as they shift the crystallization nose, which needs to be bypassed, to longer or shorter times. Figures 2.12, 2.13 and 2.14 illustrate how $I_v(T)$ (Eq. 2.39), $u(T)$ (Eq. 2.40) and $t(T)$ (Eq. 2.43) change if the driving force, the fragility and the

interfacial energy of a liquid is varied. Figure 2.12 illustrates the effect of ΔG_{l-x} (Eq. 2.10) by varying ΔS_f ⁹ from 5 to 14 J g-atom⁻¹ K⁻¹, which are values typically found for BMG forming liquids. The kinetic fragility and the interfacial energy are kept constant. As can be seen in Fig. 2.12(a), the maximum of the nucleation rate shifts to lower temperatures and changes approximately by 14 orders of magnitude, whereas $u(T)$ (2.12(b)) remains rather unaffected. The reduction of the driving force pushes the crystallization nose to five orders of magnitude longer times and lower temperatures (2.12(c)).

In Fig. 2.13 only the fragility of the liquid is varied. The fragility parameters are chosen such that it represents a very fragile liquid ($D^* = 6.8, T_0 = 421.1\text{K}$), a liquid with intermediate fragility ($D^* = 15.3, T_0 = 354.5\text{K}$) and a strong liquid ($D^* = 23.8, T_0 = 305.4\text{K}$). Fragile liquids possess a T_0 that is closer to T_g^* since their viscosity ascends more rapidly in the low temperature regime. As all liquids possess the same T_g^* (=498 K), the curves meet at the glass transition temperature. In this case, $u(T)$, shown in Fig. 2.13(b), changes by three orders of magnitude, however, its maximum remains close to T_l . The maximum of $I_v(T)$ and $t(T)$ (Fig. 2.13(a) and (c)) are both found to shift by four orders of magnitude when the fragility of the liquid changes from fragile to strong. The stronger the liquid, the higher is the viscosity at the temperature of the minimum waiting time for crystal formation T^* (nose temperature) as shown in Fig. 2.6(a), resulting in slower crystallization kinetics which shift $t(T)$ to longer times.

Although the interfacial energy only affects $I_v(T)$, it is a factor that should not be underestimated as it contributes to the power of three to the exponential function in $I_v(T)$. γ_{l-x} comprises an enthalpic and an entropic contribution, arising from non-saturated bonds and the partial ordering in the interface [44]. The model of Spaepen [93] describes the solid/liquid interface as densely packed, suggesting that the origin of γ_{l-x} is mainly entropic [44]. γ_{l-x} can be estimated from the following expression [44]:

$$\gamma_{l-x} = \alpha \frac{\Delta S_f T}{N_A^{1/3} V_m^{2/3}}, \quad (2.45)$$

where V_m is the molar volume and α ¹⁰ takes the structure of the solid into account. Equation 2.45 implies that γ_{l-x} is linked to ΔS_f of an alloy. As shown in Fig. 2.14, an increasing γ_{l-x} from 0.02 to 0.11 J/m² decreases the maximum of $I_v(T)$ by 16 orders of magnitude, resulting in an increase in the minimum waiting time for crystal formation by six orders of magnitude. As a growing γ_{l-x} hampers the formation of supercritical nuclei by increasing the nucleation barrier, it is reasonable that $I_v(T)$ and $t(T)$ are shifted to lower temperatures.

The position of the crystallization nose is connected to the critical casting thickness d_c since it determines the critical cooling rate that is needed to avoid the crystallization of the liquid. Johnson et al. established an empirical connection between the minimum waiting time for crystal formation τ_X^* at T^* and d_c [17]. τ_X^* is calculated as

$$\tau_X^* = 0.00419 d_c^{2.54}. \quad (2.46)$$

With Eq. 2.46, the effect of ΔG_{l-x} , the kinetic fragility and γ_{l-x} on τ_X^* can be converted into a d_c value. A hypothetical TTT diagram for a fragile liquid with a large ΔS_f and a low γ_{l-x} (1), a liquid of intermediate fragility with an intermediate ΔS_f

⁹The parameter a, b, c, d in Eq. 2.10 remain constant.

¹⁰ α is 0.71 and 0.86 for a bcc and a hcp structure, respectively [44].

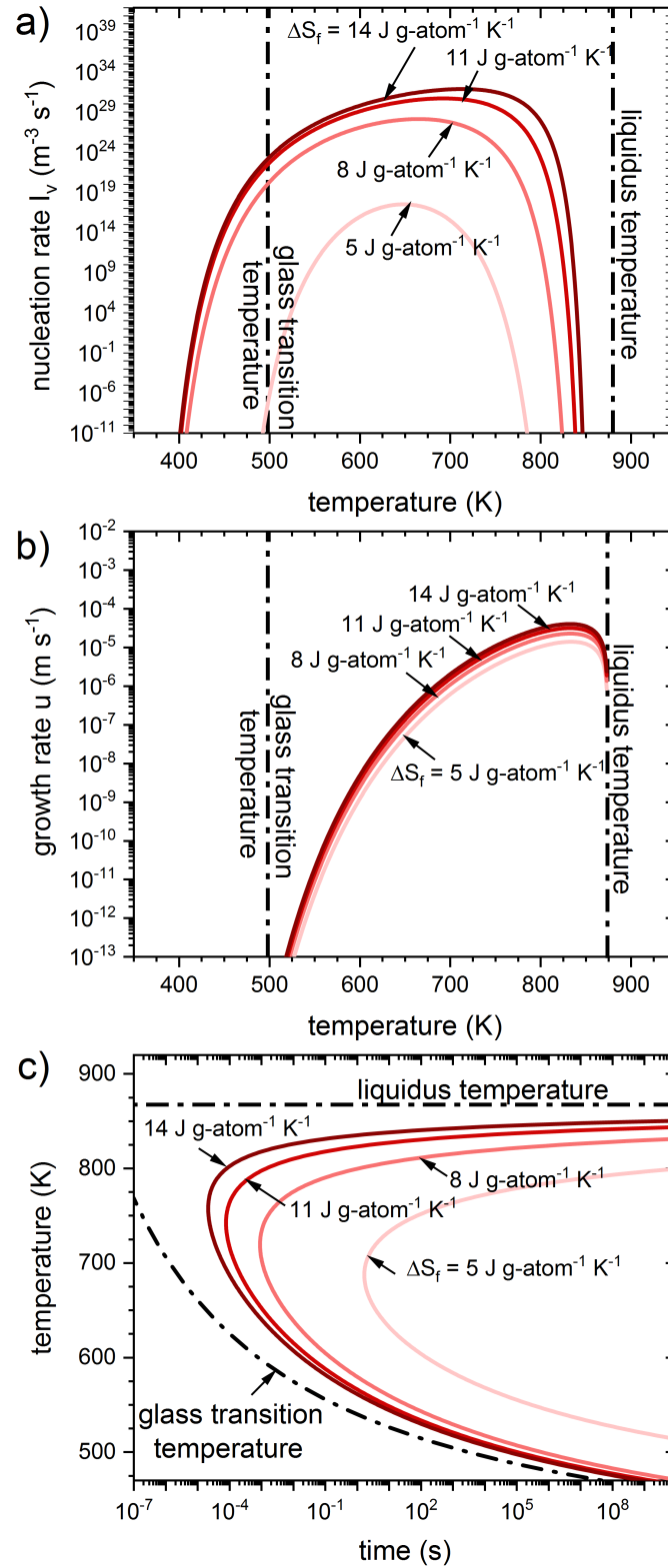


FIGURE 2.12: Effect of the Gibbs free energy difference between the liquid and the crystal (Eq. 2.10) on (a) the nucleation rate, (b) growth rate and (c) the TTT diagram. At the liquidus temperature (T_l) the Gibbs free energy difference between the liquid and the crystal vanishes. The glass transition temperature in (a) and (b) is the temperature at which the liquids reach a viscosity value of 10^{12} Pa s.

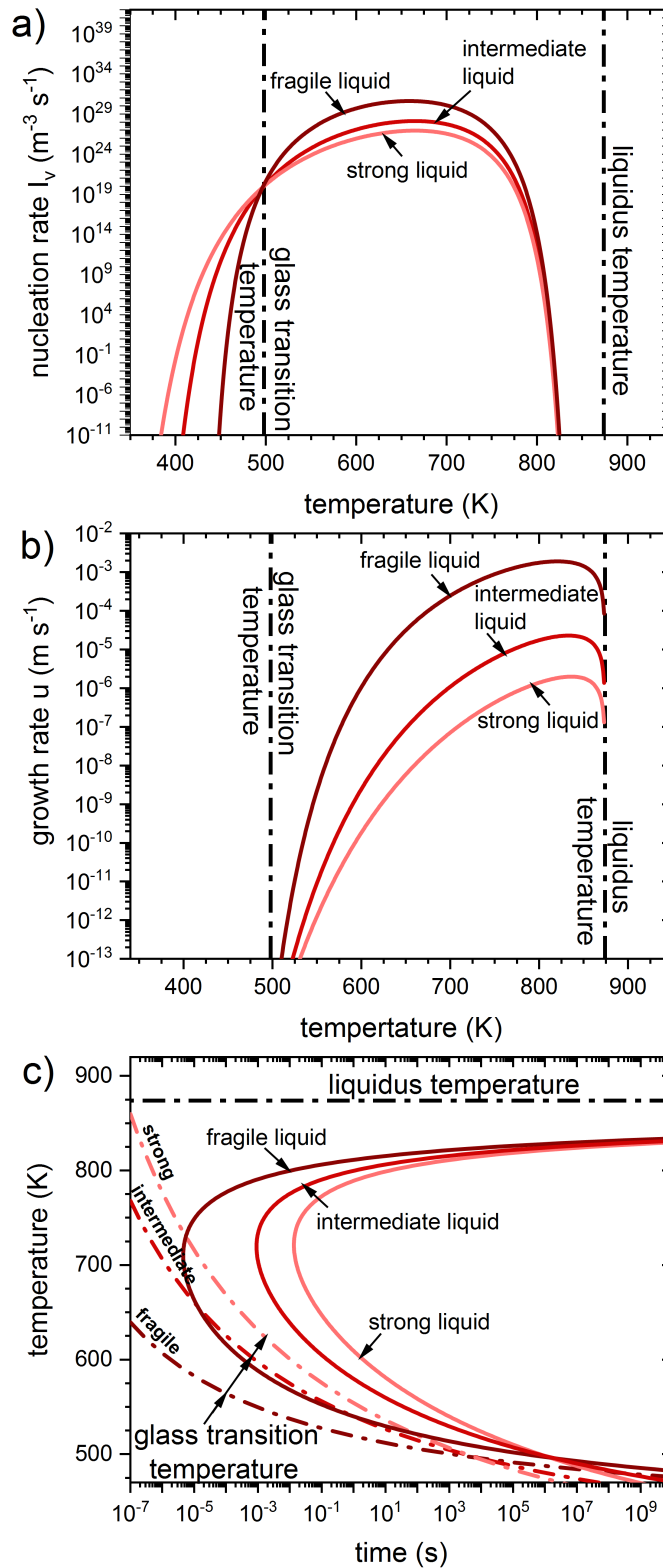


FIGURE 2.13: Effect of the kinetic fragility of the liquid (Eq. 2.18) on (a) the nucleation rate, (b) growth rate and (c) the TTT diagram. At the liquidus temperature (T_l) the Gibbs free energy difference between the liquid and the crystal vanishes. The glass transition temperature in (a) and (b) is the temperature at which the liquids reach a viscosity value of 10^{12} Pa s.

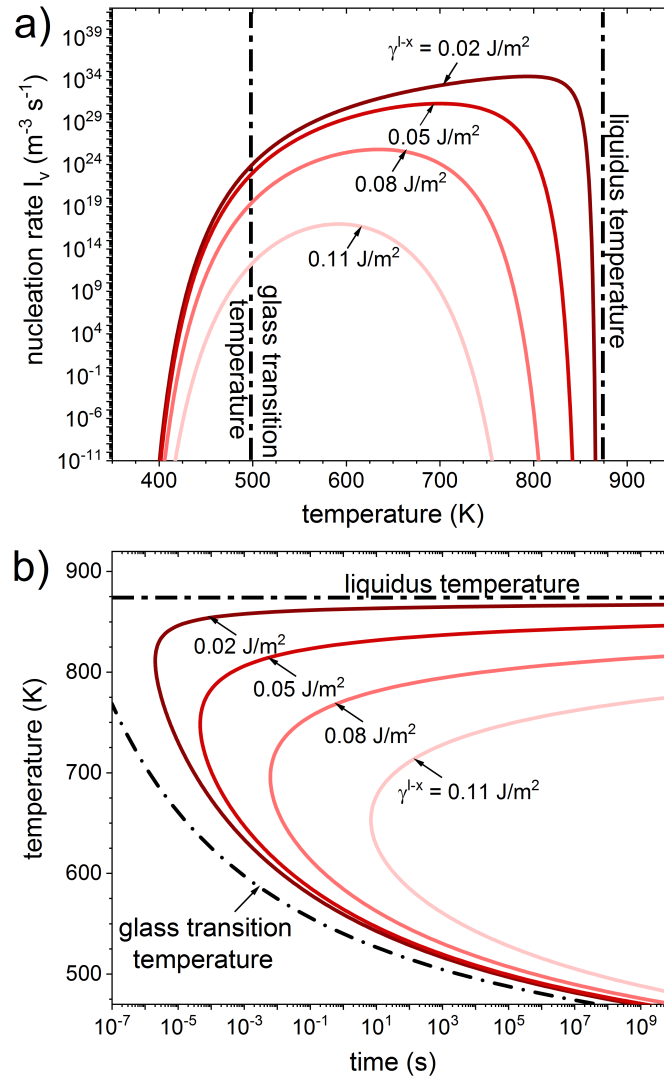


FIGURE 2.14: Effect of the interfacial energy between the liquid and the competing crystal on (a) the nucleation rate and (b) the TTT diagram. At the liquidus temperature (T_l) the Gibbs free energy difference between the liquid and the crystal vanishes. The glass transition temperature in (a) is the temperature at which the liquids reach a viscosity value of 10^{12} Pa s .

and an intermediate γ_{l-x} (2) and a strong liquid with an intermediate ΔS_f and a large γ_{l-x} (3) is shown in Fig. 2.15. The liquid with the poorest prerequisites for glass formation, liquid (1), possesses a τ_X^* in the order of 10^{-8} s . With a d_c of $7.5 \mu\text{m}$, this liquid is reminiscent of a very poor glass former that might vitrify on one side of a melt spun ribbon that is in contact with the copper wheel. As the thermodynamic and kinetic properties change to ease glass formation, τ_X^* and T^* shift to longer times and lower temperatures, respectively. Liquid (3) featuring a τ_X^* of 156 s would vitrify if cast in a mold with a diameter of 63 mm which is close to the largest d_c ever achieved for metallic bulk glass-forming liquids.

The previous considerations take intrinsic factors of the liquid into account. Extrinsic factors that affect the position of the crystallization nose are commonly attributed to heterogeneous nucleation. Heterogeneous nucleation describes the reduction of the nucleation barrier ΔG^* due to the presence of an external interface to which the

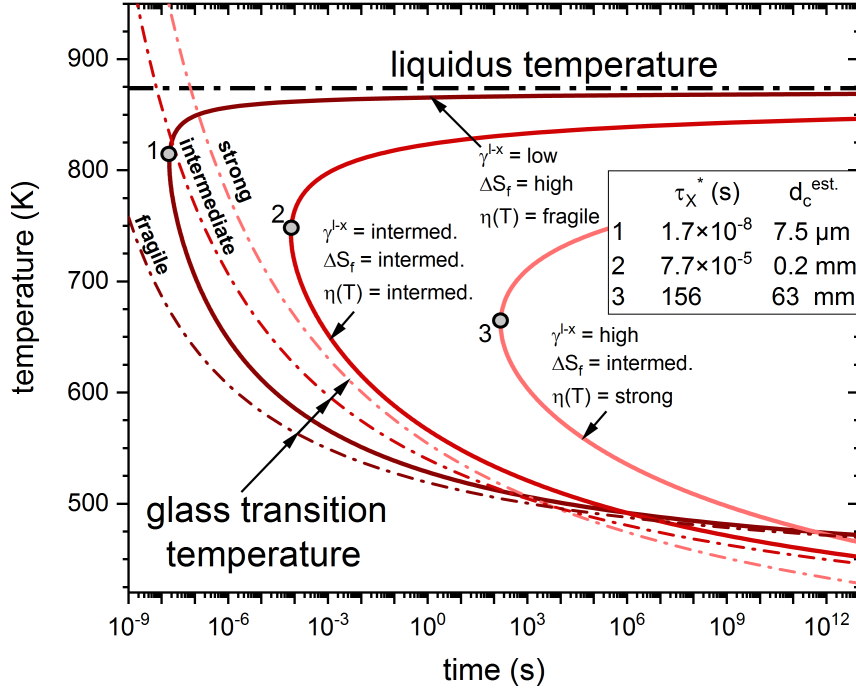


FIGURE 2.15: Effect of the interfacial energy γ_{l-x} , the Gibbs free energy difference between the liquid and the crystal (represented by the entropy of fusion ΔS_f), and the kinetic fragility of a liquid on the crystallization nose in a TTT diagram. The parameters are changed successively from liquid (1) to (3) to ease glass formation by shifting the minimum waiting time for crystal formation τ_X^* , marked with a cycle, to longer times. The critical casting thickness is estimated from Eq. 2.46 using τ_X^* .

solid embryo attaches. The potential of an interface to lower the nucleation barrier, depends on how the embryo wets the surface. The effect of the wetting can be mathematically taken into account by

$$S(\theta) = (2 + \cos(\theta))(1 - \cos(\theta))^2/4, \quad (2.47)$$

where θ is the wetting angle. If the embryo is attached to the surface ($0^\circ < \theta < 180^\circ$), the heterogeneous nucleation barrier, given by

$$\Delta G_{het}^* = \Delta G_{hom}^* S(\theta), \quad (2.48)$$

is lower than the homogeneous nucleation barrier ΔG_{hom}^* (Eq. 2.31). The catalytic effect of an artificial surface is most pronounced for low wetting angles. A wetting angle of 10° lowers the nucleation barrier by four orders of magnitude. It is for that reason that heterogeneous nucleation needs to be avoided during casting bulk glass-forming liquids. Figure 2.16 shows schematically the effect of heterogeneous nucleation on the crystallization nose and thus on R_c . The production of fully amorphous samples requires higher cooling rates if heterogeneous nucleation sites are present [94, 95]. The probability of the occurrence of heterogeneous nucleation is lowered if high purity elements are used for the alloy synthesis [94, 96]. Beside oxide particles with high melting points, the formation of oxygen stabilized phases that do not dissolve at the (original) T_l of the alloy composition, are found to initiate heterogeneous nucleation [97]. Moreover, mold walls can serve as regions for heterogeneous

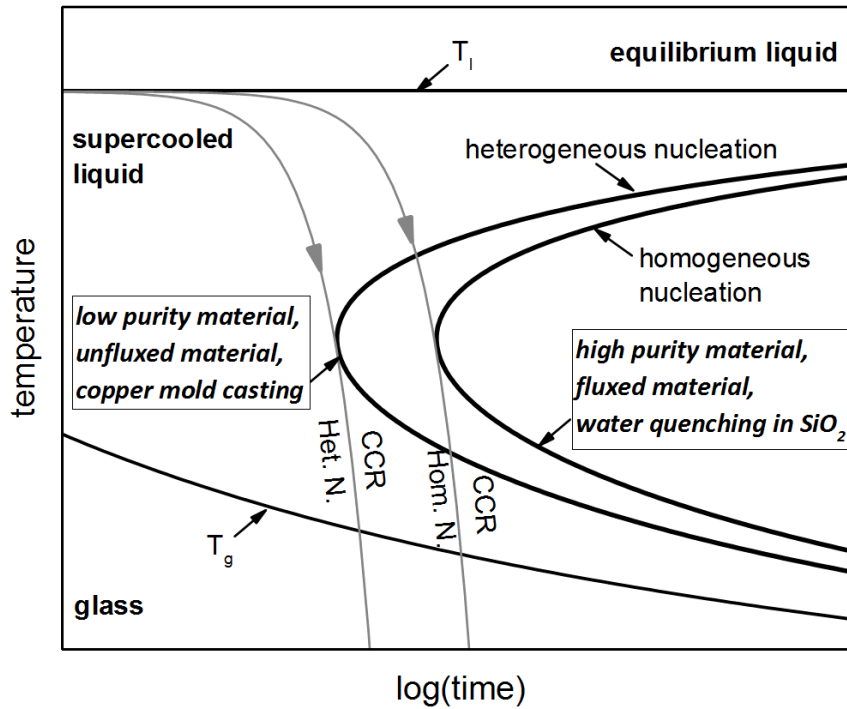


FIGURE 2.16: Effect heterogeneous nucleation sites on the schematic TTT diagram of a glass-forming liquid. Heterogeneous nucleation increases the critical cooling rate (R_c) and thus reduces the critical casting thickness of the alloy composition. The effect of heterogeneous nucleation on the nose temperature T^* and the overall shape of the crystallization nose is neglected.

nucleation. Although fused silica possesses a much lower thermal conductivity than metallic molds, the accesses to the glassy state can be simplified as embryos do not benefit from the amorphous fused silica surface [98]. Furthermore, cavities may affect the level of undercooling as observed in nucleation experiments on liquid Sn [99, 100]. At limited overheating level, residual solid Sn can be preserved in cavities which serves as nucleation site reducing the maximum achievable undercooling.

For some alloys, the detrimental effect of heterogeneous nucleation can be reduced through melting the alloy in B_2O_3 . For energetic reasons, oxide particles leave the metallic liquid and are trapped within the B_2O_3 [101]. This fluxing process purifies the liquid by lowering the oxygen content [98] and enhances the GFA significantly [102–104]. In an Al-based liquid, a salt-flux ($MgCl_2 - CaCl_2$) is found to effectively increase d_c from 1.5 mm ($R_c \approx 450K/s$) to 2.5 mm ($R_c \approx 160K/s$) [105] and electro-deoxidation in $CaCl_2$ improves the GFA in Zr- and Cu-based alloys [106].

Consequently, the shape of the time and temperature dependent crystallization process is a result of competition of the decreasing atomic mobility and the increasing driving force for crystallization, effected by the interfacial energy between the liquid and the competing crystal as well as by extrinsic factors like heterogeneous nucleation. Basically, each liquid is subject to this process and time is the decisive factor. Through ultra-fast quenching, even a pure metal (liquid Ta), possessing a R_c of approximately $5 \times 10^{12}K/s$ and a τ_X^* of 300 picoseconds, can be successfully vitrified [107].

2.5 Properties of the frozen-in and supercooled liquid

2.5.1 The entropy catastrophe

As discussed in the previous section, the temperature dependent change of the physical properties fundamentally determines the capability of a supercooling liquid to form a glass. Beside the rapid increase in viscosity upon approaching the glass transition, the ascending specific heat capacity and the associated loss in excess entropy are the most striking features accompanying the process of undercooling.

Kauzmann was the first to notice that the extrapolated course of the excess entropy (ΔS^{l-x}) leads to the puzzling scenario of a disordered, supercooled liquid, possessing a lower entropy than the ordered, competing crystal above absolute zero. The temperature at which the excess entropy vanishes is the Kauzmann temperature T_K (Fig. 2.6(c)). Kauzmann suggested that this paradox is prevented by crystallization of the supercooled liquid before reaching T_K . The hypothesis is based on the argument that the large driving force for nucleation close to T_K reduces the energy barrier for crystallization to the same height as the energy barrier for atomic rearrangements [43], impeding the access to the metastable equilibrium and forcing the liquid to crystallize. However, this argument neglects the effect of the kinetic contribution (atomic diffusion). The interplay of the atomic dynamics with thermodynamic parameters affects the appearance of the lower portion of the crystallization nose as shown in Chapter 2.4. Therefore, the crystallization time $t_x(T \rightarrow T_K)$ is expected to exceed the structural relaxation time $\tau_\alpha(T \rightarrow T_K)$ [108], which would allow the liquid to equilibrate close to T_K if the timescales were experimentally accessible (Fig. 2.17(a)).

In this case, a resolution to the Kauzmann paradox is given by Gibbs and DiMarzio suggesting that the liquid transforms via a second-order phase transition to an "ideal glass" at T_K [109]. The idea gave rise to the Adam-Gibbs theory [68], predicting a diverging timescale for structural relaxation at T_K (Eq. 2.24). This ultimately leads to an unavoidable glass transition, in accordance with the empirical VFT equation for $T_K = T_0$ ¹¹.

However, the existence of an "ideal glass transition" is questioned by Tanaka [108]. He argued that the assumption of $t_x \gg \tau_\alpha$ is based on the validity of the Stokes-Einstein equation (Eq. 2.38), connecting the atomic diffusivity with τ_α [108], which is found to break down for some of the constituent elements in the supercooled liquid region [111–113]. The decoupling of the timescales for translational diffusion, $\tau_D(T)$, and structural relaxation, $\tau_\alpha(T)$, is ascribed to dynamic heterogeneities [114] affecting the crystallization kinetics [108]. Masuhr et al. have shown that the lower portion of the isothermal crystallization nose of Vitreloy 1 ($\text{Zr}_{41.2}\text{Ti}_{13.8}\text{Cu}_{12.5}\text{Ni}_{10.0}\text{Be}_{22.5}$), shown in Fig. 2.17(b), cannot be described by Eq. 2.43 using $\eta(T)$ (or $\tau_\alpha(T)$) as input parameter, suggesting that the observed decoupling between the time scales of the diffusion of the small and medium sized atoms and τ_α changes the appearance of the crystallization nose [111]. As shown in Fig. 2.17(a), the relevance of τ_D for the crystallization process shifts the crystallization onset to shorter times, represented by the $t_x(\tau_D \text{ branch})$. As a result, the crystallization nose intersects with $\tau_\alpha(T)$ at a temperature above T_K . The intersection temperature, T_{LML} , marks the *lower limit of*

¹¹In metallic glass-forming liquids, T_K derived from $\Delta S^{l-x}(T)$ does usually not coincide with T_0 . If $S_c(T)$ in Eq. 2.22 is expressed as $S_c(T_a) - \int_T^{T_a} \frac{\Delta C_p^{l-x}(T')}{T'} dT'$, where $S_c(T_a)$ is a fitting parameter representing the configurational entropy at an arbitrary temperature T_a , T_K is found to be very close to T_0 [65, 110].

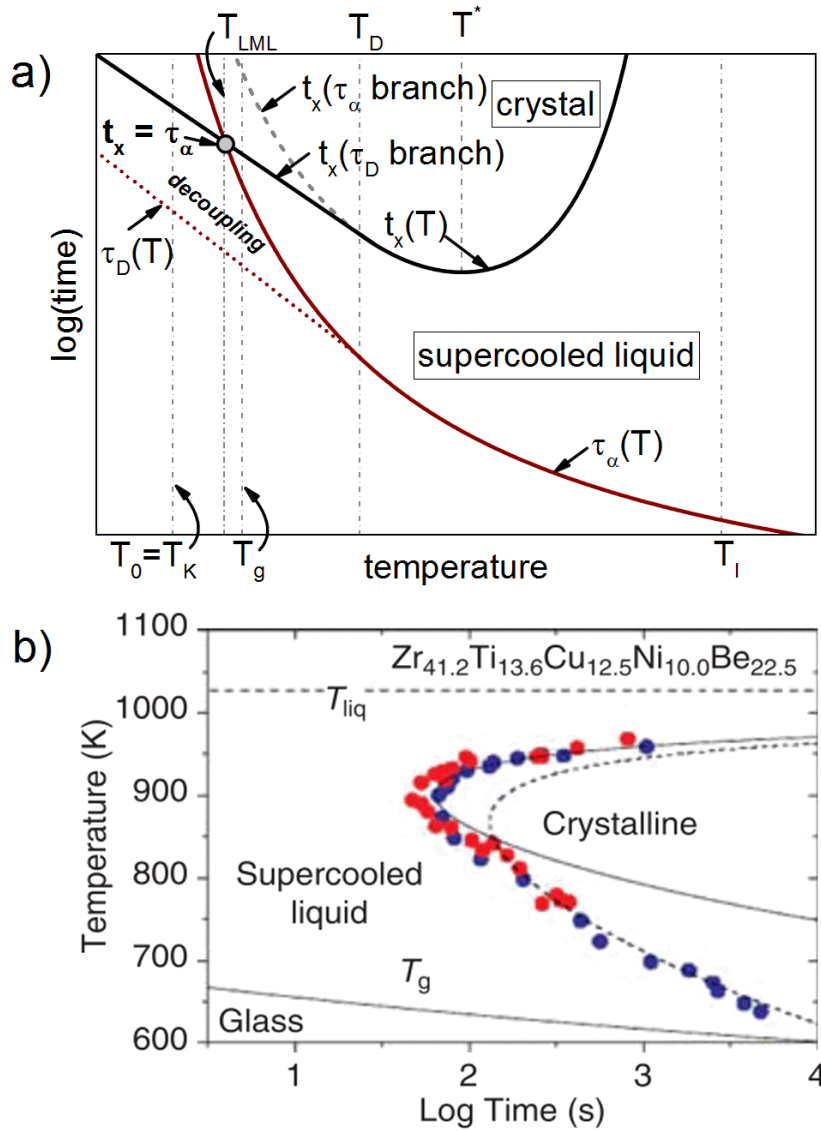


FIGURE 2.17: (a) Schematic illustration of the effect of the decoupling of the timescales for translational diffusion, $\tau_D(T)$, and structural relaxation, $\tau_\alpha(T)$ (VFT equation), on crystallization time ($t_x(T)$). As the relevant transport process for crystallization is the translational diffusion, the decoupling, occurring at T_D , changes the shape of the lower portion of the crystallization nose from the $t_x(\tau_\alpha \text{ branch})$ to the $t_x(\tau_D \text{ branch})$. This results in an intersection point between $\tau_\alpha(T)$ and $t_x(T)$ at the temperature T_{LML} which is above T_K . T_{LML} marks the lowest metastable limit below which the glass crystallizes before it reaches the metastable equilibrium. Figure after Ref. [108]. (b) TTT diagram for primary crystallization of Vit 1. The two branches ($t_x(\tau_\alpha)$ and $t_x(\tau_D)$) are represented by the solid and dashed line. T_D is approximately at 850, T_{LML} at 600 and T_0 at 413 K. Figure taken from Ref. [63].

metastability [108]. This means that a liquid cannot be cooled below T_{LML} without crystallizing or that glassy samples which are annealed below T_{LML} will crystallize before reaching the metastable equilibrium. Thereby, the entropy catastrophe is prevented.

Indeed, the experimental data in Fig. 2.17(b) show that T_{LML} is located at around 600 K, below which the metastable equilibrium should not be accessible. A similar observation has been made in the newly developed Pd-Ni-S bulk glass-forming alloy system. Although exhibiting a stable supercooled liquid region in continuous heating experiments, the samples crystallize before reaching the metastable equilibrium if annealed below the caloric T_g [115], suggesting that T_{LML} is located right below T_g . The decoupling might also be connected to a changing primary crystalline phase as observed in different metallic glass-forming systems [116, 117].

2.5.2 From the glass to the supercooled liquid: phenomena of structural relaxation

The unstable, glassy state originates from the freezing-in of the metastable, supercooled liquid whose properties are independent of time (if crystallization is excluded). Even far below T_g , the unstable glass urges to access the metastable state. However, the ceasing atomic mobility prevents approaching the metastable equilibrium on human timescales. As the temperature is raised and T_g is approached, the mobility of the atoms is slowly recovered and the glassy state starts evolving towards the metastable equilibrium which is associated with a change in the physical properties with time. The change in the physical properties upon transforming from a glass to a liquid is referred to as structural relaxation or physical aging.

It should be noted that the process of relaxation in metallic glasses can be separated into changes in the topological short-range order (TSRO) and the reversible chemical short-range order (CSRO) [118, 119]. The former refers to cooperative atomic rearrangements responsible for the increase in density and viscosity (α -relaxation) [120], whereas the latter is related to rearrangements in the chemical surrounding of atoms on nearest neighbor length scale [121]¹². This atomic short-range diffusion, effected by the distinct interactions among the elements (negative heat of mixing) [122], is assumed to be linked to the secondary β -relaxation [123]. The β -relaxation process, being connected to the α -relaxation [124], is observed in the loss modulus during a continuous temperature scan in a dynamic mechanical analyzer and occurs at lower temperatures than the α -relaxation¹³. The idea that the β -relaxation process is governed by string-like atomic rearrangements [126] was recently supported by computer simulations [124].

The signature of both relaxation phenomena is visible in various measurement signals. The following considerations focus on the α -relaxation process, although both, TSRO and CSRO, may contribute to the measurement signals.

Upon continuous heating

Depending on the cooling rate, various glassy states with different volume, enthalpy and entropy, can be frozen (the glassy states vary in their fictive temperatures, $T_{fictive}$). Upon heating a rapidly quenched sample, a heat release (exothermic) is observed in a thermogram as shown schematically in Fig. 2.18(a). The exothermic signal bears upon an enthalpy reduction (2.18(b)) associated with a densification of the sample, through the cooperative rearrangements of atoms [128–130]. The increasing atomic mobility during a temperature scan allows the glass to leave its enthalpic

¹²Recent experiments indicate that CSRO does not invoke a densification of the sample [121].

¹³At even lower temperature, the occurrence of an additional relaxation process, termed γ -relaxation, has recently been reported [125].

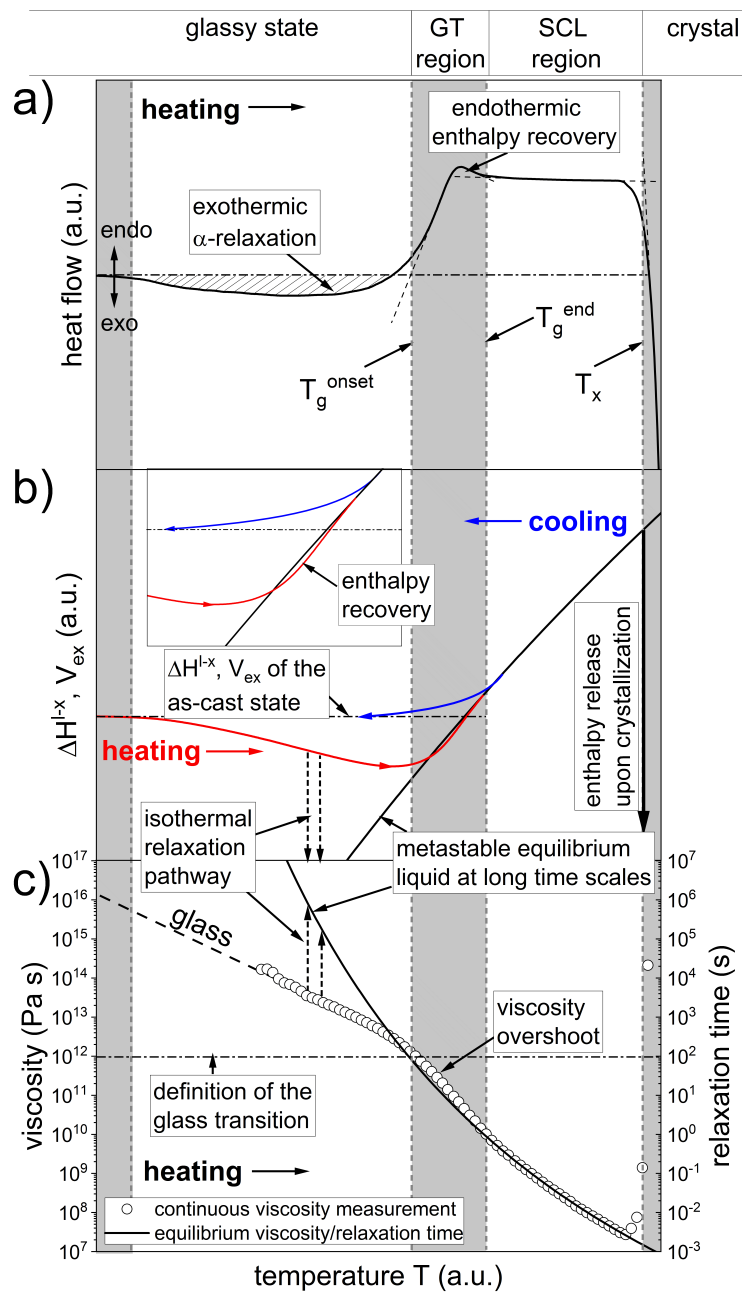


FIGURE 2.18: Change in the thermophysical properties of metallic glass upon heating at a constant rate (schematic). (a) shows the heat flow as a function of temperature. Indicated are the exothermic relaxation event, the endothermic enthalpy recovery, the onset of the glass transition, T_g^{onset} and the end of the glass transition (GT), T_g^{end} . T_x marks the temperature at which the supercooled liquid (SCL) crystallizes. (b) Enthalpy or volume difference between the liquid (or glass) and the crystal (excess enthalpy ΔH_{l-x} or excess volume V_{ex}) upon heating. The horizontal dashed line represents the enthalpic as-cast state and the dashed arrows indicate the isothermal relaxation pathway. The inset magnifies the enthalpy undershoot attributed to the enthalpy recovery effect. (c) Continuous viscosity change upon heating a metallic glass sample. The viscosity overshoot is associated with the enthalpy recovery. Experimental evidence of the viscosity overshoot can be found in Ref. [127].

as-cast level, reduce the amount of excess free volume (which is connected to an increase in the electric resistance [131]) and approach the metastable equilibrium¹⁴.

At a certain temperature, the system reaches its equilibrium value. However, in some cases, the system is not able to follow the equilibrium line due to the sluggish dynamics. As soon as the atomic mobility permits, the system accelerates its excess volume production in order to catch up with the enthalpy or volume curve of the equilibrium liquid [119]. In the DSC scan shown in Fig. 2.18(a), this effect is visible as an endothermic peak, whereas the system exceeds the viscosity of the metastable equilibrium state in a continuous viscosity measurement (Fig. 2.18(c)). This process is termed de-aging [136] or enthalpy recovery [137] and its magnitude strongly depends on the thermal history of the sample [130]. As the system reaches the equilibrium line again, the glass transition is completed (T_g^{end}) and the metastable equilibrium is reached. Upon further heating, the liquid resides in equilibrium until crystallization intervenes. Crystallization is reflected by a pronounced exothermic reaction at T_x associated with a drop in enthalpy. The formation of crystals deprives the system of its ability to flow, represented by the soaring viscosity in Fig. 2.18(c).

At constant temperature

To access the metastable equilibrium liquid at long time scales, isothermal relaxation experiments can be conducted below the calorimetric glass transition. The pathway from the glassy to the liquid state at constant temperature follows a stretched exponential function, the *Kohlrausch-Williams-Watts* (KWW) function [138] of the form:

$$\phi(t) = \phi_0 + \Delta\phi \left(1 - \exp \left(- \left(\frac{t}{\tau_{KWW}} \right)^{\beta_{KWW}} \right) \right), \quad (2.49)$$

where $\phi(t)$ is the relaxing quantity, ϕ_0 the value of ϕ at $t = 0$, $\Delta\phi$ the total change of ϕ during the relaxation process, τ_{KWW} the characteristic relaxation time and β_{KWW} the stretching exponent. The equilibrium value of ϕ can be calculated as $\phi_{eq} = \phi_0 + \Delta\phi$.

The origin of the stretched exponential behavior might be explained by two fundamentally different scenarios [139]. In the first scenario, the (homogeneous) supercooled liquid is composed of nearly identical structural units relaxing in a non-exponential manner. Alternatively, the non-exponential behavior may arise from the heterogeneous nature of the supercooled liquid, consisting of a variety of structural environments, each with an individual, exponential relaxation behavior [114], resulting in a spectrum of relaxation times [140]. The latter case is currently assumed to be correct [141], as experiments and computer simulations point towards spatially heterogeneous dynamics in supercooled liquids [83, 142–144]. Therefore, the deviation from the pure exponential behavior ($\beta_{KWW} = 1$) can be regarded as a measure of the local structural diversity within a supercooled liquid, which usually decreases with increasing temperature. This is associated with a monotonically increasing β_{KWW} with T , reaching unity in the high fluidity range [145]. Consequently, the glass, resulting from a heterogeneous liquid, features a non-uniform structure.

Figure 2.19 shows the relaxation scenario of isothermal viscosity measurements at a temperature T_1 and T_2 . The initial viscosity at the beginning of the isothermal

¹⁴The glass can also be brought to higher enthalpic states through cold deformation [132], elastostatic loading [133], ion irradiation [134] or cryogenic cycling [135]. These processes "rejuvenate" the metallic glass.

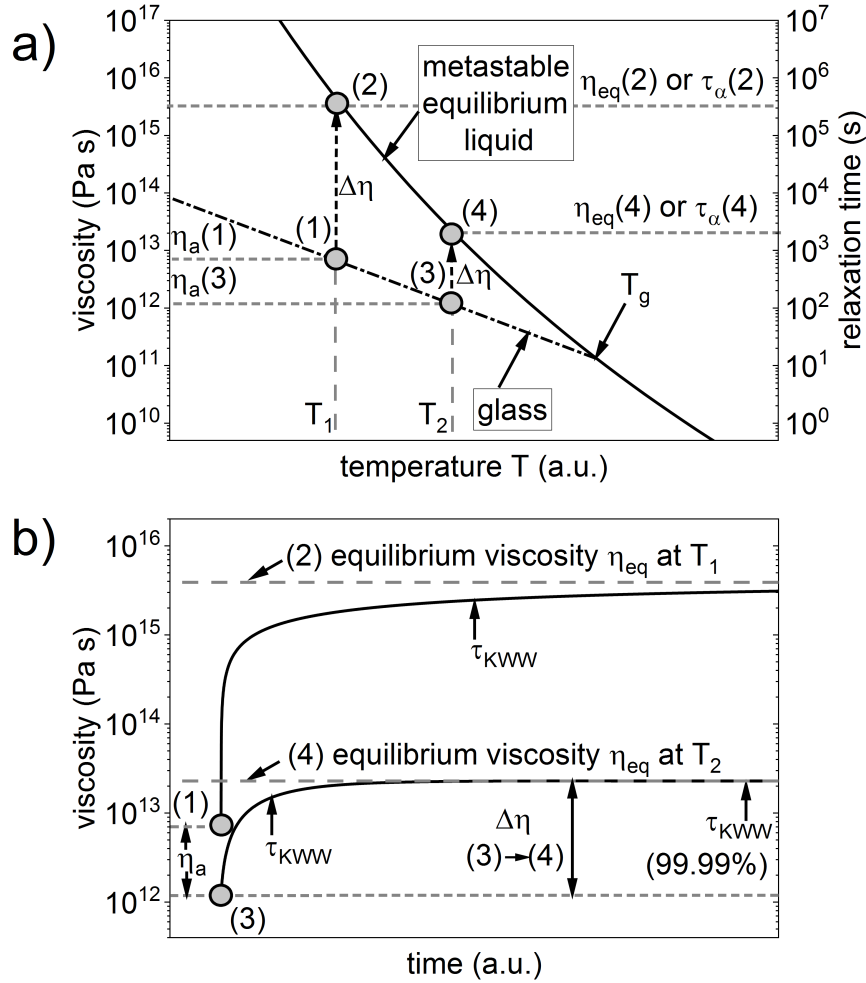


FIGURE 2.19: Isothermal viscosity relaxation at two different temperatures below T_g . (a) Isothermal relaxation pathway at T_1 ((1)→(2)) and at T_2 ((3)→(4)). η_a is the initial viscosity at the beginning of the annealing experiments and depends on the heating rate used to reach the desired temperature. $\Delta\eta$ is the viscosity increase during the relaxation experiment and η_{eq} is the equilibrium viscosity reached after a sufficiently long annealing time. η_{eq} is connected to the average intrinsic relaxation time τ_α , which is proportional but not equal to τ_{KWW} or $\tau_{KWW}(99.99\%)$. (b) Temporal evolution of the viscosity during the relaxation experiments at T_1 ((1)→(2)) and T_2 ((3)→(4)). τ_{KWW} and $\tau_{KWW}(99.99\%)$ refer to the states at which 63.21% and 99.99% of the relaxation process is completed.

segment, η_a , depends on the heating rate that is used to approach the desired temperature [127]. During the isothermal annealing, the change in viscosity of the relaxing glass can be described by Eq. 2.49 (Fig. 2.19(b)). The stretching exponent β_{KWW} is found to approach unity at the calorimetric glass transition [130, 146]. Due to the rather slow heating used to reach the annealing temperature, a large portion of the relaxation process already occurred in the heating process, narrowing the observable part of the relaxation spectrum and therefore affecting β_{KWW} . The average relaxation time τ_{KWW} , obtained as a fitting parameter in Eq. 2.49, describes the time that is needed to complete 63.21% (i.e. $1 - 1/e$, Eq. 2.49) of the isothermal relaxation process. It should be noted that τ_{KWW} is not equal but proportional to the average intrinsic relaxation time τ_α of the liquid. From Eq. 2.1 it can be estimated that τ_{KWW}

is approximately 2 orders of magnitude slower than τ_α [111]. Another value that can be derived from the relaxation experiments is the time that is needed for virtually full equilibration of the system, $\tau_{KWW}(99.99\%)$. $\tau_{KWW}(99.99\%)$ refers to the state at which 99.99% of the relaxation process is completed and can be calculated from Eq. 2.49 as

$$\tau_{KWW}(X) = \tau_{KWW}(-\ln(1 - X))^{1/\beta_{KWW}}, \quad (2.50)$$

where X ($0 < X < 1$) represents the degree of relaxation. The temperature dependence of equilibrium viscosity η_{eq} , and the relaxation times τ_{KWW} and $\tau_{KWW}(99.99\%)$ can be described by Eq. 2.18 yielding comparable values for the fragility parameter D^* [130].

2.5.3 Crystallization of the supercooled liquid

The crystallization process in metallic glass-forming liquids is determined by nucleation and growth (Chapter 2.4). The different temperature dependencies of the nucleation and growth process, shown in Fig. 2.11, lead to diverse appearance of the crystallization event. At high temperature, the growth rate passes through a maximum and the nucleation rate is simultaneously vanishingly small. This means that the formation of a supercritical nucleus depends on a statistical fluctuation in the liquid. Upon decreasing temperature, the probability that such a fluctuation occurs increases as the critical nucleus size (Eq. 2.30) and the nucleation barrier decreases (Eq. 2.29). However, the crystallization process in the upper part of the TTT diagram is a highly statistical process and the onset of crystallization at a certain temperature may occur within a time interval of thousands of seconds [147, 148]. As the formation of a supercritical nucleus is the limiting factor, the crystallization process at high temperatures is termed *nucleation controlled* [147]. In the Pd₄₃Cu₂₇Ni₁₀P₂₀ alloy composition, the formation of a single supercritical nucleus is connected to the avalanche like crystallization of the entire sample [147]. This might be traced back on the fact that the formation of the nucleus in a near eutectic alloy composition locally changes the composition in the surrounding of the nucleus, which destabilizes the liquid against crystallization and causes a chain reaction leading to the overall crystallization of the sample [147]. On the other hand, the crystallization process occurs very reproducible without considerable fluctuations in the lower portion of the TTT diagram. As the nucleation barrier is extremely small close to T_g , the crystallization of the sample is limited by the growth of spontaneously formed or pre-existing nuclei. Therefore, the crystallization process in the low temperature region is *growth controlled* (or *diffusion controlled*) [147].

In Zr-based alloys it has been observed that the crystallization process below a certain temperature is affected by a chemical decomposition ending up in the crystallization of the liquid. In free-cooling experiments on levitating droplets of Vitreloy 1, a small recalescence is observed [149] which is attributed to a phase separation below 800 K [150] into a Ti-rich (Be-lean) and a Ti-lean (Be-rich) supercooled liquid [151] followed by the formation of nano-crystals [152]. This process might be connected to the decoupling of the diffusion of the small and medium size atoms and τ_α , observed by Masuhr et al. [111]. A phase separation process is found in different alloy compositions [153, 154] and may even enhance the plasticity¹⁵ of an alloy [156, 157]. An indication of a phase separation and/or crystallization is the deviation

¹⁵Plasticity can be increased by embedding a crystalline phase into the amorphous matrix (metallic glass composites) [155].

from the equilibrium viscosity plateau value η_{eq} during an isothermal measurement which is often seen in Zr-based alloys [64, 158].

Another intriguing observation in metallic glass-forming liquids is the pronounced asymmetry in the crystallization behavior during constant heating and cooling. As shown in Fig. 2.20, the appearance of the TTT diagram changes when measured

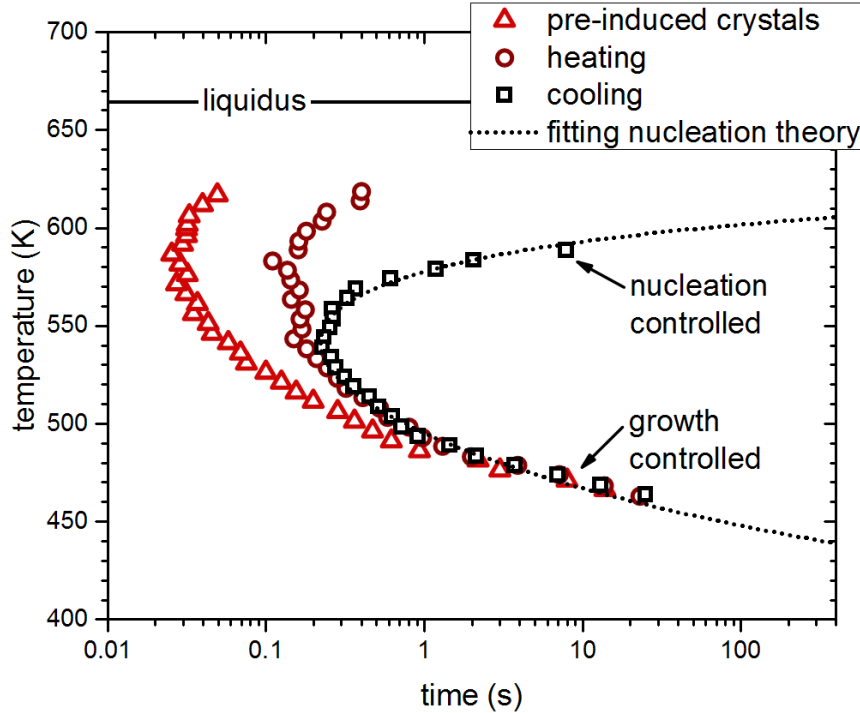


FIGURE 2.20: Isothermal TTT diagram of $\text{Au}_{49}\text{Ag}_{5.5}\text{Pd}_{2.3}\text{Cu}_{26.9}\text{Si}_{16.3}$. The crystallization event is measured upon cooling from the equilibrium melt and upon heating from the glassy state with and without pre-induced crystals. The dotted line represents the fit to the open squares using Eq. 2.43. Data points are taken from Ref. [159]. The error bars of the crystallization events can be found in Ref. [159].

upon heating. At high temperatures, crystallization upon heating is shifted to much shorter times, requiring higher rates to avoid crystallization upon heating than in cooling [159, 160]. This is due to the fact that nuclei formed during heating and cooling are exposed to different growth rates [160]. If a perfectly amorphous sample (without any crystalline structure) is heated at a constant rate, it passes through the maximum nucleation rate (I_{max}) and thereafter through the maximum growth rate (u_{max}) (see Fig. 2.11). This means that initially a large number of nuclei is formed which experience high growth rates during further heating. In contrast, upon cooling from the equilibrium liquid, nuclei formed in the temperature range of I_{max} experience significantly lower growth rates, as u_{max} is located at higher temperatures than I_{max} . This asymmetry might vanish or might be reversed, if I_{max} and u_{max} coincide or if I_{max} is found above u_{max} [160]. As $I_v(T)$ strongly depends on γ_{l-x} and ΔS_f (see Fig. 2.12 and 2.14) and the influence of ΔS_f on $u(T)$ is minor, such a scenario would be conceivable for liquids possessing very low γ_{l-x} and a large ΔS_f . According to Eq. 2.45, γ_{l-x} and ΔS_f are proportional, making the scenario described above highly improbable.

The discrepancy between critical cooling and critical heating rate is further amplified if quenched in nuclei are present in the glassy matrix [160]. Some of these clusters

may have been embryos at high temperatures, however at low temperatures, they exceed r^* and will contribute to the crystallization of the liquid. The avoidance of the crystallization process through bypassing the crystallization nose does not guarantee a glass that is free of supercritical nuclei. Such a glass is prone to crystallization upon reheating [36]. As shown in Fig. 2.20, the presence of pre-induced crystals in the glassy matrix shifts the crystallization onset upon heating to even shorter times, resulting in a significantly higher critical heating rate [159].

2.6 Structure of Metallic Liquids

In 1948, Kauzmann postulated that liquids exhibit a "*considerable amount of short-range quasicrystalline order*" far below their boiling point [43]. Frank argued in 1952 that the atoms in a liquid should arrange in icosahedral clusters for energetical reasons [161]. In some liquids, icosahedral order exists and evolves with decreasing temperature [80, 81]. The local icosahedral symmetry is incompatible with the translational symmetry of the crystal [44]. The crystallization of a liquid with icosahedral short-range order (ISRO) requires a break of this local symmetry in order to adapt the long-range ordered lattice structure of the crystal. Therefore, ISRO is thought to impede the crystallization of the liquid and ease glass formation [44]. However, the nucleation of quasicrystals might be facilitated by ISRO as the small interfacial energy lowers the nucleation barrier significantly [162–164]. In metal-metalloid glasses, Gaskell successfully reproduced the results obtained from neutron scattering experiments by using a trigonal prismatic atomic geometry, which connect randomly via edge sharing [165].

The observation of ISRO and the success of Gaskell's model for metal-metalloid glasses suggest that the local representative structural unit varies in metallic glass-forming liquids. In the model by Miracle (*the efficient cluster packing model*, ECP) the local structural element is represented by efficiently packed solute-centered atomic clusters [166]. Thereby, the solute-to-solvent radius ratio determines the local cluster coordination number. Chemical effects are not taken into account and atomic species with radii within $\pm 2\%$ are assumed to be topologically equivalent [167]. Adjacent clusters may share solvent atoms and are arranged in a face-centered cubic or hexagonal close packed structure to efficiently fill space (Fig. 2.21(a)) [166]. In this way, MRO describing the spatial relationship of clusters on a length scale of a few cluster diameters is incorporated into the model [168]. As these clusters are rather irregular and not spherical, their random orientation on the "lattice sites" does not allow the formation of a translational symmetry [169]. The spatial arrangement of the cluster yields interstices (e.g. cluster-octahedral/tetrahedral sites) which may be occupied by different solvent atoms or remain vacant [167]. In recent years, the model was further refined in order to match the experimental results in different glass-forming systems [167, 169, 170].

The results obtained by Sheng et al. suggest that glass-forming liquids contain several types of local, solute-centered coordination polyhedra [87]. It is argued that the different cluster types can be considered as quasi-equivalent as they do not vary in size or coordination number significantly (Fig. 2.21(b)). The moderate variation in coordination number results from the distortion of the representative polyhedra [87, 171, 172]. On the one hand, the formation of quasi-equivalent, solute-centered clusters is driven by the aim to efficiently fill space (topological SRO) and therefore depends on the atomic size ratios. On the other hand, it is affected by the chemical affinities among the elements (chemical SRO) [173] which favors unlike bonds

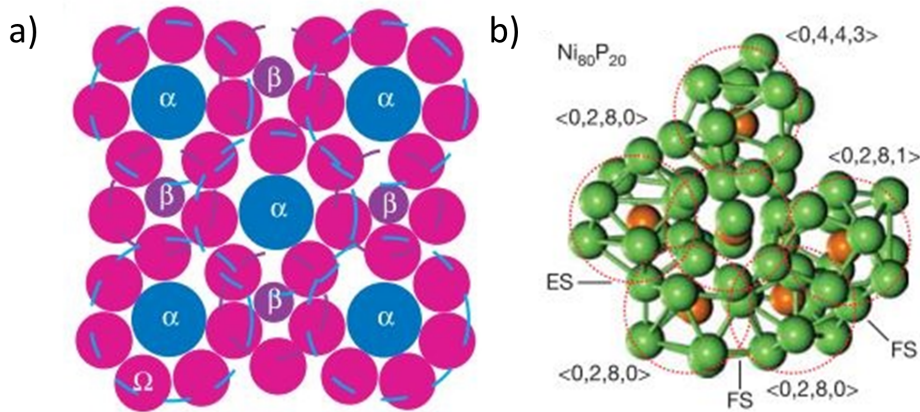


FIGURE 2.21: Short- (clusters) and medium-range order (packing of clusters) in metallic glass-forming liquids. (a) In the efficient cluster packing model solute centered clusters can be arranged in a fcc structure. Depicted is the (100) plane. Figure taken from Ref. [166] (b) Packing of solute-centered, quasi-equivalent clusters in $Ni_{80}P_{20}$. Figure taken from Ref. [87].

resulting in an avoidance of solute-solute bonds (solute-solute avoidance [165]). Moreover, it is derived from simulations that the quasi-equivalent clusters exhibit an icosahedral-like packing. This icosahedral SRO of clusters represents the atomic MRO (spatial relationship between solutes in the center of the clusters) and turned out to be independent of the type of SRO inside the clusters [87]. At a certain solute concentration, solute-solute contacts are inevitable and further types of MRO evolve. At solute concentrations of 20 to 30%, depending on the atomic size ratio, the solute atoms arrange in strings, surrounded by solvent atoms. Such "extended clusters" connect via edge-, vertex- or face sharing, representing a second type of MRO [87]. If the solute concentration is further increased, the number of solute-solute connections enlarges and string- or ring-like solute connections are observed resembling a network which is considered to be the third type of MRO [87]. The formation of string- or ring-like interconnections minimizes the number of like bonds and is therefore the energetically preferred atomic arrangement [87].

According to Sheng et al. [87], the structural features of metallic glass-forming liquids depend on the atomic size ratio, the chemical affinity of the atoms involved, as well as on the solute concentration, and can be summarized as follows:

Short-range order:

- Topological SRO (depends on atomic size ratio).
- Chemical SRO (depends on chemical affinity).

Medium range order:

- Low solute concentration: icosahedral arrangement of clusters.
- Intermediate solute concentration: string-like connection of solutes, formation of interconnected, extended clusters.
- High solute concentration: formation of string- or ring-like solute connections, network-type arrangement of solutes.

The existence of SRO in metallic glasses is confirmed by nanobeam electron diffraction (NBED) experiments [174]. Using NBED Hirata et al. showed that in $Zr_{80}Pt_{20}$ distorted icosahedra are prevalent [172]. Although these clusters are assumed to be quasi-equivalent, the existence of distorted polyhedra or geometrically unfavored motifs (GUMs) are thought to play a pivotal role for the properties of a metallic glass [171]. GUMs are the less stable local environment and respond more readily to thermal or mechanical stress [171]. Computer simulations suggest that regions with a high density of GUMs are "softer" (in terms of the local elastic constant) and contribute to the formation of shear transformation zones [171, 175]. The amount of GUMs can be controlled by the cooling rate at which a metallic glass is produced. Rapidly quenched glasses, which are usually more ductile [176], contain a higher fraction of GUMs [171].

Chapter 3

Materials and Methods

3.1 Sample preparation and analysis

Synthesis of Au-based BMGs

The Au-based BMGs were produced in a single step process. The pure elements (purity > 99.95 wt%) were melted inductively in an Al_2O_3 crucible. The stacking order of the elements in the crucible was (from bottom to top): Pd-Ag-Au-Cu-(Ga, Sn, In, Sb)-Si, which prevents the formation of Pd-Si phases with high melting points. Before heating the elements, the chamber was evacuated to $\sim 5 \times 10^{-3}$ mbar and filled with Ar (purity 99.9999 wt%). The elements were slowly heated to 1473 K and cast into a water-cooled copper mold. The casting process was conducted in an Indutherm MC15 tilt-casting device that was modified to accommodate a water-cooled mold. In order to determine the critical casting thickness of the alloys, samples were cast as plates with a thickness of 0.25 mm and 1 mm or as rods with diameters ranging from 2.5 to 5 mm. Examples of the sample geometry are shown in Fig. 3.1.

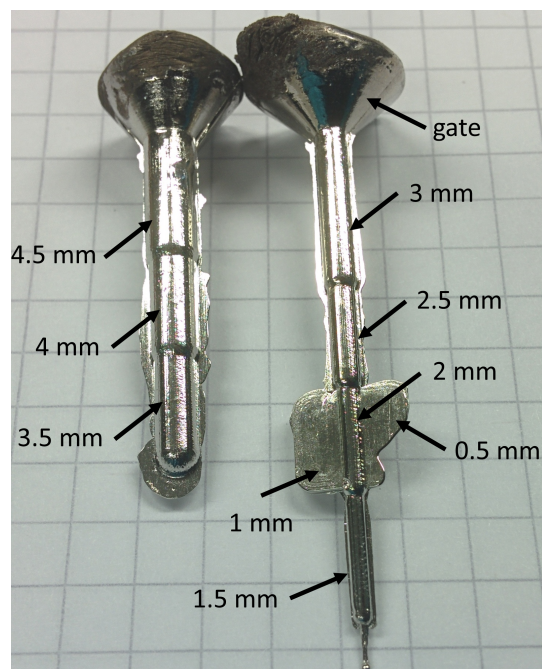


FIGURE 3.1: Tilt-cast samples of $\text{Au}_{49}\text{Ag}_{5.5}\text{Pd}_{2.3}\text{Cu}_{26.9}\text{Si}_{16.3}$ with varying diameter. The arrows indicate the diameter of the rods and the thickness of the plates. For the casting of the 0.25 mm thick plates, a different mold was used. Figure taken from Ref. [177].

Synthesis of Pt/Pd-P-based BMGs

The alloying process described in the following comprises four steps that guarantee a reproducible production of the alloys. For cost reasons the process was perfected on Fe-P- and Ni-P-based alloys [178], however it can be transferred to most of the P-containing alloys. In contrast to the alloying of S-containing alloys, the process is more challenging for P-containing compositions as P may evaporate during the heating process [179]. On the one hand, the evaporation of P changes the overall composition of the alloy and on the other hand, the evaporating P may condense as highly toxic and highly inflammable white P in the cooler regions of the fused silica tube. Therefore, the process is designed to avoid any P losses through evaporation.

In a first step, a pre-alloy is produced from the high purity elements (purity > 99.95 wt%), Pt/Pd, Cu and Ni/Co. The elements are alloyed in an arc-furnace under Ti gettered high purity Ar atmosphere. The pre-alloy is molten several times to ensure a homogeneous distribution of the elements. The final shape of the pre-alloy should be rod-like to fit into a fused silica tube. The second step in the alloying process is depicted in Fig. 3.2 and is itself separated in four process steps. The pre-alloy is placed on top of the red P pieces in a fused silica tube of 1 m length, with an inner diameter of 12 mm and a wall thickness of 1.5 mm (Fig. 3.2(I)). The tube is evacuated

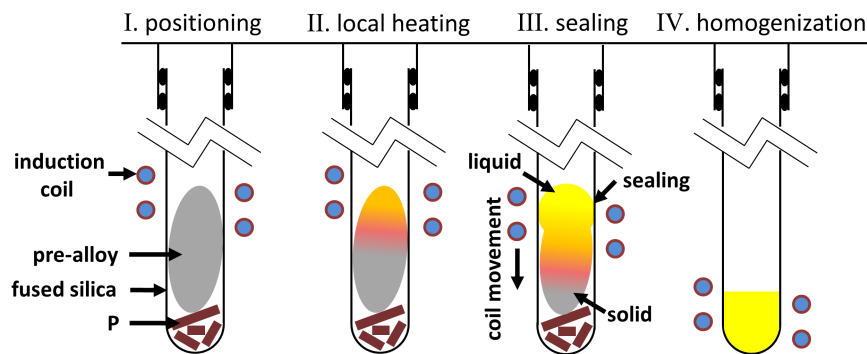


FIGURE 3.2: Alloying procedure of P-containing alloys. (I) The pre-alloy is positioned on top of the red P. (II) An induction coil is used to locally heat the pre-alloy. (III) The upper part of the pre-alloy is molten and seals the fused silica tube before P starts evaporating. (IV) The position of the coil is changed to guarantee a proper intermixing.

to at least 5×10^{-3} mbar and filled with high purity Ar (ambient pressure + 0.1 bar). An induction coil is used to quickly and locally heat the upper part of the pre-alloy (Fig. 3.2(II)). The upper part of the pre-alloy melts and thereby seals the fused silica tube before the thermal conduction in the pre-alloy causes an evaporation of the P (Fig. 3.2(III)). If the fused silica tube is sealed by the liquid metal, evaporating P is consumed. During the exothermic reaction caused by the mixing of the melt and P, the heating power is reduced, and the position of the coil is adjusted as the melt sinks to the bottom of the glass (Fig. 3.2(IV)). The homogenized alloy can subsequently be water quenched. The third step is a fluxing process [180]. The alloy is positioned at the bottom of a 1 m long fused silica tube with an inner diameter of 16 mm and a wall thickness of 1.5 mm. The sample is covered with dehydrated B_2O_3 . Both are heated in Ar atmosphere to 1473 K and held at this temperature for at least 6 h. This process purifies the melt by reducing the amount of heterogeneous nucleation sites (oxides) [101] and thereby increases the GFA of the alloy [98, 102, 180]. The fourth step, the casting process, is identical to that used to produce the Au-based BMGs.

For the calorimetric measurements and the thermomechanical analyses, rods with a diameter of 5 mm and plates with a dimension of $2/3 \times 13 \times 35 \text{ mm}^3$ were cast.

X-ray diffraction analysis

In order to verify the amorphous character of Pt/Pd-P-based samples, X-ray diffraction (XRD) analysis were conducted. Samples were cut from the region adjacent to the gate since these samples experienced the slowest cooling rate due to the liquid metal reservoir with increasing diameter at the gate (see Fig. 3.1). If the amorphous nature of this sample, which was X-rayed in cross-section, is confirmed by the XRD measurements, the entire sample is amorphous as the other parts experienced a higher cooling rate. The XRD analysis were conducted with a PANalytical X'Pert Pro diffractometer using Cu K_α radiation. In the case of the Au-BMG, the rod shaped samples were cut from the center of each section and X-rayed in cross-section. The plate samples were detached from the runner channel, grinded to the center of the plate and subsequently X-rayed.

Scanning electron microscopy

Scanning electron microscopy (SEM) investigations on the Au-based BMGs were conducted with a Zeiss NT Ltd. Sigma VP using an acceleration voltage of 20 kV. The samples were ground and polished until a polish with 1 μm diamond paste. After the polishing, the samples were stored in a freezer at 255 K, which prevented them from tarnishing [181], guaranteeing that the subsequent SEM investigations are performed on as-prepared samples.

Sample preparation using a focused ion beam

Focused ion beam (FIB) cuts and subsequent SEM investigations of the corroded surfaces of the Au-based BMGs were performed with a Zeiss Auriga 60. The Ga-ion FIB cuts were prepared at an acceleration voltage of 30 kV and the milling current was gradually reduced from 21 nA to 1 nA and in one case to 240 pA. The low milling currents at the end of the preparation sequence were used to achieve a smooth cutting. Hence for the thinnest corrosion layer, the smaller milling current of 240 pA was applied for the best milling quality. Subsequently, the FIB cuts were investigated by SEM in order to document the corrosion attack on the surface. Backscattered electron images were taken at an acceleration voltage of 2 kV. It should be noted that the ion beam milling may induce crystallization in the amorphous samples [182, 183], however this effect does not hamper the image acquisition for corrosion attack evaluation.

3.2 Corrosion tests and color measurements

Tests in artificial saliva were carried out according to DIN EN ISO 10271. The samples were immersed periodically into the testing solution of a 1 molar sodium sulphide aqueous solution. Details of the experimental setup can be found in Ref. [184]. The element release into the test solution was analyzed after seven days at 310 K using Inductively Coupled Plasma Optical Emission Spectroscopy (ICO-OES).

Color measurements were performed with a Konika Minolta CM5 spectrophotometer according to DIN5033. The Yellowness Index (YI) is calculated from the standard

color values X, Y, Z according to

$$YI = 100 \frac{1.28X - 1.06Z}{Y}, \quad (3.1)$$

and describes the deviation from a perfect white color to a yellowish brown. It is used to evaluate the color of gold alloys and divides them into four groups, premium white (<19), standard white (19-24.5), off-white (24.5-32) and non-white (>32) [185].

3.3 Measurements of the thermophysical properties

3.3.1 Calorimetric measurements

In calorimetric measurements, the heat transfer resulting from chemical reaction or physical changes is determined. Changes in heat, ΔQ , occur due to changes in temperature, ΔT , caused by the chemical or physical phenomena. The connection between ΔQ and ΔT is given by

$$\Delta Q = mc\Delta T, \quad (3.2)$$

where m is the mass of the sample and c is the specific heat capacity in $\text{J kg}^{-1} \text{K}^{-1}$. In the differential thermal analysis (DTA), the sample and a reference (usually an empty crucibles) are placed in a furnace and are subject to the same temperature protocol. The measurement signal, the temperature differences between the sample and the reference $\Delta T_{SR} (= T_S - T_R)$, is recorded by thermocouples beneath each crucible.

The calorimetric measurements were performed with a power-compensated Perkin Elmer DSC8500 (DSC = differential scanning calorimeter). In contrast to the classical DTA, the device consists of two identical micro furnaces made of a Pt-Ir alloy [186]. Each furnace possesses its own temperature sensor and heating resistor. One furnace serves as reference containing an empty pan and the other hosts the sample. Both furnaces are subject to an identical temperature protocol. In the case of exothermic or endothermic reactions, occurring in the sample, the device regulates the heating power in order to maintain the desired heating rate, which is equatable to a vanishing temperature difference between the reference and the sample furnace ($\Delta T_{SR} = 0$). The heating power difference ΔP between the sample and reference furnace is proportional to the amount of heat released or consumed by the sample.

The difference in the measurement principles of DTA and DSC can be summarized as

$$\underbrace{\Delta P}_{\text{DSC}} \sim \underbrace{\Delta Q}_{\text{DTA}} \sim \Delta T. \quad (3.3)$$

As the experiments are conducted at a constant pressure p , the change in enthalpy can be written as

$$\Delta H = \Delta U + p\Delta V, \quad (3.4)$$

where ΔU and ΔV are the changes in internal energy and volume, respectively. Using the first law of thermodynamics

$$\Delta U = \Delta Q - p\Delta V, \quad (3.5)$$

Eq. 3.4 yields

$$\Delta H = \Delta Q. \quad (3.6)$$

As the measurement signal in the DSC is the heat flow $\dot{Q} = \frac{dQ}{dt}$, the enthalpy change of a reaction between the temperatures T_1 and T_2 can be determined by

$$\Delta H = K \int_{T_1}^{T_2} \frac{\dot{Q}}{q_H} dT, \quad (3.7)$$

where q_H is the heating rate and K is a calibration constant. The DSC was calibrated for each heating rate and crucible material using the melting transition of In, Zn and Al (for C crucibles). All measurements were conducted under a constant flow of high purity Ar-gas (99.9999 wt%) at 20 ml min^{-1} .

Detection of the crystallization enthalpy

The crystallization enthalpy ΔH_x is determined from the integration of the exothermic crystallization peak. To detect the crystallization event, amorphous samples were heated at a constant rate to the solidus temperature. A subsequent scan of the fully crystalline sample serves as baseline for the integration process. As shown in Fig. 3.3 for a DSC and a DTA measurement, the heat flow curves of the first and second heating coincide at low temperatures due to the similar C_p of the glass and the crystal. The curves meet at high temperature as soon as the same structural state is reached. ΔH_x increases with increasing heating rate since crystallization occurs at a higher enthalpic state of the liquid.

Specific heat capacity

The specific heat capacity of the glassy, crystalline, supercooled liquid and equilibrium liquid state was determined using a stepwise heating protocol. In the case of an empty reference pan, the heat flow of a sample in a DSC measurement is given by the differential form of Eq. 3.2,

$$\frac{dQ}{dt}_{\text{sample}} = m_{\text{sample}} c_{\text{sample}} \frac{dT}{dt}. \quad (3.8)$$

In order to obtain accurate C_p values, the additional heat flow \dot{Q}_0 , resulting from the two crucibles, needs to be taken into account. \dot{Q}_0 is subtracted from the measured heat flow yielding

$$\dot{Q}_{\text{sample}} - \dot{Q}_0 = m_{\text{sample}} c_{\text{sample}} \dot{T}. \quad (3.9)$$

The heating rate dependence of the heat flow signal is eliminated through the measurement of a standard material. As standard material, a sapphire disk with a diameter of 5 mm is used. The heat flow of the standard material is given by

$$\dot{Q}_{\text{sapphire}} - \dot{Q}_0 = m_{\text{sapphire}} c_{\text{sapphire}} \dot{T}. \quad (3.10)$$

By combining Eq. 3.9 and 3.10 the following expression is obtained:

$$\frac{\dot{Q}_{\text{sample}} - \dot{Q}_0}{\dot{Q}_{\text{sapphire}} - \dot{Q}_0} = \frac{m_{\text{sample}} c_{\text{sample}}}{m_{\text{sapphire}} c_{\text{sapphire}}}. \quad (3.11)$$

This equation can be solved for the heat capacity of the sample

$$c_{\text{sample}} = \frac{(\dot{Q}_{\text{sample}} - \dot{Q}_0) m_{\text{sapphire}} c_{\text{sapphire}}}{(\dot{Q}_{\text{sapphire}} - \dot{Q}_0) m_{\text{sample}}}. \quad (3.12)$$

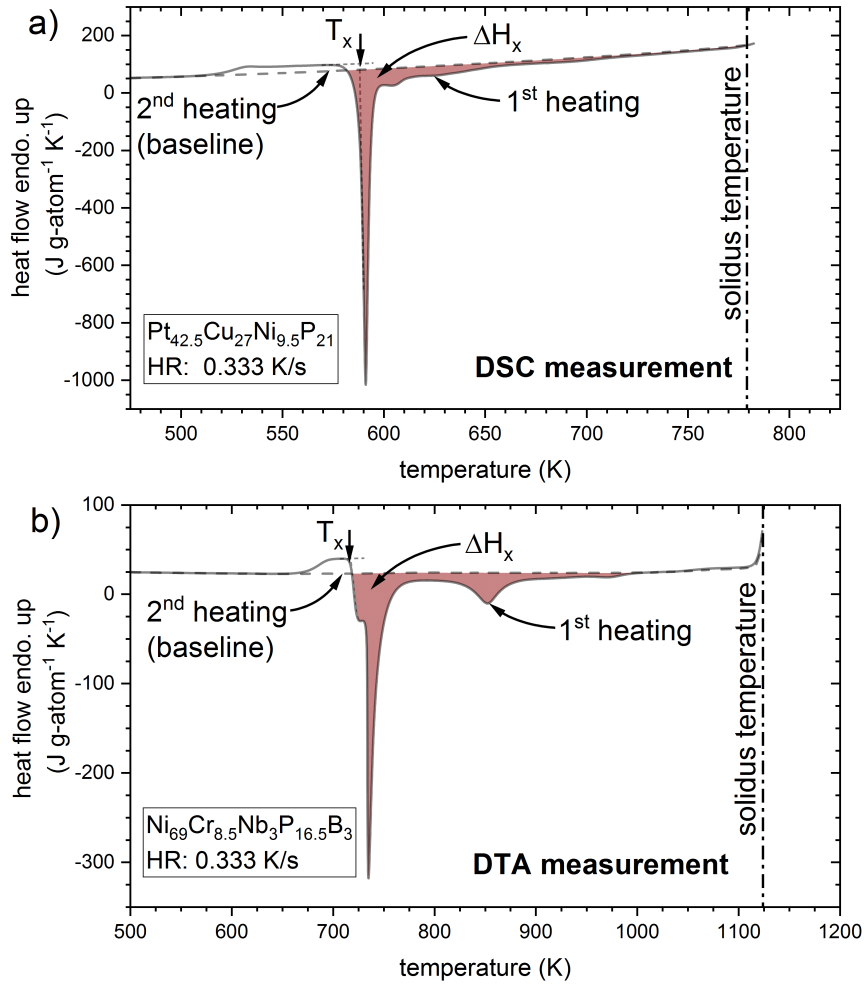


FIGURE 3.3: Determination of the crystallization enthalpy from a thermogram. The amorphous and crystalline sample is heated to the solidus temperature. The curve of the crystalline sample is used as a baseline for the integration process. (a) DSC curves of $\text{Pt}_{42.5}\text{Cu}_{27}\text{Ni}_{9.5}\text{P}_{21}$. (b) DTA curves of $\text{Ni}_{69}\text{Cr}_{8.5}\text{Nb}_3\text{P}_{16.5}\text{B}_3$. The red area corresponds to the crystallization enthalpy ΔH_x .

Equation 3.12 is rewritten to obtain the molar isobaric heat capacity [65]

$$C_{p,\text{sample}}(T) = \frac{(\dot{Q}_{\text{sample}} - \dot{Q}_0)m_{\text{sapphire}}C_{p,\text{sapphire}}(T)\mu_{\text{sample}}}{(\dot{Q}_{\text{sapphire}} - \dot{Q}_0)m_{\text{sample}}\mu_{\text{sapphire}}}. \quad (3.13)$$

In the stepwise heating protocol, the samples were heated in 10 K steps, followed by an isothermal holding of 120 s in order to equilibrate the signal. The heat flow of a single temperature step is

$$\dot{Q} = \dot{Q}_{\dot{T} \neq 0} - \dot{Q}_{\dot{T} = 0}, \quad (3.14)$$

where $\dot{Q}_{\dot{T} \neq 0}$ corresponds to the power necessary to heat the sample with a constant rate and $\dot{Q}_{\dot{T} = 0}$ is the power needed to maintain a constant temperature [65]. The same temperature protocol was applied to empty crucibles, the sapphire standard and the sample.

T_g-shift measurements

The glass transition temperature measured upon heating an amorphous sample depends on the cooling rate during casting, q_c , and on the used heating rate q_h . The dependence of T_g on the thermal history results from its connection to the temperature dependent intrinsic relaxation time τ_α of the liquid. The temperature dependence of τ_α , represented by the kinetic fragility of the liquid, can be determined from the time needed to pass through the glass transition region, the transition time τ_{trans} , given by

$$\tau_{trans} = \Delta T / q_h = \frac{T_g^{end} - T_g^{onset}}{q_h}, \quad (3.15)$$

where T_g^{onset} and T_g^{end} are the onset and end of the glass transition. τ_{trans} is equal to the total relaxation time obtained in isothermal viscosity measurements [127]. Each τ_{trans} is attributed to a single fictive temperature $T_{fictive}$, that coincides with T_g^{onset} if the heating rate of the sample is identical to the rate at which it was vitrified ($q_h = q_c$) [187]. In order to fulfill the condition $q_h = q_c$, the as-cast samples are subject to a pre-treatment as depicted in Fig. 3.4. The sample is heated at a certain rate to the

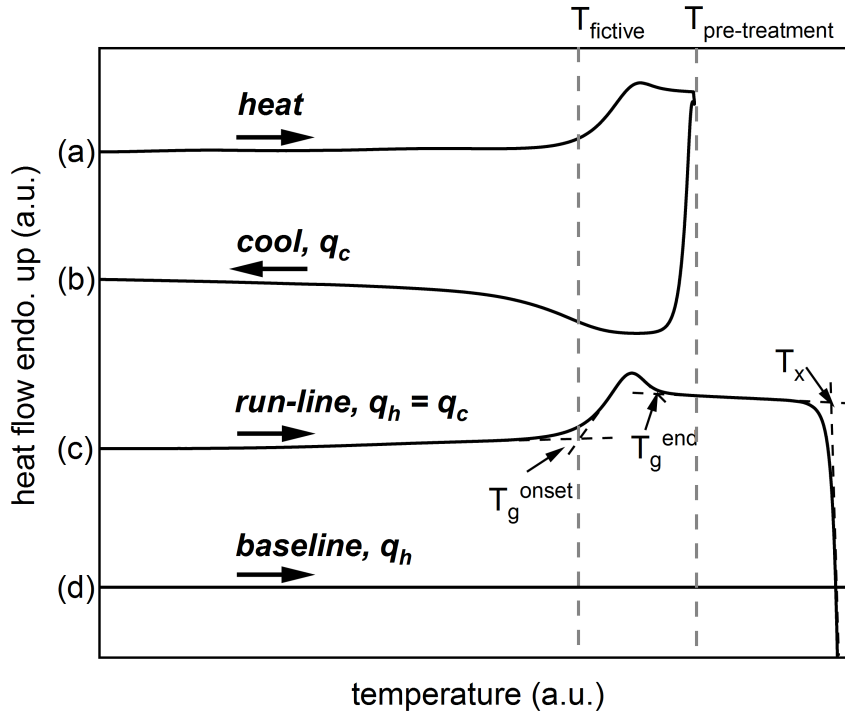


FIGURE 3.4: DSC heat flow curves of a T_g -shift measurement. (a) The sample is heated to the supercooled liquid region and cooled at a defined cooling rate q_c below the glass transition (b). In the subsequent heating protocol (c), the same rate as used during cooling is applied ($q_h = q_c$) and the sample is heated past the crystallization temperature T_x . The crystalline sample is heated with q_c again in order to obtain the baseline (d). After subtraction of the baseline, T_g^{onset} and T_g^{end} are determined on the run-line scan. T_g^{onset} coincides with $T_{fictive}$, which is located at the inflection point of the glass transition upon cooling [187]. Figure in the style of Ref. [188].

supercooled liquid region and cooled at the same rate as used in the subsequent heating protocol. In this way, T_g^{onset} coincides with $T_{fictive}$, which is located at the

inflection point of the glass transition upon cooling [187]. Evenson et al. showed that a correct description of the kinetic fragility is obtained, if the condition $q_h = q_c$ is kept for each rate [188].

Crystallization experiments

The crystallization experiments were conducted in a power-compensated Perkin Elmer DSC8500 equipped with an intracooler system that guarantees high cooling rates. The measurement procedure for the determination of the isothermal TTT diagram and the continuous heating/cooling transformation (CHT/CCT) diagram is schematically shown in Fig. 3.5. The lower portion of the isothermal and the continuous transformation diagram was measured in Al pans. In the case of the isothermal experiments, as-cast samples were heated at 2 K s^{-1} to the desired temperature and held isothermally. As the crystallization enthalpy decreases with decreasing annealing temperature and is released over a longer period of time, the sample mass is increased with decreasing annealing temperatures in order to improve the signal to noise ratio. At the lowest temperature, a sample mass of 260 mg and 410 mg for the $\text{Pt}_{42.5}\text{Cu}_{27}\text{Ni}_{9.5}\text{P}_{21}$ and $\text{Pt}_{60}\text{Cu}_{16}\text{Co}_2\text{P}_{22}$ alloy compositions was used. The crystallization onsets upon heating glassy samples at various rates were obtained from the T_g -shift measurements (see. T_x in Fig. 3.4 curve (c)). In the case of the high temperature crystallization experiments, the measurements were conducted in C crucibles. The samples with a mass of 31 mg for $\text{Pt}_{42.5}\text{Cu}_{27}\text{Ni}_{9.5}\text{P}_{21}$ and 56 mg for $\text{Pt}_{60}\text{Cu}_{16}\text{Co}_2\text{P}_{22}$ were covered with dehydrated B_2O_3 and heated to 973 K. After a holding time of 120 s, the samples were cooled to the isothermal holding temperature or cooled past the crystallization event (Fig. 3.5, blue curves). The obtained heat flow curves are shown in Chapter 5.

3.3.2 Viscosity measurements

The equilibrium viscosities in vicinity of the glass transition were determined in three-point beam bending (3PBB) experiments using a NETZSCH TMA 402 thermomechanical analyzer. Samples with rectangular cross-sections between 0.6 and 3 mm^2 and a length of 13 mm were cut from tilt-cast plates. The specimens were heated at a rate of 0.333 K s^{-1} to the desired temperature close to the glass transition and held isothermally. The viscosity of the deflecting beams was determined as

$$\eta = -\frac{gL^3}{144I_{cs}v} \left(M + \frac{\rho AL}{1.6} \right) \quad (3.16)$$

where g is the gravitational constant, I_{cs} is the cross-section moment of inertia, v is the mid-point deflection rate, M is the applied load, ρ is the density of the glass and A is the cross-sectional area and L is the length of the support span [189]. The cross-section moment of inertia with respect to the neutral fiber is $I_{cs} = bh^3/12$, where b is the width and h is the thickness of the beam. In addition to isothermal annealing, viscosity was measured with a constant heating rate until the deflection limit was reached.

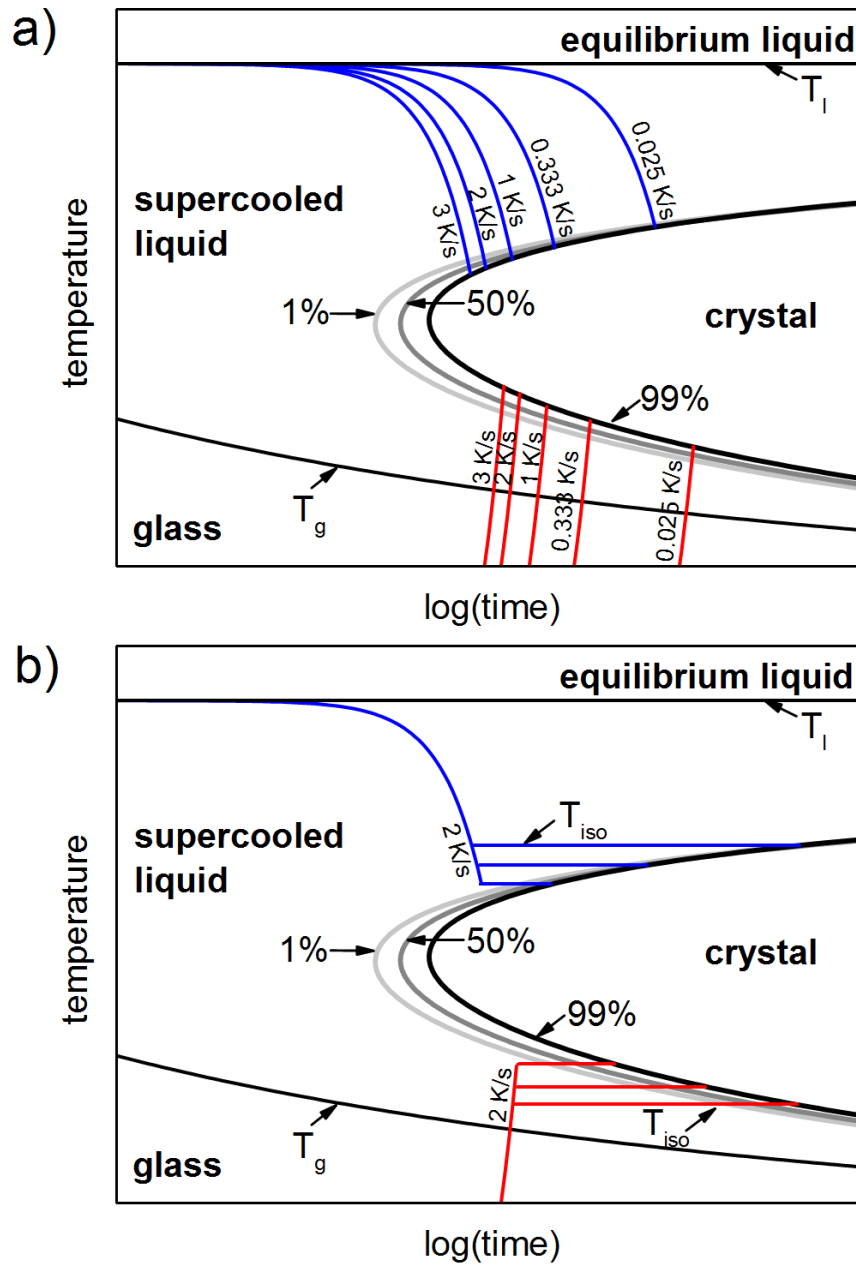


FIGURE 3.5: Measurement of (a) continuous-cooling/heating-transformation (CCT/CHT) and (b) time-temperature-transformation (TTT) diagrams.

3.4 In-situ synchrotron X-ray scattering measurements

This section is based on the book "*Underneath the Bragg Peaks*" by T. Egami and S. J. L. Billinge (Ref. [190]), containing the theoretical background of the total scattering method as well as practical instructions on the data analysis and correction.

Theoretical background of total X-ray scattering experiments

The total intensity of the scattered X-rays, I_T , contains different contributions:

$$I_T = I_C + I_{IC} + I_{MC} + I_{BG}, \quad (3.17)$$

where I_C is the coherent scattering intensity, I_{IC} the incoherent scattering intensity, I_{MC} the multiple-scattering intensity, and I_{BG} the background intensity. I_C comprises the elastic Bragg scattering (the global structure), the elastic diffuse scattering (the static local structure) and the inelastic thermal diffuse scattering, resulting from the thermal vibration of the atoms. Thereby the term elastic refers to a scattering process during which no energy between the scattered wave and the system is exchanged, whereas in the case of an inelastic scattering event, energy is transferred. As the coherently scattered waves possess a definite phase relationship, they interfere constructively and destructively and therefore contain the information on the structure and the lattice dynamics. The experimentally measured I_C is related to the scattering cross-section, $d\sigma_C/d\Omega$, describing the probability that a photon is scattered by a given volume element in a given direction, if corrected by an absorption (A), polarization (P) and normalization factor (C):

$$I_C = APC \frac{d\sigma_C}{d\Omega}. \quad (3.18)$$

The corrected, coherently scattered intensity is connected to the square of the absolute value of the wave amplitude (the sample scattering amplitude $\Psi(Q)$) and is expressed as

$$I_C(Q) = \frac{d\sigma_C(Q)}{d\Omega} = \frac{\langle f(Q) \rangle^2}{N} |\Psi(Q)|^2, \quad (3.19)$$

where Q is the diffraction vector, and $\langle f(Q) \rangle$ is the atomic form factor averaged over all the atoms N in the sample. Q is defined as

$$Q = k_{init} - k_{final}, \quad (3.20)$$

where k_{init} ($|k_{init}| = 2\pi/\lambda_{init}$) is the wavevector of the incoming, and k_{final} ($|k_{final}| = 2\pi/\lambda_{final}$) that of the scattered beam. In the case of elastic scattering, the wavelength of the incoming and scattered beam are equal and the magnitude of Q can be expressed as

$$|Q| = \frac{4\pi \sin(2\theta/2)}{\lambda}. \quad (3.21)$$

$\Psi(Q)$ is the Fourier transform of the atomic position R_v and is given by

$$\Psi(Q) = \frac{1}{\langle f(Q) \rangle} \sum_v f_v(Q) \exp(iQR_v), \quad (3.22)$$

where $f_v(Q)$ is the atomic form factor of the v -th atom. From the corrected, coherently scattered intensity $I_C(Q)$, containing Bragg and diffuse intensity, the total-scattering structure function is obtained:

$$S(Q) = 1 + \frac{I_C(Q) - \langle f(Q)^2 \rangle}{\langle f(Q) \rangle^2}. \quad (3.23)$$

$S(Q)$ converges to unity at large Q and for an isotropic scattering, as in liquids and glasses, it solely depends on the magnitude of Q . $S(Q)$ contains all the structural information and in the case of multicomponent alloy compositions, it is composed of $n(n+1)/2$ partial scattering structure functions [191],

$$S(Q) = \sum_{i \leq j} w_{ij} S_{ij}(Q), \quad (3.24)$$

where w_{ij} is the weighting factor expressed as

$$w_{ij} = \frac{c_i c_j f_i(Q) f_j(Q)}{\langle f(Q) \rangle^2}. \quad (3.25)$$

$c_{i,j}$ are given by $N_{i,j}/N$, where $N_{i,j}$ is the number of i - and j -atoms respectively. The Faber-Ziman partial structure functions are the structure functions that would be measured if the entire sample was made up only of that partial. For the Au, Pt, Pd-based liquids, the large $f(Q)$ of the noble metals and their high atomic concentration lead to the fact that the total-scattering structure function is mainly dominated by the noble metal partial structure functions. Figure 3.6(a) shows the atomic form factor¹ of the common constituents of noble metal based BMGs. The weighting factors (Eq. 3.25) for the dominant Pt partial structure functions of the Pt_{42.5}Cu₂₇Ni_{9.5}P₂₁ alloy composition is depicted in Fig. 3.6(b).

The Fourier transform of the total-scattering structure function yields the reduced pair distribution function (PDF),

$$\begin{aligned} G(r) &= 4\pi r [\rho(r) - \rho_0] \\ &= 4\pi r \rho_0 [g(r) - 1] \\ &= \frac{2}{\pi} \int_0^\infty Q [S(Q) - 1] \sin(Qr) dQ, \end{aligned} \quad (3.26)$$

where ρ_0 is the average atomic number density, $\rho(r)$ the atom-pair density function, $g(r)$ the atomic pair distribution function and r is the distance to the reference atom. As can be seen from Eq. 3.26, $\rho(r)$, $g(r)$ and $G(r)$ are related functions and contain the same structural information. The PDF exhibits peaks at certain r -values, giving the probability of finding another atom in the distance r from the reference atom averaged over all pairs of atoms in the sample. In other words, the functions describe the deviation from the average density and yield a histogram of all atom-atom distances in the solid. The usage of $G(r)$ instead of $\rho(r)$ or $g(r)$ results in two advantage. On the one hand, $G(r)$ is directly obtained from the Fourier transform of $S(Q)$ and does not require the assumption of a value for ρ_0 . On the other hand, the uncertainties on $G(r)$ are constant with r , whereas those on $\rho(r)$ or $g(r)$ fall off with $1/r$.

¹The atomic form factor of the different elements are calculated as $f(Q) = \sum_{i=1}^4 a_i \exp(-b_i(\frac{Q}{4\pi})^2) + c$. Values for a_i , b_i and c are taken from Ref. [192].

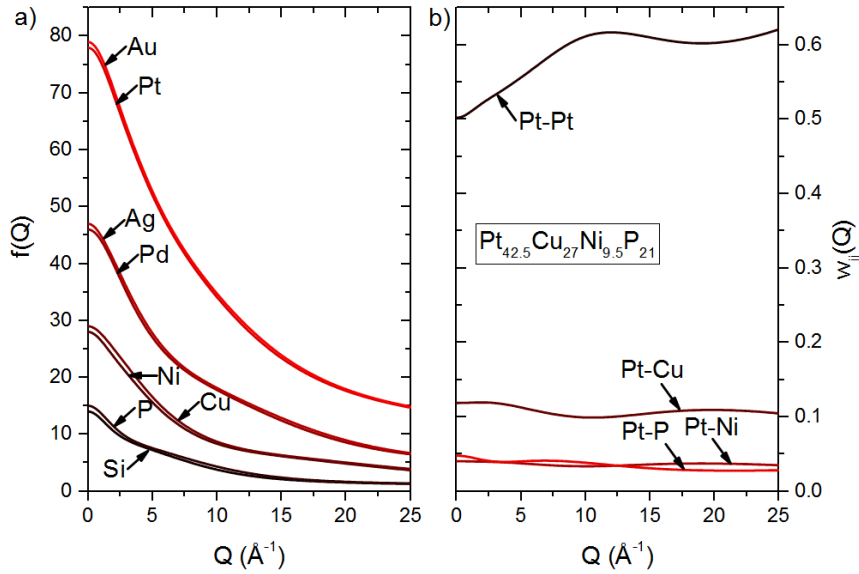


FIGURE 3.6: (a) Atomic form factor of elements that are found in noble metal based BMGs. (b) Weighting factor for the Pt partial structure function of the $\text{Pt}_{42.5}\text{Cu}_{27}\text{Ni}_{9.5}\text{P}_{21}$ alloy composition. Values for calculating $f(Q)$ and $w_{ij}(Q)$ are taken from Ref. [192].

Experimental setup and data analysis

The in-situ X-ray scattering experiments were carried out at the high resolution beamline P02.1 at PETRA III at the Deutsche Elektronen Synchrotron (DESY) in Hamburg [193]. A wavelength of 0.207 \AA (60 keV) and a beam size of $0.8 \times 0.8 \text{ mm}^2$ was used. The samples were heated and cooled at 0.333 K s^{-1} in a Linkam THMS 600 furnace and in a custom build ceramic heater. In the Linkam furnace, plate shaped samples ($0.2 \times 3 \times 13 \text{ mm}^3$), cut from tilt-cast plates ($3 \times 3 \times 35 \text{ mm}^3$), were used. The samples used in the ceramic heater were rods with a diameter of approximately 1.1 mm, cast into a water-cooled copper mold in a suction casting device as described in Ref. [194]. In order to fit into the SiO_2 capillaries with an inner diameter of 1 mm and a wall thickness of 0.1 mm, the diameter of the cast rods was reduced by grinding and they were cut to a length of $\sim 3 \text{ mm}$. In both cases, the samples were subject to a constant flow of high-purity Ar during the heating and cooling protocol. The measurements were carried out in transmission mode using a Perkin Elmer XRD1621 CsI bonded amorphous silicon detector ($2048 \text{ pixels} \times 2048 \text{ pixels}$). The dark-subtracted, two-dimensional X-ray diffraction pattern were integrated using the Fit2D data analysis software [195]. The data was further processed using the PDFgetX2 software [196]. The background² was measured at room temperature, assumed to be constant upon heating and cooling and subtracted from the integrated intensity data. The data was corrected for sample absorption, polarization and multiple scattering. The total-scattering structure function $S(Q)$ was calculated according to Eq. 3.23. $G(r)$ was obtained from Fourier transforming $S(Q)$, using a Q_{max} of $\sim 10.5 \text{ \AA}^{-1}$ (Linkam furnace) and $\sim 14.5 \text{ \AA}^{-1}$ (ceramic furnace). $S(Q)$ was corrected by determining the parameters for fluorescence and Compton scattering using an algorithm in PDFgetX2 that optimizes $G(r)$ in the low- r range. According to Eq. 3.26, $G(r)$ should behave like $-4\pi\rho_0r$ as the probability to find an atom below the nearest-neighbor peak is 0 ($g(r) \rightarrow 0$). This optimization process allows $S(Q)$ to

²Linkam furnace: empty furnace, ceramic heater: furnace with empty capillary.

oscillate around one, as it should approach 1 for $Q \rightarrow \infty$. The results by Peterson et al. show, that the low $G(r)$ optimization is a robust method, yielding the best possible PDF from a given data set [197]. The peak position of $S(Q)$ and $G(r)$ were determined from a cubic spline interpolation of the measured data points [85] using OriginPro9.1 and OriginPro2016. The uncertainty in determining the peak position using the cubic spline interpolation was estimated by Wei et al. to be 0.5% [198].

Chapter 4

Development of a gold based bulk metallic glass with improved tarnishing resistance

In 2005, Schroers et al. developed the Au-based bulk glass-forming alloy $\text{Au}_{49}\text{Ag}_{5.5}\text{Pd}_{2.3}\text{Cu}_{26.9}\text{Si}_{16.3}$ (termed in the following "mother alloy"), containing 75% weight percentage of Au (18-karat) [199]. This alloy is based on the ternary Au-Cu-Si system, possesses a d_c of 5 mm and a hardness of 350-360 HV [199, 200] exceeding that of conventional, crystalline 18-karat Au alloys significantly [34, 201]. In combination with the premium white color in the as-cast state [184], the high hardness is highly desirable for jewelry items. However, the premium white color is not stable and turns with time into an unattractive yellowish brown [181, 184]. The color change is abnormally fast, even at room temperature. The surface tarnishing further accelerates in contact with saliva or sweat [34, 181, 184, 200, 202] which makes the alloy inappropriate for jewelry or dentistry applications. The color change of an amorphous ring when worn for 52 days is shown in Fig. 4.1. The fast color change



FIGURE 4.1: Color change of an amorphous ring with the composition $\text{Au}_{49}\text{Ag}_{5.5}\text{Pd}_{2.3}\text{Cu}_{26.9}\text{Si}_{16.3}$ when worn for 52 days. Figure taken from Ref. [203].

can be traced back to the partitioning of Au and Cu and the formation of CuO_2 or Cu_2S products on the surface [184]. In a standardized corrosion test, the corrosion products dissolve into the test solution which can subsequently be analyzed. The amount of Cu-ions in the solution is used as a measure of the corrosion attack. Underneath the sample surface, the growth of amorphous SiO_2 in a dense branching morphology, resulting from the internal oxidation of the amorphous metallic matrix, is detected [184]. The processes occurring at and beneath the metal surface are schematically shown in Fig. 4.2. Eisenbart et al. observed that, if the Cu content is reduced, the tarnishing rate of $\text{Au}_{49}\text{Ag}_{5.5}\text{Pd}_{2.3}\text{Cu}_{26.9}\text{Si}_{16.3}$ changes from parabolic to a pure logarithmic which is characteristic for passivating oxidation [184]. This

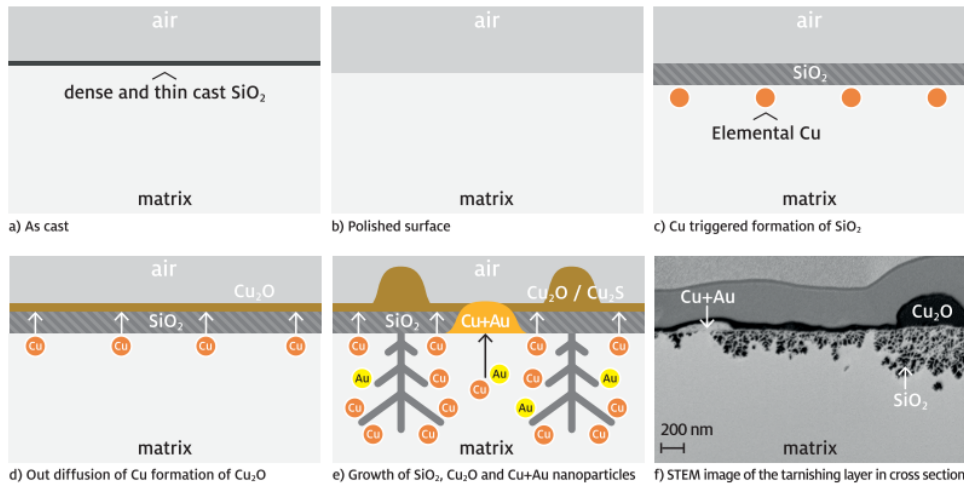


FIGURE 4.2: Tarnishing mechanism at the surface of the $\text{Au}_{49}\text{Ag}_{5.5}\text{Pd}_{2.3}\text{Cu}_{26.9}\text{Si}_{16.3}$ bulk metallic glass. (a) If the sample is vitrified in an oxygen containing atmosphere, the samples exhibits a thin and dense SiO_2 layer acting as diffusion barrier which minimizes the tarnishing process. After polishing, the native SiO_2 is removed (b) and the partitioning of elemental Cu triggers the formation of a new SiO_2 layer (c). (d) Cu diffuses through the SiO_2 to the surface and forms Cu_2O . (e) The Cu_2O is partially reduced by Si leading to the inwards growth of amorphous SiO_2 in a dense branching morphology. (f) STEM image of a cross section of tarnished $\text{Au}_{49}\text{Ag}_{5.5}\text{Pd}_{2.3}\text{Cu}_{26.9}\text{Si}_{16.3}$. Figure taken from Ref. [34].

indicates that a significant change of the Au/Si or the Cu/Si ratio might reduce the tarnishing rate to an acceptable value [184].

In general, the corrosion or oxidation resistance and the GFA of a glass-forming alloy are independent material properties. The addition of elements that improve the resistance of an alloy against external agents [34, 204–206] do not necessarily have a positive effect on the GFA [34, 204]. In the case of a jewelry alloy, constituents like Cr, Co or Ni are undesired as they are known to cause skin irritations and allergic responses [207].

The glass-forming region (GFR) in the ternary Au-Cu-Si system is located at an almost constant Si content along the eutectic trough [14, 208]. The GFR is schematically depicted in Fig. 4.3 and is characterized by low nucleation temperatures for crystallization upon solidification [209]. The maximum achievable undercooling at a fixed cooling rate depends, as discussed in Chapter 2.4, on the driving force, the atomic mobility and the interfacial energy. In continuous cooling experiments performed by Ding et al., the lowest nucleation temperatures are found at the transition point from the diamond cubic primary Si-phase to the fcc primary Au-phase [209]. It is observed that the tarnishing rate of the alloys in the GFR decrease with increasing Au content [184]. However, this simultaneously decreases T_g to temperatures far below 373 K [208], limiting their potential for commercialization.

The aim of the alloy development is the modification of the mother alloy in order to improve its tarnishing resistance and simultaneously maintain its ability to form a BMG.

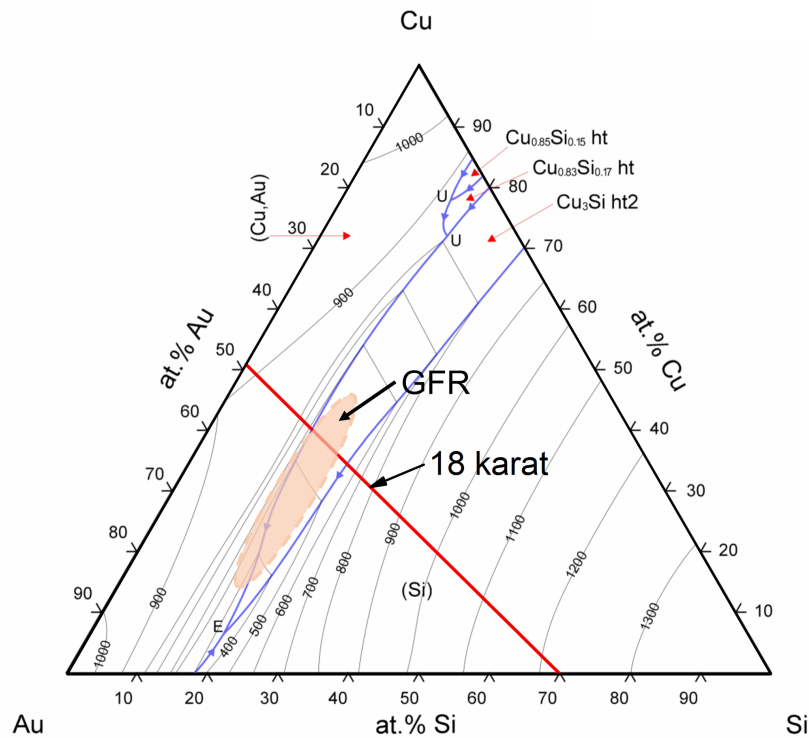


FIGURE 4.3: Liquidus projection of the Au-Cu-Si phase diagram. The glass-forming region (GFR) is located along the Au-Cu axis at an almost constant Si content. The solid, red line represents the 18-karat border, below which the alloys possess a Au content of at least 75 wt%. Figure taken from Ref. [210]. The unmodified phase diagram can be found in Ref. [211].

4.1 Alloy development

In order to improve the tarnishing resistance, the content of disadvantageous elements needs to be reduced. Earlier corrosion studies identified Cu and Si as the elements primary involved in the tarnishing process [184]. At the same time the Au content should not fall below 75 wt% for commercialization. The elements that are assumed to be topological equivalent to Cu (Fe, Co, Ni) according to the ECP model are inappropriate due to a significant reduction of the GFA or the risk of allergic responses [34].

In a first step Ga ($r_{\text{Ga}}=134$ pm [170]), which is not topologically equivalent to Cu ($r_{\text{Cu}}=126$ pm [170]), is chosen as potential substitute. In order to evaluate the effect on the GFA, 1/8 and 1/4 of the Cu in the mother alloy is substituted by Ga. This can be expressed as $\text{Au}_{49}\text{Ag}_{5.5}\text{Pd}_{2.3}\text{Cu}_{26.9-x}\text{M}_x\text{Si}_{16.3}$, where M represents the element substituting Cu and x its amount in atomic percent. Figure 4.4(a) and (b) show the XRD measurements of samples containing $x=3.4$ and $x=6.7$ at%. The samples with $x=3.4$ at% feature amorphous XRD patterns whereas the pattern of the 1 mm and 3 mm sample with $x=6.7$ at% suggest the presence of a small portion of crystals. The XRD measurements indicate that the increasing substitution of Cu by Ga reduces the GFA. The backscattered electron (BSE) images of the 1 mm and 3 mm of $\text{Au}_{49}\text{Ag}_{5.5}\text{Pd}_{2.3}\text{Cu}_{20.2}\text{Ga}_{6.7}\text{Si}_{16.3}$, depicted in Fig. 4.4(c) and (d), reveal the presence of a crystalline phase. This phase appears black in the BSE images indicating a much lower

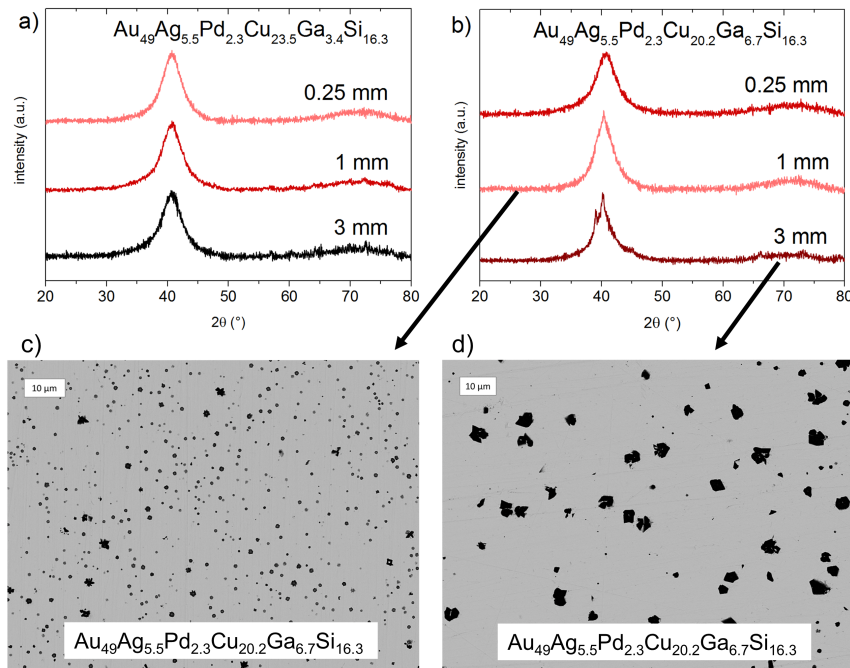


FIGURE 4.4: XRD diffraction measurements of samples with varying sample diameter a) $\text{Au}_{49}\text{Ag}_{5.5}\text{Pd}_{2.3}\text{Cu}_{23.5}\text{Ga}_{3.4}\text{Si}_{16.3}$ b) $\text{Au}_{49}\text{Ag}_{5.5}\text{Pd}_{2.3}\text{Cu}_{20.2}\text{Ga}_{6.7}\text{Si}_{16.3}$. (c) and (d) are backscattered electron images showing the Si primary phase (black) in $\text{Au}_{49}\text{Ag}_{5.5}\text{Pd}_{2.3}\text{Cu}_{20.2}\text{Ga}_{6.7}\text{Si}_{16.3}$. (c) shows a sample with 1 mm (d) a sample with 3 mm diameter. Larger crystals are formed during slower cooling. Figure taken from Ref. [210].

average atomic number than that of the adjacent amorphous matrix. Upon increasing the sample thickness from 1 mm to 3 mm, which corresponds to a reduction of the cooling rate, the crystals grow from approximately 1-5 μm to 5-10 μm . Although a crystalline fraction is formed, the remaining liquid vitrifies. The EDX analysis on the largest crystals reveal a very high concentration of Si and a small amount of the other constituents which can probably be attributed to an interaction of the electron beam with the surrounding material. Based on the neglectable solubility of the other alloying elements in Si, it can be concluded that (almost) pure Si is the primary precipitating phase. Moreover, it is observed that the substitution of Cu by Ga changes the appearance of the melting peak from (near-)eutectic to off-eutectic. This is derived from the melting curves shown in Fig. 4.5. The modification of the mother alloy shifts T_l from 661 K for $x=0$ at% to 861 K for $x=6.7$ at% due to the formation of a broad, endothermic melting shoulder. In combination with the observed nucleation of the Si primary crystals, the melting curves suggest that the substitution of Cu by Ga facilitates the formation of Si crystals as the alloy needs to pass a broad two phase region (Si+liquid) upon quenching. Reducing the Si content to 13.3 at%¹ for $x=6.7$ at% lowers T_l to 679 K. Additionally, the GFA is improved again as can be seen from the XRD measurements shown in Fig. 4.6(a). Specimens with a diameter of up to 3 mm are fully amorphous for the $\text{Au}_{51.6}\text{Ag}_{5.8}\text{Pd}_{2.4}\text{Cu}_{20.2}\text{Ga}_{6.7}\text{Si}_{13.3}$ alloy composition. Beyond a casting thickness of 3 mm, the amorphous halo in the diffraction experiments begins to sharpen which indicates the formation of the primary crystal

¹As the Si content is reduced, the content of noble metals is increased such that the ratio between Au, Ag and Pd stays constant.

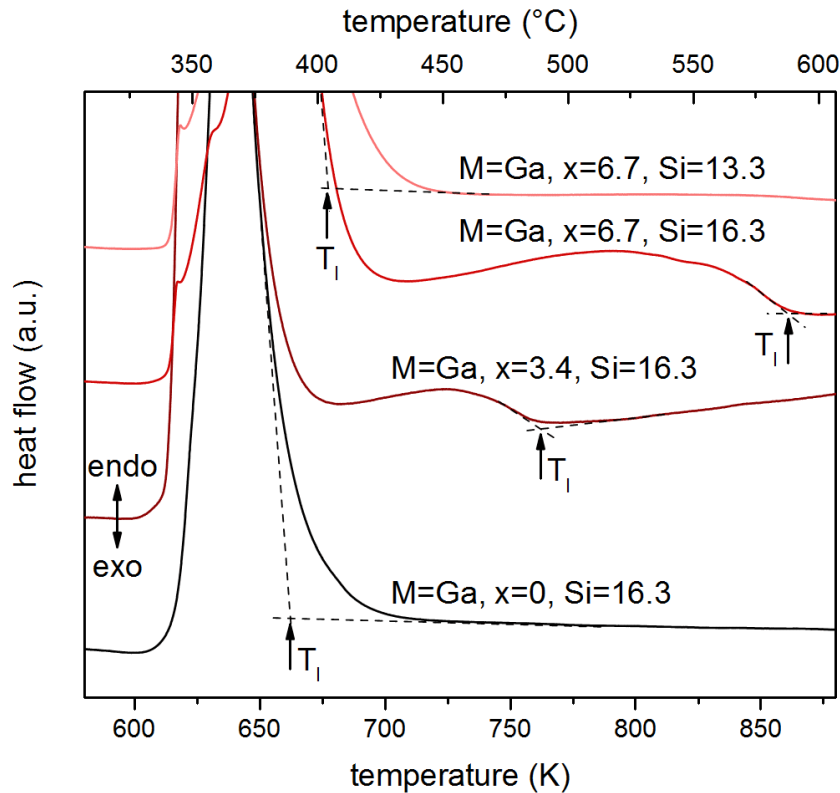


FIGURE 4.5: Variation of the liquidus temperature as a function of the Si and Ga content ($\text{Au}_{49}\text{Ag}_{5.5}\text{Pd}_{2.3}\text{Cu}_{26.9-x}\text{M}_x\text{Si}_{16.3-y}$, $\text{M}=\text{Ga}$, $x=3.4$ and 6.7 at%, $y = 0$ and 3 at%). The content of noble metals is increased by y such that the ratio between Au, Ag and Pd remains constant. Shown are the melting curves of samples that were cooled at 0.333 K/s from the equilibrium melt. Figure taken from Ref. [210].

upon quenching. Figure 4.6(b) shows the thermogram of a fully amorphous sample of $\text{Au}_{51.6}\text{Ag}_{5.8}\text{Pd}_{2.4}\text{Cu}_{20.2}\text{Ga}_{6.7}\text{Si}_{13.3}$ at a heating rate of 0.333 K/s. The alloy exhibits a T_g of 376 K and a T_x of 428 K. The extent of the supercooled liquid region ($T_x - T_g$) is 52 K, which is 6 K less than for the mother alloy [199]. This still pronounced supercooled liquid region makes the alloy suitable for thermoplastic forming.

As alternative for substitution of Cu, the elements Sn, In and Sb are taken into account. Primarily, the effect of a simple substitution without any adjustment of the other alloying elements is investigated. Figure 4.7 shows the XRD measurements of the Sn-, In-, Sb-containing compositions. An addition of $x=3.4$ at% of In or Sn yields fully amorphous samples up to a casting diameter of at least 3 mm (Fig. 4.7(a), (b)). In the case of the Sb-containing alloys, Bragg reflections can already be observed in the 1 mm sample for $x=3.4$ at% and get more pronounced for $x=6.7$ at%. An increase of the Sn and In content to $x=6.7$ at% reduces the GFA, which was similarly observed for the Ga additions. The XRD measurements of all samples with $x=6.7$ at% show evidence for the presence of a crystalline phase. However, the Sn-containing alloy only displays a sharpening of the amorphous halo, resembling that observed for the Ga-containing alloys. In contrast, the XRD pattern of the In- and Sb-containing alloy compositions exhibit distinct reflection of $(\text{Au,Ag})_3\text{In}$ and AuSb_2 , respectively. Consequently, the addition of In and Sb promote the formation of a new competing phase and an adjustment of the Si content is unlikely to improve the GFA. In the case of the Sn-containing alloy, the competing phases remain unchanged and T_l decreases

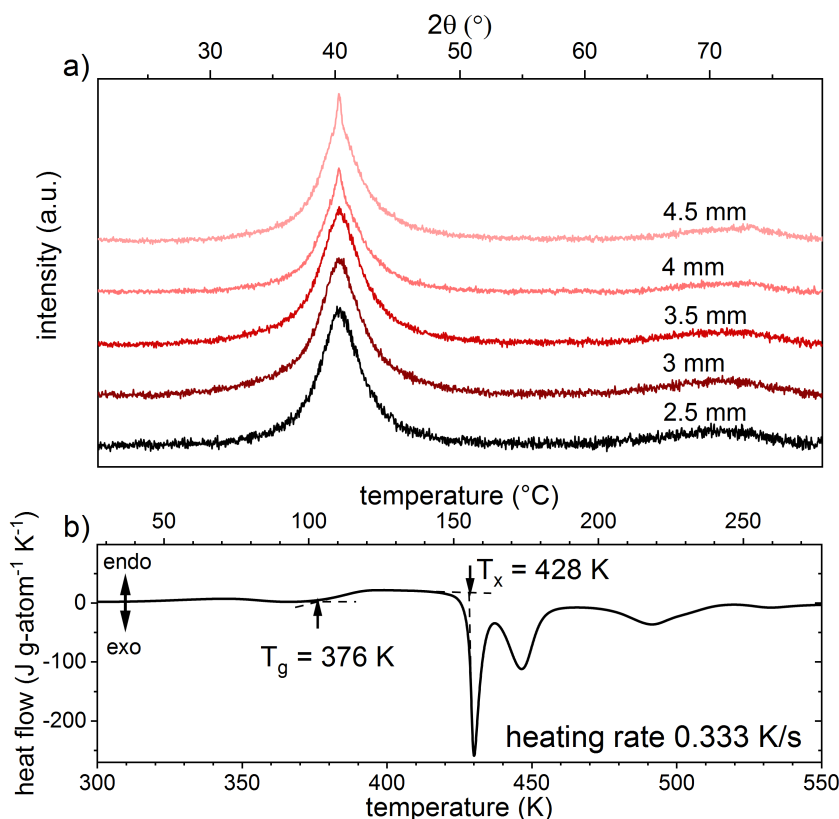


FIGURE 4.6: XRD measurements of $\text{Au}_{51.6}\text{Ag}_{5.8}\text{Pd}_{2.4}\text{Cu}_{20.2}\text{Ga}_{6.7}\text{Si}_{13.3}$ ranging from a sample diameter of 2.5 mm to 4.5 mm. (b) DSC scan of an amorphous sample with a heating rate of 0.333 K/s. The glass transition temperature is located at 376 K and the onset of crystallization at 428 K. Figure taken from Ref. [210].

upon adjusting the Si content (Fig. 4.8(a)) and the GFA is restored (Fig. 4.8(b)).

4.2 Corrosion in artificial saliva

The mother alloy, the $\text{Au}_{51.6}\text{Ag}_{5.8}\text{Pd}_{2.4}\text{Cu}_{20.2}\text{Ga}_{6.7}\text{Si}_{13.3}$ and the $\text{Au}_{51.6}\text{Ag}_{5.8}\text{Pd}_{2.4}\text{Cu}_{20.2}\text{Sn}_{6.7}\text{Si}_{13.3}$ alloy composition are exposed to artificial saliva in an immersion test for seven days at 310 K and the testing solution is subsequently analyzed. The element release per cm^2 sample surface is shown in Fig. 4.9(a). Cu is the main element found in the test solution for all three alloy compositions. However, a significant reduction of the Cu release is observed for the Sn- and Ga-containing alloys. As the overall Cu content is lower in the modified alloys, the element release is normalized to the atomic concentration of the elements in the alloy and the Cu release of the mother alloy is set to one (Fig. 4.9(b)). The normalization does not change the general trend and the Cu release is still distinctly lower. For the Ga-containing alloy, the Cu emission into the artificial saliva solution is reduced by a factor of 2.5 and for the Sn-bearing alloy by a factor of 5.8. Moreover, the SEM micrographs of focused ion beam cuts into the tarnished surface shown in Fig 4.10 reveal a less distinct corrosion attack in the surface region for the modified alloys. The penetration depth of the SiO_2 (dark particles below the Pt-cover), growing in a dense branching morphology from the surface into the bulk material, is reduced considerably for $\text{Au}_{51.6}\text{Ag}_{5.8}\text{Pd}_{2.4}\text{Cu}_{20.2}\text{Ga}_{6.7}\text{Si}_{13.3}$ and $\text{Au}_{51.6}\text{Ag}_{5.8}\text{Pd}_{2.4}\text{Cu}_{20.2}\text{Sn}_{6.7}\text{Si}_{13.3}$. In agreement

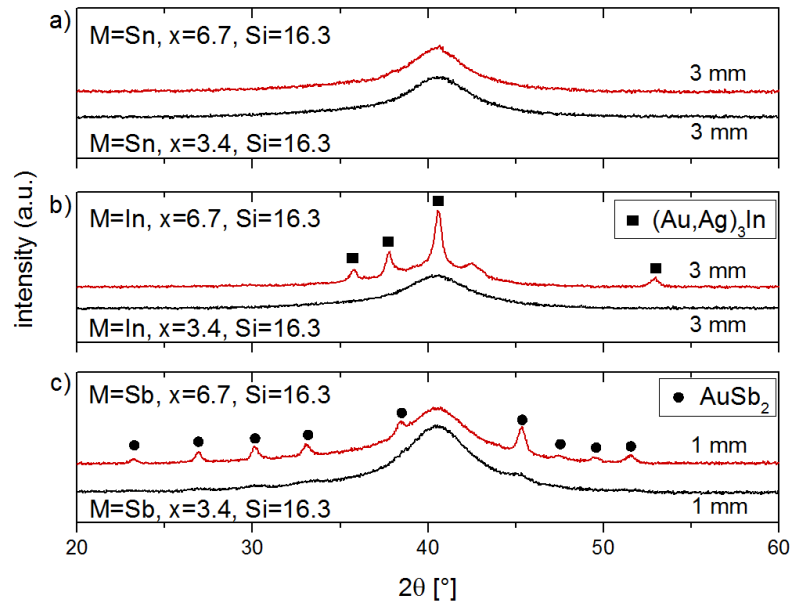


FIGURE 4.7: XRD measurement of 3 mm rods of (a) Sn- (b) In- and (c) Sb-containing compositions ($\text{Au}_{49}\text{Ag}_{5.5}\text{Pd}_{2.3}\text{Cu}_{26.9-x}\text{M}_x\text{Si}_{16.3}$, $M=\text{Sn, In, Sb}$, $x=3.4$ and 6.7 at%). The filled squares in (b) and filled circles in (c) mark the Bragg-peaks of the $(\text{Au,Ag})_3\text{In}$ and AuSb_2 phase, respectively. Figure taken from Ref. [210].

with the element release test, it is observed that the corrosion attack is even less pronounced for the Sn-containing alloy.

In order to evaluate the effect of the alloying element Ga² under real conditions, plate shaped samples ($1 \times 7 \times 24 \text{ mm}^3$) of the mother alloy and $\text{Au}_{51.6}\text{Ag}_{5.8}\text{Pd}_{2.4}\text{Cu}_{20.2}\text{Ga}_{6.7}\text{Si}_{13.3}$ were cast and worn as a necklace using a plastic lace for 417.6 h (17.4 days). At the beginning of the test, the samples were polished to a mirror finish on both sides. The YI, which is calculated from the standard color values according to Eq. 3.1, is measured at regular intervals. Figure 4.11 shows the evolution of the YI during the wearing tests. The change in color is much slower for the Ga-containing alloy which is in agreement with the element release test. During the wearing test, the YI for $\text{Au}_{51.6}\text{Ag}_{5.8}\text{Pd}_{2.4}\text{Cu}_{20.2}\text{Ga}_{6.7}\text{Si}_{13.3}$ increases from 16.5 (premium white) to 42 (off-white) whereas the YI of the mother alloy evolves from 18.5 to 74. This difference is confirmed by the optical micrographs (inset Fig. 4.11) showing the samples at the end of the test.

4.3 Discussion

The simple substitution of Cu by Ga or Sn in the mother alloy destabilizes the liquid phase, which is reflected by a distinct increase in T_l and by a reduction of the GFA in terms of the critical casting thickness. As mentioned in Chapter 1, T_{rg} is usually a good indicator for the GFA of an alloy composition. T_{rg} is 0.60 for the mother alloy, which is in good agreement with the values obtained in Refs. [199, 212]. By substituting Cu by Ga, T_g decreases and T_l increases significantly resulting in a much lower T_{rg} of 0.436 for $M=\text{Ga}$ and $x=6.7$ at%. Ga- and Sn-containing compositions

²The selection of the Ga-containing alloys for the wearing test is based on the history of the alloy development within the project of limited duration.

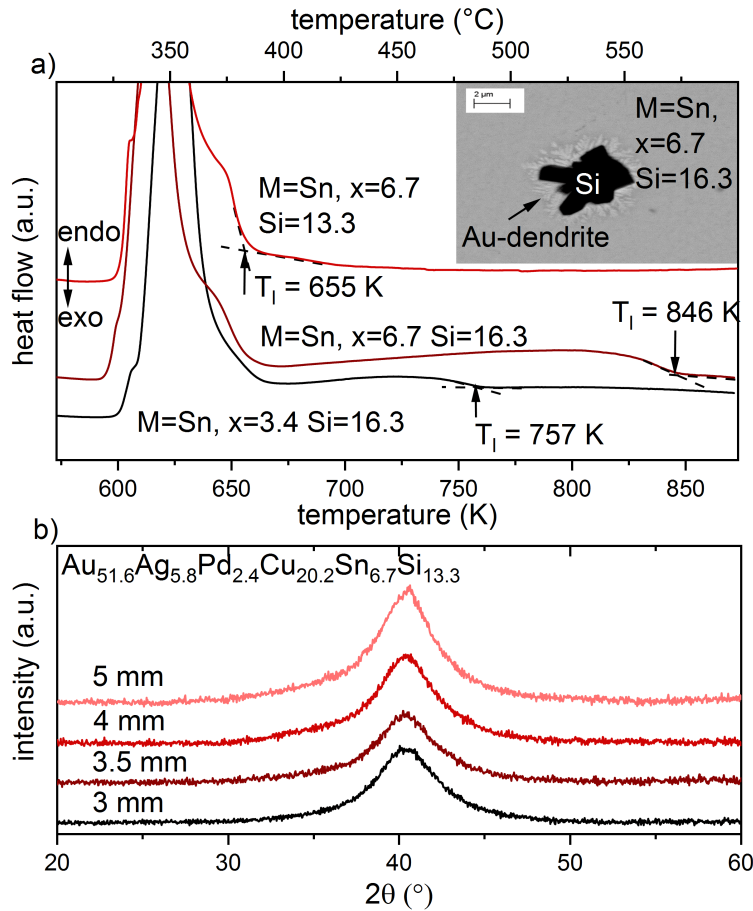


FIGURE 4.8: (a) Effect of an increasing Sn and decreasing Si content on T_1 . Shown are the melting curves of samples that were cooled with 0.333 K/s from the equilibrium melt. The inset in (a) shows a backscattered electron image in cross-section of a 3 mm rod of $\text{Au}_{49}\text{Ag}_{5.5}\text{Pd}_{2.3}\text{Cu}_{20.2}\text{Sn}_{6.7}\text{Si}_{16.3}$. Au-rich dendrites grow heterogeneously from the primary precipitating Si crystal. The scale in the inset is 2 μm . (b) XRD measurements of $\text{Au}_{51.6}\text{Ag}_{5.8}\text{Pd}_{2.4}\text{Cu}_{20.2}\text{Sn}_{6.7}\text{Si}_{13.3}$ ranging from a sample diameter of 3 - 5 mm. The critical casting thickness of this alloy composition is $4 \leq d_c < 5$. Figure taken from Ref. [210].

without adjusted Si content are off-eutectic as shown in the thermograms in Fig. 4.5 and 4.8(a). Upon quenching, these alloys need to pass through a broad two-phase region (liquid + Si) which increases the probability of the formation of the primary phase. The reduction of the Si content increases T_{rg} to 0.554 and restores the GFA to at least 3 mm. It is interesting to note, that the alloys without adjusted Si content do not readily crystallize although the primary phase is present. This might be traced back to two different facts. On the one hand, the formation of the primary Si crystals leaves a Si-depleted melt. As the reduction of the Si content in the Ga- or Sn-containing compositions is found to improve the GFA, the formation of the Si crystals leads to a self-stabilization of the residual liquid phase. On the other hand, the diamond structure of the Si crystals might be rather ineffective as heterogeneous nucleation sites for the fcc Au solid solution. However, the inset in Fig. 4.8 shows that Au dendrites can grow from the Si precipitations.

As discussed in Chapter 2, the GFA of an alloy is determined by thermodynamic

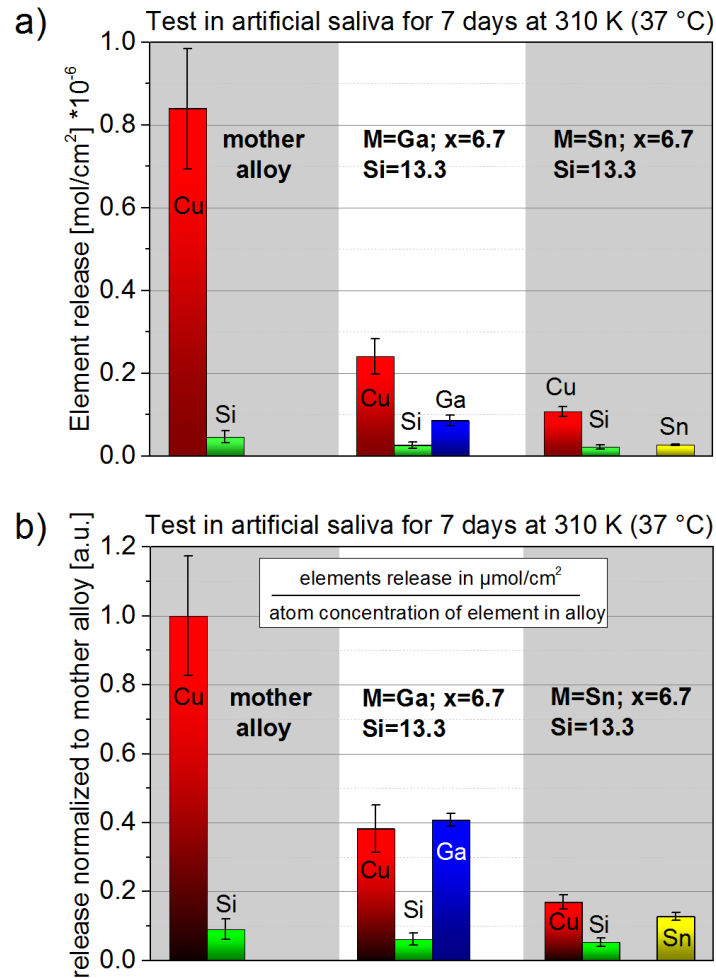


FIGURE 4.9: Release of Cu, Si, Ga and Sn into artificial saliva after a seven days immersion test at 310 K (37 °C) according to ISO 10271. (a) absolute release of the alloying elements in mol/cm² (b) release of each element normalized to the atom concentration in the sample. The Cu release of the mother alloy is set to one. Figure taken from Ref. [210].

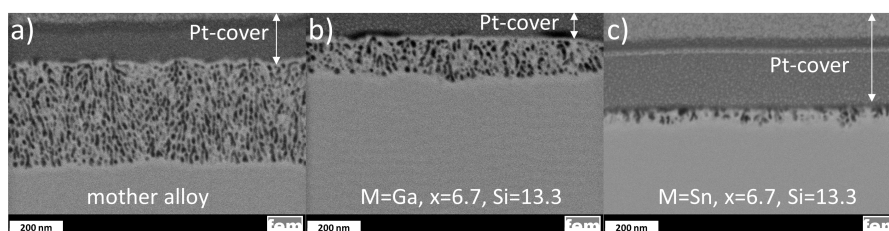


FIGURE 4.10: FIB cuts into the surface of (a) Au₄₉Ag_{5.5}Pd_{2.3}-Cu_{26.9}Si_{16.3}, (b) Au_{51.6}Ag_{5.8}Pd_{2.4}Cu_{20.2}Ga_{6.7}Si_{13.3}, (c) Au_{51.6}Ag_{5.8}-Pd_{2.4}Cu_{20.2}Sn_{6.7}Si_{13.3} after seven days immersion in artificial saliva at 310 K; SiO₂ grows in a dense branching morphology from the surface into the bulk material, the penetration depth decreases significantly with decreasing Cu and Si content; for Au_{51.6}Ag_{5.8}Pd_{2.4}Cu_{20.2}Sn_{6.7}Si_{13.3}, the oxide thickness is even less pronounced in comparison to Au_{51.6}Ag_{5.8}Pd_{2.4}Cu_{20.2}Ga_{6.7}Si_{13.3}. Figure taken from Ref. [210].

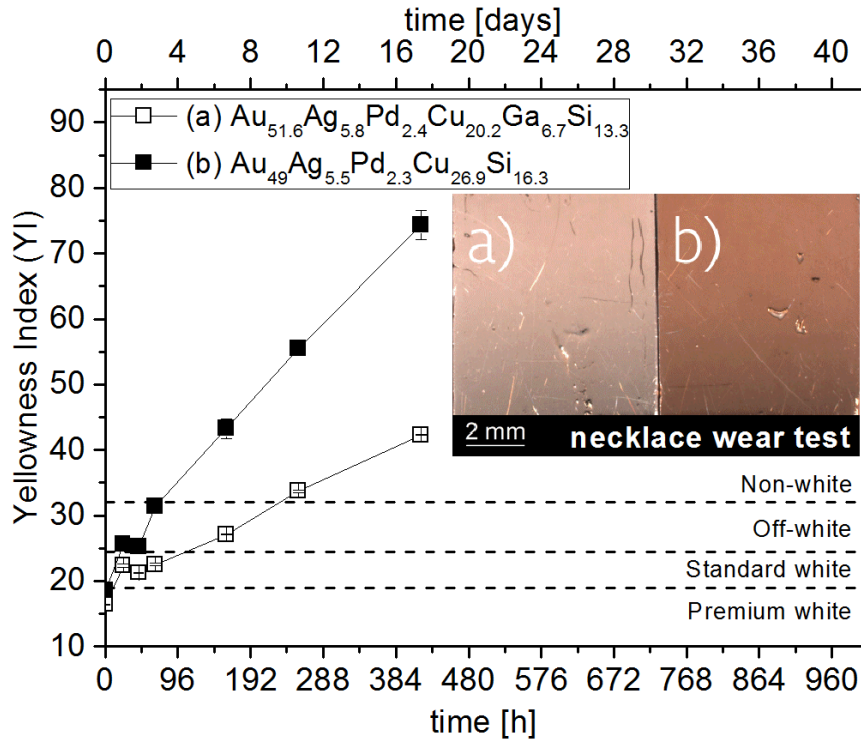


FIGURE 4.11: Necklace wearing test: plate shaped samples ($7 \times 24 \times 1 \text{ mm}^3$) of $\text{Au}_{49}\text{Ag}_{5.5}\text{Pd}_{2.3}\text{Cu}_{26.9}\text{Si}_{16.3}$ and $\text{Au}_{51.6}\text{Ag}_{5.8}\text{Pd}_{2.4}\text{Cu}_{20.2}\text{Ga}_{6.7}\text{Si}_{13.3}$ worn on a plastic lace around the neck for a total of 417.6 h (17.4 days). The YI was determined on both sides of the samples, the scatter between both sample sides is marked with error bars. The inset shows photos of the samples (a) $\text{Au}_{51.6}\text{Ag}_{5.8}\text{Pd}_{2.4}\text{Cu}_{20.2}\text{Ga}_{6.7}\text{Si}_{13.3}$ and (b) $\text{Au}_{49}\text{Ag}_{5.5}\text{Pd}_{2.3}\text{Cu}_{26.9}\text{Si}_{16.3}$ after the test. The initial premium white color has turned into a distinct brown for sample (b) while sample (a) retains a much brighter color. Figure taken from Ref. [210].

and kinetic contributions. A value that is readily accessible is the Gibbs free energy difference between the liquid and the crystal. If the Turnbull approximation (Eq. 2.12) is used, the driving force for nucleation can be estimated from ΔS_f . Figure 4.12 shows the determination of ΔH_f from which ΔS_f is calculated (Eq. 2.11) and the connection between T_{rg} and ΔS_f . It is observed that alloys possessing a small T_{rg} feature a large ΔS_f resulting in a small critical casting thickness. Accordingly, both parameters reflect the change in the GFA of the alloys under investigation. The characteristic temperatures and the values of ΔS_f , ΔH_f , T_{rg} and d_c of the different alloy compositions are summarized in Tab. 4.1.

The success of correlating T_{rg} and ΔS_f with the GFA of the alloys points to the fact that the primary competing phase remains unchanged by the alloy modifications. A variation of the primary phase would change the driving force for nucleation (see Fig. 2.3) and the interfacial energy. As these values effect the nucleation barrier (Eq. 2.31), a changing primary phase would alter the nucleation temperature T_N , defined as the temperature at which crystallization occurs at a certain cooling rate. Hence, the ratio between T_g and T_N should more precisely predict the compositional variation of the GFA than T_{rg} [209]. Although Fig. 4.13 is a fairly simple representation of the underlying mechanisms, it illustrates the decisive difference between T_{rg} and $T_g/T_N (=T_{rN})$ and their connection to the GFA. In an eutectic system, $\Delta T^{\alpha,\beta} (=T_l - T_N)$

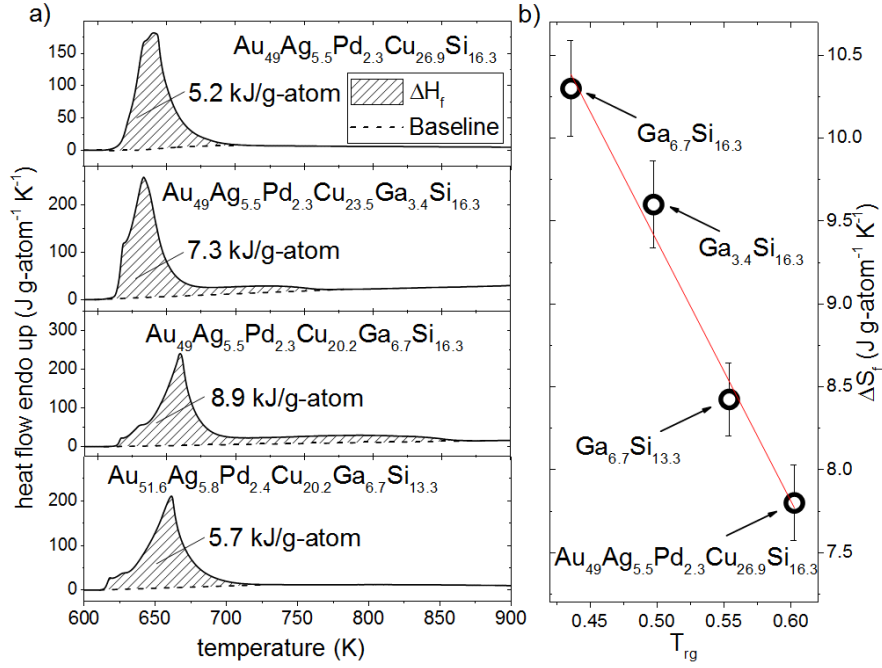


FIGURE 4.12: (a) Thermogram of the melting event of $\text{Au}_{49}\text{Ag}_{5.5}\text{Pd}_{2.3}\text{Cu}_{26.9}\text{Si}_{16.3}$, $\text{Au}_{49}\text{Ag}_{5.5}\text{Pd}_{2.3}\text{Cu}_{23.5}\text{Ga}_{3.4}\text{Si}_{16.3}$, $\text{Au}_{49}\text{Ag}_{5.5}\text{Pd}_{2.3}\text{Cu}_{20.2}\text{Ga}_{6.7}\text{Si}_{16.3}$ and $\text{Au}_{51.6}\text{Ag}_{5.8}\text{Pd}_{2.4}\text{Cu}_{20.2}\text{Ga}_{6.7}\text{Si}_{13.3}$. The enthalpy of fusion corresponds to the shaded areas. (b) Connection between the reduced glass transition temperature T_{rg} and the entropy of fusion ΔS_f , reflecting the driving force for nucleation upon undercooling. The solid line is used to guide the eye. Figure taken from Ref. [210].

TABLE 4.1: T_g (heating rate 0.333 K/s) is the onset of the glass transition, T_m the melting and T_l the liquidus temperature. ΔH_f and ΔS_f are the enthalpy and entropy of fusion, respectively. d_c represents the critical casting thickness and T_{rg} is the reduced glass transition temperature. Table taken from [210]

	T_g (K)	T_m (K)	T_l (K)	ΔH_f (kJ g-atom ⁻¹)	$\Delta S_f = \Delta H_f / T_l$ (kJ g-atom ⁻¹ K ⁻¹)	d_c (mm)	T_{rg}
A	400	614	664	5.2 ± 0.15^a	7.8	5^b	0.604
B	379	614	762	7.3 ± 0.20	9.6	≥ 1	0.497
C	376	614	863	8.9 ± 0.25	10.3	≥ 0.25	0.436
D	376	615	679	5.7 ± 0.15	8.4	3	0.554
E	370	601	655	5.6 ± 0.17	8.6	≥ 4	0.565

A, $\text{Au}_{49}\text{Ag}_{5.5}\text{Pd}_{2.3}\text{Cu}_{26.9}\text{Si}_{16.3}$

B, $\text{Au}_{49}\text{Ag}_{5.5}\text{Pd}_{2.3}\text{Cu}_{23.5}\text{Ga}_{3.4}\text{Si}_{16.3}$

C, $\text{Au}_{49}\text{Ag}_{5.5}\text{Pd}_{2.3}\text{Cu}_{20.2}\text{Ga}_{6.7}\text{Si}_{16.3}$

D, $\text{Au}_{51.6}\text{Ag}_{5.8}\text{Pd}_{2.4}\text{Cu}_{20.2}\text{Ga}_{6.7}\text{Si}_{13.3}$

E, $\text{Au}_{51.6}\text{Ag}_{5.8}\text{Pd}_{2.4}\text{Cu}_{20.2}\text{Sn}_{6.7}\text{Si}_{13.3}$

^a $\Delta H_f = 5.3 \text{ kJ/g-atom}$ [199, 212]

^b[199]

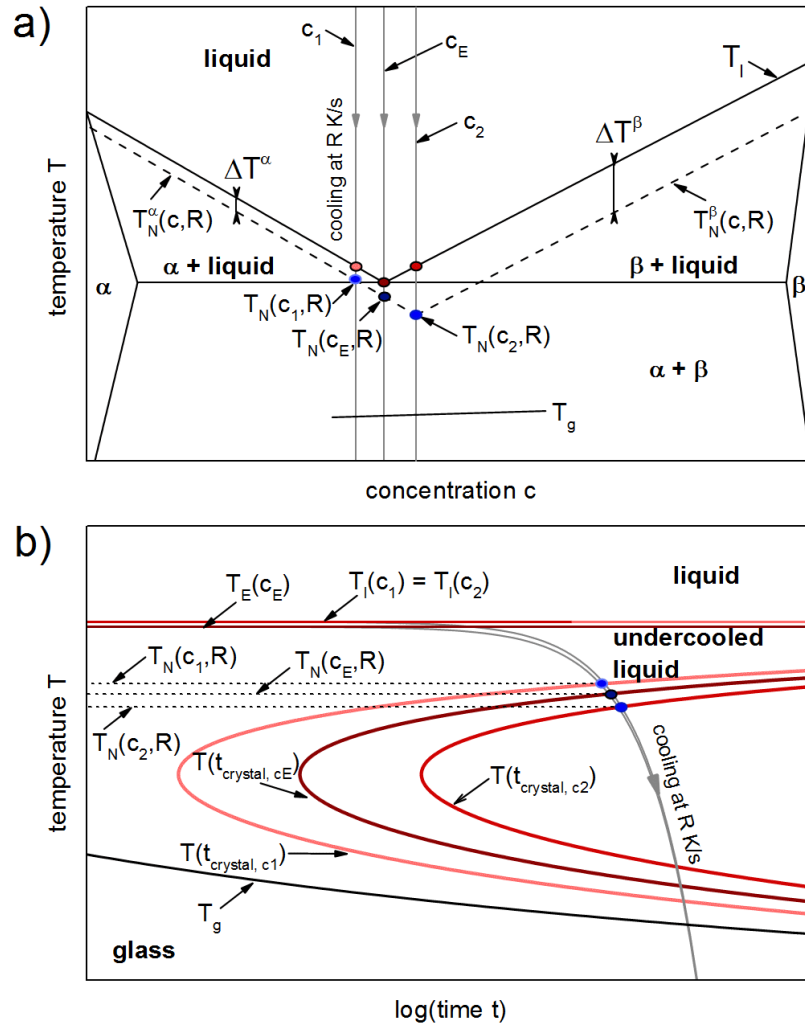


FIGURE 4.13: Effect of the primary precipitating phase on the nucleation temperature T_N and its indication on the GFA. (a) Compositional dependence of T_N at a cooling rate R in an eutectic system under non-equilibrium conditions. $\Delta T^{\alpha, \beta}$ represents the required undercooling to form supercritical nuclei of the α - or β - phase, respectively, and is assumed to be constant [209]. The highest undercooling is found at an off-eutectic composition, indicating the highest GFA. Figure after Ref. [209]. (b) Representation of T_N in a CCT diagram. A lower T_N suggests that the crystallization nose of the alloy composition is shifted to longer times and therefore, the liquid possesses a higher GFA (lower R_c).

represents the required undercooling to form a supercritical nucleus of the α - and β - phase at the cooling rate R , which leads to the crystallization of the entire liquid. In other words, $\Delta T^{\alpha, \beta}$ refers to the level of undercooling at which the cooling curve in a CCT diagram intersects with the crystallization nose (Fig. 4.13). If the liquid with the composition c_1 is cooled at the rate R as shown in Fig 4.13(a), the α -phase forms at $T_N(c_1, R)$. At the eutectic composition c_E , the non-equilibrium conditions during cooling allow the formation of the α -phase prior to the β -phase. The compositional change from c_1 and c_E reduces T_l and T_N equivalently and T_{rg} and T_{rN} represent equally well the change in GFA. At the composition c_2 , the primary phase at the cooling rate R changes from α to β and a maximum undercooling is achieved. In this

case T_{rg} decreases, whereas T_{rN} increases. As shown 4.13(b) a lower T_N implies that the upper portion of the crystallization nose is located at lower temperatures. This indicates that the crystallization nose is shifted to longer times resulting in a slower critical cooling rate. It should be noted that the upper portion of the crystallization nose is nucleation controlled. This means that for slow cooling rates the detection of the small differences in T_N among different alloy compositions might be hampered by statistical fluctuations. On the other hand, the phases involved might benefit differently from the container walls or impurities (heterogeneous nucleation), effecting the nucleation barrier [100, 209]. Nevertheless, the concept of the nucleation temperature demonstrates why many metallic glass-forming alloy compositions do not coincide with the eutectic composition. The selection of the primary competing, crystalline phase in multicomponent eutectic systems plays a decisive role for the GFA, as experimentally shown in the Pd-Ni-S system [179].

In order to visualize the effect of the compositional modifications, the ternary Au-Ga-Si and Au-Sn-Si liquidus projections are calculated (Fig. 4.14(a) and 4.14(b)). The addition of Ga or Sn shifts the overall composition of the mother alloy (pseudo-composition labeled A in Fig. 4.14(a)) from the near-eutectic GFR to an off-eutectic region (liquid + Si), where a high T_l (see Fig. 4.5 and 4.8(a)) and a large Gibbs free energy difference (see Fig. 4.12) strongly facilitates the formation of Si crystals as primary phase upon cooling (composition B in Fig. 4.14(a)). The proximity to the GFR is restored through the reduction of the Si content, shifting the composition from B to C (arrow (2) in Fig. 4.14(a)). This results in a pronounced decrease of T_l and ΔS_f . Consequently, the GFA recovers upon changing the composition from B to C. The effect of the alloy modifications, visualized in Fig. 4.14(a), interestingly well coincides with the results obtained for the more complex scenario Au-Ag-Pd-Cu-Ga-Si and Au-Ag-Pd-Cu-Sn-Si systems. The similarities between the Sn- and Ga-containing ternary phase diagrams explain why the strategy of shifting the alloy composition back to the GFR works for both elements. From a structural point, these striking parallels in terms of the GFA are highly surprising for scenario systems. The variation of the atomic size of Cu (126 pm) and the substituting elements Ga (134 pm) and Sn (155 pm) [170] suggests that the structure of the liquid is altered significantly. The observed difference in the GFA between $\text{Au}_{51.6}\text{Ag}_{5.8}\text{Pd}_{2.4}\text{Cu}_{20.2}\text{Ga}_{6.7}\text{Si}_{13.3}$ and $\text{Au}_{51.6}\text{Ag}_{5.8}\text{Pd}_{2.4}\text{Cu}_{20.2}\text{Sn}_{6.7}\text{Si}_{13.3}$ might be traced back to the larger atomic size of Sn, leading to a more efficiently packed liquid.

The corrosion experiments reveal that the substitution of Cu by Ga or Sn effectively reduces the extent of the corrosion attack. The Cu release into the test solution is reduced by a factor of 2.5 and 5.8 for the addition of Ga and Sn, respectively. Moreover, the alloying elements drastically reduced the corrosion depth. The inwards growth of the amorphous SiO_2 is reduced by ca. 50% for Ga and ca. 80% for Sn. This can partly be attributed to the overall reduction of Cu and Si, primary involved in the corrosion process. However, the difference in the corrosion depth between the Ga- and Sn-containing alloy indicates that the sixth element might take an active role in the corrosion process and affects the underlying mechanism. This is supported by the element release test that is normalized to the atomic concentration of the element in the alloy, showing a pronounced reduction of the Cu release (Fig. 4.9(b)). An explanation for the improved tarnishing resistance might be the formation of an additional oxide layer (e.g. Ga_2O_3) slowing down the outward diffusion of Cu and prohibiting the internal growth of the SiO_2 dendrites. It stands to reason that an increase of the Ga or Sn concentration further improves the tarnishing resistance of the alloys. However, the liquidus projections suggest that there might be a natural limit

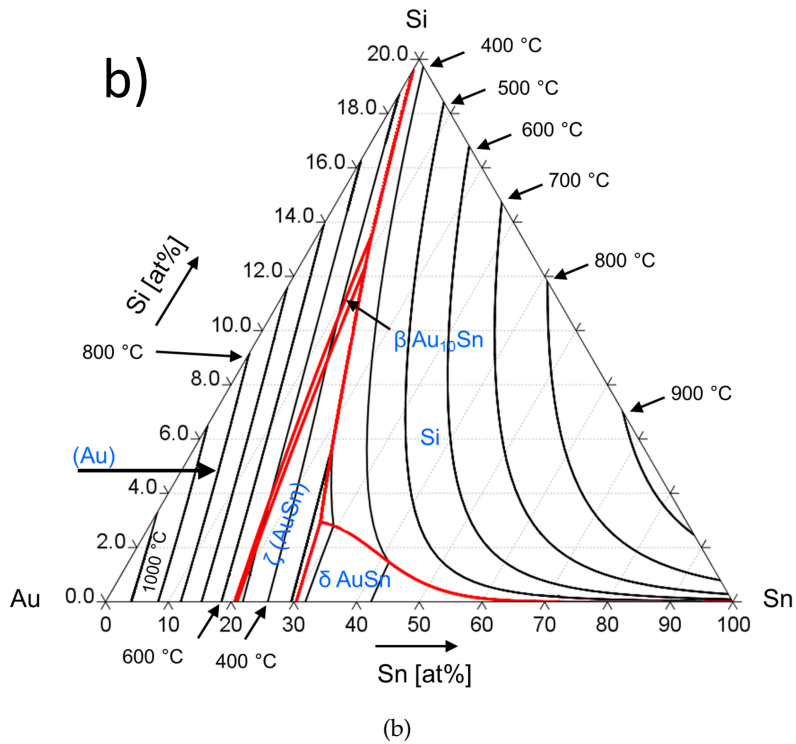
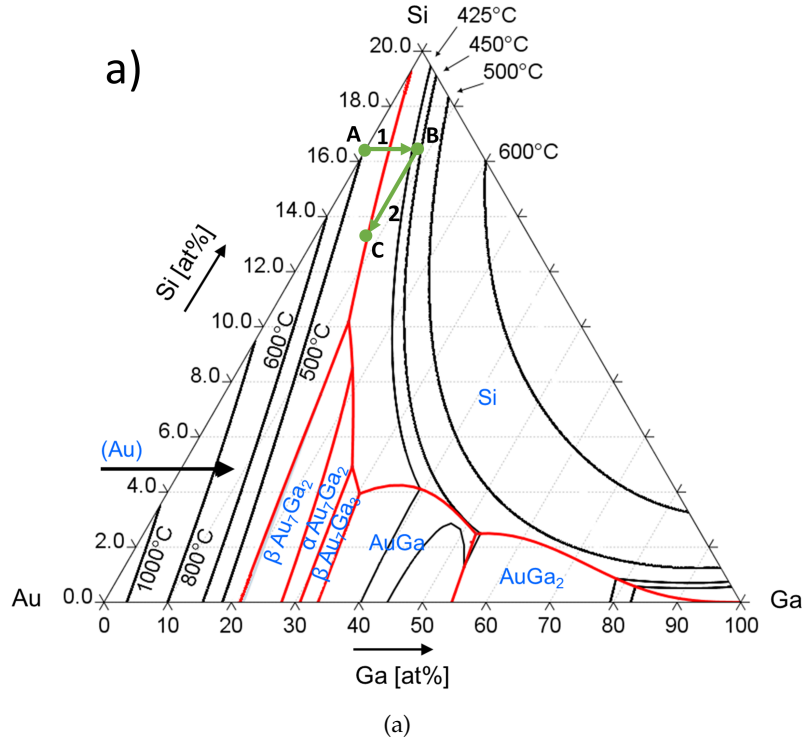


FIGURE 4.14: Calculated liquidus projections of the (a) Au-Ga-Si (SNOB3 database) and (b) Au-Sn-Si (SSOL5 database) system. It should be noted that the Si axes in these illustrations are only shown to 20 at%, so the eutectic trough is overly contorted for demonstrational reasons. Figures taken from Ref. [210].

beyond which the ability to form a glass is lost. At a Ga concentration of ~ 13 at% (and ~ 10 at% Si), the primary competing phases change from Si(-solid solution) and Au-solid solution (Au) to Si and the intermetallic phase β -Au₇Ga₂. In the case of a Sn addition, the β -Au₁₀Sn₂ and the ζ -AuSn crystalline phases are in equilibrium with the melt, when the Si content is reduced. As observed for the In- and Sb-containing alloys, a change in primary phase might be detrimental for the GFA. It should be noted that the liquidus projections in Fig. 4.14 do not take the influence of the other alloying elements into account and that the actual multicomponent liquidus projection and the competing phases might deviate. However, the calculated diagrams can be considered as useful tool that allows a better interpretation of the experimental findings.

In a recent study, the Ga content is further maximized by applying the strategy described above [213]. It is found that the alloy composition Au_{52.6}Ag_{5.8}Pd_{2.4}Cu_{18.7}Ga_{8.2}Si_{12.3}, possessing a d_c of 2 mm, is the best compromise between Ga content and GFA. As shown in Fig. 4.15, the evolution of d_c is used to draw a trend line in order to estimate the critical Ga content at which the GFA collapses. This value might be at approximately 9 at% Ga, which is lower than the

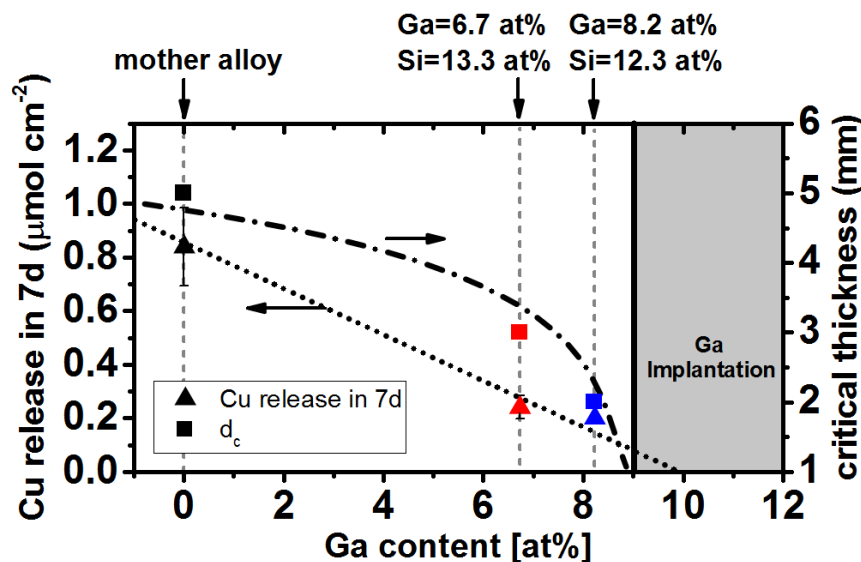


FIGURE 4.15: Effect of the substitution of Cu by Ga on the Cu release into artificial saliva and on d_c . The dashed-dotted line is a trend line illustrating the dependence of d_c on the Ga concentration. The vertical, black line marks the estimated Ga threshold concentration up to which bulk glassy samples can be obtained from the liquid state. The linear extrapolation of the Cu release suggests that it comes to halt at approximately 10 at%. Figure adapted from Ref. [213].

value derived from the phase diagram in Fig. 4.14 but in accordance to experimental observations [214]. Moreover, the Ga content at which the Cu release approaches zero is estimated from the extrapolation of the existing data. This value is expected to be at 10 at% Ga which is beyond the estimated natural alloying threshold of 9 at% [213]. In order to reach higher Ga contents and simultaneously maintain the amorphous character of the sample, Ga atoms are locally implanted in the Au_{51.6}-Ag_{5.8}Pd_{2.4}Cu_{20.2}Ga_{6.7}Si_{13.3} alloy composition using a focused ion beam. Simulations of the Ga distribution in an irradiated surface suggest a Ga concentration of 11 at% in 10 nm depth if the sample area is exposed to Ga ions for 1000 s [213]. Fig. 4.16 shows that the areas that are irradiated for 1000 s remain unaffected in the corrosion

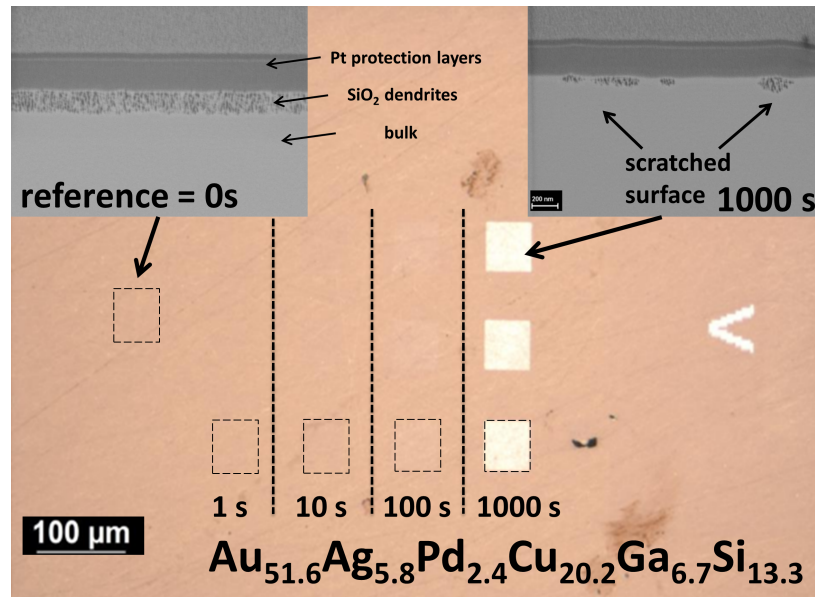


FIGURE 4.16: Effect of the Ga implantation (using focused ion beam) on the tarnishing behavior of $\text{Au}_{51.6}\text{Ag}_{5.8}\text{Pd}_{2.4}\text{Cu}_{20.2}\text{Ga}_{6.7}\text{Si}_{13.3}$ after seven days in artificial saliva. The dashed squares represent areas that were irradiated for 0, 1, 10, 100, and 1000 s. The areas that were irradiated for 1000 s possess a Ga concentration of approximately 11 at% in 10 nm depth. The insets show a cross-section of the non-irradiated and irradiated area. In contrast to the non-irradiated area, a corrosion attack in the irradiated area only occurs locally, where the surface has been scratched. Figure taken from Ref. [213].

test. However, these results are only representative for samples exposed to artificial saliva for seven days. Whether a long-term effect through the implantation of Ga is achieved needs to be evaluated. Moreover, the low penetration depth of the Ga ions makes the sample sensitive to scratches. The inset in Fig. 4.16 reveals that local damage exceeding a depth of 10 nm are prone to a corrosion attack.

4.4 Summary and Outlook

The 18kt gold based bulk glass-forming composition $\text{Au}_{49}\text{Ag}_{5.5}\text{Pd}_{2.3}\text{Cu}_{26.9}\text{Si}_{16.3}$ is modified to improve the corrosion resistance. The substitution of Cu by Ga and Sn leads to a pronounced increase of the liquidus temperature and of the driving force for crystallization (estimated from the entropy of fusion). This results in a drop of the glass-forming ability which is restored by adjusting the Si content. The reduction of the Si content shifts the alloy composition towards the glass-forming region again. This strategy is used to reduce the Cu and Si content, which are the elements responsible for the fast color change, and simultaneously maintain the ability for bulk glass formation. The modified alloy compositions exhibit a four to eight times lower element release in artificial saliva, depending on the substituting species. The results indicate that the improved tarnishing resistance is not solely traced back to the reduction of disadvantageous elements. The substituting elements Sn and Ga might rather take an active role in the corrosion process by forming an additional oxide, preventing the fast color change. However, the alloy modifications are not able to cease the tarnishing process completely. Depending on the alloy composition, the

color of the tarnished sample changes from brownish for the mother alloy, to reddish for the Ga-containing and to yellowish for the Sn-containing alloy. Figure 4.17 shows the color of the tarnished $\text{Au}_{51.6}\text{Ag}_{5.8}\text{Pd}_{2.4}\text{Cu}_{20.2}\text{Ga}_{6.7}\text{Si}_{13.3}$ and $\text{Au}_{51.6}\text{Ag}_{5.8}\text{Pd}_{2.4}\text{Cu}_{20.2}\text{Sn}_{6.7}\text{Si}_{13.3}$ alloy composition in comparison to the freshly ground mother alloy. As the colors of the tarnished samples are homogeneous, it might be conceiv-

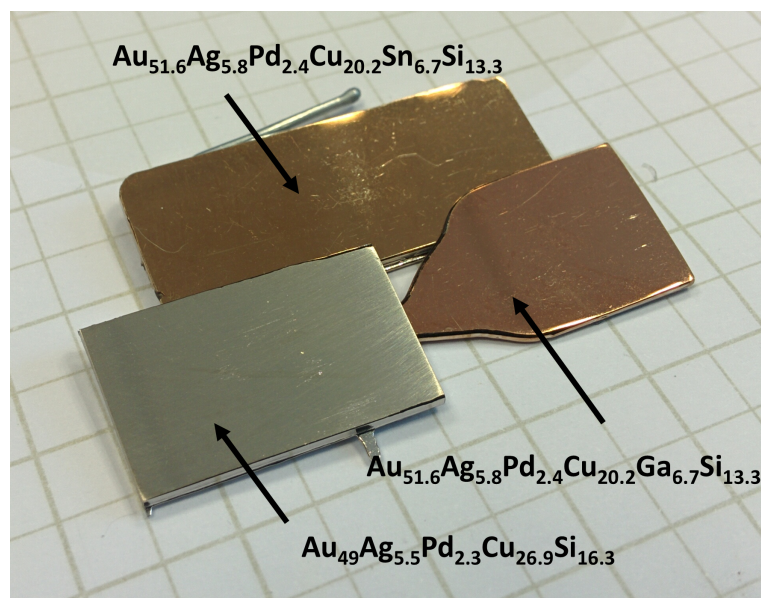


FIGURE 4.17: Photography of tarnished (reddish: $\text{Au}_{51.6}\text{Ag}_{5.8}\text{Pd}_{2.4}\text{Cu}_{20.2}\text{Ga}_{6.7}\text{Si}_{13.3}$, yellowish: $\text{Au}_{51.6}\text{Ag}_{5.8}\text{Pd}_{2.4}\text{Cu}_{20.2}\text{Sn}_{6.7}\text{Si}_{13.3}$) and freshly ground (mother alloy) samples.

able to use them as color gold. Sn and Ga are exchangeable and combinable [177] which would allow to design new colors. Before these alloys could be used as color gold it needs to be clarified if the colored surface is resistant against abrasion and how the color changes when the samples are in contact with a corrosive environment for more than seven days. Furthermore, the observation that the local increase of the Ga concentration in the surface improves the tarnishing resistance might be a suitable starting point for further research. For example, the Ga concentration at the surface might be increased through a simple immersion of the jewelry item in liquid Ga. In the case of crystalline Au alloys, this method is used to form a 10 to 100 μm thick surface layer of AuGa_2 , which is known as blue gold [215].

In order to circumvent the tarnishing issue, the combination of Cu and Si in the alloy composition needs to be avoided. As the mother alloy is based on the Au-Cu-Si system, this requirement necessitates the exploration of completely new alloying systems. The atomic size of Cu is in-between that of Si and Au, fulfilling Inoue's 12% rule (see Chapter 1). Therefore, Cu is expected to increase the packing density and improve the glass-forming ability³ and needs to be replaced adequately. Elements that are worth considering from a topological point of view (Fe, Ni, Co) are not suitable for jewelry alloys and/or exhibit a positive heat of mixing with Au [216]. Another deep eutectic is found in the Al-Au system. At ~ 22 at% Al the melt is stable down to 789 K. However, Au and Al are topologically equivalent [170] which probably requires the addition of different atomic species to increase the atomic packing

³According to Ref. [199], $\text{Au}_{55}\text{Cu}_{25}\text{Si}_{20}$ possesses a d_c of 0.5 mm whereas amorphous samples of $\text{Au}_{75}\text{Si}_{25}$ can be produced with a thickness of 10 μm [3].

in the liquid⁴. In these systems, the concept of the nucleation temperature in combination with new techniques like fast differential scanning calorimetry (FDSC) [159, 218, 219] and combinatorial approaches [209, 220–222] may pave the way to a new bulk glass-forming composition, excluding Cu and Si as alloying elements.

⁴In a Au-Al-Cu co-sputtered thin film no amorphous phase was detected [217].

Chapter 5

Pt-P-based bulk metallic glasses

The Pt-P-based alloys are among the best bulk glass-forming systems. The d_c of the alloy compositions with the highest GFA reaches a value of 2 cm [15, 223]. As shown in the following, the synergy of different contributions influences the stability of the liquid state in the Pt-P-based system. The high thermal stability of the undercooled liquid upon heating from the glassy state and upon cooling from the equilibrium liquid, their extremely low T_l , and their precious metal character predestines this class for the analysis of the thermophysical properties. Their compositional similarity to the Pd-P-based system is striking and simultaneously hardly surprising when the atomic size of Pd and Pt and the binary phase diagrams with the other constituents are compared. These similarities do not point towards distinct differences between the two alloying systems. However, d_c increases by a factor of four when Pt is replaced by Pd completely [15, 16]. Moreover, it is observed that Pd-P-based alloys exhibit a pronounced dependence of their bending plasticity on the applied cooling rate whereas the high ductility in Pt-P-based alloys is retained, even at low cooling rates [224]. The partial replacement of Pd by Pt reduces the sensitivity of the bending plasticity on the cooling rate. In general, Pt- and Pd-based alloys are among the most ductile BMGs and possess a high resistance to crack propagation [225–227]. Furthermore, some alloy compositions containing 85 wt% [15] and 95 wt% [227] of Pt meet the hallmarking conventions which makes them suitable for jewelry applications or for applications in luxury goods [228, 229]. Figure 5.1 shows the first amorphous wedding band made of a Pt-P-based bulk glass-forming alloy. Preliminary investigations on the tarnishing behavior of Pt-P-based BMGs indicate a



FIGURE 5.1: First amorphous wedding band made of $\text{Pt}_{57.3}\text{Cu}_{14.6}\text{-Ni}_{5.3}\text{P}_{22.8}$ (85 wt% Pt).

high corrosion resistance against saliva and no significant color change is observed. The establishment of Pt-P-based alloys as jewelry alloys is currently hindered by the sophisticated alloying process and the challenging recycling procedure.

5.1 Thermodynamics and kinetics of the liquid

The methods described in Chapter 3 are used to determine the thermodynamic and kinetic properties of Pt-P-based BMG forming liquids. The collected data are described with the functions given in Chapter 2. The thermodynamic and kinetic functions are later used to model the isothermal crystallization behavior of Pt-P-based liquids.

5.1.1 Thermodynamic properties

Figure 5.2 shows the specific heat capacity of the $\text{Pt}_{42.5}\text{Cu}_{27}\text{Ni}_{9.5}\text{P}_{21}$ and $\text{Pt}_{60}\text{Cu}_{16}\text{Co}_2\text{P}_{22}$ alloy compositions as function of temperature in the glassy, crystalline, supercooled and in the equilibrium liquid state. The specific heat capacity data were

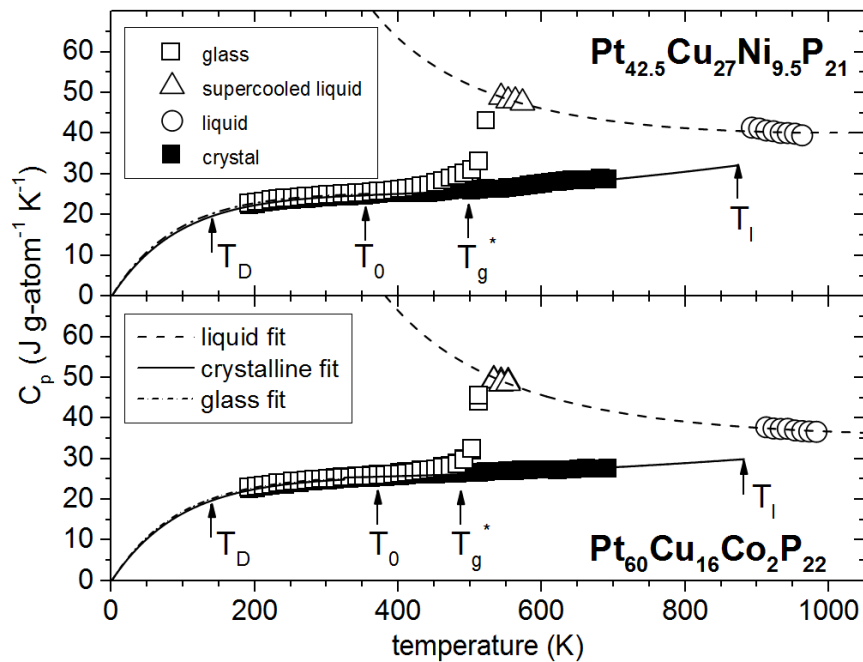


FIGURE 5.2: Specific heat capacity of the glass (\square), the crystal (\blacksquare), the supercooled liquid (\triangle) and the equilibrium liquid (\circ) of $\text{Pt}_{42.5}\text{Cu}_{27}\text{Ni}_{9.5}\text{P}_{21}$ (upper panel) and $\text{Pt}_{60}\text{Cu}_{16}\text{Co}_2\text{P}_{22}$ (lower panel). The curves (solid, dashed and dashed-dotted) represent the fits to Eqs. 2.7, 2.7 and 2.9. T_l marks the liquidus temperature at 874 K and 882 K, respectively. T_g^* is the temperature at which the supercooled liquid reaches 10^{12} Pa s, and T_0 is the temperature at which viscosity deviates towards infinity (Eq. 2.18). T_D is the Debye temperature of the glass obtained as a fitting parameter (Eq. 2.9). Data taken from Refs. [67, 75].

determined at a heating rate of 0.333 K/s, a step width of 10 K and an isothermal holding time of 120 s. The data points were collected in a temperature interval from 193 K to approximately $T_l + 90$ K. At low temperatures, the specific heat capacity of the glass is slightly above that of the crystal. Upon approaching the glass transition, C_p rises quickly until the SCL region is reached. From there on, C_p^l decreases with increasing temperature. The Equation 2.7, 2.8 and 2.9 are used to fit the experimental data. The fitting parameter for $\text{Pt}_{42.5}\text{Cu}_{27}\text{Ni}_{9.5}\text{P}_{21}$ are determined to be $a = 9.61385 \times 10^{-3} \text{ J g-atom}^{-1} \text{ K}^{-2}$, $b = 5.52829 \times 10^6 \text{ J g-atom}^{-1} \text{ K}$, $c = -6.1463 \times 10^{-3} \text{ J g-atom}^{-1}$

K^{-2} and $d = 16.4663 \times 10^{-6} \text{ J g-atom}^{-1} \text{ K}^{-3}$. The values of the fitting parameter of $\text{Pt}_{57.3}\text{Cu}_{14.6}\text{Ni}_{5.3}\text{P}_{22.8}$, and $\text{Pt}_{60}\text{Cu}_{16}\text{Co}_2\text{P}_{22}$ are listed in Tab. 5.1.

The characteristic temperature of the alloys (T_g , T_x , T_m , T_l) are determined from the thermograms of amorphous samples at a heating rate of 0.333 K/s. ΔH_x and ΔH_f are average values that were calculated from the integration of several crystallization and melting events. Prior to determining ΔH_f , the liquid was solidified at a cooling rate of 0.333 K/s. In the case of the $\text{Pt}_{42.5}\text{Cu}_{27}\text{Ni}_{9.5}\text{P}_{21}$ alloy composition, T_g is located at 514 K, T_x at 597 K, T_m at 779 K and T_l at 874 K. Hence, the extent of the supercooled liquid region upon heating at 0.333 K/s ($\Delta T=83 \text{ K}$) exceeds that of the Au-based BMGs (see Chapter 4). Moreover, T_l is approximately 1150 K lower than the melting point of pure Pt which eases the casting of the alloys significantly. The integration of the crystallization peak (shown in Fig. 3.3) and the melting peak yields a ΔH_x and ΔH_f of 7.4 and 10.5 kJ g-atom $^{-1}$, respectively. Using Eq. 2.11, ΔS_f is determined to be 12 J g-atom $^{-1} \text{ K}^{-1}$ which is twice as high as the value determined for the $\text{Pd}_{43}\text{Cu}_{27}\text{Ni}_{10}\text{P}_{20}$ alloy composition (5.8 J g-atom $^{-1} \text{ K}^{-1}$, $\Delta H_f=5.02 \text{ kJ g-atom}^{-1}$ [110], $T_l=866 \text{ K}$ [230]). The values are summarized together with those of $\text{Pt}_{57.3}\text{Cu}_{14.6}\text{Ni}_{5.3}\text{P}_{22.8}$ and $\text{Pt}_{60}\text{Cu}_{16}\text{Co}_2\text{P}_{22}$ in Tab. 5.2.

TABLE 5.1: a , b , c , d , M , and T_D are the fitting parameter of Eqs. 2.7-2.9. Values taken from Refs. [67, 75, 148].

	$a \times 10^{-3}$ J g-atom $^{-1} \text{ K}^{-2}$	$b \times 10^6$ J g-atom $^{-1} \text{ K}$	$c \times 10^{-3}$ J g-atom $^{-1} \text{ K}^{-2}$	$d \times 10^{-6}$ J g-atom $^{-1} \text{ K}^{-3}$
A	9.61384 ± 0.1676	5.52829 ± 0.0572	-6.1463 ± 0.5480	16.4663 ± 1.1836
B	5.6268	5.7648	-4.4622	11.977
C	5.46846	6.2676	-1.2242	7.7265

	$M(\text{glass})$	$M(\text{xtal})$	$T_D(\text{glass})$ K	$T_D(\text{xtal})$ K
A	0.98	0.99	133.3 ± 1	140.4 ± 2.5
B	n.a.	n.a.	n.a.	n.a.
C	0.97	0.96	144.5	139.8

A, $\text{Pt}_{42.5}\text{Cu}_{27}\text{Ni}_{9.5}\text{P}_{21}$
 B, $\text{Pt}_{57.3}\text{Cu}_{14.6}\text{Ni}_{5.3}\text{P}_{22.8}$
 C, $\text{Pt}_{60}\text{Cu}_{16}\text{Co}_2\text{P}_{22}$

Based on ΔH_f and $\Delta C_p^{l-x}(T)$, $\Delta H_{l-x}(T)$ is calculated according to Eq. 2.5 (Fig. 5.3). The calculated curve can be validated by crystallization experiments as shown by Gallino et al. for the $\text{Pd}_{43}\text{Cu}_{27}\text{Ni}_{10}\text{P}_{20}$ alloy composition [110]. The crystallization enthalpies can be obtained in continuous heating or cooling experiments at various rates or in isothermal experiments at different temperatures. Figure 5.3 shows the enthalpic pathway during isothermal annealing experiments on amorphous samples of $\text{Pt}_{42.5}\text{Cu}_{27}\text{Ni}_{9.5}\text{P}_{21}$ at 533 K and 578 K. The samples were heated from the glassy state to the desired temperature at a rate of 2 K s^{-1} . The temperatures are located in and above the glass transition region as shown in the thermogram in Fig. 5.3(1). After a short relaxation period ($< 100 \text{ s}$, see Fig. 5.7(a)) for the sample that is held at 533 K, both specimens reside in the metastable supercooled liquid state. The exothermic crystallization events are shown in Fig. 5.3(2) and the associated

TABLE 5.2: Glass transition temperature T_g (heating rate 0.333 K/s), crystallization temperature T_x (0.333 K/s), melting temperature T_m and liquidus temperature T_l of three different Pt-P-based bulk glass-forming alloys. ΔH_f and ΔS_f are the enthalpy and entropy of fusion. Values taken from Refs. [67, 75]

	T_g	T_x	T_m	T_l	ΔH_x	ΔH_f	ΔS_f
	K	K	K	K	kJ g-atom ⁻¹	kJ g-atom ⁻¹	kJ g-atom ⁻¹ K ⁻¹
A	514	597	779	874 ± 2	7.4* ± 0.3	10.5 ± 0.3	12.0
B	501	577	735	833	7.7	11.4	13.7
C	506	573	824	882 ± 5	7.3 ± 0.3	10.7 ± 0.35	12.1

A, Pt_{42.5}Cu₂₇Ni_{9.5}P₂₁

B, Pt_{57.3}Cu_{14.6}Ni_{5.3}P_{22.8}

C, Pt₆₀Cu₁₆Co₂P₂₂

* value corrected

enthalpy release is visualized as vertical arrows in the $\Delta H_{l-x}(T)$ plot. At 533 K, crystallization occurs after 17 000 s and the crystallization enthalpy, obtained from integration of the exothermic crystallization peak, is 4.18 kJ g-atom⁻¹. The higher atomic mobility at 578 K shifts crystallization to 161 s and ΔH_x increases to 4.99 kJ g-atom⁻¹. The difference in ΔH_x results from the fact that the sample at 578 K resides in a higher enthalpic state, as indicated in the enthalpy curve in Fig. 5.3. In general, the structural state obtained after isothermal annealing is not identical to the one that is melting at the solidus temperature and further transformations occur upon heating. To obtain the overall crystallization enthalpy, the specimens are heated at 0.333 K/s to the solidus temperature after the isothermal holding. The thermograms are shown in Fig. 5.3(3) and the released enthalpy for the isothermally annealed samples ranges from 2.0 to 2.3 kJ g-atom⁻¹. As within the scattering no clear trend between the amount of enthalpy released upon reheating and the holding temperature is observed, an average value of 2.20 kJ g-atom⁻¹ for Pt_{42.5}Cu₂₇Ni_{9.5}P₂₁ (2.65 kJ g-atom⁻¹ for Pt₆₀Cu₁₆Co₂P₂₂) is added to the isothermal ΔH_x . In the following melting process (Fig. 5.3(4)), ΔH_f is required to dissolve the crystalline structure and the equilibrium liquid state is reached at T_l . During the casting process (Fig. 5.3(5)), the sample follows the enthalpy curve of the liquid and eventually freezes to a glass if the crystallization process is bypassed.

The $\Delta H_{l-x}(T)$ curve represents a closed cycle and the crystallization enthalpies obtained at high and low temperatures are used to validate the specific heat capacity measurements as shown for Pt_{42.5}Cu₂₇Ni_{9.5}P₂₁ and Pt₆₀Cu₁₆Co₂P₂₂ in Fig. 5.4. In continuous and isothermal measurements, the onset temperature of crystallization and the annealing temperature are used as reference temperature for the ΔH_x -values in Fig. 5.4. Both temperatures mark the point at which the enthalpy of the sample starts to deviate from that of the liquid phase. In Fig. 5.4 it can be seen that the isothermally and continuously measured ΔH_x -values follow the course of the calculated curve. The values are within the error interval, taken as three times the standard deviation of ΔH_f (Tab. 5.2). The isothermal high temperature crystallization enthalpies of Pt₆₀Cu₁₆Co₂P₂₂, shown in Fig. 5.4(b), should be regarded as a lower limit since the formation of the primary crystal already occurs in the cooling protocol. It should be noted that the assumption of a vanishing ΔG_{l-x} at T_l sets

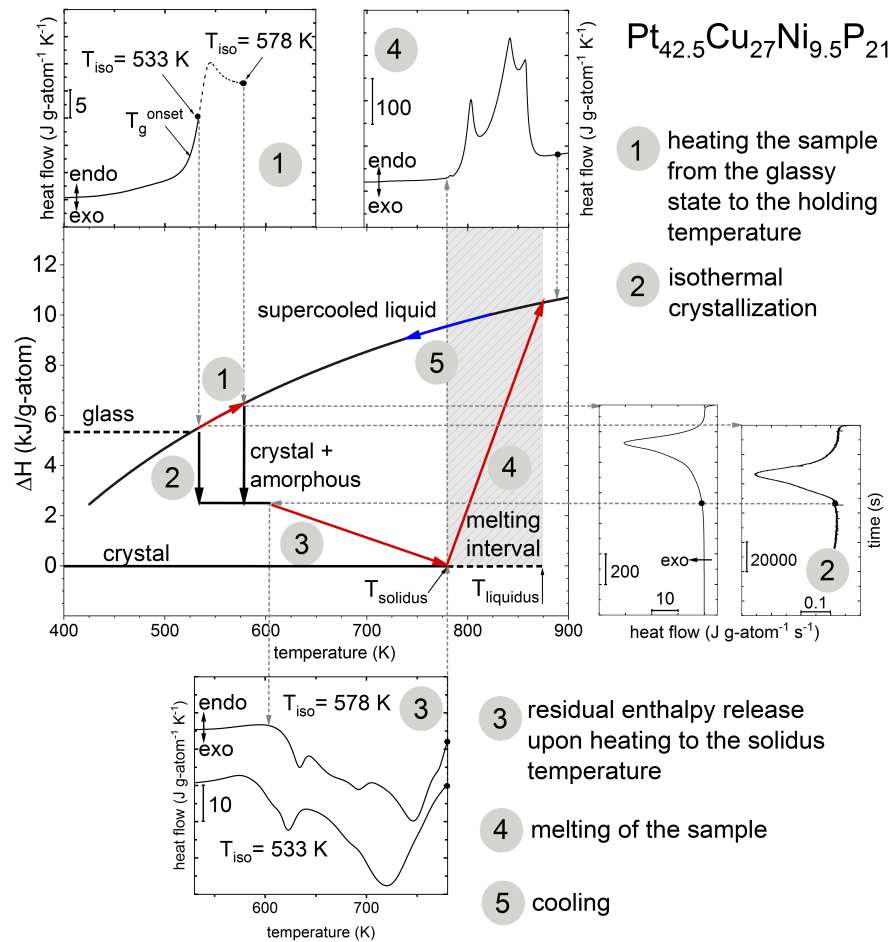


FIGURE 5.3: Enthalpy pathway of the $\text{Pt}_{42.5}\text{Cu}_{27}\text{Ni}_{9.5}\text{P}_{21}$ composition during the DSC experiments. (1) Samples are heated from the glassy state at a rate of 2 K/s to various temperatures and held there isothermally. (2) Enthalpy release upon isothermal crystallization. The amount of enthalpy release depends on the annealing temperature. (3) Enthalpy release upon heating the isothermally crystallized sample to the solidus temperature at a rate of 0.333 K/s. (4) Endothermic melting event of the sample at 0.333 K/s. (5) During cooling from the equilibrium liquid, the enthalpy of the liquid decreases with decreasing temperature and the liquid freezes at the glass transition. Figure after Ref. [230].

the enthalpy curve to the upper temperature limit. The horizontal dashed lines represent the enthalpic state frozen-in at the indicated cooling rates, as the intercept corresponds to the fictive temperature, derived from the T_g -shift measurements discussed in the following section.

5.1.2 The kinetic fragility

The kinetic fragility of the BMG forming liquids is determined by measuring the temperature dependence of the equilibrium viscosity. Figure 5.5 shows isothermal viscosity measurements below the calorimetric glass transition for the $\text{Pt}_{60}\text{Cu}_{16}\text{Co}_2\text{P}_{22}$ ($T_g(0.333 \text{ K/s}) = 506 \text{ K}$) and the $\text{Pd}_{43}\text{Cu}_{27}\text{Ni}_{10}\text{P}_{20}$ ($T_g(0.333 \text{ K/s}) = 580 \text{ K}$) alloy composition. As the temperature in the isothermal experiments is reached, the re-

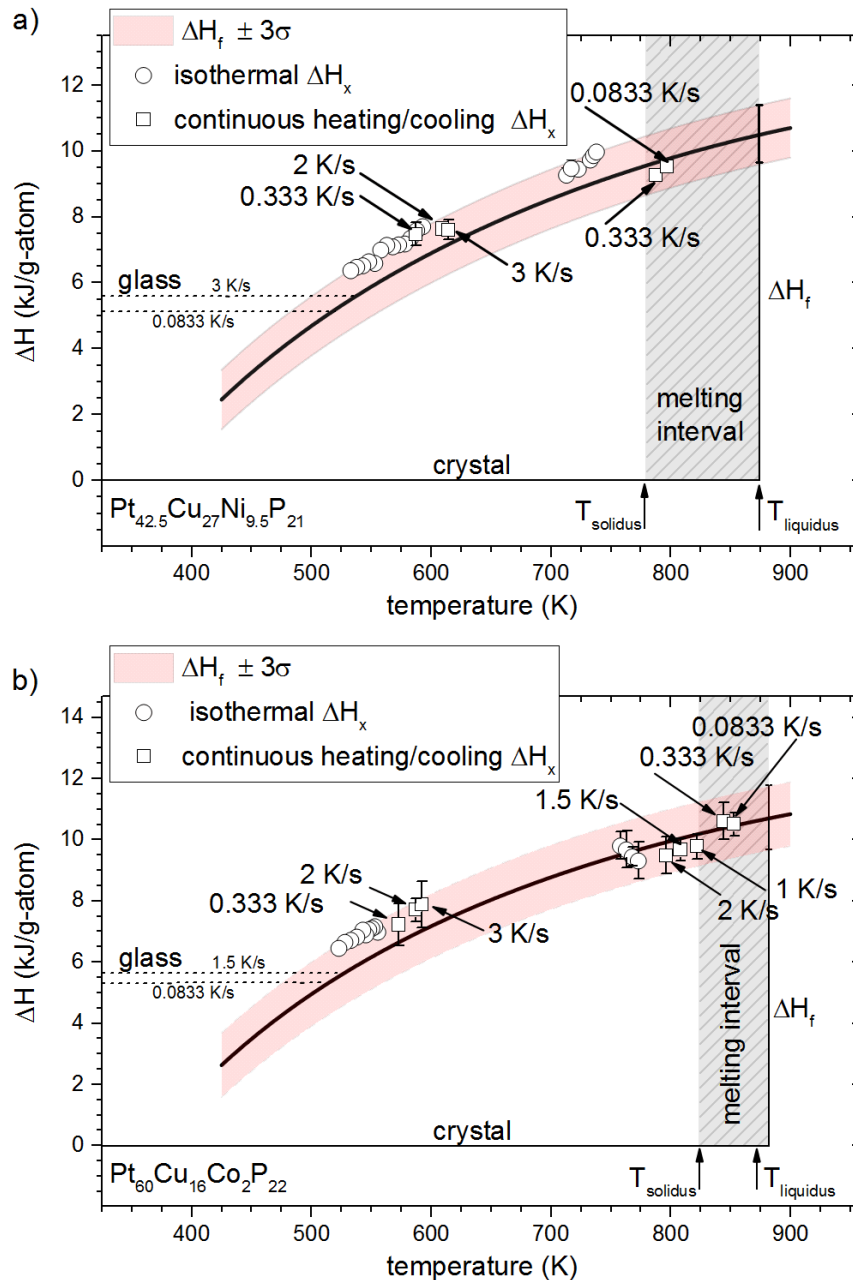


FIGURE 5.4: Enthalpy of the undercooled liquid (a) $\text{Pt}_{42.5}\text{Cu}_{27}\text{Ni}_{9.5}\text{P}_{21}$ and (b) $\text{Pt}_{60}\text{Cu}_{16}\text{Co}_2\text{P}_{22}$ with respect to the crystal as a function of temperature (bold solid line). The shaded area below and above the enthalpy curve of the liquid represents the error interval, taken as three times the standard deviation of the enthalpy of fusion. The crystallization enthalpy is determined in isothermal (\circ) and continuous heating (\square) experiments. The grey-shaded region corresponds to the melting interval of the alloys. Figure taken from Ref. [230].

relaxation of the glass towards the metastable equilibrium state is observed. This relaxation process is accompanied by an increase in viscosity and can be well described by Eq. 2.49. After a certain time, the viscosity of the sample reaches a plateau value corresponding to the metastable equilibrium value of the supercooled liquid.

Another method that is used to determine the kinetic fragility of an alloy is the T_g -shift method (see Chapter 3). As-cast samples were heated at 0.333 K/s into the

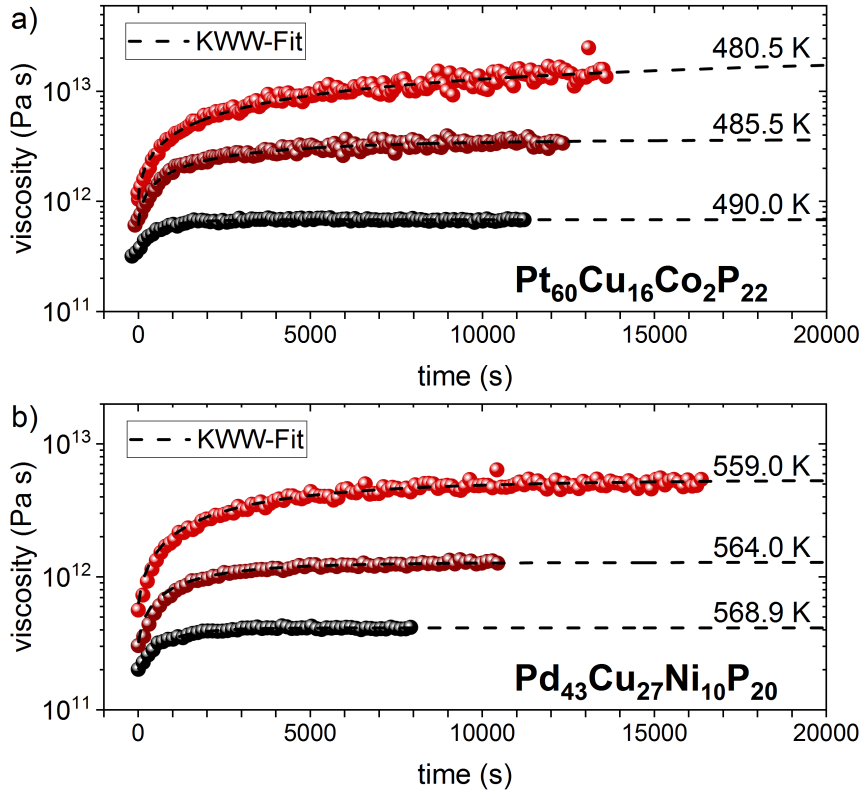


FIGURE 5.5: Isothermal evolution of viscosity below the calorimetric glass transition of $\text{Pt}_{60}\text{Cu}_{16}\text{Co}_2\text{P}_{22}$ (a) and $\text{Pd}_{43}\text{Cu}_{27}\text{Ni}_{10}\text{P}_{20}$ (b) measured by three-point beam bending. The data show the relaxation from the glassy to the supercooled liquid state, which is fitted using Eq. 2.49 (dashed line).

supercooled liquid region and cooled at various rates to room temperature. Subsequently, the samples were heated through the glass transition at the same rate as used in the cooling protocol, which is shown for the $\text{Pt}_{42.5}\text{Cu}_{27}\text{Ni}_{9.5}\text{P}_{21}$ alloy composition in Fig. 5.6. This procedure guarantees that the measured onset of the glass transition corresponds to the fictive temperature [188]. The transition time is calculated according to Eq. 3.15. From the temperature dependence of the transition time the kinetic fragility of the liquid is derived.

Figure 5.7 shows the equilibrium viscosity data, the transition times, τ_{trans} , and the continuously measured viscosity together with the DSC scans of $\text{Pt}_{42.5}\text{Cu}_{27}\text{Ni}_{9.5}\text{P}_{21}$ and $\text{Pt}_{60}\text{Cu}_{16}\text{Co}_2\text{P}_{22}$ as a function of the inverse temperature. The vertical arrows indicate the relaxation pathways of the viscosity during isothermal annealing. The VFT fit (Eq. 2.18) to the experimental isothermal equilibrium viscosity data is represented by a red, dashed line, yielding a D^* and a T_0 of 15.3 and 354.4 K for $\text{Pt}_{42.5}\text{Cu}_{27}\text{Ni}_{9.5}\text{P}_{21}$ and 11.8 and 371.4 K for $\text{Pt}_{60}\text{Cu}_{16}\text{Co}_2\text{P}_{22}$. These values indicate a fragile liquid behavior for the investigated Pt-P-based alloys, which is in accordance to the values derived for other Pt- and Pd-based alloys [231, 232]. The DSC scan depicted in the lower panel was performed with an equivalent heating rate as the continuously measured viscosities, illustrating that a significant softening occurs when the sample undergoes the transition from the glassy to the supercooled liquid state. At the end of the glass transition region, the viscosity follows the VFT fit until crystallization occurs or the TMA deflection limit is reached. The τ_{trans} values shown as half-filled pentagons are not used for the VFT fit. However, τ_{trans} follows the predicted course

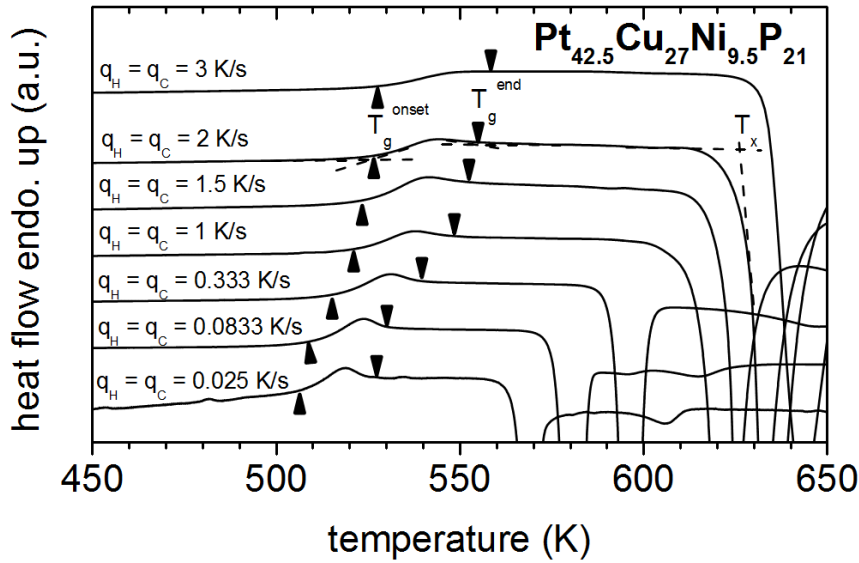


FIGURE 5.6: DSC heat flow curves of $\text{Pt}_{42.5}\text{Cu}_{27}\text{Ni}_{9.5}\text{P}_{21}$. As cast samples were equilibrated by heating them at 0.333 K/s to 550 K and cooling them down to the glassy state at different cooling rates q_c . Subsequently, scans were performed with the heating rate $q_h = q_c$. The triangles tag the onset and end of the glass transition, as obtained by the tangent construction. T_x indicates the onset of crystallization.

Figure taken from Ref. [67].

of the VFT fit, confirming the fragile liquid behavior. The factor connecting τ_{trans} and the measured viscosity ($G_{\tau-\eta}$ ¹) are calculated according Eq. 2.1. The value for the $\text{Pt}_{42.5}\text{Cu}_{27}\text{Ni}_{9.5}\text{P}_{21}$ and $\text{Pt}_{60}\text{Cu}_{16}\text{Co}_2\text{P}_{22}$ BMG forming liquids are $1.93 \times 10^8 \text{ Pa} \pm 0.46 \times 10^8 \text{ Pa}$ and $8.97 \times 10^7 \text{ Pa} \pm 1.37 \times 10^7 \text{ Pa}$. As mentioned by Masuhr et al., $G_{\tau-\eta}$ does not coincide with the high frequency shear modulus, G_∞ , in Eq. 2.1 [111]. In general, G_∞ is larger than $G_{\tau-\eta}$, which is based on the fact that τ_{trans} is proportional but not identical to the structural α -relaxation time τ_α . The proportionality can be derived from the identical slopes of $\tau_{trans}(T)$ and $\eta(T)$ in the glass transition region in Fig. 5.7, representing the fragility of the liquids (Eq. 2.20). From the measured G_∞ -values in metallic glasses [233] it is derived that τ_α is approximately two orders of magnitude faster than τ_{trans} [111].

The VFT fits of the different Pt-P-based alloys are shown in Fig. 5.8. Their kinetically fragile behavior contrasts that of many Zr-, Au-, Fe- and Mg-based BMG forming liquids, featuring large D^* values in the range of 20 to 35 [21, 40, 64, 214]. For reasons of comparison, the viscosity curve of the $\text{Fe}_{67}\text{Mo}_6\text{Ni}_{3.5}\text{P}_{12}\text{C}_{5.5}\text{B}_{2.5}$ liquid is depicted in Fig. 5.8 which decreases less rapidly upon heating the supercooled liquid, represented by a D^* value of 21.3 [40]. For the $\text{Pd}_{43}\text{Cu}_{27}\text{Ni}_{10}\text{P}_{20}$ liquid, different fragility parameters can be found in literature [110, 232]. In order to obtain a fragility value that can be compared to that of the Pt-P-based alloys, the equilibrium viscosity of $\text{Pd}_{43}\text{Cu}_{27}\text{Ni}_{10}\text{P}_{20}$ is determined at different temperatures (Fig. 5.5). The equilibrium viscosity values are added to Fig. 5.8 and the corresponding VFT fit yields a D^* of 14.0, which is higher than the values determined in previous studies ($D^*=10.3$ [110]) but comparable to that of the compositionally similar $\text{Pd}_{40}\text{Cu}_{30}\text{Ni}_{10}\text{P}_{20}$ ($D^*=14.5$ [110]) and $\text{Pd}_{42.5}\text{Cu}_{30}\text{Ni}_{7.5}\text{P}_{20}$ ($D^*=16.5$ [231]) liquids. The kinetic parameters of the alloys are summarized in Tab. 5.3.

¹A temperature dependence of $G_{\tau-\eta}$ is neglected.

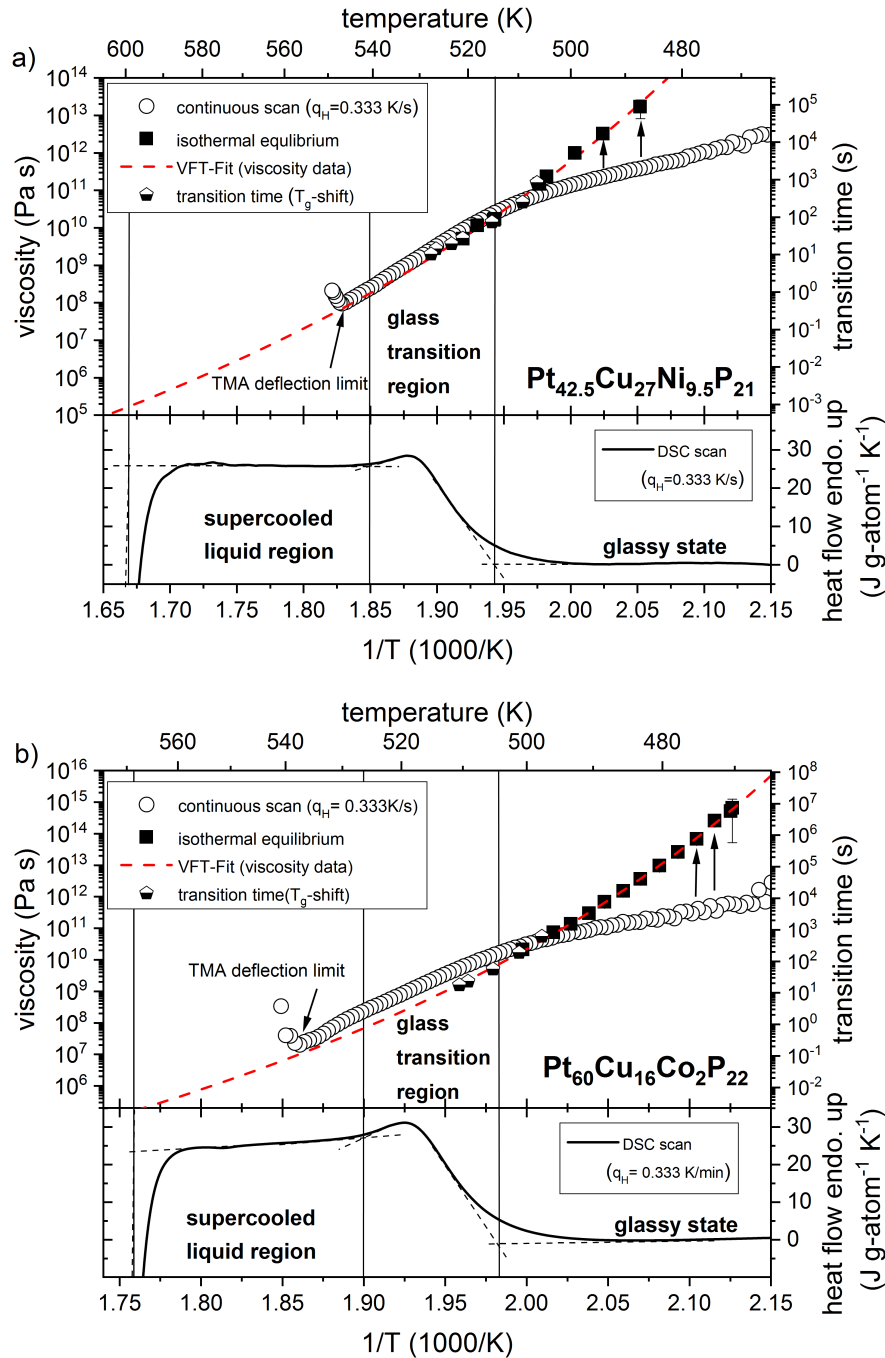


FIGURE 5.7: (a) and (b) show the isothermally determined equilibrium viscosity values (■) and viscosity values measured with a constant heating rate (0.333 K/s) in three-point beam bending experiments (○) of $\text{Pt}_{42.5}\text{Cu}_{27}\text{Ni}_{9.5}\text{P}_{21}$ and $\text{Pt}_{60}\text{Cu}_{16}\text{Co}_2\text{P}_{22}$. The long dashed line corresponds to the VFT fit (Eq. 2.18). The half-filled pentagons represent the transition times measured via the T_g -shift method in DSC (not used for the fits). Also included is a DSC scan of an amorphous sample (bottom). The calorimetric glass transition region agrees with the temperature and time window, in which the viscosity reaches its equilibrium value during the scan. Figure taken from Ref. [67].

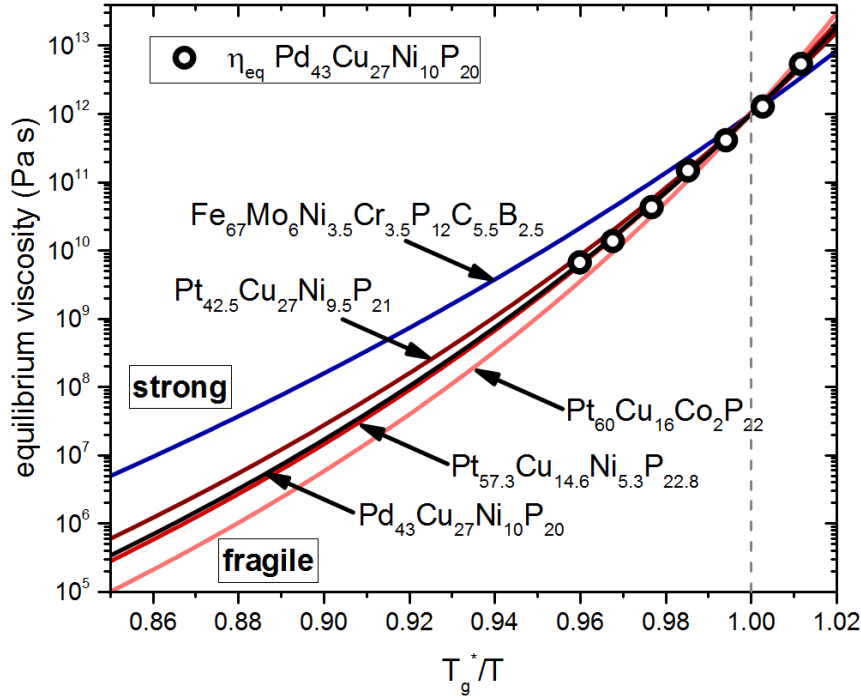


FIGURE 5.8: Angell Plot of the equilibrium viscosity (solid lines, Eq. 2.18) of different BMG forming liquids. For reasons of clarity, only the data points of the $\text{Pd}_{43}\text{Cu}_{27}\text{Ni}_{10}\text{P}_{20}$ liquid are shown.

TABLE 5.3: Kinetic parameters of Pt-P-based liquids. η_0 is the pre-exponential factor, reflecting the high temperature limit of viscosity. T_0 and D^* are the VFT temperature and the fragility parameter obtained as fitting parameter in the VFT equation. m is the fragility index and T_g^* the temperature at which the supercooled liquid reaches a value of 10^{12} Pa s. The values of the Pt-P-based alloys are taken from Ref. [67].

	$\eta_0 \times 10^5$ Pa s	D^*	m	T_0 K	T_g^* K
A	4.0	15.3 ± 0.5	56.9 ± 1.8	354.4 ± 3.5	498.0
B	4.0	13.6 ± 1	62.0 ± 4.8	352.6 ± 7	479.1
C	3.8	11.8 ± 0.1	69.2 ± 0.6	371.4 ± 0.8	487.0
D	4.0	14.0 ± 0.3	60.6 ± 1.3	412.4 ± 2.4	565.4

- A, $\text{Pt}_{42.5}\text{Cu}_{27}\text{Ni}_{9.5}\text{P}_{21}$
 B, $\text{Pt}_{57.3}\text{Cu}_{14.6}\text{Ni}_{5.3}\text{P}_{22.8}$
 C, $\text{Pt}_{60}\text{Cu}_{16}\text{Co}_2\text{P}_{22}$
 D, $\text{Pd}_{43}\text{Cu}_{27}\text{Ni}_{10}\text{P}_{20}$

5.2 Crystallization of the supercooled liquid

Figure 5.9 shows the continuous cooling, the isothermal low temperature and isothermal high temperature experiments for the $\text{Pt}_{42.5}\text{Cu}_{27}\text{Ni}_{9.5}\text{P}_{21}$ alloy composition. In the case of the high temperature measurements, the liquids were covered with B_2O_3 in order to prevent the samples from oxidation. In the continuous cooling

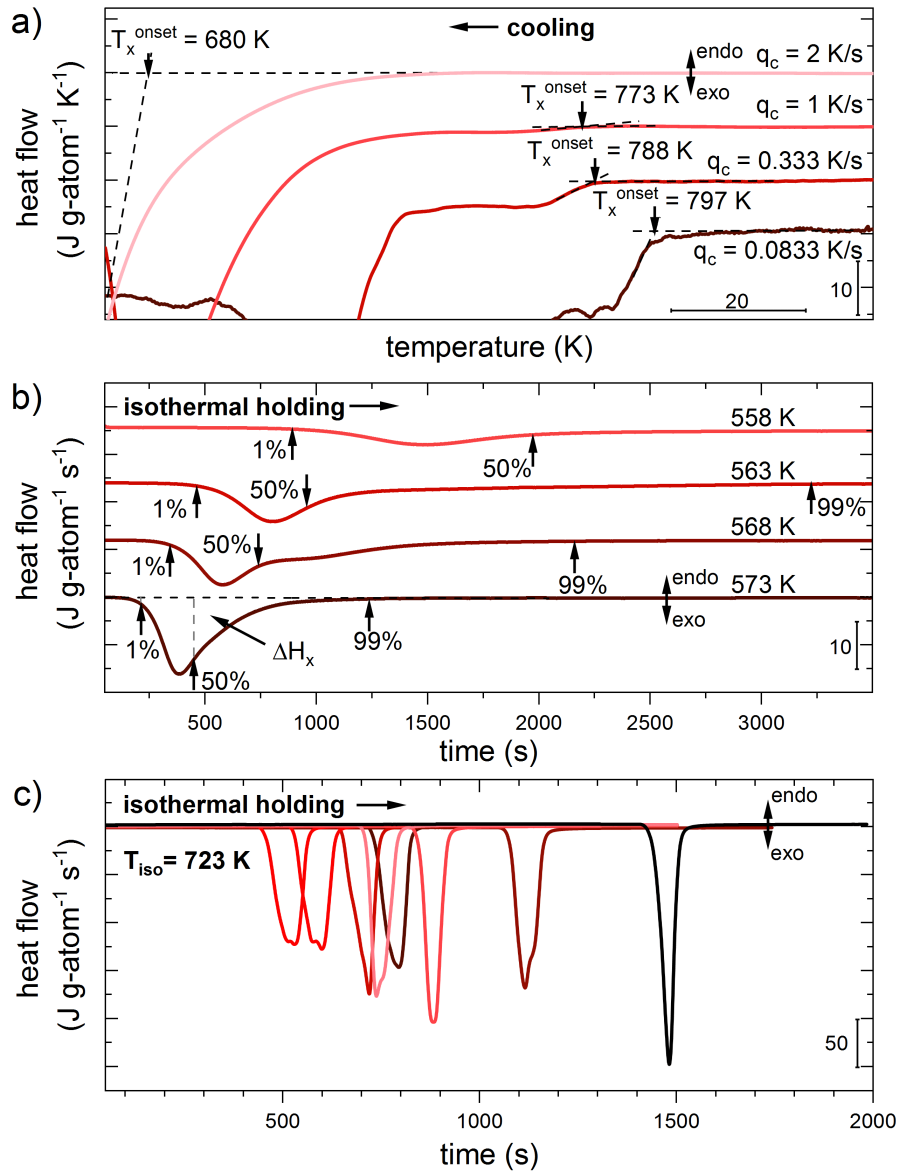


FIGURE 5.9: Crystallization experiments on $\text{Pt}_{42.5}\text{Cu}_{27}\text{Ni}_{9.5}\text{P}_{21}$. (a) heat flow signal upon cooling at various rates from 973 K ($T_l=874 \text{ K}$). The exothermic shoulder before the main crystallization peak gets less pronounced for higher cooling rates and vanishes at a rate of 2 K/s . Curves are shifted vertically and horizontally for clarity. (b) isothermal heat flow signal in vicinity of T_g . For higher temperatures, the crystallization event is more localized and shifted to shorter times. (c) isothermal heat flow signals at 150 K below T_l . The individual crystallization events occur in a broad time interval typically observed for nucleation controlled processes. Figure (a) and (b) are taken from Ref. [230].

experiments, the sample is initially heated to 973 K. After a holding time of 120 s, the liquid is cooled at various rates. The direction of the cooling process is indicated by an arrow and the heat flow signals are shifted along both axes for better comparison of the onset of crystallization, T_x^{onset} . An exothermic shoulder before the main crystallization peak is observed for slow cooling rates ($q_c \leq 1$ K/s). As the cooling rate is increased, this characteristic gets less pronounced and is not observed for a q_c of 2 K/s. The disappearance of this primary crystallization event with increasing cooling rates indicates that it is not the limiting process for glass formation. Therefore, the isothermal holding temperature in high temperature crystallization experiments, shown at 723 K in Fig. 5.9(c), is reached at a cooling rate of 2 K/s. As the crystallization process is nucleation controlled at high temperatures, it is subject to a larger statistical fluctuation and occurs over a wide time interval. In contrast, the low temperature crystallization process depicted in Fig. 5.9(b) is growth controlled and arises with little temporal fluctuation.

For the $\text{Pt}_{60}\text{Cu}_{16}\text{Co}_2\text{P}_{22}$ liquid, the heat flow curve of a continuous cooling experiment in Fig. 5.10(a) shows an even more pronounced shoulder-like exothermic signal preceding that of the main crystallization event. This pre-peak corresponds to

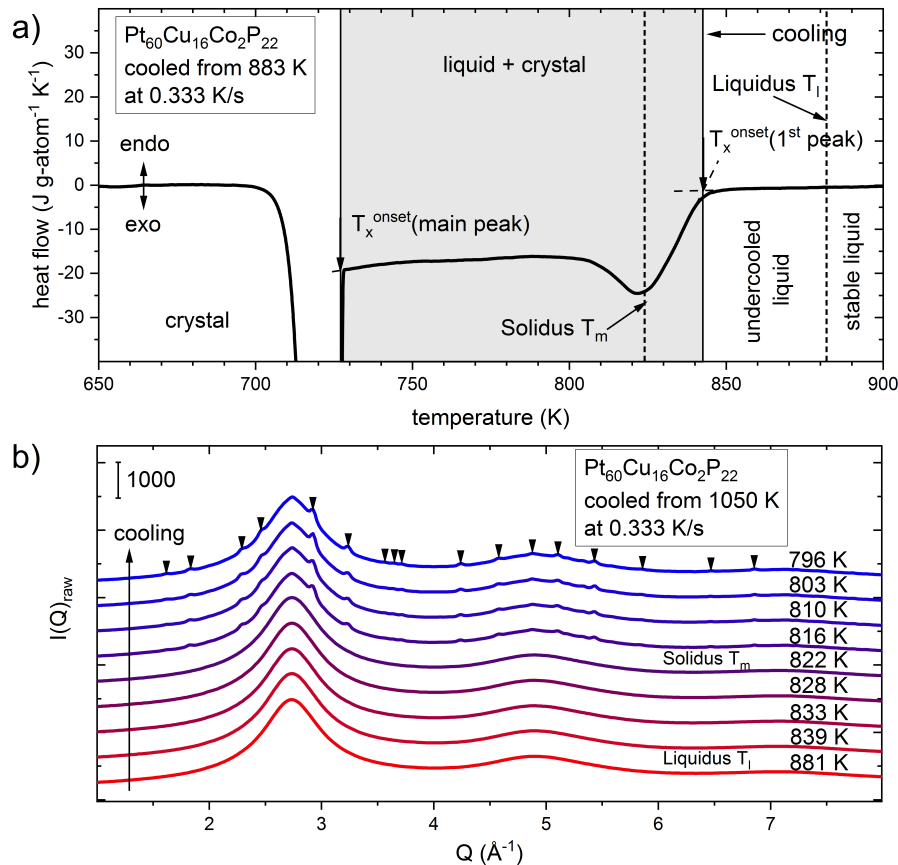


FIGURE 5.10: (a) Heat flow signal of $\text{Pt}_{60}\text{Cu}_{16}\text{Co}_2\text{P}_{22}$ ($T_l=882$ K, $T_m=824$ K) upon cooling from 973 K at a rate of 0.333 K s^{-1} . The primary crystallization sets in at 842 K and the main crystallization at 727 K. The solidus and liquidus temperature upon heating at 0.333 K s^{-1} are marked with a dashed line. (b) Raw synchrotron X-ray diffraction data collected during cooling from 1048 K with a rate of 0.333 K s^{-1} . Right below the solidus temperature Bragg-peaks form, indicating the nucleation of the primary phase. Figure taken from Ref. [230].

the formation of the primary crystalline phase as shown by in-situ synchrotron X-ray experiments (5.10(b)), revealing the development of Bragg-peaks slightly below the solidus temperature. Although T_x^{onset} of the primary phase decreases with increasing cooling rate, its formation is not suppressed even at the highest cooling rate of 3 K s^{-1} (Fig. 5.11). The CCT/CHT diagram of $\text{Pt}_{42.5}\text{Cu}_{27}\text{Ni}_{9.5}\text{P}_{21}$ and $\text{Pt}_{60}\text{Cu}_{16}\text{Co}_2\text{P}_{22}$

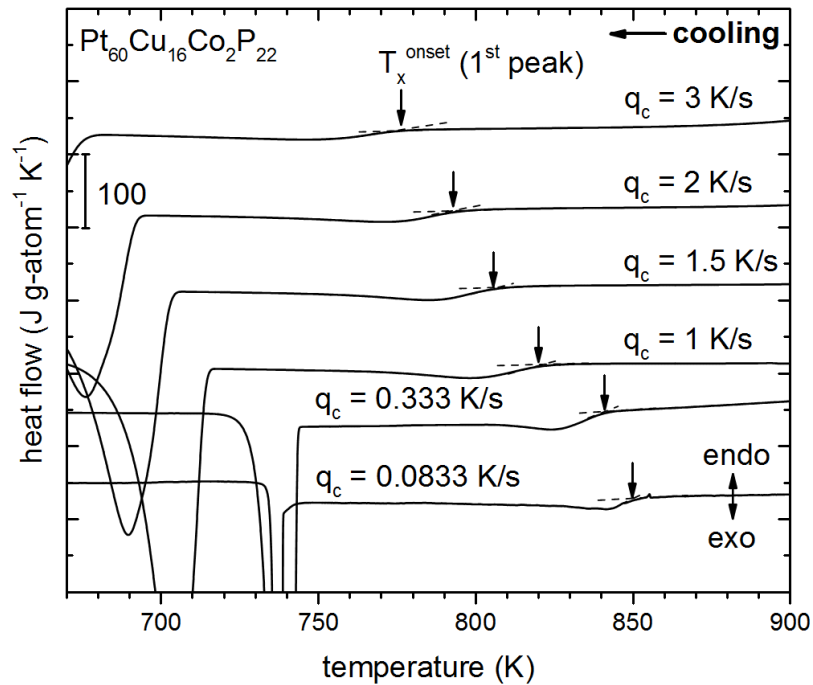


FIGURE 5.11: Heat flow signal of $\text{Pt}_{60}\text{Cu}_{16}\text{Co}_2\text{P}_{22}$ ($T_l=882 \text{ K}$) upon cooling at various rates from 973 K . The exothermic shoulder before the main crystallization peak is observed for all cooling rates. The onset of the pre-peak is marked with a downward arrow. Figure taken from Ref. [230].

P_{22} are obtained by combining the onsets of crystallization upon continuous cooling with the values of the onset temperature and the end temperature of the glass transition (T_g^{onset} and T_g^{end}) as well as the onset of crystallization (T_x) upon heating the glass as a function of the heating rate (Fig. 5.12). The onset temperature of the primary crystallization at a given cooling rate is represented by the open circles, and the half-filled and filled circles correspond to the onset and peak temperature of the main crystallization peak. At low temperatures, T_g^{onset} , T_g^{end} and T_x^{onset} are depicted as open, half-filled and filled squares. The vertical dashed lines in Fig. 5.12(a) and (b) correspond to R_c , calculated according to Eq. 1.1. For the $\text{Pt}_{42.5}\text{Cu}_{27}\text{Ni}_{9.5}\text{P}_{21}$ alloy composition it is observed that the suppression of the primary phase at higher cooling rates leads to a distinct increase in the achievable undercooling. At a cooling rate of 3 K/s , only partial crystallization takes place. During subsequent heating of the samples that were cooled at 3 K/s , 75% of the crystallization enthalpy of a fully amorphous specimen is released [230]. This indicates that the actual R_c is close to the calculated value of 2.5 K/s . However, for the $\text{Pt}_{60}\text{Cu}_{16}\text{Co}_2\text{P}_{22}$ liquid, the formation of the primary phase cannot be avoided during the calorimetric cooling experiments and the calculated R_c of 3.9 K/s needs to be exceeded by far to access the glassy state.

From the isothermal crystallization experiments, the TTT diagrams of $\text{Pt}_{42.5}\text{Cu}_{27}\text{Ni}_{9.5}\text{P}_{21}$ and $\text{Pt}_{60}\text{Cu}_{16}\text{Co}_2\text{P}_{22}$ are constructed (Fig. 5.13). The circles and squares

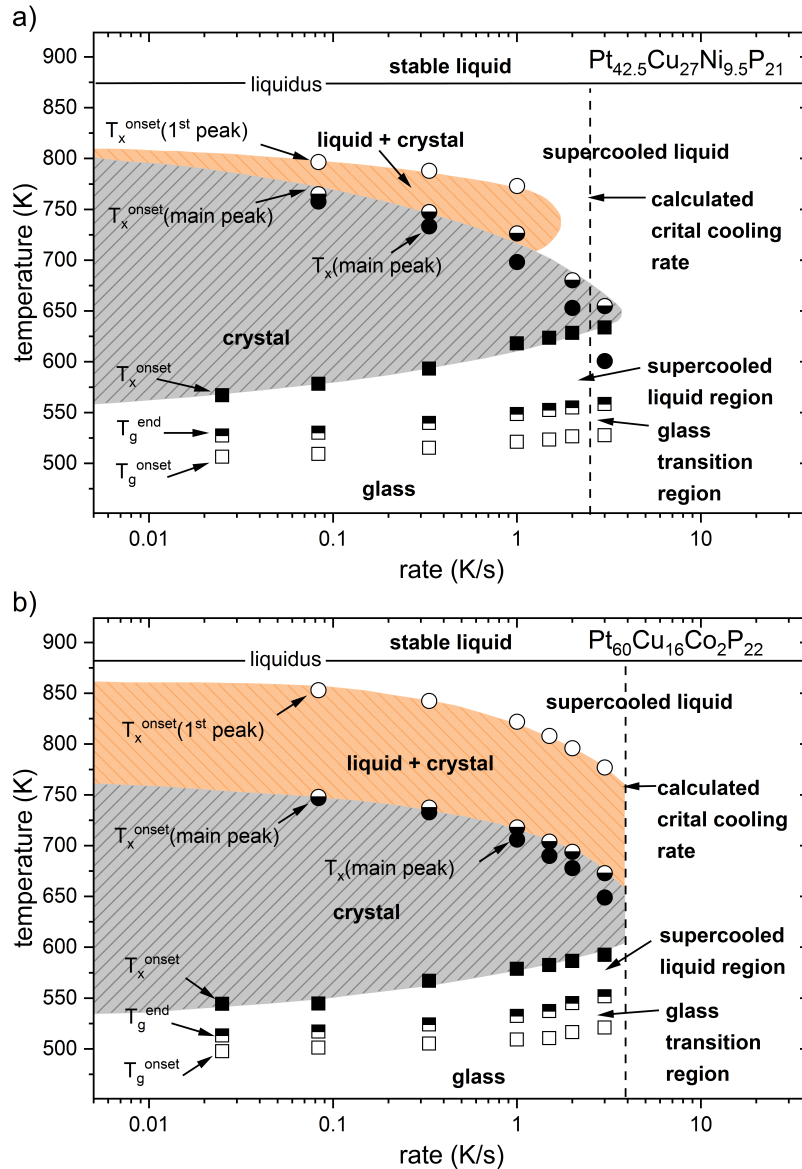


FIGURE 5.12: Continuous heating and cooling transformation diagram of (a) $\text{Pt}_{42.5}\text{Cu}_{27}\text{Ni}_{9.5}\text{P}_{21}$ and (b) $\text{Pt}_{60}\text{Cu}_{16}\text{Co}_2\text{P}_{22}$. The open circles represent the onset of the primary crystallization. The half-filled and filled circles correspond to the onset and the peak minimum of the main crystallization peak. In the low temperature regime T_g^{onset} onset, T_g^{end} and T_x^{onset} are illustrated as open, half-filled and filled squares. Prior to heating, samples were cooled from the supercooled liquid state with the same rate as used upon heating. The shaded areas represent the region where the liquid partially or fully crystallizes. The dashed line corresponds to the critical cooling rate, calculated from the critical casting thickness (Eq. 1.1). Figure taken from Ref. [230].

represent different degrees of crystallinity (1, 50, and 99%), obtained from the integration of the isothermal heat flow curves (see Fig. 5.9(b)). The solid line represents the equilibrium line of the glass transition event which is calculated according to Eq. 2.44 using the $G_{\tau-\eta}$ of $\text{Pt}_{42.5}\text{Cu}_{27}\text{Ni}_{9.5}\text{P}_{21}$ and $\text{Pt}_{60}\text{Cu}_{16}\text{Co}_2\text{P}_{22}$, respectively. The tran-

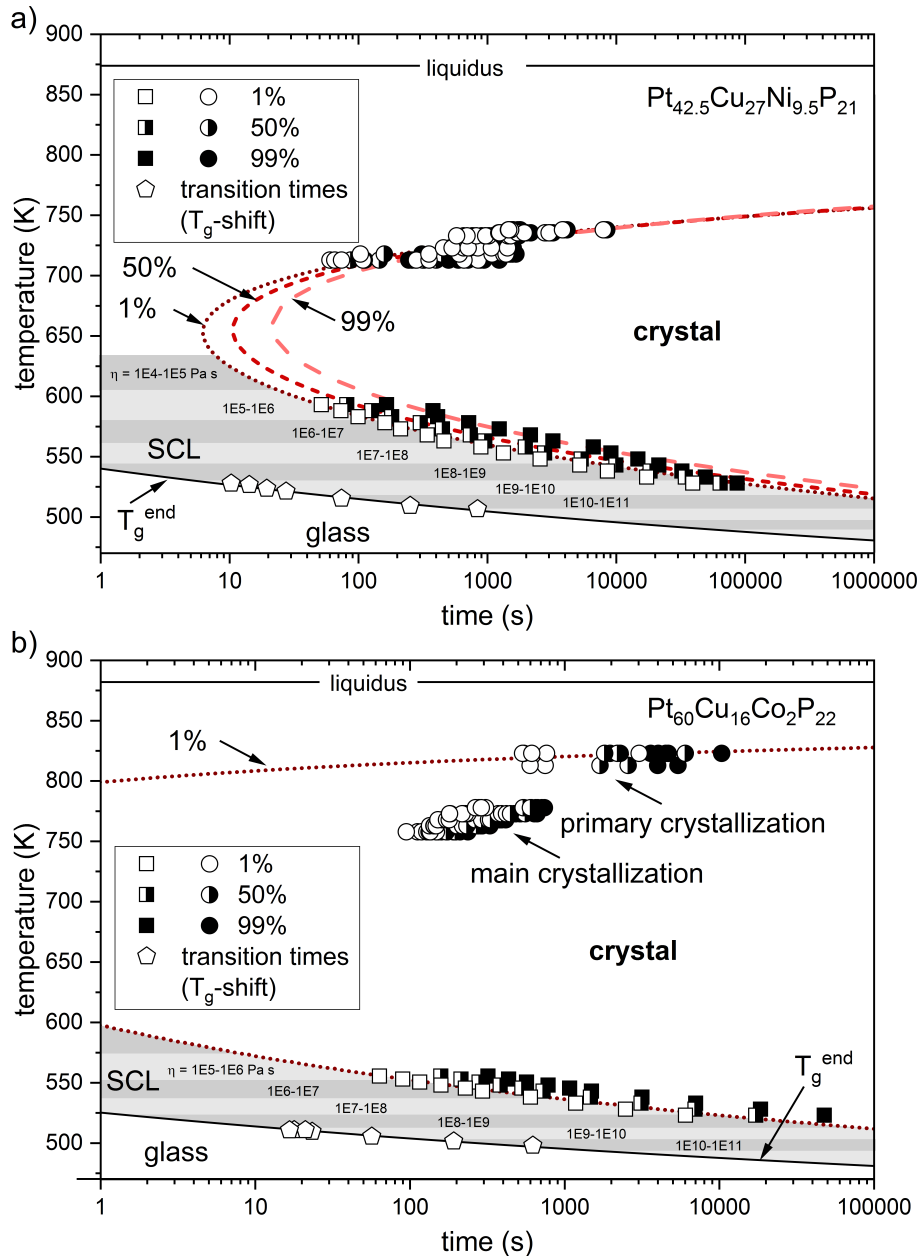


FIGURE 5.13: Time-temperature-transformation diagram of (a) $\text{Pt}_{42.5}\text{Cu}_{27}\text{Ni}_{9.5}\text{P}_{21}$ and (b) $\text{Pt}_{60}\text{Cu}_{16}\text{Co}_2\text{P}_{22}$. The open, half-filled and filled circles and squares represent the times at which 1, 50 and 99% of the crystallization is completed. In the case of $\text{Pt}_{60}\text{Cu}_{16}\text{Co}_2\text{P}_{22}$, the high temperature data is divided into primary and main crystallization. The open pentagons correspond to transition times obtained from T_g -shift measurements (Fig. 5.6). The solid line reflects the equilibrium line at which the glass is isothermally relaxed into the supercooled liquid state calculated from the VFT parameter (Tab. 5.3). The brighter and darker shaded areas represent different orders of magnitude in the equilibrium viscosity (in Pa s) of the SCL. The dotted line represents the fit to the open, the short-dashed line to the half-filled and the dashed to the filled symbols using Eq. 2.43. The data points of the main crystallization of $\text{Pt}_{60}\text{Cu}_{16}\text{Co}_2\text{P}_{22}$ are neglected for the fitting. Figure taken from Ref. [230].

sition times, obtained from T_g -shift measurements, are shown as open pentagons. Within the SCL region, each shaded section represents one order of magnitude in viscosity. The other lines are fits with Eq. 2.43 to the isothermal crystallization data and discussed later in detail.

5.3 Compositional dependent and temperature-induced structural evolution in Pt-P-based liquids

The total-scattering structure function $S(Q)$ is shown upon heating an amorphous as-cast sample of $\text{Pt}_{42.5}\text{Cu}_{27}\text{Ni}_{9.5}\text{P}_{21}$ at a heating rate rate of 0.333 K s^{-1} in Fig. 5.14. The right panel in Fig. 5.14 displays a DSC scan performed at the same heating rate serving as a temperature reference. Within the glassy and SCL state, the amorphous

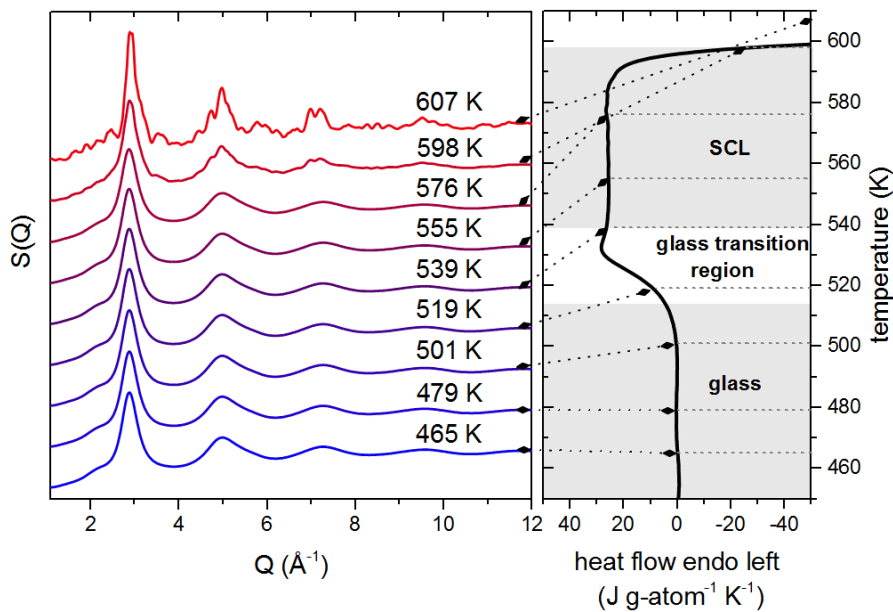


FIGURE 5.14: Temperature-induced evolution of the total-scattering structure function of $\text{Pt}_{42.5}\text{Cu}_{27}\text{Ni}_{9.5}\text{P}_{21}$. At the calorimetric crystallization onset, broad Bragg peaks evolve, indicating the formation of small crystals. Both samples were heated at 0.333 K s^{-1} .

sample exhibits the typical broad diffraction patterns. This changes as soon as the exothermic crystallization event is reached. At low temperatures, the crystallization process is growth controlled, which leads to the formation of a plethora of small crystals reflected by the arising broad Bragg-peaks. A significant feature of $S(Q)$ of $\text{Pt}_{42.5}\text{Cu}_{27}\text{Ni}_{9.5}\text{P}_{21}$ is the pre-peak at approximately 2.1 \AA^{-1} , preceding the first sharp diffraction peak (FSDP) of the amorphous structure. The exception of this characteristic becomes apparent when the total-scattering structure functions of different Pt-P and Pd-P-based BMGs are compared (Fig. 5.15). Neither the other Pt-P-based alloys, $\text{Pt}_{57.3}\text{Cu}_{14.6}\text{Ni}_{5.3}\text{P}_{22.8}$ and $\text{Pt}_{60}\text{Cu}_{16}\text{Co}_2\text{P}_{22}$, nor $\text{Pd}_{43}\text{Cu}_{27}\text{Ni}_{10}\text{P}_{20}$ exhibit such a pronounced signature at low Q -values. Another feature that is most distinct for the Pd-P-based alloy is the shoulder at the second peak in $S(Q)$ at approximately 5.7 \AA^{-1} . The dependence of the two characteristics on the Pd to Pt ratio is depicted in Fig. 5.16. With increasing Pt content, the pre-peak at low Q -values evolves whereas the shoulder of the second diffraction peak diminishes. It should be noted that the samples used for the diffraction experiments at 298 K were cut from plates of the

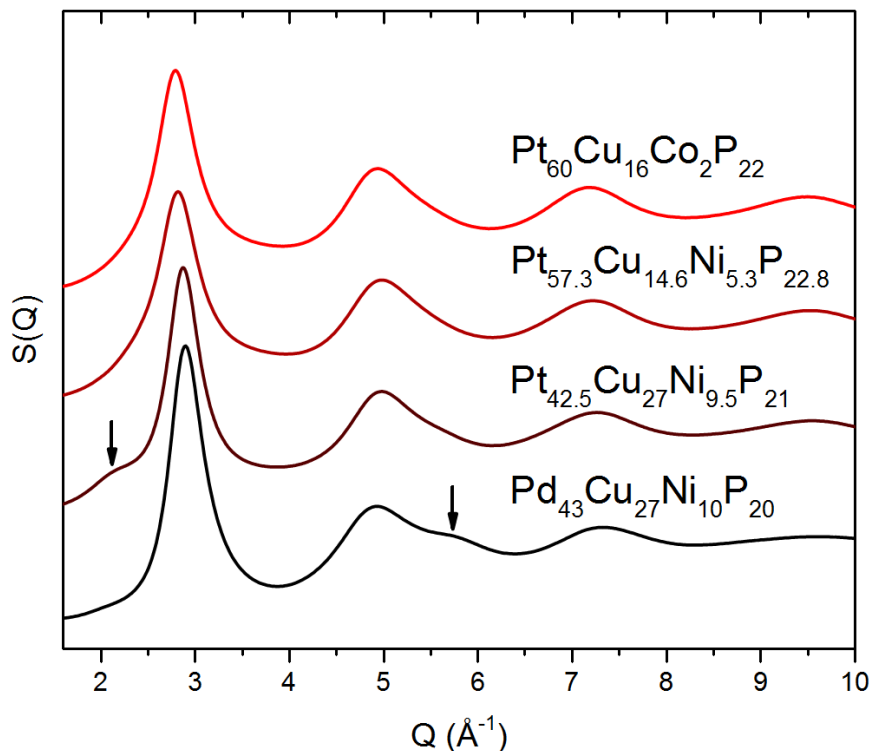


FIGURE 5.15: Total-scattering structure function of $\text{Pt}_{42.5}\text{Cu}_{27}\text{Ni}_{9.5}\text{P}_{21}$, $\text{Pt}_{57.3}\text{Cu}_{14.6}\text{Ni}_{5.3}\text{P}_{22.8}$, $\text{Pt}_{60}\text{Cu}_{16}\text{Co}_2\text{P}_{22}$ and $\text{Pd}_{43}\text{Cu}_{27}\text{Ni}_{10}\text{P}_{20}$ at 323 K. At low Q -values ($\sim 2.1 \text{ \AA}^{-1}$) only $\text{Pt}_{42.5}\text{Cu}_{27}\text{Ni}_{9.5}\text{P}_{21}$ exhibits a pre-peak. The shoulder at the second peak (5.7 \AA^{-1}) is most pronounced for the $\text{Pd}_{43}\text{Cu}_{27}\text{Ni}_{10}\text{P}_{20}$ alloy composition.

same dimension. Therefore, the samples experienced comparable cooling rates and the observed variation in $S(Q)$ do not originate from differences in the thermal history. In Fig. 5.17, the temperature depended evolution of $S(Q)$ of $\text{Pt}_{42.5}\text{Cu}_{27}\text{Ni}_{9.5}\text{P}_{21}$ and $\text{Pd}_{43}\text{Cu}_{27}\text{Ni}_{10}\text{P}_{20}$ is shown. In the low temperature regime, diffraction patterns were collected during heating cylindrical samples at 0.333 K s^{-1} . The total-scattering structure functions at high temperatures, shown in red, were obtained in continuous cooling experiments from 1153 K at 0.333 K s^{-1} . The arrows indicate the evolution of the peak maxima and minima with decreasing temperature. For both alloy compositions, the peak intensities increase, and the peak width decreases which is attribute on the one hand to a growing structural order and on the other hand to the decreasing atomic vibrations. The maximum of the FSDP shifts to higher values which is, at least in the glassy state, connected to the volume expansion of the sample as discussed in detail later. The opposing movement of the first and second diffraction peak with temperature results in a temperature invariant minimum position in-between the two peaks as indicated by the vertical arrow. The insets in Fig. 5.17 magnify the low Q -region of $S(Q)$ of $\text{Pt}_{42.5}\text{Cu}_{27}\text{Ni}_{9.5}\text{P}_{21}$ and $\text{Pd}_{43}\text{Cu}_{27}\text{Ni}_{10}\text{P}_{20}$. In the case of $\text{Pt}_{42.5}\text{Cu}_{27}\text{Ni}_{9.5}\text{P}_{21}$, the pre-peak vanishes in the equilibrium liquid and gains intensity upon undercooling the liquid. In contrast, the $\text{Pd}_{43}\text{Cu}_{27}\text{Ni}_{10}\text{P}_{20}$ liquid does not exhibit a comparable feature at low Q -values. Instead, the shoulder at the second diffraction peak evolves with decreasing temperature.

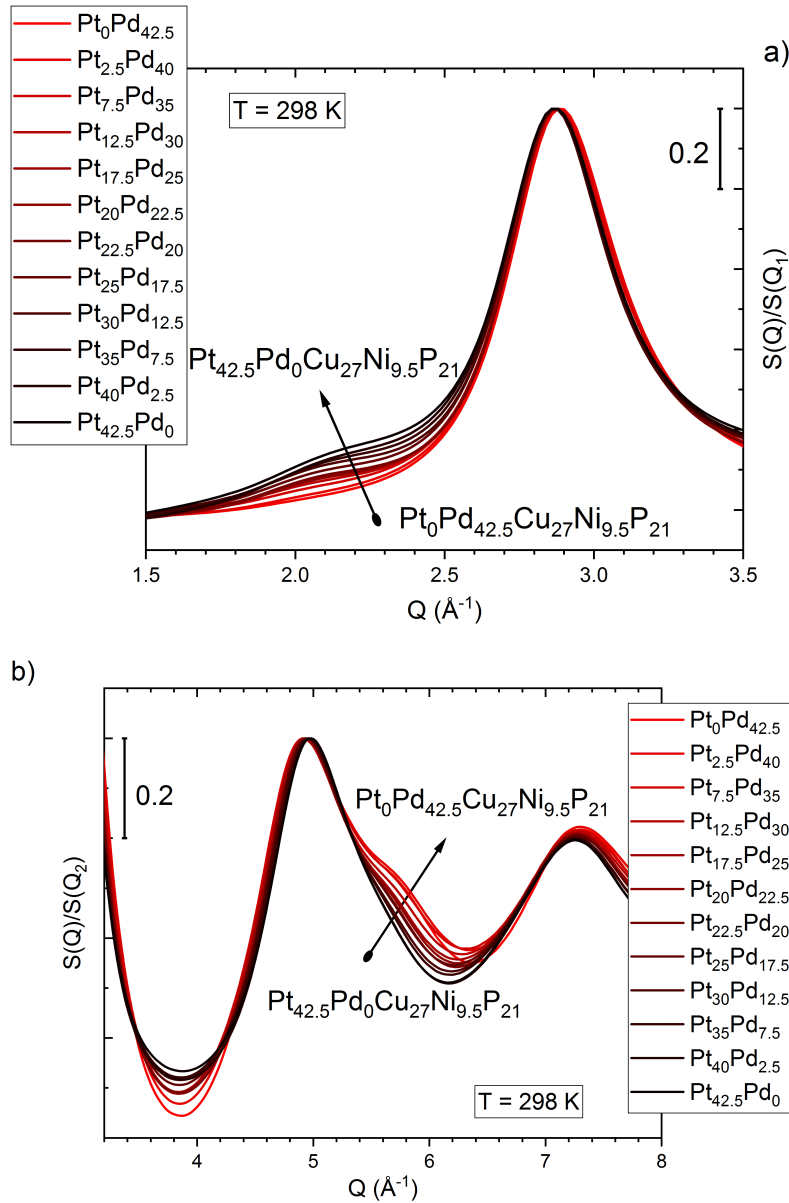


FIGURE 5.16: (a) and (b) show the dependence of the pre-peak at $\sim 2.1 \text{\AA}^{-1}$ and the shoulder at $\sim 5.7 \text{\AA}^{-1}$ on the Pt to Pd ratio. With increasing Pd concentration, the pre-peak in the low Q -range diminishes whereas the characteristic at 5.7\AA^{-1} gets more pronounced. In (a) and (b), $S(Q)$ is normalized to the peak height of the first and second sharp diffraction peak $S(Q_1)$ and $S(Q_2)$. The diffraction experiments were conducted at 298 K. All samples experienced similar cooling rates as they were cut from plates of the same dimension.

5.4 Discussion

5.4.1 Origin of the high glass-forming ability

The glass-forming ability of a liquid depends on the driving force for nucleation, the atomic mobility and the interfacial energy between the liquid and the crystal. All three quantities can be derived or estimated from the results described in the previous sections.

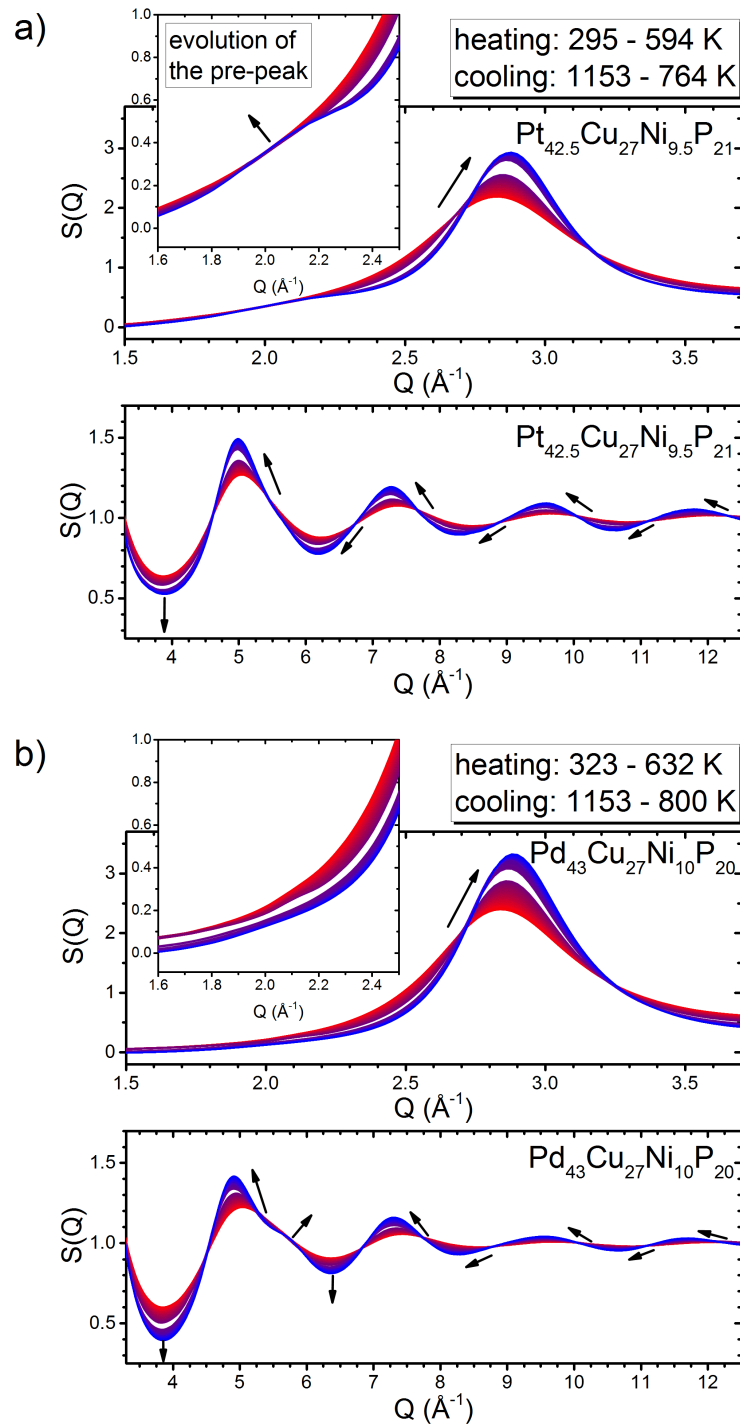


FIGURE 5.17: Total-scattering structure function of (a) $\text{Pt}_{42.5}\text{Cu}_{27}\text{Ni}_{9.5}\text{P}_{21}$ and (b) $\text{Pd}_{43}\text{Cu}_{27}\text{Ni}_{10}\text{P}_{20}$ as function of temperature. The high temperature data (red) were collected upon cooling from 1153 K and those at low temperatures (blue) upon heating from the glassy state. The upper panels show the low Q -range and the insets magnify the region where the pre-peak of $\text{Pt}_{42.5}\text{Cu}_{27}\text{Ni}_{9.5}\text{P}_{21}$ evolves with decreasing temperature. The lower panels show the oscillation of $S(Q)$ at high Q -values. The arrows illustrate the evolution of the peak maxima and minima with decreasing temperature.

The Gibbs free energy difference between the liquid and the crystal for the Pt-P-based alloy is calculated according to Eq. 2.4 and shown in comparison to that of Pd-P-based alloys in Fig. 5.18. It is evident that the Pt-P-based liquids exhibit a sig-

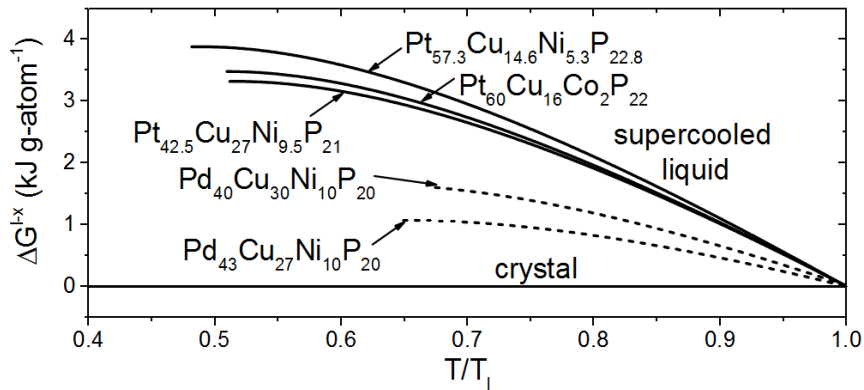


FIGURE 5.18: Gibbs free energy difference between the supercooled liquid and the crystal for Pt-P-based and Pd-P-based bulk glass-forming liquids. Figure taken from Ref. [230]. Data is taken from Refs. [67, 110, 148, 234, 235].

nificantly larger ΔG_{l-x} upon undercooling than the Pd-P-based alloys. This circumstance is also reflected by the large ΔS_f of the Pt-P-based compositions, exceeding that of Pd-P-based by a factor of two. Indeed, $\Delta G_{l-x}(T)$ of the Pd-P-based liquids is among the lowest in BMG forming systems, whereas the course of $\Delta G_{l-x}(T)$ of the Pt-P-based alloys rather resembles that of glass-forming liquids with a very limited GFA ($R_c \sim 250 - 1000 \text{ Ks}^{-1}$ [63]). The large $\Delta G_{l-x}(T)$ decreases the nucleation barrier which affects $I_v(T)$ and $u(T)$ (Fig. 2.12), hampering the glass formation.

From a kinetic point of view, the fragility of a liquid influences the GFA. Experimental observations suggest that the stronger the liquid, the higher the GFA [18, 66, 236, 237]. This becomes apparent in Fig. 2.13 showing the effect of a varying fragility on $I_v(T)$, $u(T)$ and the TTT diagram. The kinetically fragile behavior of the Pt-P-based liquids is therefore detrimental for the GFA. The usage of the temperature depended viscosity as input parameter in Eqs. 2.39 and 2.40 is based on the validity of the Stokes-Einstein relation (Eq. 2.38). It should be noted that the relation hold over 14 orders of magnitude for the Pd atoms in the $\text{Pd}_{43}\text{Cu}_{27}\text{Ni}_{10}\text{P}_{20}$ liquid [113]. However, a decoupling of the diffusivities of Pd and the smaller constituents is observed to evolve below the critical temperature T_c of the mode coupling which is located in the supercooled liquid region at 710 K [113]. In the $\text{Zr}_{46.75}\text{Ti}_{8.25}\text{Cu}_{7.5}\text{Ni}_{10}\text{Be}_{27.5}$ liquid, a decoupling of diffusivities of the large and small atomic species occurs even above T_l [238]. How this decoupling may effect the crystallization process is discussed by Tanaka [108] (see Chapter 2.5.1).

As $\Delta G_{l-x}(T)$ and the kinetic fragile behavior point towards a low GFA in Pt-P-based liquids, these two factors must be compensated by a high interfacial energy. γ_{l-x} contributes to the power of three to the nucleation barrier and distinctly affects $I_v(T)$ as shown in Fig. 2.14. From the fitting of the isothermal crystallization data, γ_{l-x} for the $\text{Pt}_{42.5}\text{Cu}_{27}\text{Ni}_{9.5}\text{P}_{21}$ alloy composition is derived. The fit to the open symbols (1%, Fig. 5.13) yields a γ_{l-x} of 0.11 J m^{-2} ($\pm 6\%^2$) and a pre-factor A_v of $8.19 \times 10^{35} \text{ Pa m}^{-3}$.

²The errors of the experimental input parameters (Tab. 5.1, 5.2 and 5.3) are combined in such a way that a maximum deviation in both directions from the original curve is achieved. In the case of ΔH_f , 3σ ($=\pm 0.9 \text{ kJ/g-atom}$) is used.

The fitting parameter of the fits to the 50 and 99% data points can be found in Tab. 5.4. In order to compare the value of γ_{l-x} of $\text{Pt}_{42.5}\text{Cu}_{27}\text{Ni}_{9.5}\text{P}_{21}$ to that of the compositional related $\text{Pd}_{43}\text{Cu}_{27}\text{Ni}_{10}\text{P}_{20}$ alloy, the crystallization data in Ref. [147] are fitted (Fig. 5.19) using the kinetic parameter listed in Tab. 5.3. The fitting process yields a γ_{l-x} of 0.068 J m^{-2} and an A_v of $2.49 \times 10^{39} \text{ Pa m}^{-3}$. The value of γ_{l-x} is smaller than the value originally derived by Schroers et al. (0.079 J m^{-2} [147]), however it is in good agreement with the results for the $\text{Pd}_{40}\text{Cu}_{30}\text{Ni}_{10}\text{P}_{20}$ alloy composition obtained by Löffler et al., who derived a value of 0.067 J m^{-2} from isothermal crystallization experiments [234]. Therewith, γ_{l-x} in $\text{Pt}_{42.5}\text{Cu}_{27}\text{Ni}_{9.5}\text{P}_{21}$ is 60% larger than

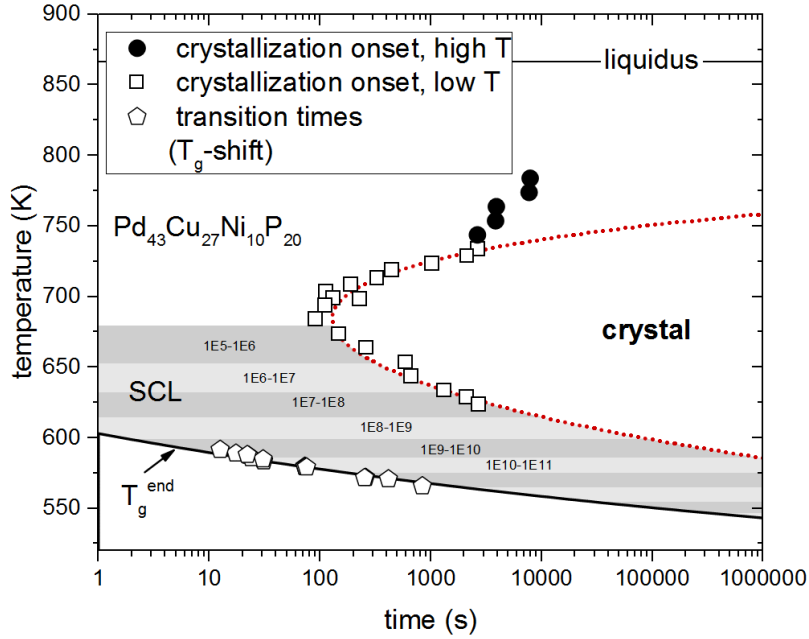


FIGURE 5.19: Time-temperature-transformation diagram of $\text{Pd}_{43}\text{Cu}_{27}\text{Ni}_{10}\text{P}_{20}$. The open squares refer to the onset time for crystallization. The data points at high temperatures indicate a change of the crystallization mechanism and are omitted in the fitting process. The dotted line represents the fit to the experimental low temperature data points. The crystallization data are taken from Ref. [147]. The solid line reflects the equilibrium line at which the glass is isothermally relaxed into the supercooled liquid state calculated from the VFT parameter (Tab. 5.3, $G_{\tau-\eta}=1.66 \times 10^8 \text{ Pa}$) and the open pentagons correspond to transition times obtained from T_g -shift measurements. The brighter and darker shaded areas represent different orders of magnitude in the equilibrium viscosity (in Pa s) of the SCL.

that in $\text{Pd}_{43}\text{Cu}_{27}\text{Ni}_{10}\text{P}_{20}$, emphasizing that γ_{l-x} plays a decisive role for the GFA in Pt-P-based alloys. Legg et al. derived a γ_{l-x} of 0.086 J m^{-2} for the $\text{Pt}_{57.3}\text{Cu}_{14.6}\text{Ni}_{5.3}\text{P}_{22.8}$ alloy composition by comparing isothermal heat flow curves with the JMAK model. The fitting of the experimental data of $\text{Au}_{49}\text{Ag}_{5.5}\text{Pd}_{2.3}\text{Cu}_{26.9}\text{Si}_{16.3}$ ³ obtained by Pogatscher et al. [159] (Fig. 2.20), yielding a γ_{l-x} of 0.039 J m^{-2} , reveals that the entire range of γ_{l-x} values is observed in precious metal based BMG forming liquids. The Zr-based alloys, $\text{Zr}_{41.2}\text{Ti}_{13.8}\text{Cu}_{12.5}\text{Ni}_{10}\text{Be}_{22.5}$ and $\text{Zr}_{60}\text{Co}_{30}\text{Al}_{10}$ exhibit low γ_{l-x} values of 0.04 and 0.014 J m^{-2} , respectively [111, 241].

³For the fitting procedure, ΔH_f and T_l are taken from Ref. [210]. Specific heat capacity data is taken from Ref. [239] and the values of D^* (=9.4) and T_0 (=308.5 K) are based on unpublished data combining high- and low-temperature data, however similar to the values in Ref. [240]

TABLE 5.4: Values of the interfacial energy γ_{l-x} and the pre-factor A_v obtained from the fitting of the isothermal crystallization data. The term crystallinity refers to the time at which 1, 50, and 99% of the total enthalpy at a certain holding temperature is released (see Fig. 5.9(b)). The crystallization data of $\text{Pd}_{43}\text{Cu}_{27}\text{Ni}_{10}\text{P}_{20}$ are labeled as onset time in Refs. [104, 147] and are therefore assumed to correspond to 1% crystallinity.

composition	crystallinity %	γ_{l-x} J/m^2	A_v Pa/m^3
$\text{Pt}_{42.5}\text{Cu}_{27}\text{Ni}_{9.5}\text{P}_{21}$	1	0.1094	8.19×10^{35}
$\text{Pt}_{42.5}\text{Cu}_{27}\text{Ni}_{9.5}\text{P}_{21}$	50	0.1079	1.31×10^{36}
$\text{Pt}_{42.5}\text{Cu}_{27}\text{Ni}_{9.5}\text{P}_{21}$	99	0.1057	4.25×10^{34}
$\text{Pd}_{43}\text{Cu}_{27}\text{Ni}_{10}\text{P}_{20}$	1	0.0680	2.49×10^{39}

For the $\text{Pt}_{60}\text{Cu}_{16}\text{Co}_2\text{P}_{22}$ liquid, the fitting of the crystallization data, shown in Fig. 5.13(b) yields a γ_{l-x} of 0.067 J m^{-2} . However, the minimum waiting time for crystal formation τ_X^* is located at 0.008 s, which is an unreasonable value for an alloy composition possessing a d_c of 16 mm. Using Eq. 2.46 it is estimated that τ_X^* should be located at 4.8 s, which is 2.5 orders of magnitude larger than the value derived from the fitting process. In the case of the $\text{Pt}_{42.5}\text{Cu}_{27}\text{Ni}_{9.5}\text{P}_{21}$ liquid, the calculated τ_X^* is ~ 8.5 s which agrees well with the experimentally determined value of 5.7 s ($\pm 14\%$). It can also be seen in the CCT/CHT diagrams in Fig. 5.12(b) that the calculated R_c for $\text{Pt}_{60}\text{Cu}_{16}\text{Co}_2\text{P}_{22}$ does not coincide with continuous cooling experiments. In contrast, R_c of $\text{Pt}_{42.5}\text{Cu}_{27}\text{Ni}_{9.5}\text{P}_{21}$ (2.5 K s^{-1}), calculated from Eq. 1.1, is close to the value estimated from Fig. 5.12(a). As 75% of the sample are amorphous at a cooling rate of 3 K s^{-1} , the experimental R_c is slightly above 3 K s^{-1} . The discrepancy between the results obtained from the crystallization experiments of $\text{Pt}_{42.5}\text{Cu}_{27}\text{Ni}_{9.5}\text{P}_{21}$ and $\text{Pt}_{60}\text{Cu}_{16}\text{Co}_2\text{P}_{22}$ might be traced back to the fact that the experimental conditions do not allow the suppression of the primary phase. In Zr-based alloys it is observed that liquids require a minimum overheating level of several hundreds of Kelvin in order to obtain the maximum GFA [242]. Hence, the restricted overheating due to the limitation of the DSC might be an explanation for the recurring crystallization of the primary phase. On the other hand, d_c was evaluated in a quenching process where the conditions differ from that prevailing in the DSC experiment. Therefore, the conditions in the DSC experiment (e.g. crucible material, amount of B_2O_3 , constant gas flow) may have facilitated the formation of the primary phase. The continuous and isothermal crystallization experiments performed on $\text{Pt}_{60}\text{Cu}_{16}\text{Co}_2\text{P}_{22}$ seem to be less representative in reflecting the GFA of the alloy, as they suggest a much smaller d_c than reported in literature.

Moreover, it should be noted that JMAK equation is based on several assumptions (see Chapter 2). It is assumed that $I_v(T)$ and $u(T)$ are independent of time. Experiments by Schroers et al. on the $\text{Pd}_{43}\text{Cu}_{27}\text{Ni}_{10}\text{P}_{20}$ have shown that transient nucleation does not play a role on the time scales under investigation [147]. Although the requirement of a polymorphic crystallization is not fulfilled in bulk glass-forming liquids, the theory is commonly able to model the crystallization behavior of such liquids [111, 147, 148, 230, 234]. One might speculate that the observed avalanche-like crystallization at high temperatures, initiated by a local composition fluctuation through the formation of a single supercritical nucleus [147], requires a limited amount of long-range diffusion.

The available data for different BMG forming liquids on the driving force for crystallization (approximated by Gibbs free energy difference between the liquid and the crystal), the kinetic fragility and the interfacial energy are summarized in Fig. 5.20. The plot visualizes that Pt-P-based alloy exhibit extremely high interfacial energies,

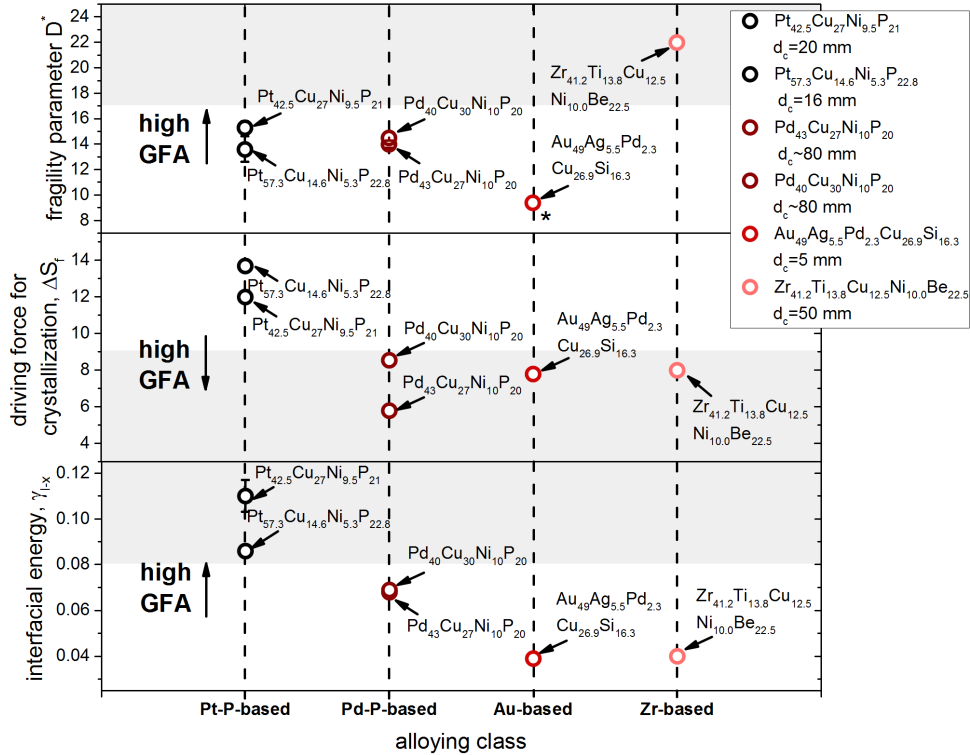


FIGURE 5.20: Comparison of the kinetic fragility, the driving force for crystallization, approximated by the entropy of fusion, and the interfacial energy of different BMG forming liquids. Data of the Pt-P-based alloys are taken from Refs. [15, 67, 75, 148, 230], for the Pd-P-based alloys from Refs. [110, 234, 237], and for the $\text{Zr}_{41.2}\text{Ti}_{13.8}\text{Cu}_{12.5}\text{Ni}_{10}\text{Be}_{22.5}$ alloy composition from Refs. [110, 111, 212, 237]. For the $\text{Au}_{49}\text{Ag}_{5.5}\text{Pd}_{2.3}\text{Cu}_{26.9}\text{Si}_{16.3}$ liquid, the thermodynamic values and the critical casting thickness d_c are taken from Refs. [199, 210]. The D^* value of $\text{Au}_{49}\text{Ag}_{5.5}\text{Pd}_{2.3}\text{Cu}_{26.9}\text{Si}_{16.3}$ is marked (*), as the alloy undergoes a fragile to strong transition [240]. The data point refers to the fragile modification of the liquid. The grayish areas indicate the parameter range facilitating bulk glass formation. The threshold values are arbitrarily set and do not have a physical meaning.

when compared to other BMG forming liquids. Apparently, the large values of the interfacial energies (over)compensates the other two contributions, namely a much larger driving forces combined with a kinetically more fragile behavior. The Pd-P-based alloys are rather stabilized by their low driving force for crystallization, but simultaneously exhibit a relatively high interfacial energy. The combination of the two properties is surprising as the interfacial energy is proportional to the entropy of fusion (Eq. 2.45). However, it explains the outstanding high GFA of the Pd-P-based liquids. The $\text{Zr}_{41.2}\text{Ti}_{13.8}\text{Cu}_{12.5}\text{Ni}_{10}\text{Be}_{22.5}$ alloy composition can be considered as thermodynamically and kinetically stabilized as it possess a low driving force and high viscosities in the SCL region, resulting in a d_c of 50 mm [237]. In contrast,

the alloy with the lowest GFA, $\text{Au}_{49}\text{Ag}_{5.5}\text{Pd}_{2.3}\text{Cu}_{26.9}\text{Si}_{16.3}$, only exhibits a low driving force. However, the effect of the fragile to strong transition that is observed in the deeply supercooled liquid of melt spun ribbons [240] on the GFA is unknown. The structural changes in the liquid that are associated with a changing fragility probably vary the driving force for crystallization and the interfacial energy. A fragile to strong transition is also observed in $\text{Zr}_{41.2}\text{Ti}_{13.8}\text{Cu}_{12.5}\text{Ni}_{10}\text{Be}_{22.5}$ in vicinity of T_l [243, 244]. The observed hysteresis in viscosity data [243] might indicate a first order transition [244], making the transition cooling rate depended. A similar transition is observed in Vit106a in the supercooled liquid region [86] and its existence is suggested for different Fe-based liquids [40, 41]. Although the interfacial energy of Fe- and Mg-based BMG forming liquids has not been evaluated yet, the strong dependence of d_c on the kinetic fragility, derived from low temperature viscosity measurements, suggests that these alloys are kinetically stabilized [21, 66]. Based on currently available data, BMG forming liquids can be divided into two classes with smooth transitions:

1. Kinetically stabilized (e.g. Zr-based [245], Fe-based [40, 66], Mg-based [21, 65, 246], strong kinetic behavior).
2. Thermodynamically stabilized:
 - (a) Driving force stabilized (Pd-based [110, 247], Zr-based [63], low driving force for crystallization).
 - (b) Interfacial energy stabilized [148, 230] (Pt-based, high energy barrier).

This classification of the BMG forming liquid is visualized in Fig. 5.21. The outer circle separates BMG forming liquids in kinetically (blue) and thermodynamically stabilized (yellow). The inner circle contains a number of BMG forming liquids the GFA of which originates from sluggish kinetics, a low driving force or a high interfacial energy (middle circle).

5.4.2 Differences between Pt- and Pd-P-based alloys and the role of short- and medium-range order

The compositional similarities, the interchangeability of Pt and Pd and the comparable kinetic fragility suggest a close connection between Pt-P- and Pd-P-based alloys. However, the previous discussion on the origin of the GFA indicates that fundamental differences between the two alloy classes must exist. The differences in the crystal growth rate (one order of magnitude, Fig. 5.22(a)) mainly results from the different Gibbs free energy difference between the liquid and the crystal, whereas the high interfacial energy of $\text{Pt}_{42.5}\text{Cu}_{27}\text{Ni}_{9.5}\text{P}_{21}$ reduces the difference in the nucleation rate to approximately two orders of magnitude. The combination of a lower growth and nucleation rate yields a minimum isothermal crystallization time of 128.5 s for $\text{Pd}_{43}\text{Cu}_{27}\text{Ni}_{10}\text{P}_{20}$ in comparison to 5.7 s for $\text{Pt}_{42.5}\text{Cu}_{27}\text{Ni}_{9.5}\text{P}_{21}$ (Fig. 5.22(b)). The interfacial energy and the entropy of fusion, representing the driving force for crystallization, are properties that are not exclusively attributed to the liquid phase as they depend on the competing crystals. However, the large variation in ΔS_f between $\text{Pd}_{43}\text{Cu}_{27}\text{Ni}_{10}\text{P}_{20}$ ($\Delta S_f = 5.8 \text{ J g-atom}^{-1} \text{ K}^{-1}$) and $\text{Pt}_{42.5}\text{Cu}_{27}\text{Ni}_{9.5}\text{P}_{21}$ ($\Delta S_f = 12 \text{ J g-atom}^{-1} \text{ K}^{-1}$) is most probably not solely traced back to different entropic states of the crystalline mixtures. It rather suggests that the two liquids possess different structural states at T_l . This working hypothesis draws the picture of a rather disordered $\text{Pt}_{42.5}\text{Cu}_{27}\text{Ni}_{9.5}\text{P}_{21}$ liquid and a $\text{Pd}_{43}\text{Cu}_{27}\text{Ni}_{10}\text{P}_{20}$ liquid the structure of which

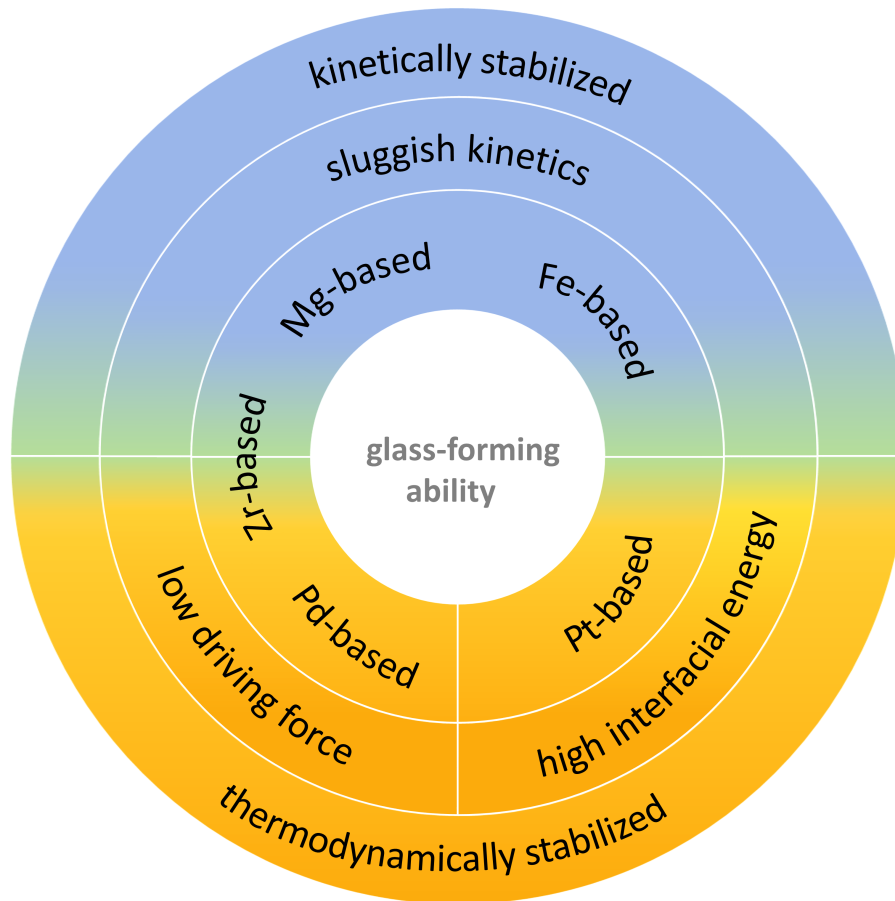


FIGURE 5.21: Schematic illustration of the origin of the glass-forming ability of different bulk metallic glass-forming systems. The thermodynamically stabilized liquids can be separated in driving force and interfacial energy stabilized. Kinetically stabilized alloys feature sluggish kinetics represented by a large D^* value. Figure taken from Ref. [230].

might already involve a certain degree of SRO in the equilibrium liquid. The entropic surplus of the Pt-P-based liquids is reduced upon cooling through a rapidly ascending specific heat capacity of the liquid which might point towards an active ordering process (Fig. 5.23). In contrast, the kinetically fragile Pd-P-based liquids only show a moderate increase in the specific heat capacity upon cooling towards the glass transition (Fig. 5.23). This behavior is usually attributed to kinetically strong BMG forming liquids as the associated viscosity also changes less rapidly (see Chapter 2).

Indeed, the different characteristics observed in the $S(Q)$ curves of the Pt-P- and Pd-P-based alloys in Fig. 5.15 indicate a varying atomic structure in the alloys. On the one hand, only the $\text{Pd}_{43}\text{Cu}_{27}\text{Ni}_{10}\text{P}_{20}$ alloy composition exhibits a pronounced shoulder towards higher Q -values at the second diffraction peak. Such a signature has been attributed to an icosahedral SRO. In the case of perfect icosahedral SRO, the ratio between the first two peak positions q_2/q_1 and the ratio between the first peak position and the location of the shoulder q_{shoulder}/q_1 is 1.71 and 2.04 [164, 248]. The ratios for the $\text{Pd}_{43}\text{Cu}_{27}\text{Ni}_{10}\text{P}_{20}$ alloy composition, $q_2/q_1=1.71$ and $q_{\text{shoulder}}/q_1=1.96$, are in good agreement with the expected values⁴. The small deviation indicates a

⁴The location of the shoulder is determined by fitting using two Gaussian functions.

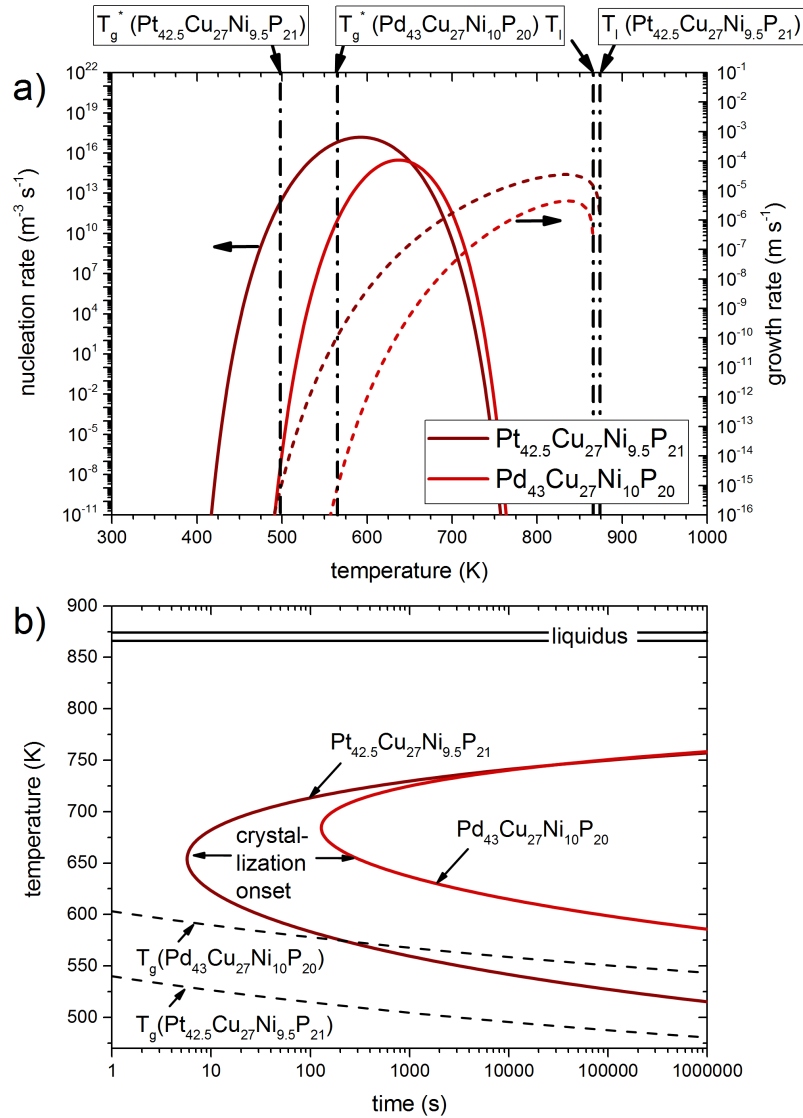


FIGURE 5.22: Comparison of the nucleation rate, growth rate (a) and crystallization time (b) of the $\text{Pt}_{42.5}\text{Cu}_{27}\text{Ni}_{9.5}\text{P}_{21}$ and the $\text{Pd}_{43}\text{Cu}_{27}\text{Ni}_{10}\text{P}_{20}$ alloy composition. Data points of the isothermal crystallization experiments are shown in Figs. 5.13(a) and 5.19.

little distortion of the icosahedral SRO [164]. In the $\text{Pd}_{40}\text{Ni}_{40}\text{P}_{20}$ liquid, Ni-centered icosahedra coexisting with P-centered tricapped trigonal prisms (TTP) are observed as representative structural units [249], supporting the picture of an at least partially icosahedral SRO in $\text{Pd}_{43}\text{Cu}_{27}\text{Ni}_{10}\text{P}_{20}$. This agrees with the results obtained by Park et al., who determined a coordination number (CN, number of nearest neighbors) of 11.4 in $\text{Pd}_{40}\text{Ni}_{40}\text{P}_{20}$ and 12.6 in $\text{Pd}_{40}\text{Cu}_{30}\text{Ni}_{10}\text{P}_{20}$ around Ni atoms [250]. Furthermore, they found that the substitution of Ni by Cu results in a bifurcation of the P environment into a Pd-Ni-P (TTP) and a Pd-Cu-P environment (tetragonal dodecahedron) [250]. The observation might be coupled to a critical Cu concentration beyond which the packing scheme changes from a simple substitution of Ni by Cu to the formation of a new structural unit [173].

On the other hand, only the $\text{Pt}_{42.5}\text{Cu}_{27}\text{Ni}_{9.5}\text{P}_{21}$ alloy composition exhibits a pronounced pre-peak at low Q -values. As argued by Ma et al., the FSDP in $S(Q)$ already contains information on the medium range order (MRO) in the liquid [251].

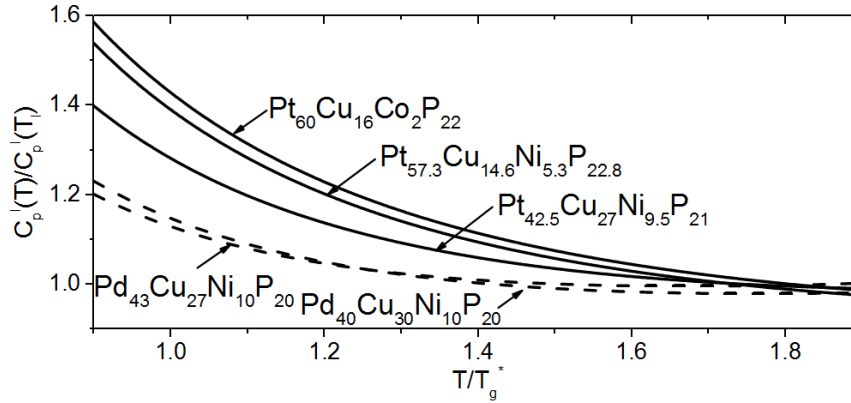


FIGURE 5.23: Specific heat capacity of the liquid normalized to the value at T_l as a function of the T_g^* -scaled temperature. The specific heat capacity in the liquid state increases more rapidly for the Pt-P-based bulk glass-forming liquids. Data taken from Refs. [67, 110, 148, 234]. Figure taken from Ref. [230].

Therefore, the characteristic of a pre-peak which is observed in different metallic glasses is attributed to a distinctly pronounced MRO [252–258]. As the $S(Q)$ of $\text{Pt}_{42.5}\text{Cu}_{27}\text{Ni}_{9.5}\text{P}_{21}$ is dominated by the Pt-Pt and the Pt-Cu partial scattering function (Fig. 3.6), the pre-peak arises most probably from Pt-Pt or Pt-Cu correlations. For the other Pt-P-based alloys, no pre-peak is observed. This might be caused by the greater weighting of the Pt-Pt partial $S(Q)$ due to the increasing Pt concentration making the Pt-Cu correlations less significant. Another possibility is that the MRO in $\text{Pt}_{42.5}\text{Cu}_{27}\text{Ni}_{9.5}\text{P}_{21}$ results from Pt-Pt correlations as the Pt atoms are on average more often separated by a distance larger than the first coordination shell, caused by the large amount of Cu, Ni and P atoms. Upon increasing the Pt concentration, the Pt atoms are less diluted and they are more frequently nearest neighbors to themselves reducing the significance of the MRO. In the $\text{Zr}_{80}\text{Pt}_{20}$ liquid, the pre-peak at low Q -values is found to arise from Pt-Pt correlations [259] and its magnitude rises as the Pt content is increased to 27 at% [253]. The origin of the MRO is the spatial arrangement of the Pt-centered, icosahedral clusters [259]. As the Pt concentration in $\text{Pt}_{42.5}\text{Cu}_{27}\text{Ni}_{9.5}\text{P}_{21}$ is higher and the atomic size of Ni, Cu and P is smaller than that of Zr, a corresponding number of Pt-Pt nearest neighbors should exist and the MRO might rather result from the spatial organization of interconnected, extended clusters or string-like connections [87]. The existence of a distinct MRO in $\text{Pt}_{42.5}\text{Cu}_{27}\text{Ni}_{9.5}\text{P}_{21}$ might also explain the compositional dependence of the kinetic fragility parameter. Consequently, the kinetically stronger behavior of $\text{Pt}_{42.5}\text{Cu}_{27}\text{Ni}_{9.5}\text{P}_{21}$ ($D^*=15.3$) in comparison to $\text{Pt}_{57.3}\text{Cu}_{14.6}\text{Ni}_{5.3}\text{P}_{22.8}$ ($D^*=13.6$) and $\text{Pt}_{60}\text{Cu}_{16}\text{Co}_2\text{P}_{22}$ ($D^*=11.8$) would result from the lower Pt-content giving rise to a more distinct MRO and the low Q pre-peak.

Although compositionally related, the $\text{Pd}_{43}\text{Cu}_{27}\text{Ni}_{10}\text{P}_{20}$ liquid does not exhibit a pre-peak. Mauro et al. noticed that the pre-peak in Zr-Pt vanishes if Pt is replaced by Pd [260]. As the pre-peak in these systems result from noble metal - noble metal correlations, the lower atomic form factor of Pd in comparison to Pt might reduce the detectability of the pre-peak [260]. However, the dominant partial-scattering structure functions in $\text{Pd}_{43}\text{Cu}_{27}\text{Ni}_{10}\text{P}_{20}$ are those of Pd-Pd and Pd-Cu, equivalent to Pt-Pt and Pt-Cu in $\text{Pt}_{42.5}\text{Cu}_{27}\text{Ni}_{9.5}\text{P}_{21}$. The varying extent of the pre-peak and the shoulder at the second diffraction peak upon substituting Pt by Pd (Fig. 5.16) rather suggest that the local representative structural units and their spatial arrangements

in $\text{Pt}_{42.5}\text{Cu}_{27}\text{Ni}_{9.5}\text{P}_{21}$ and $\text{Pd}_{43}\text{Cu}_{27}\text{Ni}_{10}\text{P}_{20}$ are different.

Upon heating the samples above the liquidus temperature, the pre-peak vanishes and the shoulder becomes less pronounced (Fig. 5.17). In many metallic liquids it is well known that icosahedral SRO prevails, even above T_l , and gets more pronounced upon approaching T_g [79–81, 261]. Moreover, the disappearance of the pre-peak in $\text{Pt}_{42.5}\text{Cu}_{27}\text{Ni}_{9.5}\text{P}_{21}$ in the equilibrium liquid in combination with the large ΔS_f and the rapidly decreasing C_p^l upon heating suggest a pronounced reduction or the entire dissolution of the MRO. It should be noted that the vanishing pre-peak might also result from the increasing atomic vibrations upon increasing temperature, diminishing the peak intensity [190]. However, it has been observed in different metallic liquids that the pre-peak remains visible even hundreds of Kelvin above T_l [255, 259] supporting the idea of the dissolution of atomic order.

Using Eq. 3.26, the total-scattering structure functions can be transformed into the reduced pair distribution function $G(r)$. The temperature-induced evolution of $G(r)$ of $\text{Pt}_{42.5}\text{Cu}_{27}\text{Ni}_{9.5}\text{P}_{21}$ and $\text{Pd}_{43}\text{Cu}_{27}\text{Ni}_{10}\text{P}_{20}$ are shown in Fig. 5.24. The arrows indicate the shifts of the peak maxima and minima with decreasing temperature. The shift of the first peak position in $G(r)$, reflecting the weighted, average nearest neighbor distance, towards higher r values with decreasing temperature is commonly observed in metallic liquids [262, 263] and might be attributed to an increasing coordination number [262, 263]. However, Ding et al. noticed that the anomalous peak shift does not necessitate a changing coordination number as it may result from the increasing asymmetry of the peak shape which is a consequence of the anharmonic nature of the interatomic interaction potential [264]. If the skewness is considered, the mean bond length is found to increase with increasing temperature [265].

The first peak position of $G(r)$ at 298 K for the $\text{Pd}_{43}\text{Cu}_{27}\text{Ni}_{10}\text{P}_{20}$ and the $\text{Pt}_{42.5}\text{Cu}_{27}\text{Ni}_{9.5}\text{P}_{21}$ alloy composition is located at approximately 2.77 and 2.79 Å. As $G(r)$ is dominated by the Pt-Pt and Pd-Pd partial reduced pair distribution functions, the first peak position represents in a first approximation the distance of two Pt and two Pd atoms, possessing an atomic radius of 1.39 Å and 1.40 Å [170]. The most apparent difference in $G(r)$ of $\text{Pt}_{42.5}\text{Cu}_{27}\text{Ni}_{9.5}\text{P}_{21}$ and $\text{Pd}_{43}\text{Cu}_{27}\text{Ni}_{10}\text{P}_{20}$ is found at the second peak, reflecting the distances in the second nearest neighbor shell (schematically shown in Fig. 5.25(a)). In both cases a sharpening and a splitting with decreasing temperature is observed. The insets in Fig. 5.24, magnifying the temperature-induced evolution of the second peak, show that two peak maxima evolve for the $\text{Pt}_{42.5}\text{Cu}_{27}\text{Ni}_{9.5}\text{P}_{21}$ liquid, whereas a single maximum with a shoulder on the high r side forms for the $\text{Pd}_{43}\text{Cu}_{27}\text{Ni}_{10}\text{P}_{20}$ alloy composition. A similar splitting of the second peak has been observed in different metallic liquids [82, 266, 267]. Simulations suggest that the peak splitting arises from the uneven distribution of different types of cluster connections (see Fig. 5.25) [82]. The atomic packing motifs may share one, two, three and four atoms [82] and the most probable position of the second nearest neighbor for each cluster connection scheme can be calculated from the average bond length as $2r_1$ (1-atom connection), $\sqrt{3}r_1$ (2-atom connection), $\sqrt{8/3}r_1$ (3-atom connection) and $\sqrt{2}r_1$ (4-atom connection) [82, 268]. As value for r_1 , the first peak position of the reduced pair distribution function is chosen, mainly representing the noble metal - noble metal correlations. The obtained positions for the second nearest neighbor are depicted as vertical dashed lines in the inset in Fig. 5.24. It should be noted that the second nearest neighbor distance in multicomponent liquids is also affected by the number of small atom in the first coordination shell that may be involved in the cluster connections influencing the appearance of the second peak.

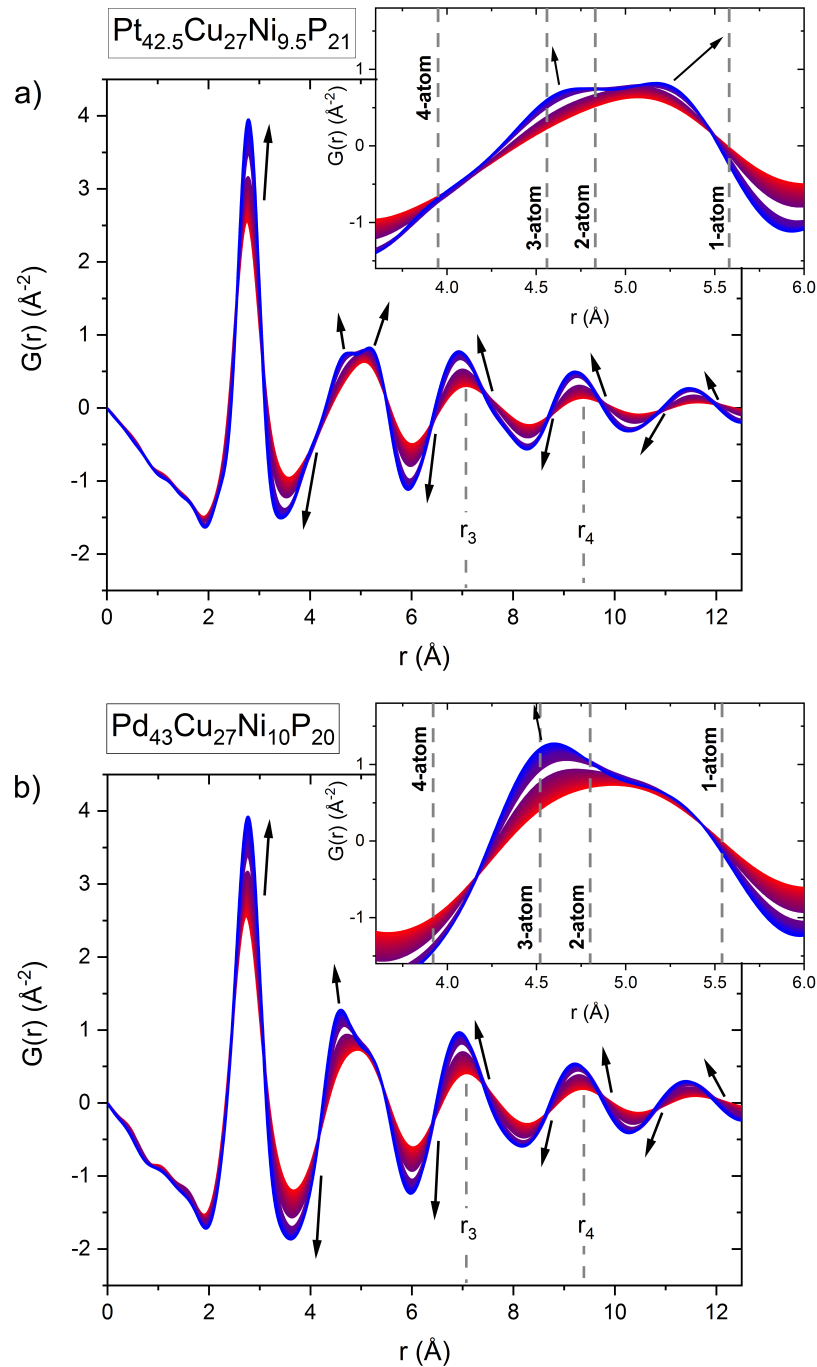


FIGURE 5.24: Reduced pair distribution function of (a) $\text{Pt}_{42.5}\text{Cu}_{27}\text{Ni}_{9.5}\text{P}_{21}$ and (b) $\text{Pd}_{43}\text{Cu}_{27}\text{Ni}_{10}\text{P}_{20}$ as a function of temperature. The high temperature data (red) were collected upon cooling from 1153 K and those at low temperatures (blue) upon heating from the glassy state. The arrows indicate the evolution of the peak maxima and minima with decreasing temperature. The vertical lines marked as r_3 and r_4 indicate the third and fourth peak position that is used to calculate the structural fragility parameter. The insets magnify the second peak, corresponding to the second nearest neighbor distances. The vertical lines in the inset mark the most probable second nearest neighbor distances if adjacent clusters share one, two, three or four atoms calculated from the first peak position.

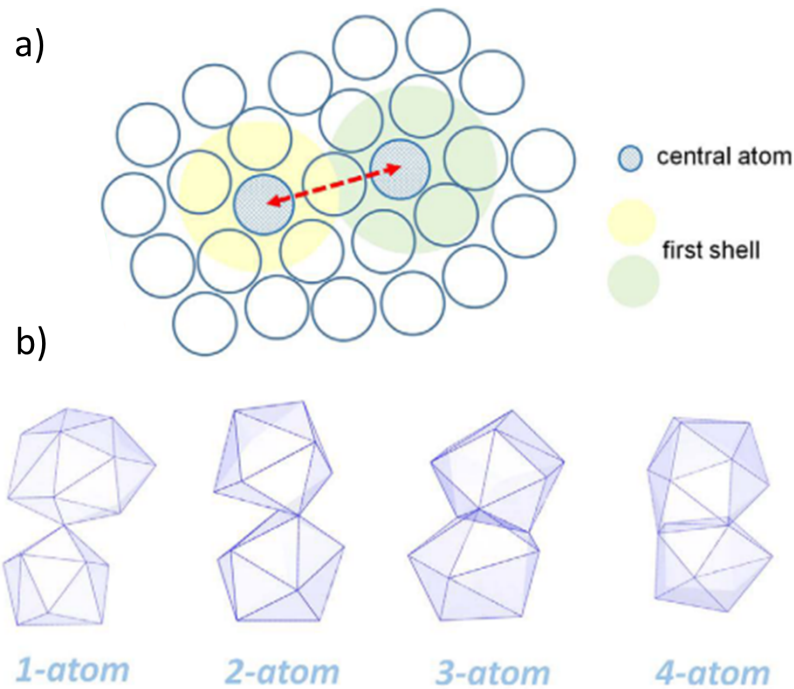


FIGURE 5.25: (a) Schematic illustration of the second nearest neighbor distance (red arrow). The second nearest neighbor atom is also a central atom of another cluster. The central atoms may share one to four nearest neighbor atoms ((b), 1-atom, 2-atom, 3-atom and 4-atom) which affects the distance between the two central atoms (second nearest neighbor distance). The distribution of connection schemes influences the shape of the second peak in the reduce pair distribution function. Figure taken from Ref. [82].

The compositional variation of $G(r)$ on the Pt-Pd axis is shown in Fig. 5.26. The calculated second nearest neighbor positions indicate that the distribution of connection schemes in the Pd-P- and the Pt-P-based alloys varies. In the Pd-P-based liquid, the peak at approximately 4.5 \AA seems to result from central atoms whose clusters are connected via face sharing (3-atom connection). As can be seen in Fig. 5.26, face sharing appears to become less dominant as Pd is replaced by Pt. Instead the 1-atom and 2-atom connection schemes gain importance. The evolving pre-peak at approximately 3.9 \AA suggests that even the 4-atom connection scheme is facilitated by the replacement of Pd. Although these connection schemes are thought to already exist in the high temperature liquid and the peak splitting is smeared out by the thermal vibrations, the structural ordering occurring during cooling also affects the distribution of the connection schemes [82]. Therefore, the sharpening of the features of the second peak observed in Fig. 5.24 are on the one hand attributed to the decreasing atomic vibrations and on the other hand to the growing portion of certain connection schemes at the expense of others [82]. In the case of $\text{Pd}_{43}\text{Cu}_{27}\text{Ni}_{10}\text{P}_{20}$, the 3-atom connections seem to prevail, and its fraction increases upon cooling whereas the structural data of $\text{Pt}_{42.5}\text{Cu}_{27}\text{Ni}_{9.5}\text{P}_{21}$ suggest a larger diversity of connection schemes. As shown in Fig. 5.27 the splitting of the second peak in $G(r)$ only becomes apparent if the maximum Q -range (Q_{max}) for the Fourier transformation of $S(Q)$ is beyond 12 \AA^{-1} . In contrast, the third and fourth peak remain rather unaffected if Q_{max} is varied between 10.5 and 16 \AA^{-1} .

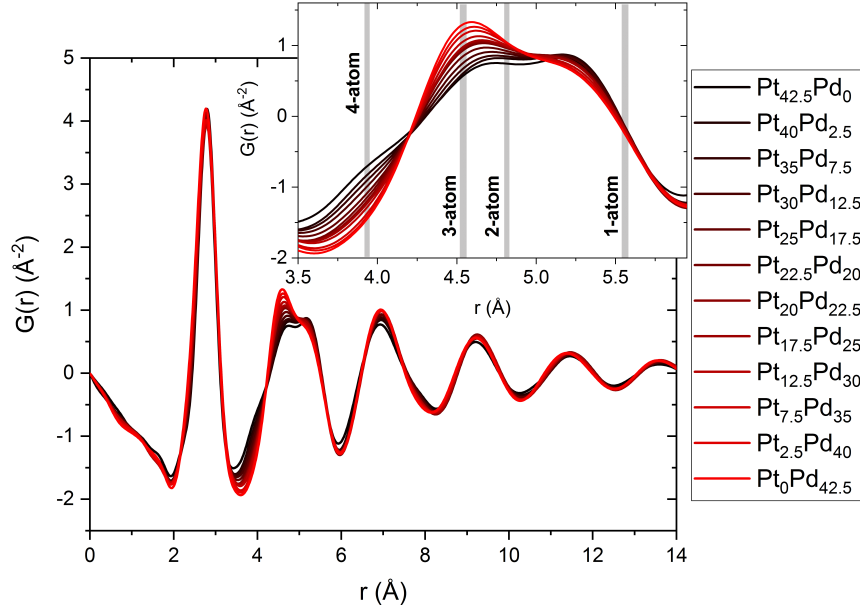


FIGURE 5.26: Compositional variation of $G(r)$ of Pt/Pd-P-based glasses at 298 K. The inset magnifies the second peak corresponding to the second nearest neighbor distances. The grey areas in the inset mark the most probable second nearest neighbor distances if adjacent clusters share one, two, three or four atoms calculated from the first peak positions.

The relevance of MRO for the kinetic fragility of BMG forming liquids has been shown by Wei et al. [85]. The experiments revealed that the temperature-induced change in the third and fourth peak position upon heating the supercooled liquid correlate with the kinetic fragility if they are interpreted in a first approximation as a volume dilatation of the third and fourth coordination shell (Eq. 2.25) [85]. The peak positions r_3 and r_4 are indicated in Fig. 5.24 and correspond to inter-cluster correlations on the length scale of approximately 3 - 4 atomic diameters representing MRO [85, 86]. The structural evolution on this length scale is shown for the three Pt-P-based alloys and the $\text{Pd}_{43}\text{Cu}_{27}\text{Ni}_{10}\text{P}_{20}$ alloy composition in Fig. 5.28(a). Figure 5.28(b) depicts the correlation between the structural and kinetic fragility parameter. The structural fragility parameter ($m_{str}^{V^4-3}$) is obtained from linear fitting of the data shown in Fig. 5.28(a). In the Pt-P-based systems, it is found that the more fragile liquids exhibit a more pronounced volume dilatation on the MRO length scale, which is in accordance to what is observed in the kinetically strong Au- and Zr-based liquids. The structural evolution upon heating Pt-P-based supercooled liquids substantiates the connection between MRO and the kinetic fragility as already indicated by the formation of the pre-peak in $\text{Pt}_{42.5}\text{Cu}_{27}\text{Ni}_{9.5}\text{P}_{21}$. The behavior of the $\text{Pd}_{43}\text{Cu}_{27}\text{Ni}_{10}\text{P}_{20}$ liquid is in stark contrast to that of the Pt-P-based liquids. Although kinetically fragile, the liquid basically exhibits no dilatation on the MRO length scale, which resembles the kinetically strong Zr-based alloys (Fig. 5.28(b)). Such an anomaly has already been observed in the thermodynamic properties of $\text{Pd}_{43}\text{Cu}_{27}\text{Ni}_{10}\text{P}_{20}$ which exhibit an extremely shallowly ascending C_p^l upon cooling, usually attributed to a kinetically strong behavior (Fig. 5.23). The different behavior on the MRO length scale might be a consequence of the varying distribution of cluster connections.

In order to investigate the structural evolution on the MRO length scale at high temperatures, the structural data collected upon heating and cooling the equilibrium

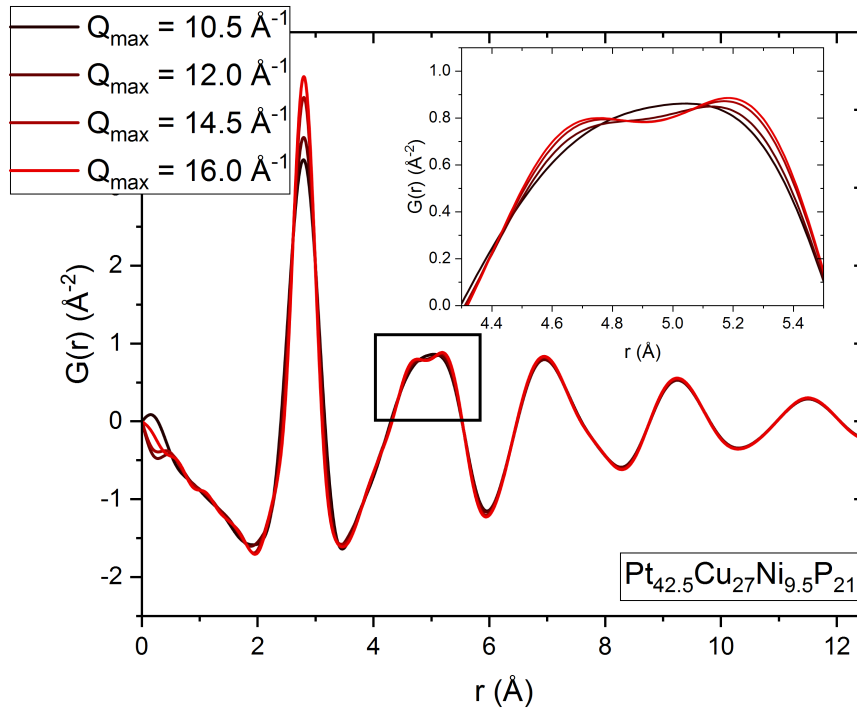


FIGURE 5.27: Influence of Q_{max} used for the Fourier transformation of $S(Q)$ on $G(r)$ of $\text{Pt}_{42.5}\text{Cu}_{27}\text{Ni}_{9.5}\text{P}_{21}$.

liquid in the ceramic furnace are used to determine m_{str}^{V4-3} (Eq. 2.26). Figure 5.29 shows the data points obtained for $\text{Pt}_{42.5}\text{Cu}_{27}\text{Ni}_{9.5}\text{P}_{21}$. At low temperatures, a m_{str}^{V4-3} of 0.049 ± 0.005 is obtained which is in good agreement with the value derived from the data points measured in the Linkam furnace (0.046). The reproducibility of the structural parameter speaks for the robustness of the data collection and data handling process. The values of the structural fragility parameter of the Pt-P-based and Pd-P-based liquids obtained in different experimental setups are listed in Tab. 5.5. In the high temperature region, the $\text{Pt}_{42.5}\text{Cu}_{27}\text{Ni}_{9.5}\text{P}_{21}$ liquid exhibits a slightly higher m_{str}^{V4-3} . However, the value derived from the data points that were collected upon heating is less representative as they cover a much smaller temperature interval. Upon cooling, a considerable undercooling is achieved and the fitting procedure yields a value of $m_{str}^{V4-3} = 0.081 \pm 0.003$ which suggests a slightly more fragile behavior at high temperatures. The high and low temperature data can also be well described by a fit combining both data sets, yielding a m_{str}^{V4-3} of 0.069 ± 0.002 . This indicates that, if at all, a minor change in the liquid fragility may occur upon cooling and that structural changes on the MRO length scale play a pivotal role in the entire temperature range of the liquid. For the $\text{Pd}_{43}\text{Cu}_{27}\text{Ni}_{10}\text{P}_{20}$ liquid, a different picture emerges as shown in Fig. 5.30. The extremely low m_{str}^{V4-3} in the deeply supercooled liquid region is contrasted with a high value of 0.099 ± 0.003 obtained upon cooling from 1153 K, suggesting that significant changes on the MRO length scale occur.

A similar behavior is observed for the Vit106a alloy composition [86] possessing a high temperature fragile and a low temperature strong liquid modification [39]. Such a transition is known as fragile-to-strong transition and appears for example in the Vit1 BMG forming liquid as rapid change in the viscosity in a small temperature interval [243] concomitantly with a peak in C_p^l [244]. The structural metric that is found to indicate a fragile-to-strong transition is the peak position of the FSDP, Q_1 . In Zr- and Au-based BMG forming liquids, $Q_1(T)$ exhibits a step-like change that

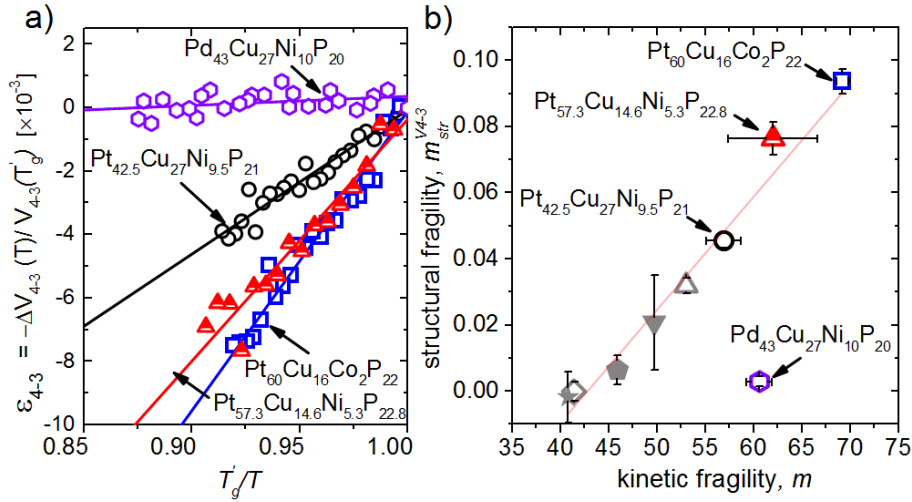


FIGURE 5.28: (a) Temperature-induced structural evolution on the MRO length scale. ϵ_{4-3} might be regarded as the volume change between the third and fourth coordination shell normalized by its volume at T'_g . (b) Correlation between the structural fragility parameter m_{str}^{V4-3} and kinetic fragility index m . Grey symbols represent Au- and Zr-based BMGs. The solid line is used to guide the eye. All samples were measured in a Linkham furnace. Data, except that of $\text{Pd}_{43}\text{Cu}_{27}\text{Ni}_{10}\text{P}_{20}$, are taken from Refs. [67, 85]. Figure adapted from Ref. [67].

TABLE 5.5: Structural fragility parameter m_{str}^{V4-3} of Pt/Pd-P-based alloys obtained upon heating (H) the low temperature supercooled liquid (SCL) or upon heating and cooling (C) the equilibrium liquid (EL). The experiments were conducted in a Linkam furnace (LF) or in a ceramic heater (CH). T'_g denotes the onset of the supercooled liquid in the structure data. Values marked with ^a and ^b are taken from Refs. [85] and [67], respectively.

composition	furnace	temperature interval	m_{str}^{V4-3}	T'_g (K)
$\text{Pt}_{42.5}\text{Cu}_{27}\text{Ni}_{9.5}\text{P}_{21}$	LF	SCL, H	0.0455 ^a	531 ^a
$\text{Pt}_{42.5}\text{Cu}_{27}\text{Ni}_{9.5}\text{P}_{21}$	CH	SCL, H	0.049 ± 0.005	527
$\text{Pt}_{42.5}\text{Cu}_{27}\text{Ni}_{9.5}\text{P}_{21}$	CH	EL, H	0.116 ± 0.011	527
$\text{Pt}_{42.5}\text{Cu}_{27}\text{Ni}_{9.5}\text{P}_{21}$	CH	EL, C	0.081 ± 0.003	527
$\text{Pd}_{43}\text{Cu}_{27}\text{Ni}_{10}\text{P}_{20}$	LF	SCL, H	0.003 ± 0.001	588
$\text{Pd}_{43}\text{Cu}_{27}\text{Ni}_{10}\text{P}_{20}$	CH	SCL, H	0.009 ± 0.006	596
$\text{Pd}_{43}\text{Cu}_{27}\text{Ni}_{10}\text{P}_{20}$	CH	EL, H	0.104 ± 0.002	596
$\text{Pd}_{43}\text{Cu}_{27}\text{Ni}_{10}\text{P}_{20}$	CH	EL, C	0.099 ± 0.003	596
$\text{Pt}_{57.3}\text{Cu}_{14.6}\text{Ni}_{5.3}\text{P}_{22.8}$	LF	SCL, H	0.076 ± 0.005^b	517 ^b
$\text{Pt}_{60}\text{Cu}_{16}\text{Co}_2\text{P}_{22}$	LF	SCL, H	0.0936 ^a	520 ^a

is attributed to structural modifications in the liquid state [86, 240, 244]. $Q_1(T)$ of the $\text{Pt}_{42.5}\text{Cu}_{27}\text{Ni}_{9.5}\text{P}_{21}$ and the $\text{Pd}_{43}\text{Cu}_{27}\text{Ni}_{10}\text{P}_{20}$ liquid are shown in Fig. 5.31. Interestingly, $\text{Pd}_{43}\text{Cu}_{27}\text{Ni}_{10}\text{P}_{20}$ exhibits a continuously decreasing Q_1 , that neither shows a significant change in slope nor a step-like change. In contrast to the $\text{Pt}_{42.5}\text{Cu}_{27}\text{Ni}_{9.5}\text{P}_{21}$ alloy composition, the glass transition and the supercooled liquid region of $\text{Pd}_{43}\text{Cu}_{27}\text{Ni}_{10}\text{P}_{20}$ cannot be distinguished from the glassy state in $Q_1(T)$. This behavior has already been observed in the $\text{Pd}_{40}\text{Cu}_{30}\text{Ni}_{10}\text{P}_{20}$ alloy composition [269].

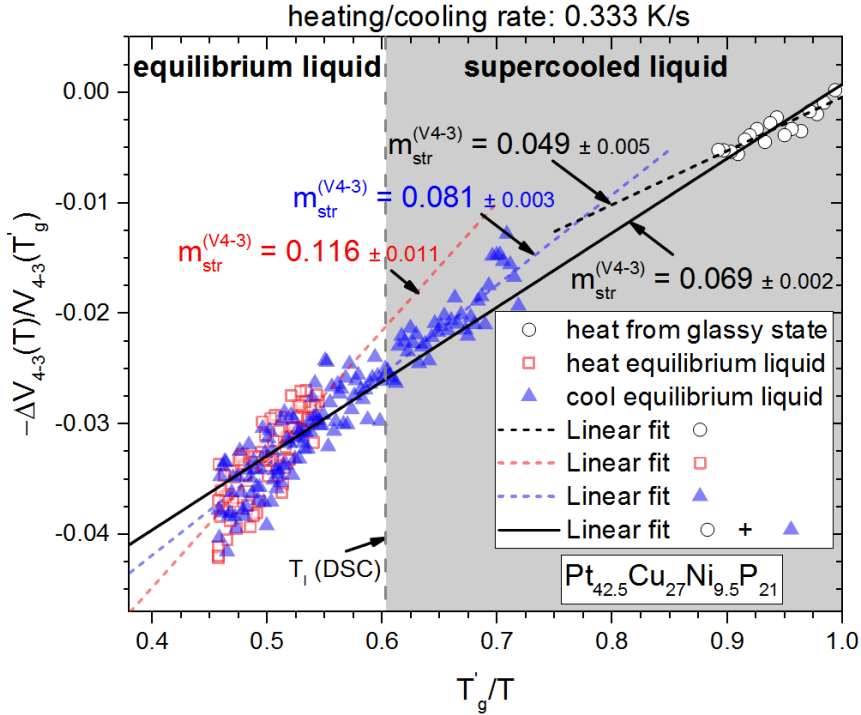


FIGURE 5.29: Temperature-induced structural evolution on the MRO length scale in $\text{Pt}_{42.5}\text{Cu}_{27}\text{Ni}_{9.5}\text{P}_{21}$ upon heating the deeply supercooled liquid and upon heating and cooling the high temperature liquid. The sample was processed in a ceramic heater in SiO_2 capillaries.

According to Yavari et al., $Q_1(T)$ is related to the volume coefficient of thermal expansion γ_{th} via

$$\left(\frac{Q_1(T_{ref})}{Q_1(T)}\right)^3 = \frac{V(T)}{V(T_{ref})} = 1 + \gamma_{th}(T - T_{ref}), \quad (5.1)$$

where V is the volume and T_{ref} is an arbitrary temperature in the glassy state [270]. For the $\text{Pd}_{40}\text{Cu}_{30}\text{Ni}_{10}\text{P}_{20}$ alloy composition, this correlation was found to hold in the glassy state [270] whereas in other metallic glasses a deviation from the exponent three was observed [271]. Investigations of Mattern et al. revealed that the correlation to the volumetric expansion collapses in the SCL state [272]. Hence, the difference observed in $Q_1(T)$ of $\text{Pt}_{42.5}\text{Cu}_{27}\text{Ni}_{9.5}\text{P}_{21}$ and $\text{Pd}_{43}\text{Cu}_{27}\text{Ni}_{10}\text{P}_{20}$ can most probably not be traced back to a varying thermal expansion in the SCL and equilibrium liquid state. Although the structural fragility parameter at high and low temperatures suggest a changing fragility in $\text{Pd}_{43}\text{Cu}_{27}\text{Ni}_{10}\text{P}_{20}$, $Q_1(T)$ does not indicate such a first order transition [244]. The structural metric $Q_1(T)$ rather suggest a continuous ordering process upon cooling in both liquids that accelerates in $\text{Pt}_{42.5}\text{Cu}_{27}\text{Ni}_{9.5}\text{P}_{21}$ as the glass transition is approached, coinciding with the more rapidly ascending specific heat capacity. Moreover, the total-scattering structure functions and the reduced pair distribution functions of $\text{Pt}_{42.5}\text{Cu}_{27}\text{Ni}_{9.5}\text{P}_{21}$ and $\text{Pd}_{43}\text{Cu}_{27}\text{Ni}_{10}\text{P}_{20}$ suggest different ordering processes occurring on different length scales. It should be noted that a second amorphous phase has been observed in the hypoeutectic region of the ternary Pd-Ni-P system indicated by an exothermic event in the supercooled liquid region upon heating [273].

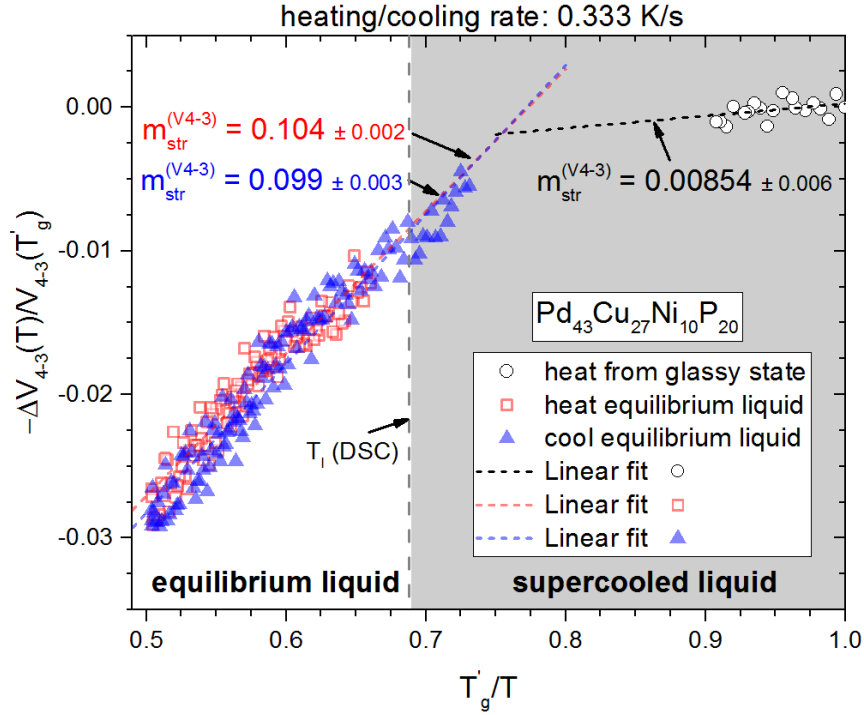


FIGURE 5.30: Temperature-induced structural evolution on the MRO length scale in $\text{Pd}_{43}\text{Cu}_{27}\text{Ni}_{10}\text{P}_{20}$ upon heating the deeply supercooled liquid and upon heating and cooling the high temperature liquid. The sample was processed in a ceramic heater in SiO_2 capillaries.

At this point, the connection between structural changes occurring upon cooling and the kinetic fragility appears to be more complex and cannot be explained by a single parameter or length scale. Although the kinetic fragility in Pt-P-based BMG forming liquids seems to be strongly effected by MRO, the length scales involved in the viscous slowdown in Pd-P-based liquids apparently vary. The structural differences between both alloy families result in distinctly different macroscopic properties. Kumar et al. noticed that $\text{Pd}_{43}\text{Cu}_{27}\text{Ni}_{10}\text{P}_{20}$ is extremely sensitive to relaxation induced embrittlement whereas the ductility of $\text{Pt}_{57.3}\text{Cu}_{14.6}\text{Ni}_{5.3}\text{P}_{22.8}$ is maintained even in the highly relaxed state [176]. This effect is attributed to a significantly varying critical fictive temperature $T_{fictive}^{crit}$ below which the embrittlement occurs. The differences between the two systems is visualized in the TTT diagrams in Fig. 5.32. Glasses possessing a $T_{fictive}$ below $T_{fictive}^{crit}$ behave brittle in bending. $T_{fictive}$ of a glass can either be lowered by annealing or by reducing the cooling rate (by increasing the casting thickness). In the case of the Pt-P-based alloy, $T_{fictive}^{crit}$ is located at such low temperatures that samples vitrified in a casting process are always ductile ($R_e \gg R_c$, where R_e is critical cooling rate for embrittlement). On the other hand, the $T_{fictive}^{crit}$ in $\text{Pd}_{43}\text{Cu}_{27}\text{Ni}_{10}\text{P}_{20}$ is found at much higher temperatures and a brittle glass vitrifies if the cooling rate is in-between R_e and R_c . As the sensitivity to embrittlement decreases when Pd is partially replaced by Pt [224], the value of $T_{fictive}^{crit}$ is probably connected to the structural changes observed in Fig. 5.16 and 5.26. Interestingly, the simulations of Ding et al. showed that clusters with 2- and 4-atom connections reacted more flexible on shear strain and their local deformation exceeds that of the macroscopic strain [82]. Clusters that connect via 1-atom experience an almost identical strain as microscopically applied. In contrast, the local strain of clusters with 3-atom connections is the smallest and remains under the microscopically imposed shear strain. In

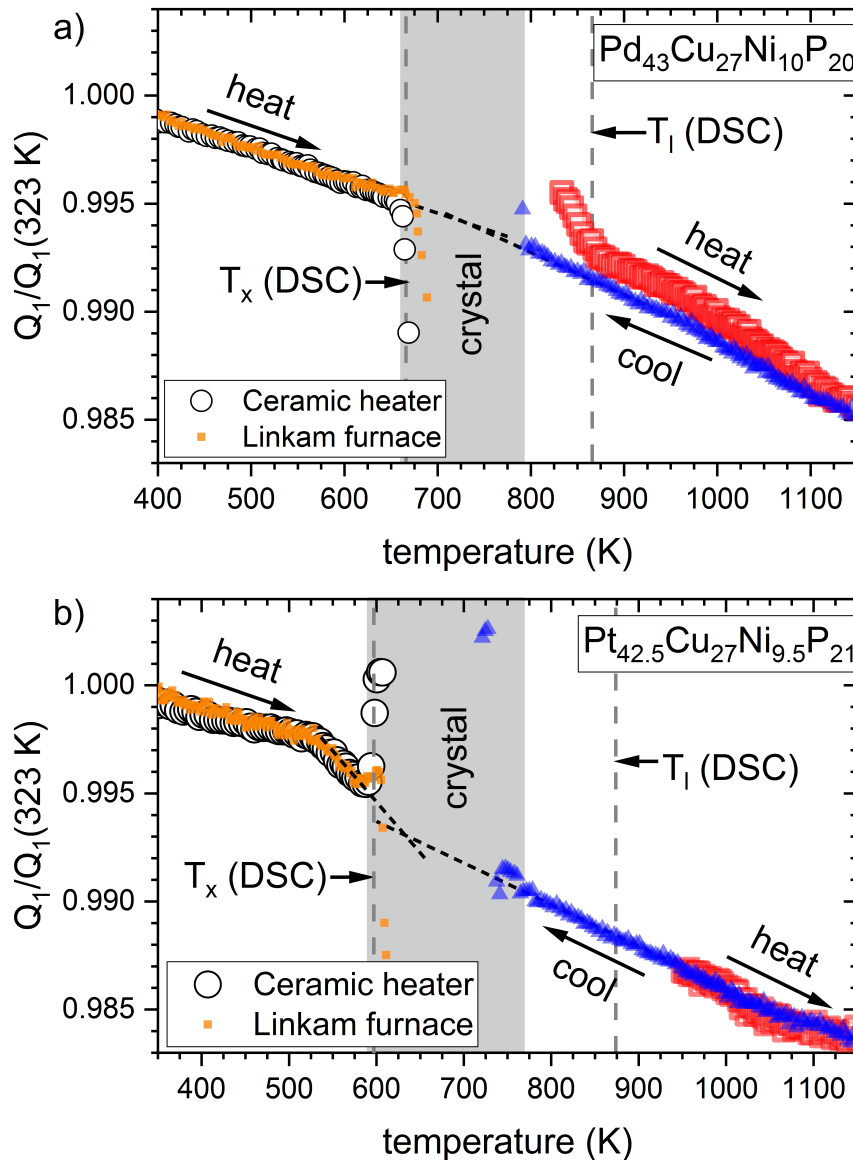


FIGURE 5.31: Peak position of the FSDP of (a) $\text{Pd}_{43}\text{Cu}_{27}\text{Ni}_{10}\text{P}_{20}$ and (b) $\text{Pt}_{42.5}\text{Cu}_{27}\text{Ni}_{9.5}\text{P}_{21}$ normalized to its value at 323 K as function of temperature. The orange squares are obtained from a sample that was heated in a Linkam furnace and the open circles from a sample heated in the ceramic furnace. The high temperature data are shown upon heating (red) and upon cooling (blue).

other words, the 3-atom connections are stiffer than the other connection schemes. Hence, the high $T_{fictive}^{crit}$ might originate from the fact that the stiff 3-atom connections prevail in $\text{Pd}_{43}\text{Cu}_{27}\text{Ni}_{10}\text{P}_{20}$. One might speculate that their portion exceeds a critical value if the glass is annealed for a certain time or the cooling rate falls below R_e . On the other hand, the larger diversity of connection schemes in Pt-P-based alloys guarantees a ductile behavior even at low $T_{fictive}$. Although the macroscopic G/B ratio (G = shear modulus, B = bulk modulus) for both alloy classes remains below the critical value of 0.41 [224, 225] at which the transition from a ductile to brittle behavior is suggested [274], the locally increasing stiffness through the ascending portion of 3-atom connections in $\text{Pd}_{43}\text{Cu}_{27}\text{Ni}_{10}\text{P}_{20}$ might hamper the formation of multiple shear bands and increase the sensitivity to crack initiation and propagation.

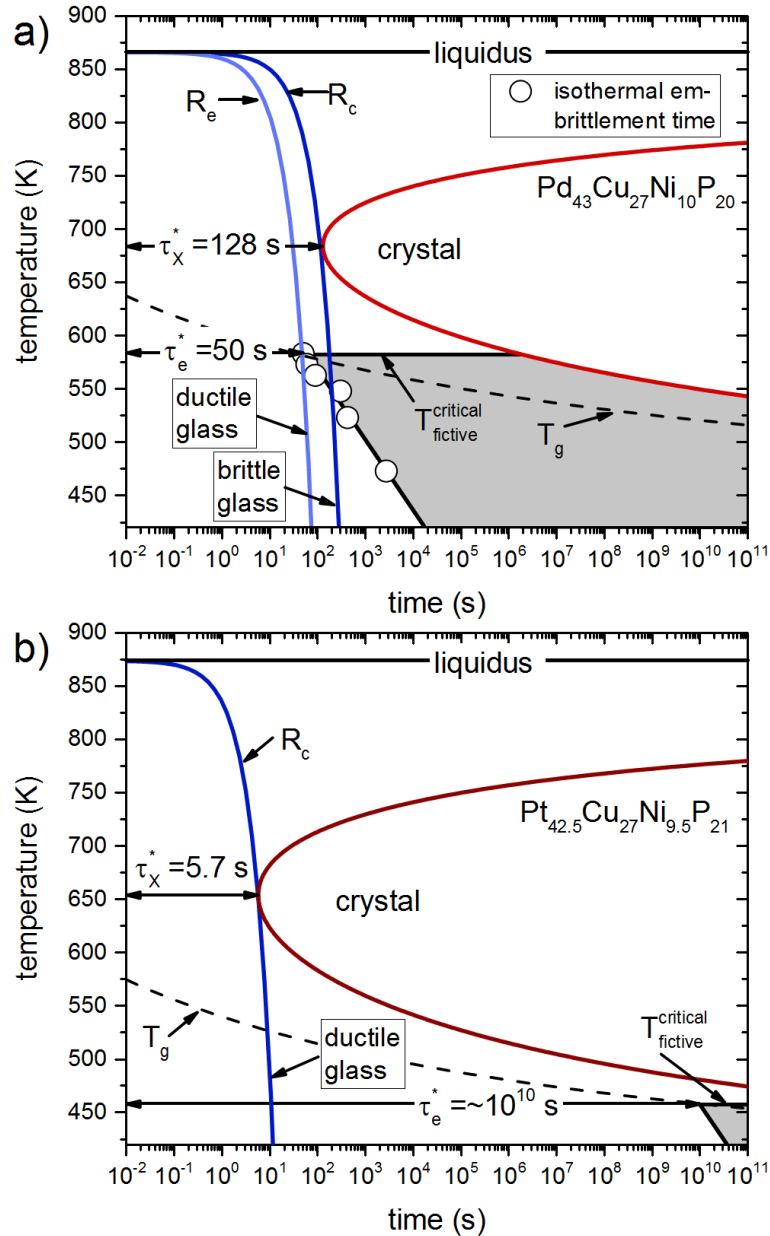


FIGURE 5.32: Critical fictive temperature of (a) Pd₄₃Cu₂₇Ni₁₀P₂₀ and (b) Pt_{42.5}Cu₂₇Ni_{9.5}P₂₁ in an isothermal TTT diagram. Glasses possessing a $T_{fictive}$ lower than the critical fictive temperature for embrittlement, $T_{fictive}^{crit}$, do not show ductility in bending experiments. The Pt_{42.5}Cu₂₇Ni_{9.5}P₂₁ liquid is assumed to possess a $T_{fictive}^{crit}$ that is 57 K below the calorimetric T_g measured at 0.333 K s⁻¹ as determined for the Pt_{57.3}Cu_{14.6}Ni_{5.3}P_{22.8} alloy composition [176]. τ_X^* and τ_e^* are the minimum crystallization and the minimum embrittlement time. R_c is the critical cooling rate needed to bypass crystallization and R_e is the critical cooling rate below which the sample loses ductility. Although not entirely correct in an isothermal TTT diagram, the continuous cooling curves visualize the difference between R_e and R_c . The data points in (a) are the isothermal embrittlement time beyond which the annealed sample possess a $T_{fictive}$ below $T_{fictive}^{crit}$ [176]. Figure adapted from Ref. [176].

5.5 Summary and Outlook

The thermophysical properties of different Pt-P-based alloys were determined. Measurements of the specific heat capacity in the supercooled and equilibrium liquid state revealed a rapidly ascending specific heat capacity upon cooling. This is in accordance with their kinetically fragile behavior, derived from isothermal viscosity and T_g -shift measurements. Moreover, continuous and isothermal crystallization experiments at high and low temperatures for the $\text{Pt}_{42.5}\text{Cu}_{27}\text{Ni}_{9.5}\text{P}_{21}$ and $\text{Pt}_{60}\text{Cu}_{16}\text{Co}_2\text{P}_{22}$ alloy compositions were conducted. The thermophysical properties were used to model the isothermal crystallization and an extremely high interfacial energy for the $\text{Pt}_{42.5}\text{Cu}_{27}\text{Ni}_{9.5}\text{P}_{21}$ liquid is determined. As Pt-P-based liquids possess a kinetically fragile behavior and a large driving force for crystallization, the high interfacial energy between the liquid and the crystal is considered to be the origin of the high glass-forming ability compensating the other two contributions. In contrast, the compositionally similar Pd-P-based liquids are stabilized by a very low driving force for crystallization, reflected by an entropy of fusion that is approximately half of that of the Pt-P-based liquids.

From a structural point of view, the large entropy of fusion of the Pt-P-based alloys points towards a rather disordered structure in the equilibrium liquid. The entropic surplus is rapidly reduced upon cooling and the structural investigations suggest the formation of medium range order in the supercooled liquid the extent of which depends on the Pt content and affects the kinetic fragility. The alloy with the lowest Pt content, $\text{Pt}_{42.5}\text{Cu}_{27}\text{Ni}_{9.5}\text{P}_{21}$, shows the kinetically strongest behavior and exhibits a pre-peak in the total-scattering structure function that indicates the existence of a distinctly pronounced medium range order. The empirical connection between the structural fragility parameter and the kinetic fragility index confirms the pivotal role of medium range order in Pt-P-based bulk glass-forming liquids. The comparison of the $\text{Pt}_{42.5}\text{Cu}_{27}\text{Ni}_{9.5}\text{P}_{21}$ and $\text{Pd}_{43}\text{Cu}_{27}\text{Ni}_{10}\text{P}_{20}$ liquid revealed significant differences. Beside the differences in the entropy of fusion, the specific heat capacity of Pd-P-based liquids ascend less rapidly upon cooling. On the other hand, the structural investigations suggest that different structural units may exist in both alloy families. Computer simulation on various metallic glass-forming liquids [82] were used as basis for the interpretation of the structural data. It is concluded that the distribution of cluster connection schemes evolving upon cooling is distinctly different in Pd-P- and Pt-P-based liquids. Moreover, it was found that the structural fragility parameter of $\text{Pd}_{43}\text{Cu}_{27}\text{Ni}_{10}\text{P}_{20}$, indicating strong liquid dynamics at low temperatures, does not coincide with the value of the kinetic fragility. However, at high temperatures the structural changes on the medium range order length scale of $\text{Pt}_{42.5}\text{Cu}_{27}\text{Ni}_{9.5}\text{P}_{21}$ and $\text{Pd}_{43}\text{Cu}_{27}\text{Ni}_{10}\text{P}_{20}$ resemble each other and indicate a kinetically fragile behavior. In both liquids, the peak position of the first sharp diffraction peak does not exhibit a step-like change as commonly observed in metallic liquids exhibiting a fragile to strong transition [86, 240, 244]. The compositionally, thermodynamically, kinetically and structurally similarities and differences between the two alloy families suggest that complex structural changes on different length scales occur upon cooling. Although topologically identical [167, 170], the substitution of Pd by Pt causes pronounced changes in the total-scattering structure function and in the reduced pair distribution function. These structural differences seem to be responsible for the varying sensitivity to the annealing induced embrittlement.

The exact nature of the structural differences and how they evolve upon cooling may only be accessible in computer simulation. Simulations would yield the temperature

induced evolution of the partial- and total-scattering structure function which can subsequently be compared to the experimental results. However, the simulation of complex multicomponent metallic liquids remains difficult and the observable time scales are still several orders of magnitude smaller than the experimental time scale in the deeply supercooled liquid [77]. The results of Kumar et al. on annealing induced embrittlement of the Pt- and Pd-P-based alloys [176, 224] have shown that relaxation and rejuvenation experiments may be the methods of choice to characterize the structural differences in the two alloy families. The possibility to gradually substitute the two elements allows the investigation of the compositional effect on the relaxation phenomena and on the crystallization behavior. The continuous change of characteristics in the total-scattering structure function and the reduced pair distribution function indicate a steady variation in the driving force for crystallization and the interfacial energy. As both values contribute differently to the crystallization time, a maximum in the glass-forming ability might be located on the Pt-Pd-axis and the value for d_c of the current record holder $\text{Pd}_{42.5}\text{Cu}_{30}\text{Ni}_{7.5}\text{P}_{20}$ might be exceeded. The extraordinary thermal stability in the supercooled liquid state, their low liquidus temperature and their noble metal character predestinate the two families for the fundamental research on bulk metallic glass-forming liquids.

Appendix A

Copyright Permissions

Figure	Reference	License number
2.4	[59]	4441780595532
2.5	[71]	4441781207864
2.7	[76]	RNP/18/OCT/008266
2.8	[77]	http://creativecommons.org/licenses/by/4.0/
2.9	[85]	4441810395581
2.17(b)	[63]	4441811139282
2.21	[166], [87]	4441820027063, 4441820243864
5.25	[82]	http://creativecommons.org/licenses/by/4.0/

Bibliography

- [1] D. Turnbull. Kinetics of heterogeneous nucleation. *The Journal of Chemical Physics*, 18(2):198–203, 1950.
- [2] D. Turnbull. Formation of crystal nuclei in liquid metals. *Journal of Applied Physics*, 21(10):1022–1028, 1950.
- [3] W. Klement, R. H. Willens, P. Duwez. Non-crystalline Structure in Solidified Gold–Silicon Alloys. *Nature*, 187(4740):869–870, 1960.
- [4] X. H. Lin, W. L. Johnson. Formation of Ti-Zr-Cu-Ni bulk metallic glasses. *Journal of Applied Physics*, 78(11):6514–6519, 1995.
- [5] A. J. Drehman, A. L. Greer, D. Turnbull. Bulk Formation of a Metallic Glass: Pd₄₀Ni₄₀P₂₀. *Applied Physics Letters*, 41(8):716–717, 1982.
- [6] A. Inoue, K. Kita, T. Zhang, et al. An Amorphous La₅₅Al₂₅Ni₂₀ Alloy Prepared by Water Quenching. *Materials Transactions*, 30(9):722–725, 1989.
- [7] A. Inoue, T. Zhang, N. Nishiyama, et al. Preparation of 16mm diameter rod of amorphous Zr₆₅Al_{7.5}Ni₁₀Cu_{17.5} alloy. *Material Transactions, JIM*, 34(12):1234–1237, 1993.
- [8] A. Inoue, T. Nakamura, N. Nishiyama, et al. Mg-Cu-Y Bulk Amorphous Alloys with High Tensile Strength Produced by a High-Pressure Die Casting Method. *Materials Transactions, JIM*, 33(10):937–945, 1992.
- [9] A. Peker, W. L. Johnson. A highly processable metallic glass: Zr_{41.2}Ti_{13.8}Cu_{12.5}Ni_{10.0}Be_{22.5}. *Applied Physics Letters*, 63(17):2342–2344, 1993.
- [10] M. F. Ashby, A. L. Greer. Metallic glasses as structural materials. *Scripta Materialia*, 54(3):321–326, 2006.
- [11] A. R. Yavari, J. J. Lewandowski, J. Eckert. Mechanical Properties of Bulk Metallic Glasses. *MRS Bulletin*, 32(08):635–638, 2007.
- [12] G. Kumar, H. X. Tang, J. Schroers. Nanomoulding with amorphous metals. *Nature*, 457(7231):868–872, 2009.
- [13] B. Bochtler, M. Stolpe, B. Reiplinger, et al. Consolidation of amorphous powder by thermoplastic forming and subsequent mechanical testing. *Materials and Design*, 140:188–195, 2018.
- [14] H. Guo, W. Zhang, C. Qin, et al. Glass-Forming Ability and Properties of New Au-Based Glassy Alloys with Low Au Concentrations. *Materials Transactions*, 50:1290–1293, 2009.
- [15] J. Schroers, W. L. Johnson. Highly Processable Bulk Metallic Glass-forming alloys in the Pt–Co–Ni–Cu–P system. *Applied Physics Letters*, 84(18):3666, 2004.
- [16] N. Nishiyama, K. Takenaka, H. Miura, et al. The world’s biggest glassy alloy ever made. *Intermetallics*, 30:19–24, 2012.
- [17] W. L. Johnson, J. H. Na, M. D. Demetriou. Quantifying the origin of metallic glass formation. *Nature communications*, 7:10313, 2016.

- [18] J.H. Na, M. D. Demetriou, M. Floyd, et al. Compositional landscape for glass formation in metal alloys. *Proceedings of the National Academy of Sciences*, 111(25):9031–9036, 2014.
- [19] J. Shen, Q. Chen, J. Sun, et al. Exceptionally high glass-forming ability of an FeCoCrMoCBy alloy. *Applied Physics Letters*, 86(15):1–3, 2005.
- [20] G. R. Garrett, M. D. Demetriou, J. Chen, et al. Effect of microalloying on the toughness of metallic glasses. *Applied Physics Letters*, 101(24):241913, 2012.
- [21] Q. Zheng, J. Xu, E. Ma. High glass-forming ability correlated with fragility of Mg-Cu(Ag)-Gd alloys. *Journal of Applied Physics*, 102(11):113519, 2007.
- [22] O. N. Senkov, D. B. Miracle, V. Keppens, et al. Development and Characterization of Low-Density Ca-Based Bulk Metallic Glasses: An Overview. *Metallurgical and Materials Transactions A*, 39(8):1888–1900, 2008.
- [23] Q. K. Jiang, G. Q. Zhang, L. Yang, et al. La-based bulk metallic glasses with critical diameter up to 30mm. *Acta Materialia*, 55(13):4409–4418, 2007.
- [24] P. Gong, K. Yao, X. Wang, et al. A new centimeter-sized Ti-based quaternary bulk metallic glass with good mechanical properties. *Advanced Engineering Materials*, 15(8):691–696, 2013.
- [25] S. L. Zhu, X. M. Wang, A. Inoue. Glass-forming ability and mechanical properties of Ti-based bulk glassy alloys with large diameters of up to 1 cm. *Intermetallics*, 16(8):1031–1035, 2008.
- [26] A. Inoue. Stabilization of metallic supercooled liquid and bulk amorphous alloys. *Acta Materialia*, 48(1):279–306, 2000.
- [27] C. Suryanarayana, A. Inoue. *Bulk Metallic Glasses*. CRC Press, 2011.
- [28] David Turnbull. Under what conditions can a glass be formed? *Contemporary Physics*, 10(5):473–488, 1969.
- [29] A. L. Greer. Confusion by design. *Nature*, 366(6453):303–304, 1993.
- [30] Z.P. Lu, Y. Li, S.C. Ng. Reduced glass transition temperature and glass forming ability of bulk glass forming alloys. *Journal of Non-Crystalline Solids*, 270(1-3):103–114, 2000.
- [31] J. Schroers. Bulk metallic glasses. *Physics Today*, 66:32–37, 2013.
- [32] A. Kuball, O. Gross, B. Bochtler, et al. Sulfur-bearing metallic glasses: A new family of bulk glass-forming alloys. *Scripta Materialia*, 146:73–76, 2018.
- [33] Y. Li, S. Zhao, Y. Liu, et al. How Many Bulk Metallic Glasses Are There? *ACS Combinatorial Science*, 19(11):687–693, 2017.
- [34] M. Eisenbart. “On the Processing and the Tarnishing Mechanism of Gold-based Bulk Metallic Glasses”. PhD Thesis. Saarland University, 2015. DOI: [10.22028/D291-23143](https://doi.org/10.22028/D291-23143). URL: <http://scidok.sulb.uni-saarland.de/volltexte/2016/6521/>.
- [35] A. R. Yavari. A new order for metallic glasses. *Nature*, 439(7075):405–406, 2006.
- [36] C. A. Angell. Glass-Formers and Viscous Liquid Slowdown since David Turnbull: Enduring Puzzles and New Twists. *MRS Bulletin*, 33(05):544–555, 2008.
- [37] C. A. Angell. Glass Transition. *Encyclopedia of Materials: Science and Technology*, 4:3565–3575, 2001.

- [38] J. Q. Wang, Y. Shen, J. H. Perepezko, et al. Increasing the kinetic stability of bulk metallic glasses. *Acta Materialia*, 104:25–32, 2016.
- [39] Z. Evenson, T. Schmitt, M. Nicola, et al. High temperature melt viscosity and fragile to strong transition in Zr–Cu–Ni–Al–Nb(Ti) and Cu₄₇Ti₃₄Zr₁₁Ni₈ bulk metallic glasses. *Acta Materialia*, 60(12):4712–4719, 2012.
- [40] B. Bochtler, O. Gross, I. Gallino, et al. Thermo-physical characterization of the Fe₆₇Mo₆Ni_{3.5}Cr_{3.5}P₁₂C_{5.5}B_{2.5} bulk metallic glass forming alloy. *Acta Materialia*, 118:129–139, 2016.
- [41] B. Bochtler, O. Gross, R. Busch. Indications for a fragile-to-strong transition in the high- and low-temperature viscosity of the Fe₄₃Cr₁₆Mo₁₆C₁₅B₁₀ bulk metallic glass-forming alloy. *Applied Physics Letters*, 111(26):261902, 2017.
- [42] M. H. Cohen, G. S. Grest. Liquid-glass transition, a free-volume approach. *Physical Review B*, 20(3):1077–1098, 1979.
- [43] W. Kauzmann. The nature of the glassy state and the behavior of liquids at low temperatures. *Chemical Reviews*, 43:219–256, 1948.
- [44] D. M. Herlach. Non-equilibrium solidification of undercooled metallic metals. *Materials Science and Engineering: R: Reports*, 12(4-5):177–272, 1994.
- [45] O. Kubaschewski, C. B. Alcock, P. J. Spencer. No Title. *Materials Thermochemistry*, 6th ed.(Pergamon, New York):1993.
- [46] S. Inaba, S. Oda, K. Morinaga. Heat capacity of oxide glasses at high temperature region. *Journal of Non-Crystalline Solids*, 325(1-3):258–266, 2003.
- [47] X. Guo, J. C. Mauro, M. Potuzak, et al. Structural relaxation in annealed hyperquenched basaltic glasses: Insights from calorimetry. *Journal of Non-Crystalline Solids*, 358(11):1356–1361, 2012.
- [48] R. Busch, Y. J. Kim, W. L. Johnson. Thermodynamics and kinetics of the undercooled liquid and the glass transition of the Zr_{41.2}Ti_{13.8}Cu_{12.5}Ni_{10.0}Be_{22.5} alloy. *Journal of Applied Physics*, 77(8):4039, 1995.
- [49] J. W. Christian. "Solidification and Melting". In: *The Theory of Transformations in Metals and Alloys*. Elsevier, 2002:623–701.
- [50] D. A. Porter, K. E. Easterling. *Phase Transformations in Metals and Alloys*. Boston, MA: Springer US, 1992.
- [51] R. Bormann, K. Zöltzer. Determination of the thermodynamic functions and calculation of phase diagrams for metastable phases. *Physica Status Solidi (a)*, 131(2):691–705, 1992.
- [52] W. L. Johnson. Thermodynamic and kinetic aspects of the crystal to glass transformation in metallic materials. *Progress in Materials Science*, 30(2):81–134, 1986.
- [53] P. W. Atkins, J. de Paula. *Physikalische Chemie*. WILEY-VCH Verlag, 2006.
- [54] I. Avramov. Viscosity activation energy. *Physics and Chemistry of Glasses: European Journal of Glass Science and Technology Part B*, 48(1):61–63, 2007.
- [55] G.S. Fulcher. Analysis of Recent Measurements of the Viscosity of Glasses. *J. Am. Ceram. Soc.* 8(6):339, 1925.
- [56] H. Vogel. Das Temperaturabhängigkeitsgesetz der Viskosität von Flüssigkeiten. *Phys. Z.*, 22:645, 1921.

- [57] G. Tammann, W. Hesse. Die Abhängigkeit der Viscosität von der Temperatur bei unterkühlten Flüssigkeiten. *Z. Anorg. Allg. Chem.*, 156:245, 1926.
- [58] G. W. Scherer. Editorial Comments on a Paper by Gordon S. Fulcher. *Journal of the American Ceramic Society*, 75(5):1060–1062, 1992.
- [59] C. A. Angell. Formation of glasses from liquids and biopolymers. *Science*, 267:1924–1935, 1995.
- [60] S.V. Nemilov. Correlation of crystallization character of glass melts with the temperature dependence of their viscosity and the degree of spatial structural connectiveness. *Glass Phys. Chem.* 21(91):379, 1995.
- [61] C. A. Angell. Entropy and fragility in supercooling liquids. *Journal of Research of the National Institute of Standards and Technology*, 102(2):171, 1997.
- [62] C. A. Angell. Perspectives on the Glass Transition. *J. Phys. Chem. Solids*, 49(8):863–871, 1988.
- [63] R. Busch, J. Schroers, W. H. Wang. Thermodynamics and Kinetics of Bulk Metallic Glass. *MRS Bulletin*, 32(08):620–623, 2007.
- [64] Z. Evenson, S. Raedersdorf, I. Gallino, et al. Equilibrium viscosity of Zr–Cu–Ni–Al–Nb bulk metallic glasses. *Scripta Materialia*, 63(6):573–576, 2010.
- [65] R. Busch, W. Liu, W. L. Johnson. Thermodynamics and kinetics of the Mg₆₅Cu₂₅Y₁₀ bulk metallic glass forming liquid. *Journal of Applied Physics*, 83(8):4134–4141, 1998.
- [66] J. H. Na, M. D. Demetriou, W. L. Johnson. Fragility of iron-based glasses. *Applied Physics Letters*, 99(16):161902, 2011.
- [67] O. Gross, B. Bochtler, M. Stolpe, et al. The kinetic fragility of Pt–P- and Ni–P-based bulk glass-forming liquids and its thermodynamic and structural signature. *Acta Materialia*, 132:118–127, 2017.
- [68] G. Adam, J. H. Gibbs. On the Temperature Dependence of Cooperative Relaxation Properties in Glass-Forming Liquids. *Journal of Chemical Physics*, (43):139–146, 1965.
- [69] P. G. Debenedetti. *Metastable liquids : concepts and principles*. Princeton University Press, 1996.
- [70] M. Goldstein. Viscous liquids and the glass transition. V. Sources of the excess specific heat of the liquid. *The Journal of Chemical Physics*, 64(11):4767, 1976.
- [71] L.-M. Martinez, C. A. Angell. A thermodynamic connection to fragility of glass-forming liquids. *Nature*, 410(6829):663–667, 2001.
- [72] L.-M. Wang, R. Richert. Measuring the Configurational Heat Capacity of Liquids. *Physical Review Letters*, 99(18):185701, 2007.
- [73] H. L. Smith, C. W. Li, A. Hoff, et al. Separating the configurational and vibrational entropy contributions in metallic glasses. *Nature Physics*, 13(9):900–905, 2017.
- [74] C. A. Angell. Thermodynamic aspects of the glass transition in liquids and plastic crystals. *Pure and Applied Chemistry*, 63(10):1387–1392, 1991.
- [75] Isabella Gallino, Oliver Gross, Giulia Dalla Fontana, et al. On the kinetic and thermodynamic fragility of the Pt₆₀Cu₁₆Co₂P₂₂ and Pt_{57.3}Cu_{14.6}Ni_{5.3}P_{22.8} bulk metallic glasses. *Journal of Alloys and Compounds*, 615:S35–S39, 2014.

- [76] J. Ding, Y. Q. Cheng, H. Sheng, et al. Short-range structural signature of excess specific heat and fragility of metallic-glass-forming supercooled liquids. *Physical Review B - Condensed Matter and Materials Physics*, 85(6):1–5, 2012.
- [77] J. Ding, E. Ma. Computational modeling sheds light on structural evolution in metallic glasses and supercooled liquids. *npj Computational Materials*, 3(1):9, 2017.
- [78] J. Ding, Y. Cheng, E. Ma. Charge-transfer-enhanced prism-type local order in amorphous Mg₆₅Cu₂₅Y₁₀: Short-to-medium-range structural evolution underlying liquid fragility and heat capacity. *Acta Materialia*, 61(8):3130–3140, 2013.
- [79] Y. Q. Cheng, H. W. Sheng, E. Ma. Relationship between structure, dynamics, and mechanical properties in metallic glass-forming alloys. *Physical Review B - Condensed Matter and Materials Physics*, 78(1):1–7, 2008.
- [80] D. Holland-Moritz, T. Schenk, V. Simonet, et al. Short-range order in undercooled metallic liquids. *Materials Science and Engineering A*, 375-377(1-2 SPEC. ISS.):98–103, 2004.
- [81] T. Schenk, D. Holland-Moritz, V. Simonet, et al. Icosahedral Short-Range Order in Deeply Undercooled Metallic Melts. *Physical Review Letters*, 89(7):1–4, 2002.
- [82] J. Ding, E. Ma, M. Asta, et al. Second-Nearest-Neighbor Correlations from Connection of Atomic Packing Motifs in Metallic Glasses and Liquids. *Scientific Reports*, 1–9, 2015.
- [83] M. Li, C. Z. Wang, S. G. Hao, et al. Structural heterogeneity and medium-range order in Zr_x Cu_{100-x} metallic glasses. *Physical Review B - Condensed Matter and Materials Physics*, 80(18):1–7, 2009.
- [84] K. N. Lad, N. Jakse, A. Pasturel. Signatures of fragile-to-strong transition in a binary metallic glass-forming liquid. *Journal of Chemical Physics*, 136(10):2012.
- [85] S. Wei, M. Stolpe, O. Gross, et al. Linking structure to fragility in bulk metallic glass-forming liquids. *Applied Physics Letters*, 106(18):2015.
- [86] M. Stolpe, I. Jonas, S. Wei, et al. Structural changes during a liquid-liquid transition in the deeply undercooled Zr_{58.5}Cu_{15.6}Ni_{12.8}Al_{10.3}Nb_{2.8} bulk metallic glass forming melt. *Physical Review B*, 93(1):014201, 2016.
- [87] H. W. Sheng, W. K. Luo, F. M. Alamgir, et al. Atomic packing and short-to-medium-range order in metallic glasses. *Nature*, 439(7075):419–425, 2006.
- [88] N. A. Mauro, M. Blodgett, M. L. Johnson, et al. A structural signature of liquid fragility. *Nature Communications*, 5:1–7, 2014.
- [89] D. R. Uhlmann. Glass formation. *Journal of Non-Crystalline Solids*, 25(1-3):42–85, 1977.
- [90] D. R. Uhlmann. A kinetic treatment of glass formation. *Journal of Non-Crystalline Solids*, 7(4):337–348, 1972.
- [91] A. L. Greer, K. F. Kelton. *Nucleation in Condensed Matter*. Pergamon, 2010.
- [92] J. W. Christian. “General Introduction”. In: *The Theory of Transformations in Metals and Alloys*. Elsevier, 2002:1–22.
- [93] F. Spaepen. A structural model for the solid-liquid interface in monatomic systems. *Acta Metallurgica*, 23(6):729–743, 1975.

- [94] A. Gebert, J. Eckert, L. Schultz. Effect of oxygen on phase formation and thermal stability of slowly cooled Zr₆₅Al_{7.5}Cu_{17.5}Ni₁₀ metallic glass. *Acta Materialia*, 46(15):5475–5482, 1998.
- [95] Y. J. Kim, R. Busch, W. L. Johnson, et al. Metallic glass formation in highly undercooled Zr_{41.2}Ti_{13.8}Cu_{12.5}Ni_{10.0}Be_{22.5} during containerless electrostatic levitation processing. *Applied Physics Letters*, 65(17):2136–2138, 1994.
- [96] X. H. Lin, W. L. Johnson, W. K. Rhim. Effect of Oxygen Impurity on Crystallization of an Undercooled Bulk Glass Forming Zr-Ti-Cu-Ni-Al Alloy. *Materials Transactions, JIM*, 38(5):473–477, 1997.
- [97] J. J. Wall, C. T. Liu, W. K. Rhim, et al. Heterogeneous nucleation in a glass-forming alloy. *Applied Physics Letters*, 92(24):2–4, 2008.
- [98] D. Granata, E. Fischer, V. Wessels, et al. Fluxing of Pd–Si–Cu bulk metallic glass and the role of cooling rate and purification. *Acta Materialia*, 71:145–152, 2014.
- [99] B. Yang, J. H. Perepezko, J. W. P. Schmelzer, et al. Dependence of crystal nucleation on prior liquid overheating by differential fast scanning calorimeter. *Journal of Chemical Physics*, 140(10):1–7, 2014.
- [100] J. H. Perepezko, M. K. Hoffmeyer, M. P. De Cicco. Analysis of Melt Undercooling and Crystallization Kinetics. *Metallurgical and Materials Transactions A: Physical Metallurgy and Materials Science*, 46(11):4898–4907, 2015.
- [101] L. Sun, Q. Wu, Y. Xu, et al. Study on solidification behaviour of Pd₄₀Ni₄₀P₂₀ alloy by fluxing method. *Physica B Condensed Matter*, 240:205–210, 1997.
- [102] D. Granata, E. Fischer, V. Wessels, et al. The detrimental effect of flux-induced boron alloying in Pd–Si–Cu bulk metallic glasses. *Applied Physics Letters*, 106(1):011902, 2015.
- [103] T. D. Shen, R. B. Schwarz. Bulk ferromagnetic glasses in the Fe–Ni–P–B System. *Acta Materialia*, 49(5):837–847, 2001.
- [104] J. Schroers, W. L. Johnson, R. Busch. Crystallization Kinetics of the Bulk-Glass-Forming Pd₄₃Ni₁₀Cu₂₇P₂₀ Melt. *Applied Physics Letters*, 77(8):1158, 2000.
- [105] B. J. Yang, W. Y. Lu, J. L. Zhang, et al. Melt fluxing to elevate the forming ability of Al-based bulk metallic glasses. *Scientific Reports*, 7(1):2017.
- [106] A. Castellero, S. Bossuyt, M. Stoica, et al. Improvement of the glass-forming ability of Zr₅₅Cu₃₀Al₁₀Ni₅ and Cu₄₇Ti₃₄Zr₁₁Ni₈ alloys by electro-deoxidation of the melts. *Scripta Materialia*, 55(1):87–90, 2006.
- [107] L. Zhong, J. Wang, H. Sheng, et al. Formation of monatomic metallic glasses through ultrafast liquid quenching. *Nature*, 512(7513):177–180, 2014.
- [108] H. Tanaka. Possible resolution of the Kauzmann paradox in supercooled liquids. *Physical review. E, Statistical, nonlinear, and soft matter physics*, 68:011505, 2003.
- [109] J. H. Gibbs, E. A. DiMarzio. Nature of the Glass Transition and the Glassy State. *The Journal of Chemical Physics*, 28(3):373–383, 1958.
- [110] I. Gallino, J. Schroers, R. Busch. Kinetic and thermodynamic studies of the fragility of bulk metallic glass forming liquids. *Journal of Applied Physics*, 108(6):063501, 2010.

- [111] A. Masuhr, T. A. Waniuk, R. Busch, et al. Time Scales for Viscous Flow, Atomic Transport, and Crystallization in the Liquid and Supercooled Liquid States of $\text{Zr}_{41.2}\text{Ti}_{13.8}\text{Cu}_{12.5}\text{Ni}_{10.0}\text{Be}_{22.5}$. *Physical Review Letters*, 82(11):2290–2293, 1999.
- [112] U. Geyer, W. L. Johnson, S. Schneider, et al. Small atom diffusion and breakdown of the Stokes-Einstein relation in the supercooled liquid state of the $\text{Zr}_{46.7}\text{Ti}_{8.3}\text{Cu}_{7.5}\text{Ni}_{10}\text{Be}_{27.5}$ alloy. *Applied Physics Letters*, 69(17):2492–2494, 1996.
- [113] A. Bartsch, K. Rätzke, A. Meyer, et al. Dynamic arrest in multicomponent glass-forming alloys. *Physical Review Letters*, 104(19):1–4, 2010.
- [114] M. D. Ediger, C. A. Angell, S. R. Nagel. Supercooled liquids and glasses. *Journal of Physical Chemistry*, 100:13200–13212, 1996.
- [115] A. Kuball, V. Pacheco, O. Gross, et al. Thermodynamics and kinetics of $\text{Pd}_{31}\text{Ni}_{42}\text{S}_{27}$ bulk glass forming alloy. [to be published].
- [116] A. Kuball, M. Stolpe, R. Busch. Crystallization behavior of the $\text{Al}_{86}\text{Ni}_{8}\text{Y}_6$ metallic glass forming alloy upon rapid cooling. *Journal of Alloys and Compounds*, 737:398–404, 2017.
- [117] K. Kosiba, S. Scudino, R. Kobold, et al. Transient nucleation and microstructural design in flash-annealed bulk metallic glasses. *Acta Materialia*, 127:416–425, 2017.
- [118] T. Egami. STRUCTURAL RELAXATION IN METALLIC GLASSES. *Annals of the New York Academy of Sciences*, 371:238–251, 1981.
- [119] A. van den Beukel, J. Sietsma. The glass transition as a free volume related kinetic phenomenon. *Acta Metallurgica et Materialia*, 38(3):383–389, 1990.
- [120] A. van den Beukel, S. van der Zwaag, A. L. Mulder. A semi-quantitative description of the kinetics of structural relaxation in amorphous $\text{Fe}_{40}\text{Ni}_{40}\text{B}_{20}$. *Acta Metallurgica*, 32(11):1895–1902, 1984.
- [121] Z. Evenson, T. Koschine, S. Wei, et al. The effect of low-temperature structural relaxation on free volume and chemical short-range ordering in a $\text{Au}_{49}\text{Cu}_{26.9}\text{Si}_{16.3}\text{Ag}_{5.5}\text{Pd}_{2.3}$ bulk metallic glass. *Scripta Materialia*, 103:14–17, 2015.
- [122] H. B. Yu, K. Samwer, W. H. Wang, et al. Chemical influence on β -relaxations and the formation of molecule-like metallic glasses. *Nature Communications*, 4:1–6, 2013.
- [123] Z. Evenson, S. E. Naleway, S. Wei, et al. β relaxation and low-temperature aging in a Au-based bulk metallic glass: From elastic properties to atomic-scale structure. *Physical Review B*, 89(17):174204, 2014.
- [124] H.-B. Yu, R. Richert, K. Samwer. Structural rearrangements governing Johari-Goldstein relaxations in metallic glasses. *Science Advances*, 3(11):e1701577, 2017.
- [125] S. Küchemann, R. Maaß. Gamma relaxation in bulk metallic glasses. *Scripta Materialia*, 137:5–8, 2017.
- [126] J. D. Stevenson, P. G. Wolynes. A universal origin for secondary relaxations in supercooled liquids and structural glasses. *Nature Physics*, 6(1):62–68, 2010.
- [127] R. Busch, E. Bakke, W.L. Johnson. Viscosity of the supercooled liquid and relaxation at the glass transition of the $\text{Zr}_{46.75}\text{Ti}_{8.25}\text{Cu}_{7.5}\text{Ni}_{10}\text{Be}_{27.5}$ bulk metallic glass forming alloy. *Acta Materialia*, 46(13):4725–4732, 1998.

- [128] O. Haruyama, H. Sakagami, N. Nishiyama, et al. The free volume kinetics during structural relaxation in bulk Pd-P based metallic glasses. *Materials Science and Engineering A*, 448-451:497–500, 2007.
- [129] M. E. Launey, R. Busch, J. J. Kruzic. Effects of free volume changes and residual stresses on the fatigue and fracture behavior of a Zr-Ti-Ni-Cu-Be bulk metallic glass. *Acta Materialia*, 56(3):500–510, 2008.
- [130] Z. Evenson, R. Busch. Equilibrium viscosity, enthalpy recovery and free volume relaxation in a Zr₄₄Ti₁₁Ni₁₀Cu₁₀Be₂₅ bulk metallic glass. *Acta Materialia*, 59(11):4404–4415, 2011.
- [131] O. Haruyama, M. Tando, H. M. Kimura, et al. Structural relaxation in Pd-Cu-Ni-P metallic glasses. *Materials Science and Engineering A*, 375-377(1-2 SPEC. ISS.):292–296, 2004.
- [132] M. Stolpe, J. J. Kruzic, R. Busch. Evolution of shear bands, free volume and hardness during cold rolling of a Zr-based bulk metallic glass. *Acta Materialia*, 64:231–240, 2014.
- [133] S.-C. Lee, C.-M. Lee, J.-W. Yang, et al. Microstructural evolution of an elastically compressed amorphous alloy and its influence on the mechanical properties. *Scripta Materialia*, 58(7):591–594, 2008.
- [134] D. J. Magagnosc, G. Kumar, J. Schroers, et al. Effect of ion irradiation on tensile ductility, strength and fictive temperature in metallic glass nanowires. *Acta Materialia*, 74:165–182, 2014.
- [135] S. V. Ketov, Y. H. Sun, S. Nachum, et al. Rejuvenation of metallic glasses by non-affine thermal strain. *Nature Materials*, 14:867, 2015.
- [136] J. Zhao, S. L. Simon, G. B. McKenna. Using 20-million-year-old amber to test the super-Arrhenius behaviour of glass-forming systems. *Nature Communications*, 4:1783, 2013.
- [137] I. M. Hodge. Enthalpy relaxation and recovery in amorphous materials. *Journal of Non-Crystalline Solids*, 169(3):211–266, 1994.
- [138] G. Williams, D. C. Watts. Non-symmetrical dielectric relaxation behaviour arising from a simple empirical decay function. *Transactions of the Faraday Society*, 66:80, 1970.
- [139] R. Richert. Homogeneous dispersion of dielectric responses in a simple glass. *Journal of Non-Crystalline Solids*, 172-174(PART 1):209–213, 1994.
- [140] P. G. Debenedetti, F. H. Stillinger. Supercooled liquids and the glass transition. *Nature*, 410:259–267, 2001.
- [141] M. D. Ediger. Spatially Heterogeneous Dynamics in Supercooled Liquids. *Annu. Rev. Phys. Chem.* 51:99–128, 2000.
- [142] E. Vidal Russell, N. E. Israeloff. Direct observation of molecular cooperativity near the glass transition. *Nature*, 408(6813):695–698, 2000.
- [143] L. Berthier. Dynamic Heterogeneity in Amorphous Materials. *Physics*, 4:42, 2011.
- [144] B. Ruta, Y. Chushkin, G. Monaco, et al. Atomic-scale relaxation dynamics and aging in a metallic glass probed by X-ray photon correlation spectroscopy. *Physical Review Letters*, 109(16):1–5, 2012.
- [145] C. A. Angell, K. L. Ngai, G. B. McKenna, et al. Relaxation in glassforming liquids and amorphous solids. *Journal of Applied Physics*, 88(6):3113–3157, 2000.

- [146] I. Gallino, M. B. Shah, R. Busch. Enthalpy relaxation and its relation to the thermodynamics and crystallization of the Zr_{58.5}Cu_{15.6}Ni_{12.8}Al_{10.3}Nb_{2.8} bulk metallic glass-forming alloy. *Acta Materialia*, 55(4):1367–1376, 2007.
- [147] J. Schroers, Y. Wu, R. Busch, et al. Transition from nucleation controlled to growth controlled crystallization in Pd₄₃Ni₁₀Cu₂₇P₂₀ melts. *Acta Materialia*, 49(14):2773–2781, 2001.
- [148] B. A. Legg, J. Schroers, R. Busch. Thermodynamics, kinetics, and crystallization of Pt_{57.3}Cu_{14.6}Ni_{5.3}P_{22.8} bulk metallic glass. *Acta Materialia*, 55(3):1109–1116, 2007.
- [149] R. Busch, Y. J. Kim, W. L. Johnson, et al. Hemispherical total emissivity and specific heat capacity of deeply undercooled Zr_{41.2}Ti_{13.8}Cu_{12.5}Ni_{10.0}Be_{22.5} melts. *Applied Physics Letters*, 66(23):3111, 1995.
- [150] Y. J. Kim, R. Busch, W. L. Johnson, et al. Experimental determination of a time–temperature–transformation diagram of the undercooled Zr_{41.2}Ti_{13.8}Cu_{12.5}Ni_{10.0}Be_{22.5} alloy using the containerless electrostatic levitation processing technique. *Applied Physics Letters*, 68(8):1057–1059, 1996.
- [151] J.-M. Liu. Demonstration of spinodal decomposition in amorphous Cu_{12.5}Ni₁₀Zr₄₁Ti₁₄Be_{22.5} alloy. *Solid State Communications*, 105(1):71–75, 1998.
- [152] S. Schneider, P. Thiyagarajan, W. L. Johnson. Formation of nanocrystals based on decomposition in the amorphous Zr_{41.2}Ti_{13.8}Cu_{12.5}Ni₁₀Be_{22.5} alloy. *Applied Physics Letters*, 68(4):493–495, 1996.
- [153] A. A. Kündig, M. Ohnuma, D. H. Ping, et al. In situ formed two-phase metallic glass with surface fractal microstructure. *Acta Materialia*, 52(8):2441–2448, 2004.
- [154] J. He, N. Mattern, J. Tan, et al. A bridge from monotectic alloys to liquid-phase-separated bulk metallic glasses: Design, microstructure and phase evolution. *Acta Materialia*, 61(6):2102–2112, 2013.
- [155] J. Eckert, J. Das, S. Pauly, et al. Mechanical properties of bulk metallic glasses and composites. *Journal of Materials Research*, 22(2):285–301, 2007.
- [156] X. H. Du, J. C. Huang, K. C. Hsieh, et al. Two-glassy-phase bulk metallic glass with remarkable plasticity. *Applied Physics Letters*, 91(13):2005–2008, 2007.
- [157] S. S. Chen, H. R. Zhang, I. Todd. Phase-separation-enhanced plasticity in a Cu_{47.2}Zr_{46.5}Al_{5.5}Nb_{0.8} bulk metallic glass. *Scripta Materialia*, 72-73:47–50, 2014.
- [158] T. A. Waniuk, R. Busch, A. Masuhr, et al. Equilibrium viscosity of the Zr_{41.2}Ti_{13.8}Cu_{12.5}Ni₁₀Be_{22.5} bulk metallic glass-forming liquid and viscous flow during relaxation, phase separation, and primary crystallization. *Acta Materialia*, 46(15):5229–5236, 1998.
- [159] S. Pogatscher, P. J. Uggowitzer, J. F. Löffler. In-situ probing of metallic glass formation and crystallization upon heating and cooling via fast differential scanning calorimetry. *Applied Physics Letters*, 104(25):251908, 2014.
- [160] J. Schroers, A. Masuhr, W. L. Johnson, et al. Pronounced asymmetry in the crystallization behavior during constant heating and cooling of a bulk metallic glass-forming liquid. *Physical Review B*, 60(17):11855–11858, 1999.
- [161] F. C. Frank. Supercooling of Liquids. *Proceedings of the Royal Society A: Mathematical, Physical and Engineering Sciences*, 215(1120):43–46, 1952.

- [162] D. R. Nelson, F. Spaepen. Polytetrahedral Order in Condensed Matter. *Solid State Physics*, 42:1–90, 1989.
- [163] D. Holland-Moritz, D. M. Herlach, K. Urban. Observation of the undercoolability of quasicrystal-forming alloys by electromagnetic levitation. *Physical Review Letters*, 71(8):1196–1199, 1993.
- [164] K. F. Kelton, G. W. Lee, A. K. Gangopadhyay, et al. First x-ray scattering studies on electrostatically levitated metallic liquids: demonstrated influence of local icosahedral order on the nucleation barrier. *Physical review letters*, 90(19):195504, 2003.
- [165] P. H. Gaskell. A new structural model for transition metal–metalloid glasses. *Nature*, 276(5687):484–485, 1978.
- [166] D. B. Miracle. A structural model for metallic glasses. *Nature materials*, 3(10):697–702, 2004.
- [167] D. B. Miracle. The efficient cluster packing model - An atomic structural model for metallic glasses. *Acta Materialia*, 54:4317–4336, 2006.
- [168] D. B. Miracle, T. Egami, K. M. Flores, et al. Structural Aspects of Metallic Glasses. *MRS Bulletin*, 32(August):629–634, 2007.
- [169] D. B. Miracle. A Physical Model for Metallic Glass Structures: An Introduction and Update. *JOM*, 64:846–855, 2012.
- [170] K. J. Laws, D. B. Miracle, M. Ferry. A predictive structural model for bulk metallic glasses. *Nature Communications*, 6(1):8123, 2015.
- [171] E. Ma. Tuning order in disorder. *Nature Materials*, 14(6):547–552, 2015.
- [172] A. Hirata, L. J. Kang, T. Fujita, et al. Geometric frustration of icosahedron in metallic glasses. *Science*, 341(6144):376–379, 2013.
- [173] Y. Q. Cheng, E. Ma. Atomic-level structure and structure-property relationship in metallic glasses. *Progress in Materials Science*, 56(4):379–473, 2011.
- [174] A. Hirata, P. Guan, T. Fujita, et al. Direct observation of local atomic order in a metallic glass. *Nature Materials*, 10(1):28–33, 2011.
- [175] J. Ding, S. Patinet, M. L. Falk, et al. Soft spots and their structural signature in a metallic glass. *Proceedings of the National Academy of Sciences*, 111(39):14052–14056, 2014.
- [176] G. Kumar, P. Neibecker, Y. H. Liu, et al. Critical fictive temperature for plasticity in metallic glasses. *Nature Communications*, 4:1536, 2013.
- [177] Forschungsinstitut für Edelmetalle und Metallchemie (fem), Lehrstuhl für Metallische Werkstoffe (LMW). *Schlussbericht zu dem IGF-Vorhaben 17716N: Legierungsentwicklung und thermoplastisches Formen von 18kt Weißgoldlegierungen*. 2017.
- [178] B. Bochtler. “Characterization of a novel iron-phosphorus based bulk metallic glass forming alloy”. Masterthesis. Saarland University, 2015.
- [179] Alexander Kuball, Benedikt Bochtler, Oliver Gross, et al. On the Bulk Glass Formation in the Ternary Pd-Ni-S System. *Acta Materialia*, 158:13–22, 2018.
- [180] H. W. Kui, a. L. Greer, D. Turnbull. Formation of Bulk Metallic Glass By Fluxing. *Applied Physics Letters*, 45(6):615–616, 1984.
- [181] M. Eisenbart, U. E. Klotz, R. Busch, et al. On the abnormal room temperature tarnishing of an 18 karat gold bulk metallic glass alloy. *Journal of Alloys and Compounds*, 615:S118–S122, 2014.

- [182] J. England, M. W. Phaneuf, A. Laquerre, et al. Ion beam assisted crystallization of amorphous silicon layers using high current density Gallium beams. *Nuclear Instruments and Methods in Physics Research Section B: Beam Interactions with Materials and Atoms*, 272:409–413, 2012.
- [183] J. Carter, E. G. Fu, M. Martin, et al. Effects of Cu ion irradiation in Cu₅₀Zr₄₅Ti₅ metallic glass. *Scripta Materialia*, 61(3):265–268, 2009.
- [184] M. Eisenbart, U. E. Klotz, R. Busch, et al. A colourimetric and microstructural study of the tarnishing of gold-based bulk metallic glasses. *Corrosion Science*, 85:258–269, 2014.
- [185] C. W. Corti. What is a White Gold ? Progress on the Issues ! *The Santa Fe Symposium*, (May):103–120, 2005.
- [186] G. W. H. Höhne, W. F. Hemminger, H.-J. Flammersheim. *Differential Scanning Calorimetry*. 2003.
- [187] C. A. Angell. Liquid fragility and the glass transition in water and aqueous solutions. *Chemical Reviews*, 102(8):2627–2650, 2002.
- [188] Z. Evenson, I. Gallino, R. Busch. The effect of cooling rates on the apparent fragility of Zr-based bulk metallic glasses. *Journal of Applied Physics*, 107(12):123529, 2010.
- [189] H. E. Hagy. Experimental Evaluation of Beam-Bending Method of Determining Glass Viscosities in the Range 108 to 1015 Poises. *Journal of the American Ceramic Society*, 46(2):93–97, 1963.
- [190] T. Egami, S. J. L. Billinge. *UNDERNEATH THE BRAGG PEAKS Structural Analysis of Complex Materials*. Pergamon, 2012.
- [191] T. E. Faber, J. M. Ziman. A theory of the electrical properties of liquid metals. *Philosophical Magazine*, 11:153–173, 1964.
- [192] P. J. Brown, A. G. Fox, E. N. Maslen, et al. Intensity of diffracted intensities. *International Tables for Crystallography*, C:554–595, 2006.
- [193] A. C. Dippel, H. P. Liermann, J. T. Delitz, et al. Beamline P02.1 at PETRA III for high-resolution and high-energy powder diffraction. *Journal of Synchrotron Radiation*, 22:675–687, 2015.
- [194] A. Kuball. “Investigations and improvements of glass formation in Al-based metallic glasses”. Master Thesis. Saarland University, 2016.
- [195] A. Hammersley. Fit2d: an introduction and overview. *European Synchrotron Radi Facility International Report ESRF97HA02T*, 68:1997.
- [196] X. Qiu, J. W. Thompson, S. J. L. Billinge. PDFgetX2: A GUI-driven program to obtain the pair distribution function from X-ray powder diffraction data. *Journal of Applied Crystallography*, 37(4):678, 2004.
- [197] P. F. Peterson, E. S. Božin, T. Proffen, et al. Improved measures of quality for the atomic pair distribution function. *Journal of Applied Crystallography*, 36(1):53–64, 2003.
- [198] S. Wei, M. Stolpe, O. Gross, et al. Structural evolution on medium-range-order during the fragile-strong transition in Ge₁₅Te₈₅. *Acta Materialia*, 129:259–267, 2017.
- [199] J. Schroers, B. Lohwongwatana, W. L. Johnson, et al. Gold based bulk metallic glass. *Applied Physics Letters*, 87(6):404–406, 2005.

- [200] S. Mozgovoy, J. Heinrich, U. E. Klotz, et al. Investigation of mechanical, corrosion and optical properties of an 18 carat Au-Cu-Si-Ag-Pd bulk metallic glass. *Intermetallics*, 18:2289–2291, 2010.
- [201] G. Beck, H.-H. Beyer, W. Gerhartz, et al. *Edelmetalltaschenbuch, Degussa Frankfurt am Main*. 1995.
- [202] P. Rizzi, I. Corazzari, G. Fiore, et al. Ion release and tarnishing behavior of Au and Pd based amorphous alloys in artificial sweat. *Corrosion Science*, 77:135–142, 2013.
- [203] U. E. Klotz, M. Eisenbart. Gold-based bulk metallic glasses: hard like steel, moldable like plastics. *The Santa Fe Symposium*, 1–16, 2013.
- [204] S. L. Wang, H. X. Li, X. F. Zhang, et al. Effects of Cr contents in Fe-based bulk metallic glasses on the glass forming ability and the corrosion resistance. *Materials Chemistry and Physics*, 113:878–883, 2009.
- [205] J. Jayaraj, Y. C. Kim, K. B. Kim, et al. Corrosion behaviors of Fe_{45-x}Cr₁₈Mo₁₄C₁₅B₆Y₂M_x (M = Al, Co, Ni, N and x = 0, 2) bulk metallic glasses under conditions simulating fuel cell environment. *Journal of Alloys and Compounds*, 434-435:237–239, 2007.
- [206] S. Stanojevic, I. Gallino, H. Aboulfadl, et al. Oxidation of glassy Ni-Nb-Sn alloys and its influence on the thermodynamics and kinetics of crystallization. *Acta Materialia*, 102:176–186, 2016.
- [207] Yoko Yoshihisa, Tadamichi Shimizu. Metal Allergy and Systemic Contact Dermatitis: An Overview. *Dermatology Research and Practice*, 2012:1–5, 2012.
- [208] W. Zhang, H. Guo, M. W. Chen, et al. New Au-based bulk glassy alloys with ultralow glass transition temperature. *Scripta Materialia*, 61:744–747, 2009.
- [209] S. Ding, J. Gregoire, J. J. Vlassak, et al. Solidification of Au-Cu-Si alloys investigated by a combinatorial approach. *Journal of Applied Physics*, 111(11):114901, 2012.
- [210] O. Gross, M. Eisenbart, L.-Y. Schmitt, et al. Development of novel 18-karat, premium-white gold bulk metallic glasses with improved tarnishing resistance. *Materials & Design*, 140:495–504, 2018.
- [211] C. Baetzner, N. Lebrun, MSIT® Materials Science International Team. *Au-Cu-Si Ternary Phase Diagram Evaluation · Phase diagrams, crystallographic and thermodynamic data: Datasheet from MSI Eureka in SpringerMaterials*. Ed. by G Effenberg. URL: http://materials.springer.com/msi/docs/sm%7B%5C_%7Dmsi%7B%5C_%7Dr%7B%5C_%7D10%7B%5C_%7D014848%7B%5C_%7D01.
- [212] Z. Evenson. “On the thermodynamic and kinetic properties of bulk glass forming metallic systems”. PhD Thesis. Saarland University, 2012.
- [213] Nico Neuber, Oliver Gross, Miriam Eisenbart, et al. The role of Ga addition on the thermodynamics, kinetics, and tarnishing properties of the Au-Ag-Pd-Cu-Si bulk metallic glass forming system. *Acta Materialia*, 165:315–326, 2019.
- [214] N. Neuber. “Alloy Development and Thermophysical Characterization of Amorphous 18kt White Gold Bulk Metallic Glasses with Improved Tarnishing Resistance”. Master Thesis. Saarland University, 2017.
- [215] U. E. Klotz. Metallurgy and processing of coloured gold intermetallics – Part I : Properties and surface processing. 43(1):4–10, 2010.

- [216] A. Takeuchi, A. Inoue. Metallic Glasses By Atomic Size Difference, Heat of Mixing and Period of Constituent Elements and Its Application To Characterization of the Main Alloying Element. *Materials Transactions*, 46(12):2817–2829, 2005.
- [217] J. Liu, Y. Liu, P. Gong, et al. Combinatorial exploration of color in gold-based alloys. *Gold Bulletin*, 48(3-4):111–118, 2015.
- [218] F. X. Bai, J. H. Yao, Y. X. Wang, et al. Crystallization kinetics of an Au-based metallic glass upon ultrafast heating and cooling. *Scripta Materialia*, 132:58–62, 2017.
- [219] S. Pogatscher, D. Leutenegger, J. E. K. Schawe, et al. Solid–solid phase transitions via melting in metals. *Nature Communications*, 7:11113, 2016.
- [220] P. Tsai, K. M. Flores. A combinatorial strategy for metallic glass design via laser deposition. *Intermetallics*, 55:162–166, 2014.
- [221] S. Ding, Y. Liu, Y. Li, et al. Combinatorial development of bulk metallic glasses. *Nature Materials*, 13(5):494–500, 2014.
- [222] P. Bordeenithikasem, J. Liu, S. A. Kube, et al. Determination of critical cooling rates in metallic glass forming alloy libraries through laser spike annealing. *Scientific Reports*, 7(1):7155, 2017.
- [223] J. H. Na, M. D. Demetriou, O. Abarca, et al. *US20150267286A1: Bulk platinum-copper-phosphorus glasses bearing boron, silver, and gold*. 2015.
- [224] G. Kumar, S. Prades-Rodel, A. Blatter, et al. Unusual brittle behavior of Pd-based bulk metallic glass. *Scripta Materialia*, 65(7):585–587, 2011.
- [225] J. Schroers, W. L. Johnson. Ductile Bulk Metallic Glass. *Physical Review Letters*, 93(25):255506, 2004.
- [226] M. D. Demetriou, M. F. Floyd, C. Crewdson, et al. Liquid-like platinum-rich glasses. *Scripta Materialia*, 65:799–802, 2011.
- [227] M. D. Demetriou, M. E. Launey, G. Garrett, et al. A damage-tolerant glass. *Nature Materials*, 10(2):123–128, 2011.
- [228] B. Lohwongwatana, J. Schroers, W. L. Johnson. “Liquidmetal - Hard 18k and .850 Pt Alloys that can be processed like plastics or blown like glass”. In: *Proceedings of The Santa Fe Symposium on Jewellery Manufacturing Technology*. 2007:289–303.
- [229] J. Schroers, N. Paton. Amorphous metal alloys form like plastics. *Advanced Materials & Processes*, 164(1):61–63, 2006.
- [230] O. Gross, S. S. Riegler, M. Stolpe, et al. On the high glass-forming ability of Pt-Cu-Ni/Co-P-based liquids. *Acta Materialia*, 141:109–119, 2017.
- [231] H. Kato, T. Wada, M. Hasegawa, et al. Fragility and thermal stability of Pt- and Pd-based bulk glass forming liquids and their correlation with deformability. *Scripta Materialia*, 54(12):2023–2027, 2006.
- [232] G. J. Fan, H. J. Fecht, E. J. Lavernia. Viscous flow of the Pd₄₃Ni₁₀Cu₂₇P₂₀ bulk metallic glass-forming liquid. *Applied Physics Letters*, 84(4):487–489, 2004.
- [233] M. D. Demetriou, J. S. Harmon, M. Tao, et al. Cooperative shear model for the rheology of glass-forming metallic liquids. *Physical Review Letters*, 97(6):41–44, 2006.

- [234] J. F. Löffler, J. Schroers, W. L. Johnson. Time–temperature–transformation diagram and microstructures of bulk glass forming Pd₄₀Cu₃₀Ni₁₀P₂₀. *Applied Physics Letters*, 77(5):681–683, 2000.
- [235] I.-R. Lu, G. Wilde, G. P. Görler, et al. Thermodynamic properties of Pd-based glass-forming alloys. *Journal of Non-Crystalline Solids*, 250-252:577–581, 1999.
- [236] R. Busch, E. Bakke, W. L. Johnson. On the Glass Forming Ability of Bulk Metallic Glasses. *Materials Science Forum*, 235-238(1-2):327–336, 1997.
- [237] W. L. Johnson, J. H. Na, M. D. Demetriou. Quantifying the origin of metallic glass formation. *Nature communications*, 7:10313, 2016.
- [238] S. W. Basuki, A. Bartsch, F. Yang, et al. Decoupling of component diffusion in a glass-forming Zr_{46.75}Ti_{8.25}Cu_{7.5}Ni₁₀Be_{27.5} melt far above the liquidus temperature. *Physical Review Letters*, 113(16):1–5, 2014.
- [239] I. Gallino, D. Cangialosi, Z. Evenson, et al. Hierarchical aging pathways and reversible fragile-to-strong transition upon annealing of a metallic glass former. *Acta Materialia*, 144:400–410, 2018.
- [240] S. Hechler, B. Ruta, M. Stolpe, et al. Microscopic evidence of the connection between liquid-liquid transition and dynamical crossover in an ultra-viscous metallic glass former. *Phys. Rev. Lett.* 085603:1–6, 2018.
- [241] Z. Wang, S. V. Ketov, C.L. Chen, et al. Nucleation and thermal stability of an icosahedral nanophase during the early crystallization stage in Zr-Co-Cu-Al metallic glasses. *Acta Materialia*, 132:298–306, 2017.
- [242] S. Mukherjee, Z. Zhou, J. Schroers, et al. Overheating threshold and its effect on time-temperature-transformation diagrams of zirconium based bulk metallic glasses. *Applied Physics Letters*, 84(24):5010–5012, 2004.
- [243] C. Way, P. Wadhwa, R. Busch. The influence of shear rate and temperature on the viscosity and fragility of the Zr_{41.2}Ti_{13.8}Cu_{12.5}Ni_{10.0}Be_{22.5} metallic-glass-forming liquid. *Acta Materialia*, 55(9):2977–2983, 2007.
- [244] S. Wei, F. Yang, J. Bednarcik, et al. Liquid-liquid transition in a strong bulk metallic glass-forming liquid. *Nature communications*, 4:2083, 2013.
- [245] S. Mukherjee, J. Schroers, W. L. Johnson, et al. Influence of Kinetic and Thermodynamic Factors on the Glass-Forming Ability of Zirconium-Based Bulk Amorphous Alloys. *Physical Review Letters*, 94:245501, 2005.
- [246] M. Frey, R. Busch, W. Possart, et al. On the thermodynamics, kinetics, and sub-T_g relaxations of Mg-based bulk metallic glasses. *Acta Materialia*, 155:117–127, 2018.
- [247] G. J. Fan, J. F. Löffler, R. K. Wunderlich, et al. Thermodynamics, enthalpy relaxation and fragility of the bulk metallic glass-forming liquid Pd₄₃Ni₁₀Cu₂₇P₂₀. *Acta Materialia*, 52(3):667–674, 2004.
- [248] S. Sachdev, D. R. Nelson. Theory of the Structure Factor of Metallic Glasses. *Physical Review Letters*, 53(20):1947–1950, 1984.
- [249] P. F. Guan, T. Fujita, A. Hirata, et al. Structural origins of the excellent glass forming ability of Pd₄₀Ni₄₀P₂₀. *Physical Review Letters*, 108(17):1–5, 2012.
- [250] C. Park, M. Saito, Y. Waseda, et al. Structural Study of Pd-Based Amorphous Alloys with Wide Supercooled Liquid Region by Anomalous X-ray Scattering. *Materials Transactions, JIM*, 40(6):491–497, 1999.

- [251] D. Ma, A. D. Stoica, X.-L. Wang. Power-law scaling and fractal nature of medium-range order in metallic glasses. *Nature materials*, 8(1):30–4, 2009.
- [252] T. Nakamura, E. Matsubara, M. Sakurai, et al. Structural study in amorphous Zr-noble metal (Pd, Pt and Au) alloys. *Journal of Non-Crystalline Solids*, 312-314:517–521, 2002.
- [253] D. J. Sordelet, R. T. Ott, M. Z. Li, et al. Structure of Zr x Pt100-x Metallic Glasses. *Metallurgical and Materials Transactions A*, 39(8):1908–1916, 2008.
- [254] K. S. Bondi, A. K. Gangopadhyay, Z. Marine, et al. Effects of microalloying with 3d transition metals on glass formation in AlYFe alloys. *Journal of Non-Crystalline Solids*, 353(52-54):4723–4731, 2007.
- [255] W. Hoyer, R. Jödicke. Short-range and medium-range order in liquid Au-Ge alloys. *Journal of Non-Crystalline Solids*, 192-193:102–105, 1995.
- [256] L. Wang, Y. Q. Wang, C. Peng, et al. Medium-range structural order in liquid Ni₂₀Al₈₀ alloy: Experimental and molecular dynamics studies. *Physics Letters, Section A: General, Atomic and Solid State Physics*, 350(5-6):405–409, 2006.
- [257] Y. W. Bai, X. F. Bian, X. Q. Lv, et al. Heredity of medium-range order structure from melts to amorphous solids. *Journal of Applied Physics*, 112(8):083524, 2012.
- [258] S. A. Khan, X. D. Wang, Q. P. Cao, et al. Structural signature in Au-based amorphous alloys. *Acta Materialia*, 140:31–38, 2017.
- [259] N. A. Mauro, V. Wessels, J. C. Bendert, et al. Short- and medium-range order in Zr₈₀Pt₂₀ liquids. *Physical Review B - Condensed Matter and Materials Physics*, 83(18):1–8, 2011.
- [260] N. A. Mauro, K. F. Kelton. Medium range order in Zr-noble metal eutectic liquids. *Journal of Non-Crystalline Solids*, 358(23):3057–3059, 2012.
- [261] Y. Q. Cheng, E. Ma, H. W. Sheng. Alloying strongly influences the structure, dynamics, and glass forming ability of metallic supercooled liquids. *Applied Physics Letters*, 93(11):111913, 2008.
- [262] H. Lou, X. Wang, Q. Cao, et al. Negative expansions of interatomic distances in metallic melts. *Proceedings of the National Academy of Sciences of the United States of America*, 110(25):10068–72, 2013.
- [263] A. K. Gangopadhyay, M. E. Blodgett, M. L. Johnson, et al. Anomalous thermal contraction of the first coordination shell in metallic alloy liquids. *Journal of Chemical Physics*, 140(4):2014.
- [264] J. Ding, M. Xu, P. F. Guan, et al. Temperature effects on atomic pair distribution functions of melts. *Journal of Chemical Physics*, 140(6):2014.
- [265] S. V. Sukhomlinov, M. H. Müser. Determination of accurate, mean bond lengths from radial distribution functions. *The Journal of Chemical Physics*, 146(2):024506, 2017.
- [266] X. J. Liu, Y. Xu, X. Hui, et al. Metallic liquids and glasses: Atomic order and global packing. *Physical Review Letters*, 105(15):1–4, 2010.
- [267] X. W. Fang, C. Z. Wang, S. G. Hao, et al. Spatially resolved distribution function and the medium-range order in metallic liquid and glass. *Scientific Reports*, 1:19–21, 2011.
- [268] C. H. Bennett. Serially deposited amorphous aggregates of hard spheres. *Journal of Applied Physics*, 43(6):2727–2734, 1972.

- [269] N. Mattern, H. Hermann, S. Roth, et al. Structural behavior of Pd₄₀Cu₃₀Ni₁₀P₂₀ bulk metallic glass below and above the glass transition. *Applied Physics Letters*, 82(16):2589–2591, 2003.
- [270] A. R. Yavari, A. L. Moulec, A. Inoue, et al. Excess free volume in metallic glasses measured by X-ray diffraction. *Acta Materialia*, 53(6):1611–1619, 2005.
- [271] Q. Zeng, Y. Lin, Y. Liu, et al. General 2.5 power law of metallic glasses. *Proceedings of the National Academy of Sciences*, 113(7):1714–1718, 2016.
- [272] N. Mattern, M. Stoica, G. Vaughan, et al. Thermal behaviour of Pd₄₀Cu₃₀Ni₁₀P₂₀ bulk metallic glass. *Acta Materialia*, 60(2):517–524, 2012.
- [273] S. Lan, Y. Ren, X. Y. Wei, et al. Hidden amorphous phase and reentrant supercooled liquid in Pd-Ni-P metallic glasses. *Nature Communications*, 8:14679, 2017.
- [274] J. J. Lewandowski, W. H. Wang, A. L. Greer. Intrinsic plasticity or brittleness of metallic glasses. *Philosophical Magazine Letters*, 85(2):77–87, 2005.